

University of Hong Kong

Doctoral Thesis

Electromagnetic response in two dimensional flat band systems

Author:
Xu Zhang

Supervisor:
Prof. Zi Yang Meng

A thesis submitted in fulfillment of the requirements for the degree of Doctor of Philosophy

in the

Department of Physics
Faculty of Science

August 17, 2024

Abstract of thesis entitled

Electromagnetic response in two dimensional flat band systems

Submitted by

Xu Zhang

for the degree of Doctor of Philosophy

at The University of Hong Kong

in August, 2024

Electromagnetic response has become the most powerful way for detecting, controlling and displaying in all kinds of electronics. The well developed band theory plays an essential role in understanding and designing semiconductor devices. However, with the discovery of fractional quantized Hall conductance and high-temperature superconductor, band theory based on mean field approximation with perturbation has been challenged because of poor prediction in those systems. The reason why mean field breaks down is generally attributed to the existence of flat bands, where the interaction cannot be seen as perturbation compared with the marginal kinetic energy of flat band particles. This new field beyond mean field called strong correlation requires researchers spare no effort to derive a reasonable numerical result or analytical explanation.

At the same time with the discover of two dimensional materials represented by graphene, study based on two dimensional materials becomes popular because of the simplicity compared with three dimensions and also the band topology rising from quantized Hall conductance. And very recently, the discovery of a new method tuning band flatness of two dimensional materials represented by twisted bilayer graphene calls researcher from strong correlation field into this party.

In this thesis entitled electromagnetic response in two dimensional flat band systems, I will introduce my study within three typical two dimensional flat band systems, i.e., twisted bilayer graphene, twisted transition metal dichalcogenides and Landau level with moiré potential as Chapter 3, Chapter 4 and Chapter 5 respectively. Flat band limit is usually taken in analytical derivation, and determinant quantum Monte Carlo introduced in Chapter 2 together with some developments by me is the main numerical methodology in my study. Order and degeneracy of ground state, single-particle and two-particle Green's function and excitation spectra, finite temperature phase and phase transition, linear and nonlinear conductance are main results of this thesis for involved topics.

Finally, I would like to say this field of two dimensional strong correlation materials is still full of vigour and vitality with striking experiment or theory emerging from time to

time. Some uncovered topics of my study may be mentioned at the end of corresponding chapters and left for the future research.

Electromagnetic response in two dimensional flat band systems

by

Xu Zhang
B.S. *Nankai University*

A Thesis Submitted in Partial Fulfilment
of the Requirements for the Degree of
Doctor of Philosophy

at

University of Hong Kong
August, 2024

Copyright ©2024, by Xu Zhang
all rights reserved.

Declaration

I, Xu Zhang, declare that this thesis titled, "Electromagnetic response in two dimensional flat band systems", which is submitted in fulfillment of the requirements for the Degree of Doctor of Philosophy, represents my own work except where due acknowledgement have been made. I further declared that it has not been previously included in a thesis, dissertation, or report submitted to this University or to any other institution for a degree, diploma or other qualifications.

Signed: _____

Date: August 17, 2024

For Mama and Papa

Acknowledgements

The special space for the first paragraph is left blank to acknowledge **nobody**. This poor man is hooked by the goddess of physics incurably such that every time he clumsily turn to a girl in real space he fails. Thus, the people listed in paragraphs below are so indispensable for him, that they do not only help him physically, but more importantly also give him countless spirit support.

The author firstly would like to thank his dad and mum, Yunlai Zhang and Xiuxia Wu. In Chinese, their given names mean "clouds coming" and "rosy clouds shining". It is their love and kindness raise this young man up, build him a handsome and genteel shape today. He loves them a thousand times and a thousand years.

Next, the author would like to thank supervisors who shine his road forward in the adventure of physics. They are Prof. Jiangping Hu, Zi Yang Meng and Kai Sun by timeline. Prof. Jiangping Hu has helped him find the taste of a good research and Prof. Zi Yang Meng has guided him to use the sharp numerical weapon Quantum Monte Carlo. Finally, Prof. Kai Sun has arranged him as a kind host in Michigan and shared lots of theoretical skills and knowledge with him. It is their sense of responsibility for passing the knowledge spark to the next generation that helps him grow up from a little rookie to a knight who has essential equipments beating a monster in physical world on his own. The author also would like to thank many other predecessors who are willing to discuss with him, share their wisdom and also offer him a position when he was anxiously looking for a postdoc. It is their passion for physics and acknowledgement firm his decision of moving on in his adventure.

Last but not least, the author would like to thank his friends who have shared him their kindness and helped him both in study and life. He gives his special thanks to his group mates Gaopei Pan, Bin-Bin Chen and Heqiu Li who have discussed, helped and finished most of his works. The author also especially thanks Nan Cheng in Prof. Kai Sun's group who gives him countless help during his visit in Michigan. He thanks his good friend Mingyang Liu, Chengkang Zhou, Jiarui Zhao, Huiyuan Zheng, Chengxin Xiao, Xuchen Yang, Jianju Tang, Huanwen Wang, Ruibin Liu and many others in department of physics for discussing all kinds of physics and non-physics questions in his everyday life. Actually, the name list is so long that it is impossible to list them all. The author sincerely acknowledge all of them who has given him suggestions, guidances and supports.

Xu Zhang
University of Hong Kong
August 17, 2024

List of Publications

Journals:

[1] **Xu Zhang**, Gaopei Pan, Yi Zhang, Jian Kang, Zi Yang Meng, "Momentum space quantum monte carlo on twisted bilayer graphene," Chinese Physics Letters 38 (7), 077305 (2021).

[2] Gaopei Pan, **Xu Zhang**, Heqiu Li, Kai Sun, Zi Yang Meng, "Dynamical properties of collective excitations in twisted bilayer graphene," Physical Review B 105 (12), L121110 (2022).

[3] **Xu Zhang**, Kai Sun, Heqiu Li, Gaopei Pan, Zi Yang Meng, "Superconductivity and bosonic fluid emerging from moiré flat bands," Physical Review B 106 (18), 184517 (2022).

[4] **Xu Zhang**, Gaopei Pan, Xiao Yan Xu, Zi Yang Meng, "Fermion sign bounds theory in quantum monte carlo simulation," Physical Review B 106 (3), 035121 (2022).

[5] Gaopei Pan, **Xu Zhang**, Hongyu Lu, Heqiu Li, Bin-Bin Chen, Kai Sun, Zi Yang Meng, "Thermodynamic characteristic for a correlated flat-band system with a quantum anomalous hall ground state," Physical Review Letters 130 (1), 016401 (2023).

[6] **Xu Zhang**, Gaopei Pan, Bin-Bin Chen, Heqiu Li, Kai Sun, Zi Yang Meng, "Polynomial sign problem and topological Mott insulator in twisted bilayer graphene," Physical Review B 107 (24), L241105 (2023).

[7] Meizhen Huang, Zefei Wu, **Xu Zhang**, Xuemeng Feng, Zishu Zhou, Shi Wang, Yong Chen, Chun Cheng, Kai Sun, Zi Yang Meng, Ning Wang, "Intrinsic nonlinear Hall effect and gate-switchable Berry curvature sliding in twisted bilayer graphene," Physical Review Letters 131 (6), 066301 (2023).

[8] Cheng Huang, **Xu Zhang**, Gaopei Pan, Heqiu Li, Kai Sun, Xi Dai, Zi Yang Meng, "Evolution from quantum anomalous Hall insulator to heavy-fermion semimetal in twisted bilayer graphene," Physical Review B 109 (12), 125404 (2024).

[9] **Xu Zhang**, Gaopei Pan, Bin-Bin Chen, Kai Sun, Zi Yang Meng, "Integral algorithm of exponential observables for interacting fermions in quantum Monte Carlo simulations," Physical Review B 109 (20), 205147 (2024).

[10] Bin-Bin Chen, **Xu Zhang**, Yuxuan Wang, Kai Sun, Zi Yang Meng, "Phases of SO(5) Nonlinear Sigma Model with a Topological Term on a Sphere: Multicritical Point and Disorder Phase," Physical Review Letters 132 (24), 246503 (2024).

[11] Soumya Sankar, Ruizi Liu, Cheng-Ping Zhang, Qi-Fang Li, Caiyun Chen, Xue-Jian Gao, Jiangchang Zheng, Yi-Hsin Lin, Kun Qian, Ruo-Peng Yu, **Xu Zhang**, Zi Yang Meng, Kam Tuen Law, Qiming Shao, Berthold Jäck, "Experimental Evidence for a Berry Curvature Quadrupole in an Antiferromagnet," Physical Review X 14 (2), 021046 (2024).

[12] **Xu Zhang**, Kai Sun, Zi Yang Meng, "The" Sign problem" of the 3rd order anomalous Hall effect in topological magnetic materials," arXiv:2303.00819 (2023).

[13] Bin-Bin Chen, **Xu Zhang**, Zi Yang Meng, "Emergent Conformal Symmetry at the Multicritical Point of (2+1)D SO(5) Model with Wess-Zumino-Witten Term on Sphere," arXiv preprint arXiv:2405.04470 (2024).

Contents

Abstract i

Declaration i

Acknowledgements ii

List of Publications iii

List of Figures vii

List of Tables xiii

List of Abbreviations xv

1 Introduction 1
- 1.1 Why flat band and why two dimension . . . 1
- 1.2 Method: the pain and the gain . . . 3
- 1.3 Two dimensional flat band systems . . . 3
- 1.4 Summary of original results . . . 4

2 Methodology 5
- 2.1 Linear response and semi-classical Boltzmann equation . . . 5
  - 2.1.1 Linear response and Hall conductance . . . 5
  - 2.1.2 Semi-classical Boltzmann equation . . . 11
- 2.2 Determinant Quantum Monte Carlo (DQMC) . . . 13
  - 2.2.1 General formula in momentum space . . . 13
  - 2.2.2 Observable measurement . . . 17
  - 2.2.3 Numerical stability . . . 19
  - 2.2.4 Configuration update . . . 21
- 2.3 Sign problem and sign bounds theory . . . 24
  - 2.3.1 Introduction to sign problem . . . 24
  - 2.3.2 Sign bounds theory . . . 24
- 2.4 Exponential observable measurement . . . 26
  - 2.4.1 Rényi entropy and Rényi entanglement entropy . . . 26
  - 2.4.2 Entanglement Entropy in DQMC language . . . 28
- 2.5 Further discussion . . . 31

3 Twisted bilayer graphene (TBG) 33
3.1 Outline . . . 33
3.2 Graphene and Dirac dispersion . . . 33
3.3 Bistritzer-MacDonald (BM) model for small angle TBG . . . 36
3.4 Gate-tunable nonlinear Hall effect in topological flat bands . . . 39
3.5 Projected Coulomb interaction and half filling ground state . . . 48
3.5.1 DQMC for TBG Hamiltonian with Coulomb Interaction . . . 49
3.5.2 Exact solution and DQMC results for ground state and excitation 52
3.6 Polynomial sign problem and topological insulators at chiral integer fillings 60
3.6.1 Ground state energy, degeneracy and sign bounds . . . 60
3.6.2 DQMC results for sign bounds and $\nu = \pm 1$ case . . . 65
3.7 Further discussion . . . 70

4 Twisted transition metal dichalcogenides (TTMD) 71
4.1 Outline . . . 71
4.2 K valley and Γ valley flat bands and half filling insulators . . . 71
4.2.1 Γ valley twisted double layer WS_2 . . . 72
4.2.2 K valley twisted double layer $MoTe_2$ . . . 76
4.3 Inter-valley attraction and superconductor near $SU(2)$ limit . . . 80
4.4 Further discussion . . . 87

5 Landau level with moiré potential 89
5.1 Landau level basis of Dirac fermion in magnetic field . . . 89
5.2 Hofstadter's butterfly in super-Moiré of graphene . . . 92
5.3 Further discussion . . . 104

A Mathematical preparation on Quantum Monte Carlo 105
A.1 Markov chain Monte Carlo . . . 105
A.2 Wick's theorem . . . 107
A.3 Suzuki–Trotter expansion . . . 110
A.4 Hubbard–Stratonovich transformation . . . 110

B Universality class and scaling behavior 113

C Young Diagram 117

D Stochastic analytic continuation (SAC) 121

Bibliography 125

List of Figures

2.1 Band structure along high-symmetry lines from Bistritzer-MacDonald (BM) model for twisted bilayer graphene (TBG). Blue and red bands are flat bands from two valleys and dark bands are remote bands separated with a finite gap. The detailed parameters for the plot can be found in Chapter 3. 15

2.2 The 2nd and 3rd Rényi entropy for 4×4 dichotomy half-filled square lattice Hubbard model. Blue dots in (a), (b) indicates $S_A^{(2)}$, $S_A^{(3)}$ from DQMC integral algorithm and the dark dashed line is result of density matrix renormalization group (DMRG) at zero temperature. This figure comes from Ref [3]. 30

3.1 The schematic plot of honeycomb lattice with A, B sublattice. Green circles label unit cells and orange arrows define vectors. 34

3.2 Illustration of real space AA,AB,BA region and reciprocal lattice vectors G_1, G_2 in (a) and momentum space graphene Brillouin zone (BZ), moiré BZ and q_1, q_2, q_3 definition in (b). These figures come from Ref [77, 78] . 37

3.3 Schematic moiré BZ without strain and the high symmetry red lines are shown in (a). The band structure with strain along the red lines is shown in (b). This figure comes from supplemental material of Ref [4]. 40

3.4 Band structure and Berry curvature Ω for flat valence band with electrostatic energy difference V from $-0.2eV$ to $0.18eV$ are shown in (a) and (b) from top left to bottom right with interval $0.02eV$. 43

3.5 Basic characterization of the TBG device. (a) Schematic structure of the 1.30° TBG device. The carrier density n and the displacement field D are controlled by the top and bottom gates with gate voltage V_{tg} and V_{bg}, respectively. (b) The four-probe measurement scheme. Here, we measure the longitudinal voltage V_{xx} and Hall voltage V_{xy} in the presence of an AC longitudinal current I^ω. (c) The longitudinal resistance $R_{xx} = V_{xx}/I^\omega$ (top panel) and the carrier density measured via the Hall effect n_H (middle panel) as functions of ν and V_{bg} ($V_{tg} = 0V$). The vertical dashed lines denote the CNP and fully filled moiré bands. The second harmonic Hall voltage $V_\perp^{2\omega}$ as a function of filling factor ν measured at $I^\omega = 100nA$ and $T = 1.5K$ is shown in bottom panel. These figures come from Ref [4]. 46

3.6 Electric field tunable nonlinear Hall effect. (a) Filling and displacement field mapping of $V_{\perp}^{2\omega}$ measured at $T = 1.5K$. Dashed lines marked with p and n indicate $\nu = -1.5$ and $\nu = +1$, respectively. Dash dotted lines marked with 1, 2 and 3 indicate three different fields: $D = +0.4,\ 0,\ -0.4V/nm$. Their intersection points are named as shown in the figure. (b) $V_{\perp}^{2\omega}$ versus D measured at $\nu = -1.5$ at $I^{\omega} = 100nA$. (c) $V_{\perp}^{2\omega}$ versus I^{ω} at various displacement fields at $\nu = -1.5$. Dots are the experimental data and the solid lines are parabolic fittings. (d),(e) Same as (b) and (c) for $\nu = +1$. These figures come from Ref [4]. 47

3.7 Electric field tunable nonlinear Hall effect signal from experiment and simulation. Filling and displacement field mapping of $V_{\perp}^{2\omega}$ and Λ at $T = 1.5K$ from experiment and simulation are shown in (a) and (b) respectively. 47

3.8 (a) Upper panel shows the BZ folding in TBG, with the small hexagon representing the moiré BZ. $K_{1,2}^{\pm}$ are the Dirac points for valley $\pm$ and layer 1 and 2, θ is the rotating angle. In lower panel, G_1 and G_2 are the reciprocal lattice vectors of the moiré BZ. The yellow dots are the allowed momentum transfer $q + G$ points in DQMC. Here we consider momentum transfer up to G, which means for a 6×6 mesh in moiré BZ, the allowed number of $q + G$ is 126. (b) and (c) show the comparison at the CNP of the single-particle excitation gap at the chiral limit ($u_0 = 0$) and realistic case ($u_0 = 0.06$) between exact solution and the DQMC results. The DQMC gaps are obtained from fitting the imaginary time decay of the fermion Green's function. These figures come from Ref [5]. 50

3.9 (a) Single-particle spectra at $T = 0.667meV$, $u_0 = 60meV$ and $L = 9$, which shows an insulating gap $\sim 10meV$. The dashed lines are the analytic computation of the lowest single-particle excitation at the flat-band limit. (b) Dynamical spectra of IVC with the same parameters. Sharp and ferromagnetic-like valley waves are observed near $q = \Gamma$ and a fit of $c\,q^2$ gives rise to $c = 31.32 \pm 0.03$ (black solid line in (b)). At the energy scale of twice the single-particle gap, $\sim 20meV$, valley waves are over-damped into the particle-hole continuum. The dashed lines are the analytic computation of the Goldstone mode at the flat-band limit. (c) $S(q = \Gamma)$, the correlation of order parameters, for VP and IVC at $u_0 = 33$ meV and $L = 6$, as a function of temperature. (b) The same quantity at $u_0 = 60$ meV with both $L = 6$ and $L = 9$. When kinetic energy is ignored, the two order parameters are almost degenerate. When the kinetic energy is taken into account ("with kin"), this degeneracy is lifted. At $u_0 = 33$ meV, the splitting between VP and IVC is weak. This splitting becomes more pronounced at $u_0 = 60$ meV, indicating that IVC is more favored at low temperatures in comparison to VP, although the competition between these two symmetry-breaking channels remains. These figures come from Ref [6]. 56

3.10 $\langle sign \rangle$ versus filling ν (a,c,e) and $\langle sign \rangle_b$ versus filling ν (b,d,f) at low temperature $T = 1meV$. The fillings of $\nu < 0$ are symmetric with respect to $\nu = 0$ via the particle-hole symmetry. (a-b) are the chiral limit $\gamma = 0$ cases, (c-d) are the non-chiral $\gamma = 0$ cases where we take $u_0 = 0.06eV$ and (e-f) are the chiral limit $\gamma = 4$ cases. (a,c,d) are the average sign $\langle sign \rangle$ for $L = 3(N_k = 9)$ and $L = 4(N_k = 16)$ measured from DQMC for filling from $\nu = 0$ to $\nu = 4$. (b,d,f) are the sign bounds $\langle sign \rangle_b$ for $L = 3(N_k = 9)$ and $L = 4(N_k = 16)$ measured from DQMC (solid line) and derived from exact solution (ES) at the low temperature limit for filling $\nu = 1, 2$ (dash line values). The ES values in (b) are 1119/3278, 3630/111493 for $L = 3$ at $\nu = 1, 2$ and 945/4357, 183/14912 for $L = 4$ at $\nu = 1, 2$. The ES values are 1/10 for $L = 3$, 1/17 for $L = 4$ at $\nu = 2$ in (d) and 100/2601 for $L = 3$, 71/5201 for $L = 4$ at $\nu = 2$ in (f). These figures come from Ref [2]. 67

3.11 (a) Chern band polarization correlation function S versus T. At low temperature, the Chern number approaches to 1. (b) 2D Ising universality class crossing to determine the phase transition point at $T_c \sim 1.8meV$, denoted by the dashed line. These figures come from Ref [2]. 68

3.12 (a) Analytical excitation spectra along a high symmetry path in moiré BZ. The red line labels the single particle excitations. Blue lines show the 10 lowest charge neutral excitons between bands with the same Chern number. The yellow lines label the 10 lowest charge neutral excitons between opposite Chern bands, which are responsible to the restoration of time reversal symmetry. (b-d) Local density of states $N(\omega)$, the single particle spectra $A(\Gamma, \omega)$ and $A(M, \omega)$ obtained from the DQMC-SAC scheme as a function of T. Different lines are lifted in y direction with the amount of $\Delta\beta = \Delta(1/T)$ for clarity. Between the high temperature metal-like phase and the low temperature TMI phase, pseudogap behavior can be found at $T^\star \sim 2meV$ above $T_c = 1.8meV$. These figures come from Ref [2]. 69

4.1 (a) Band structure of Γ valley TTMD 1.1° twisted WS_2. (b) Band structure of K valley 1.2° twisted $MoTe_2$. These figures come from Ref [171, 172]. 72

4.2 (a) Excitation spectra of Γ valley TTMD 1.2° twisted WS_2 where red lines label single-particle excitations and blue lines label two-particle charge-neutral excitations. (b) Zoom in for the two lowest lines in (a) where a soft Goldstone mode can be observed. 75

4.3 (a) Excitation spectra of K valley TTMD 1.2° twisted $MoTe_2$ where red lines label single-particle excitations and blue lines label two-particle charge-neutral excitations. (b) Zoom in for the two lowest lines in (a) where a gap can be observed. 78

4.4 DQMC simulations of the flat-band limit (left column) and away from the flat-band limit (right column). The bandwidths of non-interacting band structures are set to 0 and $0.8meV$ respectively. (a-b) Phase diagrams. In the flat-band limit (a), a finite chemical potential drives the system into a trivial insulator with either empty ($\mu \ll 0$) or complete filled ($\mu \gg 0$) bands. In (b), the yellow/purple region is the pseudogap (PG)/ super-compressible bosonic fluid (SCBF) phase, and the blue region marks the superconducting (SC) dome. (c-d) Density of states for a 9×9 system at $\mu = 0$. The Cooper gap survives above the superconducting transition temperature and turns into a pseudogap above $T \sim 0.3$ for both flat-band limit (c) and finite band dispersion (d). The single-particle spectrum is almost determined by the strength of interaction since the band dispersion is small. (e-f) Critical scaling of $P \times L^{\eta}$ versus T with BKT anomalous dimension $\eta = 1/4$. The crossing point of different system sizes ($L = 6, 7, 8, 9$) marks the superconducting transition temperature: $T_c \sim 0$ in (e) and ~ 0.13 in (f). (g-h) Inverse of compressibility κ for $L = 6, 7, 8, 9$ at $\mu = 0$. At low temperature, diverged compressibility κ in (g) converges in superconducting phase as shown in (h). These figures come from Ref [7]. 81

4.5 Excitation spectrum for inter-valley attractive model where the system size is 12×12. Red line and blue lines are used to label single-particle excitation and charge-2e excitation along high symmetry lines. This figure comes from Ref [7]. 86

5.1 Schematic plot of deriving super-moiré reciprocal vectors. Dashed lines label x and y axis from aligned hbn, the blue arrows label the reciprocal vectors from graphene/hbn moiré, the orange arrow labels the reciprocal vector from twisted hbn/hbn and the yellow arrows label the super-moiré reciprocal vectors. 93

5.2 Density of states and Drude conductance versus filling $\nu_{g/h}$ of graphene/hbn moiré bands. (a) Density of states (without normalization) versus filling with $V_{h/h} = 0$ (blue line) and $V_{h/h} = 100meV$ (red line). (b) Drude conductance along G_1 and G_2 directions with $V_{h/h} = 0$ (blue and red lines) and with $V_{h/h} = 100meV$ (purple and yellow lines) versus filling. . . 96

5.3 Energy spectra versus magnetic flux p/q for $V_{h/h} = 0$ (a) and $V_{h/h} = 100meV$ (b). The dark dots and red dots label states from different valleys and the colored gaps are identified with quantized Hall conductance by Diophantine equation. Only [-20,20] quantized Hall conductance are plotted and we take a cutoff for $N(p, \theta) \times p \approx 2200$ for (a) and $N(p, \theta) \times p \approx 22000$ for (b). 101

5.4 Density of states map with filling of graphene/hbn bands $\nu_{g/h}$ and magnetic flux p/q for $V_{h/h} = 0$ (a) and $V_{h/h} = 100meV$ (b). The cutoff setting is the same as used in Fig 5.3 and we take $kT = 2meV$ for plotting broadening density of states where deep blue indicates low density of states corresponding a gap. One can read the quantized Hall conductivity from the slop of blue lines directly. 102
5.5 Drude conductance σ_{xx} map with filling of graphene/hbn bands $\nu_{g/h}$ and magnetic flux p/q for $V_{h/h} = 0$ (a) and $V_{h/h} = 100meV$ (b). The cutoff setting is the same as used in Fig 5.3 and we take $kT = 2meV$ for computing $\frac{\partial f^0}{\partial \epsilon_n}$. One can see the small $V_{h/h} = 100meV$ can produce obvious oscillation at integer super-moiré flux while the amplitude of σ_{xx} becomes much smaller than $V_{h/h} = 0$. 104

List of Tables

3.1 List of the sign structure for TBG Hamiltonian [5]. 52
3.2 Scaling of the sign bound $\langle sign \rangle_b$ at low temperature and large moiré lattice size $N_k = L^2$ [2]. A power-law function of N_k indicates that the sign problem is (at most) polynomial. ✗ indicates the sign bound decays to zero exponentially. 65

List of Abbreviations

2D	**2** **D**imensions
AC	**A**lternating **C**urrent
BCS	**B**ardeen-**C**ooper-**S**chrieffer
BKT	**B**erezinskii-**K**osterlitz-**T**houless
BM	**B**istritzer-**M**acDonald
BZ	**B**rillouin **Z**one
CDW	**C**harge **D**ensity **W**ave
CNP	**C**harge **N**eutrality **P**oint
DC	**D**irect **C**urrent
DMRG	**D**ensity **M**atrix **R**enormalization **G**roup
DQMC	**D**eterminant **Q**uantum **M**onte **C**arlo
ED	**E**xact **D**iagonalization
ES	**E**xact **S**olution
FQAH	**F**ractional **Q**uantum **A**nomalous **H**all
hbn	**h**exagonal **b**oron **n**itride
IVC	**I**nter-**V**alley **C**oherent
LHS	**L**eft-**H**and **S**ide
LL	**L**andau **L**evel
PG	**P**seudo**G**ap
PMF	**P**robability **M**ass **F**unction
QAH	**Q**uantum **A**nomalous **H**all
QMC	**Q**uantum **M**onte **C**arlo
RG	**R**enormalization **G**roup
RHS	**R**ight-**H**and **S**ide
SAC	**S**tochastic **A**nalytic **C**ontinuation
SC	**S**uper**C**onductivity
SCBF	**S**uper-**C**ompressible **B**osonic **F**luid
SP	**S**pin **P**olarization
TBG	**T**wisted **B**ilayer **G**raphene
TMI	**T**opological **M**ott **I**nsulator
TTMD	**T**wisted **T**ransition **M**etal **D**ichalcogenides
VP	**V**alley **P**olarization

Chapter 1

Introduction

1.1 Why flat band and why two dimension

After the Third Industry Revolution[1], electromagnetic response becomes one of leading power for changing the world. With the development of quantum mechanics, physicists realize it is the electrons dominant the electromagnetic response in materials. However, tracking 10^{23} electrons in a material can never be a possible work and some approximations have to be involved.

A single electron within a single atomic potential (e.g., hydrogen atom problem) is always easy to solve and we call those solutions atomic orbitals. Now imagine there are many atoms which are well separated with each other. Even though the high energy atomic orbitals from different atoms may have overlap, as long as it is the low energy situation one cares, the low energy orbitals can be seen as almost orthogonal. Taking all of those low energy orbitals into consideration, we have a basis (not complete since we ignore high energy orbitals) for describing many electrons within a gas-like material. Actually in this case, one may notice the dynamics of electrons is actually trivial since they almost stay in the bond state of the atoms they belong to and it is the dynamics of those atoms which really dominants the property of this gas-like material.

Now we enlarge the density of atoms which makes electrons low energy orbitals overlap. Atoms will bond with each other to form a solid with a crystal structure. The dynamics of atoms is almost killed (except for low energy vibration which gives the phonon modes and can play importance role in superconductor pairing) and the center of each atomic orbital is set down. Since low energy atomic orbitals cannot be seen as orthogonal, we need Schmidt orthogonalization to reorganize the basis (sometimes those low energy atomic orbitals are not good enough since we are away from atomic limit and some other orbitals, like plane waves, should also be involved in this orthogonalization process). We allocate those orbitals to each unit cell to keep the discrete

[1] The Third Industrial Revolution (from Wikipedia) is a historical period that began in the mid-20th century to the early 21st century. It is characterized by a rapid shift from traditional industries, as established during the Industrial Revolution, to an economy centered on information technology. The onset has been linked to the development of the transistor in 1947 and the optical amplifier in 1957. These technological advances have had a significant impact on the way information is processed and transmitted.

translation symmetry and then one can write down the Hamiltonian $\hat{H} = \hat{H}_0 + \hat{H}_I$ in Fock space by computing the overlap of $\langle i|\hat{H}_0|j\rangle$ and $\langle ij|\hat{H}_I|kl\rangle$, where $\hat{H}_0, \hat{H}_I$ are two-fermion and four-fermion operators and $|i\rangle$ labels ith orthogonal orbital. If we assume $\langle ij|\hat{H}_I|kl\rangle \ll \langle i|\hat{H}_0|j\rangle$, we can always write down the zero-order perturbation Hamiltonian in momentum space due to the discrete translation symmetry.

$$H_0 = \sum_{k,i,j} h_{k;i,j} c^\dagger_{k,i} c_{k,j} \tag{1.1}$$

At each momentum k, this Hamiltonian whose dimension is equal to amount of orthogonal orbitals in each unit cell (let's call it N_i) can be diagonalized separately. When we consider large-size limit (thermodynamic limit), the k mesh will become so dense that one derives the N_i-band solution for this Hamiltonian.

But how good is this $H \approx H_0$ approximation? Let's check the self-consistent property case by case below. One can put the chemical potential between two band (charge excitation has a gap) or within a band (charge excitation is gapless) to identify an insulator or a metal (still assume $\langle ij|\hat{H}_I|kl\rangle \ll \langle i|\hat{H}_0|j\rangle$ now). For a gapped system, usually we are qualitatively safe since perturbation $\frac{\langle ij|\hat{H}_I|kl\rangle}{\Delta} \ll 1$ can be promised where Δ is the smallest many-body energy gap (for a gapped system it is just the band gap), i.e., an insulator is still an insulator with a modified gap. For chemical potential lying in the center of a dispersive band, the many-body energy spectrum is gapless and Fermi surface can be either breakdown (e.g., due to attractive interaction to form a superconductor or due to nesting to form a charge density wave insulator) or survive in a Fermi liquid. By considering all kinds of order parameters and computing the ground state, one can also qualitatively determine the perturbative ground state from a mean field solution. However, for the chemical potential lying in a flat band, $\langle ij|\hat{H}_I|kl\rangle$ is so large compared with the band width that the assumption $\langle ij|\hat{H}_I|kl\rangle \ll \langle i|\hat{H}_0|j\rangle$ breaks down, together with mean field theory. This mysterious, primitive and attractive field is called strong correlation, and the flat band will just be one storyline of this thesis.

On the other hand, from the point view of renormalization group for O(N) symmetry system with dimension larger than four, the mean field phase transition theory is quantitatively correct while the mean field breaks down for dimension equal or less than two due to the large fluctuation. Mermin-Wagner theorem states there is no long-range order associated with breaking of continuous symmetries (e.g., O(2)) in dimension equal or less than two while the critical XY phase with quasi-long-range order gives a vivid example that this lower critical dimension two is far from trivial. Actually, two spacial dimension (plus one imaginary time quantum dimension) becomes the most simple and non-trivial island of studying all kinds of non-trivial phase and phase transition, especially after the discovery of the first two dimensional materials, graphene. And just several years later, the realization of tunable flat bands in two dimensional materials (e.g., twisted bilayer graphene) even attracts more and more young and energetic researchers (including me) in strong correlation field to study electromagnetic response in those two dimensional flat band systems.

1.2 Method: the pain and the gain

To consider four-fermion interaction, a naive way is to diagonalize the Hamiltonian within many-body Hilbert space. However, the dimension of this space will grow exponentially with the system size $\propto 2^{N_i \times N_k}$ (each state on each k point can be either occupied or empty for fermion). If we are considering the simplest strong correlation case that one flat band is well separated with remote bands and the interaction is much smaller than the band gap, as the band insulator case, one can assume the remote bands give no contribution and ignore those degrees of freedom. Now directly we reduce the complexity to $\propto 2^{N_k}$. However, one may notice this rude force cutoff will break the completeness of the wave function so that the original fermions (anti-commute) now become ill-defined (not anti-commute). But remember the real particle we study should be fermion and it is the approximation we take breaks this rule so that we will recover this constrain by directly require those pseudo-particles after cutoff are fermions (anti-commute). This step is the pain we have to pay.

The gain is that no matter how many bands at the very beginning, we can always reduce it to a single flat band (or few flat bands) problem. This means even though we take redundant atomic orbitals in a unit cell or we use continuous model folded in a Brillouin zone which has even infinite bands, the final effective model is always the same. The definition of particle density and the current density coming from the commutation relation of particle density and the Hamiltonian should also be modified after this projection. Since we require the particle after the cutoff should be the "effective" fermion, the density operator should be based on it but not directly from the original real space definition and the current operator should come from the commutation between this "effective" particle density operator and the "effective" Hamiltonian after the cutoff to promise the current conservation.

Now we have introduced all the implicit setting in studying of this thesis. I will mainly use exact diagonalization, analytical solution and numerical determinant quantum Monte Carlo method in the study, and the further approximation of each method will be mentioned accordingly in the corresponding sections.

1.3 Two dimensional flat band systems

Different from the traditional way of tuning flat band with strong magnetic field forming Landau level, utilize the moiré potential by tuning twist angle of stacked two dimensional materials recently becomes a fancy and effective method to form flat band system. After the introduction of the methodology and my contribution for the development in Chapter 2, I will introduce two main moiré materials with flat bands, twisted bilayer graphene and twisted transition metal dichalcogenides, as Chapter 3 and Chapter 4. In the last Chapter 5, I will turn back to strong magnetic field Landau level case but with moiré potential involved, and discuss the moiré materials under both electric and

magnetic regulation. Some utilized textbook knowledge or technical details is reviewed in appendixes as backup.

1.4 Summary of original results

To identify the contribution from the author, I summarize the original results in this section.

In Chapter 2, I build the sign bounds theory for estimating the sign problem behavior in Quantum Monte Carlo near some exactly solvable limits [1, 2]. Besides, I develop an integral algorithm which has the same complexity with traditional Quantum Monte Carlo while it can simulate exponential observable (e.g., free energy, entropy, entanglement entropy) stably [3]. Those tools expand the simulation ability of traditional Quantum Monte Carlo and make it possible to simulate systems with polynomial sign problem or identify the entanglement feature (e.g., integer or fractional quantum hall states).

In Chapter 3, I explain the observed gate-switchable nonlinear Hall response in twisted bilayer graphene may come from Berry curvature sliding on topological flat bands [4]. With projecting Coulomb interaction on flat bands, I also develop momentum space Quantum Monte Carlo method for simulating twisted bilayer graphene at charge neutrality [5] and identify the inter-valley coherent ground state [6]. Departing from charge neutrality point, I list the exactly solvable cases with ground state degeneracy and polynomial sign problem at all kinds of integer fillings, and study finite temperature topological phase transition at $\nu = \pm 1$ [2].

In Chapter 4, I discuss K valley and Γ valley twisted transition metal dichalcogenides with flat-band limit at charge neutrality. By assuming inter-valley attraction, my collaborators and I find an exactly solvable $SU(2)$ limit in flat-band twisted 2D material such as K valley twisted transition metal dichalcogenides. Ground states, excitation spectra and correlation functions are identified at $SU(2)$ limit. Superconductor and super-compressible bosonic fluid phase have been proposed and confirmed numerically near $SU(2)$ limit [7].

In Chapter 5, I explain the observed integer magnetic flux quantum oscillation numerically with the super-Moiré picture. This scheme can realize both fractional and integer magnetic flux quantum oscillation as long as the super-Moiré potential is large enough to hybridize different Landau levels. Projecting interaction on fractal magnetic bands can be an interesting direction to study the strong correlation effect there in the future.

Chapter 2

Methodology

2.1 Linear response and semi-classical Boltzmann equation

In this section, I will introduce the linear response theory under electric field perturbation [8–11], derive the Hall conductance formula for mean field system, give the definition of the Berry curvature and Chern number in 2D case accordingly and introduce the widely used semi-classical formula for computing linear and nonlinear conductivity for mean field Hamiltonian [12–14].

2.1.1 Linear response and Hall conductance

For a conductive material, when applying an electric field E, there will an induced current J. According to Taylor expansion and noticing there should be no current at zero electric field, one expects

$$\langle eJ_\alpha(x,t)\rangle = \sum_\beta \sigma_{\alpha\beta}E_\beta(x,t) + \sum_{\beta,\gamma}\chi_{\alpha\beta\gamma}E_\beta(x,t)E_\gamma(x,t) + \cdots , \tag{2.1}$$

where eJ is the charge current density, α,β,γ label orthogonal directions and σ,χ are linear and nonlinear (the second order) response coefficients called linear and nonlinear conductance. By considering linear response at small electric field case, we will show σ can be derived from correlation of current operators and the Hall conductance σ_{xy} at single particle product ground state is determined by Berry curvature in two dimension.

First, we shall introduce our Hamiltonian in first-quantized form with periodic-perturbed electric field, which is alternating current (AC) electric field perturbation (Or we are taking velocity gauge by setting scalar potential zero. One can also equivalently take length gauge by setting time independent vector field) and the direct current (DC)

case can be derived by taking low frequency limit. The Hamiltonian is written below

$$\begin{aligned} H &= \sum_i \frac{1}{2m}\left(p_i - \frac{e}{c}A\left(x_i,t\right)\right)^2 + \sum_{i<j} V_{ij} \\ &= \sum_i \frac{1}{2m}{p_i}^2 + \sum_{i<j} V_{ij} - \sum_i \frac{e}{2mc}\left(p_i \cdot A\left(x_i,t\right) + A\left(x_i,t\right)\cdot p_i\right) + \sum_i \frac{e^2}{2mc^2}A^2\left(x_i,t\right) \\ &= H_0 + H'(t). \end{aligned} \tag{2.2}$$

Here p_i, x_i are momentum and position operators for particle i, $A(x_i,t)$ is the time-position oscillation vector field inducing electric field and V_{ij} is the two-particle interaction term. In the final line, one can see the Hamiltonian with electric field can be written formally as the case without electric field H_0 adding the time dependent perturbation $H'(t)$. According to Schrödinger equation, when choosing gauge $\nabla \cdot A = 0$, one can derive particle density and particle current density for a N-fermion wave function $\Psi(x_1, x_2, ...)$. (Explicitly, one applies $\Psi^*(x_1, x_2, ...)$ on Schrödinger equation, minors its Hermitian conjugate and integrates over N-fermion position space. Since V_{ij} and A^2 terms are canceled, this integral is decoupled between N fermions and each part contributes the same in the summation over i. The total time derivative is for the particle density and take one ∇ out from the other side of equation gives the surface integral of current density.)

$$\begin{aligned} \rho(x) &= N\int D[x_{i\neq 1}]\Psi^*\left(x, x_2, \ldots\right)\Psi\left(x, x_2, \ldots\right) \\ J(x,t) &= \frac{N}{2m}\int D[x_{i\neq 1}]\left[\Psi^*\left(x, x_2, \ldots\right)\left(p - \frac{e}{c}A(x,t)\right)\Psi\left(x, x_2, \ldots\right) + c.c.\right] \end{aligned} \tag{2.3}$$

As coming from their definitions, particle density and particle current density satisfy equation of continuation

$$-\frac{\partial\rho(x,t)}{\partial t} = \nabla\cdot\frac{N}{2m}\int D[x_{i\neq 1}]\left[\Psi^*\left(x, x_2, \ldots\right)\left(p - \frac{e}{c}A(x,t)\right)\Psi\left(x, x_2, \ldots\right) + c.c.\right]. \tag{2.4}$$

We define the current density operator below. The correctness can be proved by directly comparing $\langle J\rangle$ and $J(x,t)$.

$$J = \frac{1}{2m}\sum_i\left[\left(p_i - \frac{e}{c}A\left(x_i,t\right)\right)\delta\left(x - x_i\right) + \delta\left(x - x_i\right)\left(p_i - \frac{e}{c}A\left(x_i,t\right)\right)\right] \tag{2.5}$$

One can see interaction only influences wave function but not current density operator from this picture. Now let's transform it into lattice second-quantized picture, the general Hamiltonian H_0 in momentum space is

$$H_0 = \sum_k h_k c_k^\dagger c_k + \sum_{q\neq 0}\frac{V(q)}{2\Omega}\left(\sum_{k_1} c_{k_1}^\dagger c_{k_1+q}\sum_{k_2} c_{k_2}^\dagger c_{k_2-q}\right). \tag{2.6}$$

Here $V(q)$ is the Fourier transformation of the interaction and Ω is the volume of the

whole system. After transforming charge density operator $\rho_i \equiv c_i^\dagger c_i$ into momentum space $\rho_q = \frac{1}{\sqrt{N}} \sum_k c_{k+q}^\dagger c_k$, we can write down continuous equation in momentum space.

$$i\frac{1}{\sqrt{N}} \sum_k \left(h_{k+q} - h_k\right) c_{k+q}^\dagger c_k = i\left[H_0, \rho_q\right] = \frac{\partial \rho_q}{\partial t} = iq \cdot j_q \tag{2.7}$$

When q is small, we have Fourier transformed current density operator written as

$$j_q \approx \frac{1}{\sqrt{N}} \sum_k \frac{\partial h_k}{\partial k_q} c_{k+\frac{q}{2}}^\dagger c_{k-\frac{q}{2}} \tag{2.8}$$

We can see again, interaction between particles will not influence the form of current density operator. Since we have not considered vector potential for now, we use j to label this current density operator for distinguishing J labeling total current density operator. According to our first-quantized result, the average of charge current density operator is

$$\langle J(x,t)\rangle = \frac{N}{m\Omega}\left\langle p - \frac{e}{c}A(x,t)\right\rangle = \langle j(x,t)\rangle - \frac{n_0 e}{mc}A(x,t). \tag{2.9}$$

Review the Taylor expansion $\langle eJ_\alpha(x,t)\rangle = \sum_\beta \sigma_{\alpha\beta}E_\beta(x,t) + \cdots$ and in velocity gauge $E(x,t) = -\frac{1}{c}\frac{\partial A(x,t)}{\partial t}$, we simply choose $A(x,t) = Ee^{i(q\cdot x - wt)}$ so that $E(x,t) = \frac{iw}{c}Ee^{i(q\cdot x-wt)}$. After this gauge-choosing step, term $\frac{n_0 e}{mc}A(x,t)$ in $\langle J(x,t)\rangle$ is just $\frac{n_0 e}{mc}Ee^{i(q\cdot x-wt)}$. One only needs to compute $\langle j(x,t)\rangle$, compare the coefficients above certain order of E to derive the conductance. We consider this computation below in interaction picture.

$$\langle j(x,t)\rangle = \left\langle \psi \middle| T\left[e^{i\int_{-\infty}^{t} H'(t_1)dt_1}\right] j(x,t) T\left[e^{-i\int_{-\infty}^{t} H'(t_1)dt_1}\right] \middle| \psi \right\rangle \tag{2.10}$$

Here $T[...]$ is the time order and $|\psi\rangle$ is the state without perturbation $H'(t)$. After expanding $T\left[e^{-i\int_{-\infty}^{t} H'(t_1)dt_1}\right]$ up to the leading order of $H'(t)$

$$T\left[e^{-i\int_{-\infty}^{t} H'(t_1)dt_1}\right] \approx 1 - i\int_{-\infty}^{t} H'(t_1)\, dt_1 \tag{2.11}$$

By noticing $\sum_i \frac{e^2}{2mc^2}A^2(x_i,t) = \frac{e^2}{2mc^2}\int dx \ \sum_i \delta(x-x_i)\cdot A^2(x,t) = \frac{Ne^2E^2}{2mc^2}e^{i2(q\cdot x - wt)}$ which commutes with any particle-conserved operator and the left part in $H'(t)$ is just $-\sum_i \frac{e}{2mc}\left(p_i \cdot A(x_i,t) + A(x_i,t)\cdot p_i\right) = -\frac{e}{c}\int dx\ j\cdot A(x,t) = -\frac{eE}{c}\cdot j_q e^{-iwt}$. Keep terms up to linear order E in the result

$$\langle j(x,t)\rangle \approx i\frac{eE}{c}\int_{-\infty}^{t} e^{-iwt'}\left\langle\psi\middle|\left[j(x,t), j\left(q,t'\right)\right]\middle|\psi\right\rangle dt'. \tag{2.12}$$

Compare these results with $\langle eJ_\alpha(x,t)\rangle = \sum_\beta \sigma_{\alpha\beta}E_\beta(x,t) + \cdots$, we derive linear conductance

$$\sigma_{\alpha\beta}(q,w) = \frac{e^2}{w\Omega}\int_0^\infty dt e^{iwt}\left\langle\psi\right|\left[j_\alpha(-q,t), j_\beta(q,0)\right]\left|\psi\right\rangle + i\frac{n_0e^2}{mw}\delta_{\alpha,\beta} \tag{2.13}$$

This is the famous Kubo formula applying to linear electric field response case. The DC case can be derived by taking $q\to 0, w\to 0$ limit. In numerical practice, one can see the computation of conductance is equivalent to the computation of time-dependent correlation of current density operators.

As a quick example, we would like to compute $\Re(\sigma_{\alpha\beta}(q,w))$ for a given single-particle-product state $|\psi\rangle$.

$$\begin{aligned}
& \frac{e^2}{w\Omega}\int_0^\infty dt e^{iwt}\left\langle\psi\right|\left[j_\alpha(-q,t), j_\beta(q,0)\right]\left|\psi\right\rangle \\
= \;& \frac{e^2}{w\Omega}\int_0^\infty dt e^{iwt}\sum_{k_1,k_2}\left\langle m_1\middle|\frac{\partial h_{k_1}}{\partial k_{1\alpha}}\middle|n_1\right\rangle\left\langle m_2\middle|\frac{\partial h_{k_2}}{\partial k_{2\beta}}\middle|n_2\right\rangle \\
\cdot \;& \left[\left\langle c^\dagger_{k_1-\frac{q}{2},m_1}(t)c_{k_1+\frac{q}{2},n_1}(t)c^\dagger_{k_2+\frac{q}{2},m_2}c_{k_2-\frac{q}{2},n_2}\right\rangle\right. \\
- \;& \left.\left\langle c^\dagger_{k_2+\frac{q}{2},m_2}c_{k_2-\frac{q}{2},n_2}c^\dagger_{k_1-\frac{q}{2},m_1}(t)c_{k_1+\frac{q}{2},n_1}(t)\right\rangle\right] \\
= \;& \frac{e^2}{w\Omega}\int_0^\infty dt e^{iwt}\sum_{k}\left\langle n_2\middle|\frac{\partial h_k}{\partial k_\alpha}\middle|n_1\right\rangle\left\langle n_1\middle|\frac{\partial h_k}{\partial k_\beta}\middle|n_2\right\rangle \\
\cdot \;& \left[\left\langle c^\dagger_{k-\frac{q}{2},n_2}(t)c_{k-\frac{q}{2},n_2}\right\rangle\left\langle c_{k+\frac{q}{2},n_1}(t)c^\dagger_{k+\frac{q}{2},n_1}\right\rangle\right. \\
- \;& \left.\left\langle c^\dagger_{k+\frac{q}{2},n_1}c_{k+\frac{q}{2},n_1}(t)\right\rangle\left\langle c_{k-\frac{q}{2},n_2}c^\dagger_{k-\frac{q}{2},n_2}(t)\right\rangle\right]
\end{aligned} \tag{2.14}$$

Here we chose $c^\dagger_{k_2+\frac{q}{2},m_2}$ as creating operator for m_2 band with momentum $k_2+\frac{q}{2}$ in single-particle-product basis. In the last line, we use Wick's theorem (see Appendix A for detail) where only momentum conserving terms can give non-zero contribution. Now we have not assumed the kinetic term h is diagonalized in this basis. Take $q\to 0$ and write $\left\langle c_{k+\frac{q}{2},n_1}(t)c^\dagger_{k+\frac{q}{2},n_1}\right\rangle$ with equal time Green's function $G_{n_1,n_1}(k)\equiv\left\langle c_{k,n_1}c^\dagger_{k,n_1}\right\rangle$.

$$\begin{aligned}
& \frac{e^2}{w\Omega}\int_0^\infty dt e^{iwt}\sum_{k}\left\langle n_2\middle|\frac{\partial h_k}{\partial k_\alpha}\middle|n_1\right\rangle\left\langle n_1\middle|\frac{\partial h_k}{\partial k_\beta}\middle|n_2\right\rangle \\
\cdot \;& \left[e^{-i\left(\varepsilon_{k,n_2}+\varepsilon_{k,n_1}\right)t}\left(I_{n_2,n_2}-G_{n_2,n_2}(k)\right)G_{n_1,n_1}(k)\right. \\
- \;& \left.e^{i\left(\varepsilon_{k,n_1}+\varepsilon_{k,n_2}\right)t}\left(I_{n_1,n_1}-G_{n_1,n_1}(k)\right)G_{n_2,n_2}(k)\right]
\end{aligned} \tag{2.15}$$

Here ε_{k,n_2} is the single particle excitation energy on band n_2 with momentum k. Now we can compute the integral $\int_0^\infty dt e^{iwt}e^{-i\left(\varepsilon_{k,n_2}+\varepsilon_{k,n_1}\right)t}$ by multiplying a converging factor

$e^{-\delta t}$.

$$\begin{aligned} & \frac{e^2}{w\Omega}\Re\left\{\sum_k \left\langle n_2\middle|\frac{\partial h_k}{\partial k_\alpha}\middle|n_1\right\rangle\left\langle n_1\middle|\frac{\partial h_k}{\partial k_\beta}\middle|n_2\right\rangle\right. \\ \cdot\quad & \left[\frac{1}{\delta - i\left(w-\left(\varepsilon_{k,n_2}+\varepsilon_{k,n_1}\right)\right)}\left(I-G_{n_2,n_2}(k)\right)G_{n_1,n_1}(k)\right. \\ -\quad & \left.\left.\frac{1}{\delta - i\left(w+\left(\varepsilon_{k,n_2}+\varepsilon_{k,n_1}\right)\right)}\left(I-G_{n_1,n_1}(k)\right)G_{n_2,n_2}(k)\right]\right\} \end{aligned} \tag{2.16}$$

By taking $\delta \to 0, w \to 0$ and according to L'Hôpital's rule we have

$$\begin{aligned} & \frac{e^2}{\Omega}\Re\left[\sum_k \left\langle n_2\middle|\frac{\partial h_k}{\partial k_\alpha}\middle|n_1\right\rangle\left\langle n_1\middle|\frac{\partial h_k}{\partial k_\beta}\middle|n_2\right\rangle\frac{-i}{\left(\varepsilon_{k,n_2}+\varepsilon_{k,n_1}\right)^2}\left(G_{n_1,n_1}(k)-G_{n_2,n_2}(k)\right)\right] \\ = \quad & \frac{e^2}{\Omega}\Im\left[\sum_k\left(\left\langle n_2\middle|\frac{\partial h_k}{\partial k_\alpha}\middle|n_1\right\rangle\left\langle n_1\middle|\frac{\partial h_k}{\partial k_\beta}\middle|n_2\right\rangle\frac{1}{\left(\varepsilon_{k,n_2}+\varepsilon_{k,n_1}\right)^2}\left(G_{n_1,n_1}(k)-G_{n_2,n_2}(k)\right)\right)\right] \end{aligned} \tag{2.17}$$

Let's check the effectiveness of this expression now. It is straightforward to see there is no contribution from two occupied bands or two empty bands ($G_{n_1,n_1}(k) - G_{n_2,n_2}(k) = 0$), or the case $\alpha = \beta$ (The whole expression is real so that there is no imaginary part). Then only Hall conductance ($\alpha \neq \beta$) and the contribution from occupied and empty bands can be non-zero.

$$\frac{e^2}{\Omega}\Im\left[\sum_{k,n_O,n_E}\frac{\left(\left\langle n_O\middle|\frac{\partial h_k}{\partial k_\alpha}\middle|n_E\right\rangle\left\langle n_E\middle|\frac{\partial h_k}{\partial k_\beta}\middle|n_O\right\rangle-\left\langle n_E\middle|\frac{\partial h_k}{\partial k_\alpha}\middle|n_O\right\rangle\left\langle n_O\middle|\frac{\partial h_k}{\partial k_\beta}\middle|n_E\right\rangle\right)}{\left(\varepsilon_{k,n_O}+\varepsilon_{k,n_E}\right)^2}\right] \tag{2.18}$$

Here n_O means occupied bands and n_E means empty bands. If the given single-particle-product state $|\psi\rangle$ is the eigenstate of h_k so that the single particle excitation above it can be computed as $h_k|n\rangle = \varepsilon_{k,n}|n\rangle$, the expression above can be reduced to the famous form.

$$\begin{aligned} & \frac{e^2}{\Omega}\Im\left[\sum_{k,n_O,n_E}\left(\partial_{k_\alpha}(\langle n_O|)|n_E\rangle\langle n_E|\partial_{k_\beta}(|n_O\rangle)-\partial_{k_\beta}(\langle n_O|)|n_E\rangle\langle n_E|\partial_{k_\alpha}(|n_O\rangle)\right)\right] \\ = \quad & e^2\Im\left[\sum_{n_O}\int\frac{d^Dk}{(2\pi)^D}\left(\partial_{k_\alpha}(\langle n_O|)\partial_{k_\beta}(|n_O\rangle)-\partial_{k_\beta}(\langle n_O|)\partial_{k_\alpha}(|n_O\rangle)\right)\right] \end{aligned} \tag{2.19}$$

By defining the Berry curvature $F_{n;\alpha,\beta}(k) \equiv \left(\partial_{k_\alpha}(\langle n|)\partial_{k_\beta}(|n\rangle) - \partial_{k_\beta}(\langle n|)\partial_{k_\alpha}(|n\rangle)\right)$ for band n at momentum k, one can see the Hall conductance is equal to the integral of Berry curvature from all occupied bands. When taking two dimension case (i.e., $D = 2$) and bands n_O are fully occupied with a gap to n_E, one can see this surface integral becomes a loop integral with integrand vector $A_\alpha = \langle n_O|\partial_{k_\alpha}|n_O\rangle$. According to residue theorem, the loop integral along the momentum space boundary (or the first Brillouin zone for lattice system) is determined by $2\pi i$ times the amount of singular poles encircled

by the loop. Then Hall conductance in this case is equal to $\frac{e^2C}{2\pi}$, where integer C is the so-called total Chern number for the occupied bands. If we introduce the ignored $\hbar$ back and recover the standard formula, the quantized conductance is $\frac{e^2}{2\pi\hbar} = \frac{e^2}{h}$.

Finite temperature Hall conductance is a more useful quantity which can be used to compare with experiment data directly. It turns out the derivation is almost the same as the given wavefunction (i.e., zero temperature ground state wavefunction) case above. One just needs to replace the wavefunction overlap $\langle\psi|...|\psi\rangle$ by the ensemble average $\frac{\mathrm{Tr}(e^{-\beta H}...)}{\mathrm{Tr}(e^{-\beta H})}$. For the fermion bilinear $c^\dagger c$ Hamiltonian, Wick' theorem still works for the Green's function $G_{n_1,n_1}(k) \equiv \frac{\mathrm{Tr}(e^{-\beta H}c_{k,n_1}c^\dagger_{k,n_1})}{\mathrm{Tr}(e^{-\beta H})} = \frac{e^{\beta\varepsilon_{k,n_1}}}{1+e^{\beta\varepsilon_{k,n_1}}}$.

$$
\begin{aligned}
& \frac{e^2}{\Omega}\Im\left[\sum_k\left(\left\langle n_2\left|\frac{\partial h_k}{\partial k_\alpha}\right|n_1\right\rangle\left\langle n_1\left|\frac{\partial h_k}{\partial k_\beta}\right|n_2\right\rangle\frac{1}{\left(\varepsilon_{k,n_2}+\varepsilon_{k,n_1}\right)^2}\left(G_{n_1,n_1}(k)-G_{n_2,n_2}(k)\right)\right)\right] \\
= & \frac{e^2}{\Omega}\Im\left[\sum_{k,n_1,n_2}\langle n_2|\,\partial_{k_\alpha}(|n_1\rangle)G_{n_1,n_1}(k)\partial_{k_\beta}(\langle n_1|)\,|n_2\rangle-\langle n_1|\,\partial_{k_\beta}(|n_2\rangle)G_{n_2,n_2}(k)\partial_{k_\alpha}(\langle n_2|)\,|n_1\rangle\right] \\
= & \frac{e^2}{\Omega}\Im\left[\sum_{k,n}G_{n,n}(k)(\partial_{k_\beta}(\langle n|)\partial_{k_\alpha}(|n\rangle)-\partial_{k_\alpha}(\langle n|)\partial_{k_\beta}(|n\rangle))\right] \\
= & e^2\Im\left[\sum_n\int_k\frac{d^Dk}{(2\pi)^D}f_n(k)(\partial_{k_\alpha}(\langle n|)\partial_{k_\beta}(|n\rangle)-\partial_{k_\beta}(\langle n|)\partial_{k_\alpha}(|n\rangle))\right]
\end{aligned}
\tag{2.20}
$$

To derive the last line, we have used the fact that Fermi-Dirac distribution $f_n(k) \equiv \frac{1}{1+e^{\beta\varepsilon_{k,n}}} = 1 - G_{n,n}(k)$. When $D = 2$, the physical meaning of the last line is basically the weighted summation of Berry curvature where the weight is the occupation possibility of a particle on state $|k, n\rangle$. This is the formula we usually use to compute the finite temperature Hall conductance in systems where quasi-particle-band is a good approximation.

Actually, since the Hall conductance is quantized (based on the amount of singular poles in wavefunction), one can imagine the Hall conductance is robust against perturbation as long as the perturbation will not introduce or reduce more poles (there is a proof for this argument based on Ward identity [15]). This is promised by the band gap between conduct and valence bands. If this band gap is protected by certain symmetry, we say the insulator with nontrivial Hall conductance is the symmetry protected topological insulator. Also because of this robustness of Chern number, there is a handy numerical trick [16] to compute it for quasi-particle-band system and also Green's function form [17–19] applying to interactive systems where a band description may be absent. However, one should be careful that this derivation is based on the argument that adiabatic evolution connects the real interactive ground state with a single-particle product state. When this connection fails, one should use the real ground state wavefunction for computing the correct Chern number [20].

2.1.2 Semi-classical Boltzmann equation

The robust quantized Hall conductance is amazing. However, real life is hard. The general conductance, coming from all kinds of scattering process, is so complicated that lots of approximation should be taken to derive a reasonable result matching well with experiments. Semi-classical Boltzmann equation is a well-known and pleasing frame to compute conductance which matches well with experiments in most cases except for some strong correlated phases [12, 21, 22]. The idea is assuming the perturbed scattering process only affects the distribution of electrons in bands and replacing the Fermi-Dirac distribution at equilibrium $f^{(0)}(k)$ case by the nonequilibrium distribution $f(k)$. On one hand, the nonequilibrium distribution is determined by the scattering possibility from one occupied momentum k' to empty k minus occupied momentum k to empty k'; One the other hand, the nonequilibrium distribution $f(r,k,t)$ is determined by its parameters r,k,t where classical position and momentum is involved. Based on this idea, assuming the scattering possibility from unit momentum $\frac{dk'}{(2\pi)^D}$ and unit time dt to unit momentum $\frac{dk}{(2\pi)^D}$ is $W_{k',k}\frac{dk}{(2\pi)^D}dt$ we can write down

$$\frac{df(k)}{dt} = -\int \frac{dk'}{(2\pi)^D}\left[f(k)W_{k,k'}(1-f(k')) - f(k')W_{k',k}(1-f(k))\right]. \tag{2.21}$$

If one takes the relaxation-time approximation where scattering is assumed to be a rare event and the system is almost in Fermi-Dirac distribution, possibility of the scattering in k can be expressed as $f^{(0)}(k)\frac{dt}{\tau}$ where τ is the relaxation time and $\frac{1}{\tau}$ has the physical meaning that possibility of scattering in unit time. Based on this approximation, one can write down the formula above in a simple way

$$\frac{df(k)}{dt} = -\frac{f(k)-f^{(0)}(k)}{\tau}. \tag{2.22}$$

Now let's look at the left-hand side (LHS), expand the derivative of time by derivative of variables for distribution function.

$$\frac{df}{dt} = \frac{\partial f}{\partial t} + v\cdot\frac{\partial f}{\partial r} + F\cdot\frac{\partial f}{\partial k} \tag{2.23}$$

Here v is velocity and F is force. If we assume the distribution is homogeneous so that $\frac{\partial f}{\partial r} = 0$, one can derive the semi-classical Boltzmann equation we usually use

$$-\frac{f-f^{(0)}}{\tau} = \frac{\partial f}{\partial t} + F\cdot\frac{\partial f}{\partial k} \tag{2.24}$$

A benefit of this form is the distribution f can be solve recursively up to any order electric field perturbation E by assuming the force coming from an AC field $F = qEe^{iwt}$. We show the result up to second order of E below. First, expand every f in the equation based on order of perturbation E (i.e., $f = f^{(0)} + f^{(1)} + f^{(2)} + \cdots$). Notice the zero order is Fermi-Dirac distribution $f^{(0)} = \frac{1}{1+e^{\beta\varepsilon}}$ and match the first order and the second

order terms on both sides of the equation

$$f^{(1)} = -\tau \frac{\partial f^{(1)}}{\partial t} - \tau q e^{iwt} E \cdot \frac{\partial f^{(0)}}{\partial k}$$
$$f^{(2)} = -\tau \frac{\partial f^{(2)}}{\partial t} - \tau q e^{iwt} E \cdot \frac{\partial f^{(1)}}{\partial k} \tag{2.25}$$

Because $f^{(0)}$ is independent with t, integrate the first line over t will derive $f^{(1)}$.

$$f^{(1)} = \frac{-q\tau}{1 + iw\tau} e^{iwt} E \cdot \frac{\partial f^{(0)}}{\partial k} \tag{2.26}$$

Plug the expression of $f^{(1)}$ in the second line and integrate it over t will derive $f^{(2)}$

$$f^{(2)} = \frac{(q\tau)^2}{(1 + iw\tau)(1 + i2w\tau)} e^{i2wt} E \cdot \frac{\partial f^{(0)}}{\partial k} E \cdot \frac{\partial f^{(0)}}{\partial k} \tag{2.27}$$

Having known the nonequilibrium distribution, now we are ready to compute the conductance. The semi-classical way to compute the charge current density is expressing it by integrating the velocity over all occupied particles

$$J_\alpha = q \int \frac{d^D k}{(2\pi)^D} f(k) v_\alpha(k) \tag{2.28}$$

The naive velocity comes from the energy-momentum dispersion $v_\alpha^{(0)}(k) = \partial_{k_\alpha} \varepsilon(k)$. However, based on our last section we have known there should be one additional term for Hall conductance which is independent with relaxation time. One can see if we introduce a so-called anomalous velocity term $v_\alpha^{(1)}(k) = -q(E \times \Omega)_\alpha$ which is the linear order of electric field, one can recover the Hall conductance expression as well as deriving nonlinear Hall term from Berry curvature contribution [13, 14]. First, we expand charge current density according to the field $J_\alpha = J_\alpha^{(1)} + J_\alpha^{(2)} + \cdots$. There is no zero order because the charge current density should be zero without electric field. Explicitly, we expand $f(k)$ up to the second order, include the anomalous velocity and match terms in each order.

$$J_\alpha^{(1)} = -q^2 \int \frac{d^D k}{(2\pi)^D} f^{(0)}(k)(E \times \Omega(k))_\alpha + q \int \frac{d^D k}{(2\pi)^D} f^{(1)}(k) \partial_{k_\alpha} \varepsilon(k)$$
$$J_\alpha^{(2)} = -q^2 \int \frac{d^D k}{(2\pi)^D} f^{(1)}(k)(E \times \Omega(k))_\alpha + q \int \frac{d^D k}{(2\pi)^D} f^{(2)}(k) \partial_{k_\alpha} \varepsilon(k) \tag{2.29}$$

As I introduced in the last section, compare the charge current density with the definition of linear and quadratic conductance $J_\alpha^{(1)} = \sigma_{\alpha\beta} E_\beta, J_\alpha^{(2)} = \chi_{\alpha\beta\gamma} E_\beta E_\gamma$, one can derive

the linear and quadratic conductance.

$$\begin{aligned}\sigma_{\alpha\beta} &= -q^2\epsilon_{\alpha\beta\gamma}\int\frac{d^Dk}{(2\pi)^D}f^{(0)}(k)\Omega_\gamma(k)\\ &+ \frac{q^2\tau}{1+iw\tau}\int\frac{d^Dk}{(2\pi)^D}f^{(0)}(k)\partial_{k_\alpha}\partial_{k_\beta}\varepsilon(k)\\ \chi_{\alpha\beta\gamma} &= -\frac{q^3\tau}{1+iw\tau}\epsilon_{\alpha\beta\eta}\int\frac{d^Dk}{(2\pi)^D}f^{(0)}(k)\partial_{k_\gamma}\Omega_\eta(k)\\ &+ \frac{q^3\tau^2}{(1+iw\tau)(1+i2w\tau)}\int\frac{d^Dk}{(2\pi)^D}f^{(0)}(k)\partial_{k_\alpha}\partial_{k_\beta}\partial_{k_\gamma}\varepsilon(k)+(\beta\leftrightarrow\gamma)\end{aligned} \tag{2.30}$$

Here $\epsilon_{\alpha\beta\gamma}$ is the Levi-Civita symbol which gives a minus sign when switching two labels and $(\beta\leftrightarrow\gamma)$ in the last line means a term derived by exchanging β,γ labels in the term above (By definition $J^{(2)}_\alpha = \chi_{\alpha\beta\gamma}E_\beta E_\gamma$, $\chi_{\alpha\beta\gamma}$ should be symmetric when exchanging β,γ). Now one can see we recover the Hall conductance which is the first term of $\sigma_{\alpha\beta}$ and also compute the contribution from Berry curvature dipole in quadratic conductance which is the first term in $\chi_{\alpha\beta\gamma}$. The left parts are from the normal velocity $v^{(0)}_\alpha(k)$ and we call them Drude terms. Those formulas will be used in Chapter 3 and Chapter 5.

2.2 Determinant Quantum Monte Carlo (DQMC)

In this section, I will introduce the general formula of DQMC [23, 24] which can solve interacting fermion system unbiasedly using momentum space density-density interaction as an example [5, 25], derive how to compute the configuration weight and the observable based on Green's function, give a numerically stable formula in a practical code and finish this section with introducing a widely used time-saving code process.

2.2.1 General formula in momentum space

As we have seen in the last section, the response of a system can be derived from the corresponding correlation (or Green's function). Identifying a phase by long-range (or quasi-long-range) correlation of a local order parameter also demands to compute Green's function. In a word, except for some topological properties from ground state wavefunction, most of fermionic many-body macroscopic characters can be described in a language of Green's function. The complexity then becomes how to compute it for an interactive many-body system. With the development from [26–32], Determinant Quantum Monte Carlo (DQMC) gradually grows up as a powerful tool for numerically computing interactive many-fermion system at finite temperature [23, 24]. Recently motivated by strong correlation phenomena in twisted bilayer graphene, momentum space DQMC becomes popular in simulation of all kinds of flat band materials [2, 5–7, 19, 25, 33]. I will show the general formula of DQMC in momentum space below, where the general idea of it can be extended for implementing DQMC in other basis.

Let's assume we have a kinetic Hamiltonian H_0 written in diagonalized band basis.

$$H_0 = \sum_{k,n} \varepsilon_{k,n} c^\dagger_{k,n} c_{k,n} \tag{2.31}$$

The main interaction comes from density-density interplay in real space (The interaction written in normal order form can transform into density-density form with an additional chemical potential shift).

$$H_I = \frac{1}{2} \int dr_1 dr_2 V(r_1 - r_2) (\sum_X \psi^\dagger_X(r_1)\psi_X(r_1))(\sum_{X'} \psi^\dagger_{X'}(r_2)\psi_{X'}(r_2)) \tag{2.32}$$

Here we use X, X' to label local degree of freedom such as spin, valley, layer or sublattice in Moiré system. After Fourier transformation, one has the interaction written in momentum space plane wave basis shown below

$$H_I = \frac{1}{2\Omega} \sum_q V(q) (\sum_{k_1,X} c^\dagger_{k_1,X} c_{k_1+q,X})(\sum_{k_2,X'} c^\dagger_{k_2,X'} c_{k_2-q,X'}). \tag{2.33}$$

Here $\Omega \equiv \int dr$ is the volume of real space and $V(q) \equiv \int d(r_1 - r_2) e^{iq\cdot(r_1-r_2)} V(r_1 - r_2)$ is the Fourier transformation of $V(r_1 - r_2)$. Considering chemical potential term, one can define a density variation operator

$$\delta\rho_q = \sum_{k_1,X} (c^\dagger_{k_1,X} c_{k_1+q,X} - \mu\delta_{q,0}), \tag{2.34}$$

and the interaction together with chemical potential can be expressed as

$$H_I = \frac{1}{2\Omega} \sum_q V(q) \delta\rho_q \delta\rho_{-q}. \tag{2.35}$$

Now we have a Hamiltonian whose kinetic terms are written in band basis while interactive terms are in plane wave basis. We should pick a single basis before next step. Flat band with a large gap from remote bands has a great advantage that interaction can be large enough compared with band dispersion which induces strong correlation phase, and small enough compared with the band gap so that states in remote bands can approximately be seen as playing no role at low energy case so that one can only keep the states within flat bands (as the case shown in Fig 2.1). Based on these considerations, we express our interaction in band basis by introducing a unitary transformation which is the same one diagonalizing H_0 from momentum space plane wave basis.

$$c^\dagger_{k,n} = \sum_X u_{n,X}(k) c^\dagger_{k,X} \tag{2.36}$$

After transformation, we have $\delta\rho_q$ below

$$\delta\rho_q = \sum_{k,n,m} \lambda_{n,m}(k, k+q)(c^\dagger_{k,n} c_{k+q,m} - \mu\delta_{q,0}\delta_{n,m}). \tag{2.37}$$

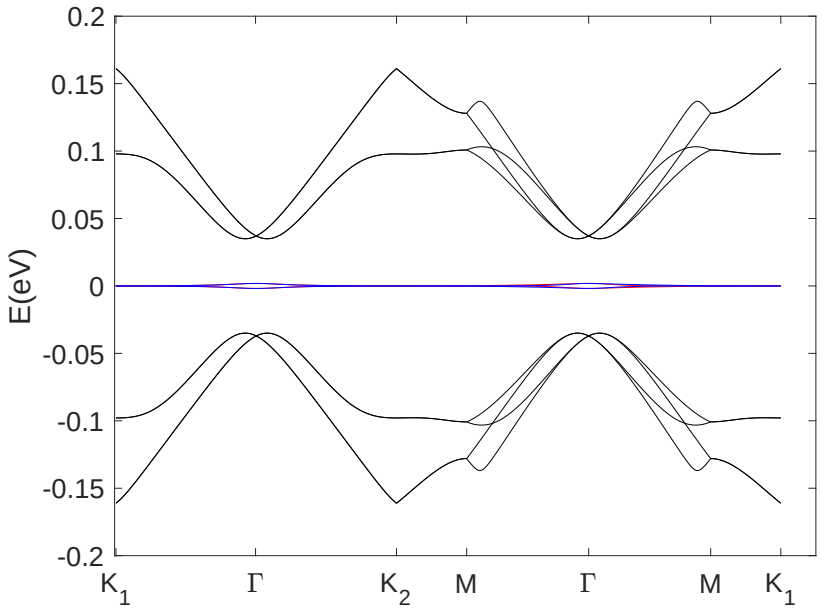


Figure 2.1: Band structure along high-symmetry lines from Bistritzer-MacDonald (BM) model for twisted bilayer graphene (TBG). Blue and red bands are flat bands from two valleys and dark bands are remote bands separated with a finite gap. The detailed parameters for the plot can be found in Chapter 3.

Here $\lambda_{n,m}(k,k+q) \equiv \sum_X u^*_{X,n}(k)u_{X,m}(k+q)$ is the overlap between wavefunctions of band n,m and $\delta_{n,m}$ comes from orthogonal and complete relation. If we keep all the n,m labels in the summation, this transformation is exact but the huge amount band degree of freedom will unnecessarily complicate numerical simulation for low energy physics. As the case in in TBG Fig 2.1, we only keep flat band labels in our simulation and take a cut off for q (e.g., keep q momentum points within triple Brillouin zone) for $V(q)$ and $\lambda_{n,m}(k,k+q)$. Now, we have our start point Hamiltonian written in momentum space band basis as shown below

$$H = \sum_{k,n} \varepsilon_{k,n} c^\dagger_{k,n} c_{k,n} + \frac{1}{4\Omega} \sum_{|q|\neq 0} V(q) \left[(\delta\rho_q + \delta\rho_{-q})^2 - (\delta\rho_q - \delta\rho_{-q})^2 \right]. \tag{2.38}$$

Here we have used the inverse symmetry $V(q) = V(-q)$ and combined $\pm q$ terms together ($q = 0$ corresponding to background cancels with static nucleus potential contribution because of charge neutral condition). We would like to write down the partition function of this Hamiltonian according to Suzuki–Trotter expansion and Hubbard–Stratonovich

transformation (see Appendix A for details).

$$\begin{aligned} Z &\approx \mathrm{Tr}(\prod_{t=1}^{N_\beta} e^{-\Delta t H_0} e^{-\Delta t H_I(t)}) \\ &\approx \mathrm{Tr}(\prod_t \left\{ e^{-\Delta t H_0} \prod_{|q|\neq 0} e^{-\frac{\Delta t V(q)}{4\Omega}\left[(\delta\rho_q+\delta\rho_{-q})^2-(\delta\rho_q-\delta\rho_{-q})^2\right]} \right\}) \\ &\approx \sum_{\{l_{|q|,t}\}} \prod_t \left[\frac{1}{16}\gamma(l_{|q_1|,t})\gamma(l_{|q_2|,t})\right] \\ &\cdot \mathrm{Tr}(\prod_t \left\{ e^{-\Delta t H_0} \prod_{|q|\neq 0} e^{i\eta(l_{|q_1|,t})\sqrt{\frac{\Delta t V(q)}{4\Omega}}(\delta\rho_q+\delta\rho_{-q})} e^{\eta(l_{|q_2|,t})\sqrt{\frac{\Delta t V(q)}{4\Omega}}(\delta\rho_q-\delta\rho_{-q})} \right\}) \end{aligned} \tag{2.39}$$

Here we use $\{l_{|q|,t}\}$ to label the set including all the auxiliary fields. At each t for each $|q|$ we have two auxiliary fields $l_{|q_1|,t}, l_{|q_2|,t} = \pm 1, \pm 2$ and $\gamma(\pm 1) = 1 + \frac{\sqrt{6}}{3}, \gamma(\pm 2) = 1 - \frac{\sqrt{6}}{3}, \eta(\pm 1) = \pm\sqrt{(2(3-\sqrt{6}))}, \eta(\pm 2) = \pm\sqrt{(2(3+\sqrt{6}))}$. For convenience, we define $P(\{l_{|q|,t}\}) \equiv \prod_t \left[\frac{1}{16}\gamma(l_{|q_1|,t})\gamma(l_{|q_2|,t})\right]$ $(P(\{l_{|q|,t}\}) > 0, \sum_{\{l_{|q|,t}\}} P(\{l_{|q|,t}\}) = 1)$ and $\hat{B}_t(\{l_{|q|,t}\}) \equiv e^{-\Delta t H_0} \prod_{|q|\neq 0} e^{i\eta(l_{|q_1|,t})\sqrt{\frac{\Delta t V(q)}{4\Omega}}(\delta\rho_q+\delta\rho_{-q})} e^{\eta(l_{|q_2|,t})\sqrt{\frac{\Delta t V(q)}{4\Omega}}(\delta\rho_q-\delta\rho_{-q})}$. The partition function in short hand form is

$$Z \approx \sum_{\{l_{|q|,t}\}} P(\{l_{|q|,t}\}) \,\mathrm{Tr}(\prod_t \hat{B}_t(\{l_{|q|,t}\})). \tag{2.40}$$

One can see for $\prod_t \hat{B}_t(\{l_{|q|,t}\})$, it is product of exponential fermion bilinear and we will utilize this property to compute $\mathrm{Tr}(\prod_t \hat{B}_t(\{l_{|q|,t}\}))$ conveniently. The left difficulty from exponentially large summation of configuration space can be solved by importance sampling Monte Carlo. For example, if one wants to compute the ensemble average for operator $\hat{O}$, one should write it in the form below

$$\begin{aligned} \hat{O} &\equiv \frac{\mathrm{Tr}(e^{-\beta H}\hat{O})}{\mathrm{Tr}(e^{-\beta H})} \\ &\approx \sum_{\{l_{|q|,t}\}} \frac{P(\{l_{|q|,t}\})\,\mathrm{Tr}(\prod_t \hat{B}_t(\{l_{|q|,t}\}))}{\sum_{\{l'_{|q|,t}\}} P(\{l'_{|q|,t}\})\,\mathrm{Tr}(\prod_t \hat{B}_t(\{l'_{|q|,t}\}))} \frac{\mathrm{Tr}(\prod_t \hat{B}_t(\{l_{|q|,t}\})\hat{O})}{\mathrm{Tr}(\prod_t \hat{B}_t(\{l_{|q|,t}\}))}. \end{aligned} \tag{2.41}$$

The red part can be seen as the normalized Probability Mass Function (PMF) (if $\mathrm{Tr}(\prod_t \hat{B}_t(\{l_{|q|,t}\}))$ is positive for every $\{l_{|q|,t}\}$). According to the knowledge in Appendix A, one can sample according to this weight in detailed balanced Markov chain to derive the result we want. The left problem will be how to compute the weight and the observable for a given auxiliary field $\{l_{|q|,t}\}$ formally. This will be the content of our next section.

2.2.2 Observable measurement

As we learned from Wick's theorem in Appendix A, any observable which can be expressed as many-particle Green's function can be derived from two-point Green's function for single particle Hamiltonian (e.g., order parameter, energy, compressibility, specific heat and all kinds of susceptibility for response can be derived from correlation). After decouple routine in the last section, the system can be seen as single particle Hamiltonian for a given configuration field. We will show the formula to compute those two-point Green's function below. Let's firstly prove the lemma below

$$\mathrm{Tr}(e^{\sum_{i,j} T_{i,j} c_i^\dagger c_j}) = \det(I + e^T) \tag{2.42}$$

where I and T on the right-hand side (RHS) represent N dimensional identity matrix and the matrix with $T_{i,j}$ elements separately (T can be diagonalized). The idea of the proof is write the left-hand side (LHS) in T diagonal basis with eigenvalues λ_i by a similarity transformation, then the trace operator in this basis will give either 1 or e^{λ_i} for ith eigenstate so that $\mathrm{Tr}(e^{\sum_{i,j} T_{i,j} c_i^\dagger c_j}) = \prod_i (1 + e^{\lambda_i}) = \det(I + e^T)$. Next we need the input that closed commutation relation for $c_i^\dagger c_j$ operator

$$\begin{aligned} & \left[\sum_{i,j} X_{i,j} c_i^\dagger c_j, \sum_{i',j'} Y_{i',j'} c_{i'}^\dagger c_{j'}\right] \\ = & \sum_{i,j,i',j'} X_{i,j} Y_{i',j'} (\delta_{i',j} c_i^\dagger c_{j'} - \delta_{i,j'} c_{i'}^\dagger c_j) \\ = & \sum_{i,j} \sum_{l} (X_{i,l} Y_{l,j} - Y_{i,l} X_{l,j}) c_i^\dagger \hat{c}_j \end{aligned} \tag{2.43}$$

One can easily define a matrix with element $Z_{i,j} \equiv [X, Y]_{i,j}$ so that the commutation result is also in $\sum_{i,j} Z_{i,j} c_i^\dagger c_j$ form. Based on this input, we can derive the formula we want

$$\mathrm{Tr}(\prod_t \hat{B}_t) = \det(I + \prod_t B_t) \tag{2.44}$$

In the formula above, B_t is the matrix form of $\hat{B}_t$ in single-particle subspace, product of $\hat{B}_t$ can be expressed as $e^{\sum_{i,j} T_{i,j} c_i^\dagger c_j}$ where T matrix comes from all kinds of commutations from exponent part of $\hat{B}_t$ when multiplying them together by Baker–Campbell–Hausdorff formula and one can recover the matrix product form in the final determinant. With this effort, one just needs to handle a matrix with dimension N but not an exponentially large one for computing the weight $\mathrm{Tr}(\prod_t \hat{B}_t(\{l_{|q|,t}\}))$ for each configuration which has polynomial computation complexity.

Let's turn to the observable $\frac{\mathrm{Tr}(\prod_t \hat{B}_t(\{l_{|q|,t}\})\hat{O})}{\mathrm{Tr}(\prod_t \hat{B}_t(\{l_{|q|,t}\}))}$ now. As we mentioned at the beginning of this section, one just needs to derive the two-point Green's function formula after decouple routine for computing all kinds of observables. The expression for equal-time

Green's function is derived as

$$\begin{aligned} G_{i,j}(0,0) &\equiv \frac{\mathrm{Tr}(\prod_t \hat{B}_t c_i c_j^\dagger)}{\mathrm{Tr}(\prod_t \hat{B}_t)} \\ &= \frac{\partial \log(\mathrm{Tr}(\prod_t \hat{B}_t e^{\alpha(\delta_{i,j}-c_j^\dagger c_i)}))}{\partial\alpha}|_{\alpha=0} \\ &= \frac{\partial\left[\alpha\delta_{i,j}+\mathrm{Tr}_N(\log(I+\prod_t B_t e^{-\alpha\delta_{r=j,c=i}}))\right]}{\partial\alpha}|_{\alpha=0} \\ &= \delta_{i,j}-\mathrm{Tr}_N((I+\prod_t B_t)^{-1}\prod_t B_t\delta_{r=j,c=i}) \\ &= \left[I-(I+\prod_t B_t)^{-1}\prod_t B_t\right]_{i,j} \\ &= \left[(I+\prod_t B_t)^{-1}\right]_{i,j} \end{aligned} \tag{2.45}$$

Here Tr_N is the trace for $N\times N$ matrix and $\delta_{r=j,c=i}$ is the matrix with only j row i column nonzero element 1. One can see all kinds of two-point correlation can be read from $N\times N$ matrix $(I+\prod_t B_t)^{-1}$ directly. As for nonequal-time Green's function, we need an input that

$$\begin{aligned} e^{c^\dagger Ac}c_i e^{-c^\dagger Ac} &= \sum_k \left[e^{-A}\right]_{i,k} c_k \\ e^{c^\dagger Ac}c_j^\dagger e^{-c^\dagger Ac} &= \sum_k c_k^\dagger \left[e^{A}\right]_{k,j}. \end{aligned} \tag{2.46}$$

Here A can be any matrix. A quick proof is based on the Campbell identity $e^X Y e^{-X} = \sum_{n=0}^\infty \frac{[X^n,Y]}{n!}$. Since $\left[(c^\dagger Ac)^n, c_i\right] = \sum_k (-1)^n A_{i,k}^n c_k$ and $\left[(c^\dagger Ac)^n, c_j^\dagger\right] = \sum_k c_k^\dagger A_{k,j}^n$, we can easily recover the formula above. One can derive the nonequal-time Green's function according to the relation above.

$$\begin{aligned} G_{i,j}(t,0) &\equiv \frac{\mathrm{Tr}(\hat{B}(\beta,t)c_i\hat{B}(t,0)c_j^\dagger)}{\mathrm{Tr}(\hat{B}(\beta,0))} \\ &= \sum_k [B(t,0)]_{i,k}\frac{\mathrm{Tr}(\hat{B}(\beta,0)c_k c_j^\dagger)}{\mathrm{Tr}(\hat{B}(\beta,0))} \\ &= \left[B(t,0)(I+B(\beta,0))^{-1}\right]_{i,j} \end{aligned} \tag{2.47}$$

Here we define $\hat{B}(t_1,t_2) \equiv \prod_{t=t_1}^{t_2} \hat{B}_t$ and $B(t_1,t_2)$ as the matrix form for $\hat{B}(t_1,t_2)$ written in single-particle basis. Similarly, one can derive $G_{i,j}(t,t), G_{i,j}(0,t)$ below

$$\begin{aligned}
G_{i,j}(t,t) &\equiv \frac{\mathrm{Tr}(\hat{B}(\beta,t)c_i c_j^\dagger \hat{B}(t,0))}{\mathrm{Tr}(\hat{B}(\beta,0))} \\
&= \sum_{k,l} [B(t,0)]_{i,k} \frac{\mathrm{Tr}(\hat{B}(\beta,0)c_k c_l^\dagger)}{\mathrm{Tr}(\hat{B}(\beta,0))} \left[(B(t,0))^{-1}\right]_{l,j} \\
&= \left[B(t,0)(I+B(\beta,0))^{-1}(B(t,0))^{-1}\right]_{i,j} \\
&= \left[(I+B(t,0)B(\beta,t))^{-1}\right]_{i,j}; \\
G_{i,j}(0,t) &\equiv -\frac{\mathrm{Tr}(\hat{B}(\beta,t)c_j^\dagger \hat{B}(t,0)c_i)}{\mathrm{Tr}(\hat{B}(\beta,0))} \\
&= -\left[(I-(I+B(\beta,0))^{-1})(B(t,0))^{-1}\right]_{i,j} \\
&= -\left[(I+B(\beta,0))^{-1}B(\beta,t)\right]_{i,j}
\end{aligned} \tag{2.48}$$

Now we have the complete formulas for computing all kinds of correlation, equal-time or nonequal-time, as long as we have known the $B(t_1,t_2)$ matrix for a given auxiliary field configuration. And this $B(t_1,t_2)$ matrix can be computed easily since it is just the product of exponential fermion bilinear matrix. The dimension of the matrix is the same as the single-particle subspace N and such a computation is just the $O(N^3)$ time complexity. However, this matrix product can be time consuming and cause numerical instability as we will see later so that one should reduce those processes in a practical code. Since we have learned all the necessary components for the DQMC, I will introduce how to optimize those ideas in a practical code below.

2.2.3 Numerical stability

In this section, I will introduce details about how to compute the Green's function stably for a given configuration field in DQMC. This step is essential for simulation after updating several imaginary-time layers (or even a single layer when the stability is worse). The problem comes from computing the inverse for a nearly singular matrix (naively multiplying two matrices with different magnitude elements will cause this problem), for example, $G_{i,j}(t,t) = \left[(I+B(t,0)B(\beta,t))^{-1}\right]_{i,j}$. A reasonable way to compute $B(t,0)$ where many matrix product involved is using QR decomposition. Since matrix Q is unitary, we rename it with U. The singular part can only come from upper triangular matrix R, we take the norm of each row of R out to form a diagonal matrix D which contains all the magnitude information and then rename the left part of R as matrix V. Now we have the QR version of UDV decomposition for matrix B as shown

below.

$$B = \begin{pmatrix} \mathrm{X} & \mathrm{X} & \mathrm{X} \\ \mathrm{X} & \mathrm{X} & \mathrm{X} \\ \mathrm{X} & \mathrm{X} & \mathrm{X} \end{pmatrix} \begin{pmatrix} \mathbf{X} & \mathrm{X} & \mathrm{X} \\ 0 & \mathbf{X} & \mathrm{X} \\ 0 & 0 & \mathbf{X} \end{pmatrix} = \begin{pmatrix} \mathrm{X} & \mathrm{X} & \mathrm{X} \\ \mathrm{X} & \mathrm{X} & \mathrm{X} \\ \mathrm{X} & \mathrm{X} & \mathrm{X} \end{pmatrix} \begin{pmatrix} \mathbf{X} & 0 & 0 \\ 0 & \mathbf{X} & 0 \\ 0 & 0 & \mathbf{X} \end{pmatrix} \begin{pmatrix} \mathrm{X} & \mathrm{X} & \mathrm{X} \\ 0 & \mathrm{X} & \mathrm{X} \\ 0 & 0 & \mathrm{X} \end{pmatrix} \tag{2.49}$$

Here we use X to label small element and $\mathbf{X}$ to label the possibly larger one (compared with 1). For B_1, we have $B_1 = U(1)D(1)V(1)$. To store B_2B_1, one can product $B_2U(1)D(1)$ first to form a matrix

$$\begin{pmatrix} \mathbf{X} & \mathrm{X} & \mathrm{X} \\ \mathbf{X} & \mathrm{X} & \mathrm{X} \\ \mathbf{X} & \mathrm{X} & \mathrm{X} \end{pmatrix}. \tag{2.50}$$

Here one can see there is no mixing between different magnitude elements. Then UDV decomposing this matrix gives $U(2)D(2)$ and combining the left two upper triangular matrices gives $V(2)$ so that one derives $B_2B_1 = U(2)D(2)V(2)$. One can do this all the way to store $B(t,0)$ as $B(t,0) = U(t)D(t)V(t)$. In practice, we also need to store $B(\beta,t)$ which begins at B_β and right products $B_{\beta-1}$. Similarly, one just needs to use QR to decompose the transpose of B_β, extracts the norm of R to form D to derive $B_\beta = V'(\beta)D'(\beta)U'(\beta)$ and $B(\beta,t) = V'(t)D'(t)U'(t)$. Now we have separated the singular parts in $B(t,0)$ and $B(\beta,t)$, the computation for $G(t,t) = (I + B(t,0)B(\beta,t))^{-1}$ in a numerically stable way is

$$\begin{aligned} G(t,t) &= \left[I + U(t)D(t)V(t)V'(t)D'(t)U'(t)\right]^{-1} \\ &= \left[I + U(t)D_L(t)D_S(t)V(t)V'(t)D'_S(t)D'_L(t)U'(t)\right]^{-1} \\ &= U'^{-1}D'^{-1}_L\left[D_L^{-1}U^{-1}U'^{-1}D'^{-1}_L + D_SVV'D'_S\right]^{-1}D_L^{-1}U^{-1} \end{aligned} \tag{2.51}$$

Here in the second line, we replace any element smaller than 1 in $D(t)$ and $D'(t)$ by 1 to define $D_L(t)$ and $D'_L(t)$ and replace each element larger than 1 by 1 to define $D_S(t)$ and $D'_S(t)$ so that $D(t) = D_L(t)D_S(t), D'(t) = D'_L(t)D'_S(t)$. One can see the advantage of this operation in the last line (we omit (t) there for shorthand) where there is no large magnitude anymore, which means the multiplication there should be stable since the magnitude of result $G(t,t)$ is $O(1)$. With the same spirit, we can compute all kinds of Green's function in a numerically stable way.

$$\begin{aligned} G(0,0) &= \left[I + V'(t)D'(t)U'(t)U(t)D(t)V(t)\right]^{-1} \\ &= V^{-1}D_L^{-1}\left[D'^{-1}_LV'^{-1}V^{-1}D_L^{-1} + D'_SU'UD_S\right]^{-1}D'^{-1}_LV'^{-1} \\ G(t,0) &= \left[I + U(t)D(t)V(t)V'(t)D'(t)U'(t)\right]^{-1}U(t)D(t)V(t) \\ &= U'^{-1}D'^{-1}_L\left[D_L^{-1}U^{-1}U'^{-1}D'^{-1}_L + D_SVV'D'_S\right]^{-1}D_SV \\ G(0,t) &= -\left[I + V'(t)D'(t)U'(t)U(t)D(t)V(t)\right]^{-1}V'(t)D'(t)U'(t) \\ &= -V^{-1}D_L^{-1}\left[D'^{-1}_LV'^{-1}V^{-1}D_L^{-1} + D'_SU'UD_S\right]^{-1}D'_SU' \end{aligned} \tag{2.52}$$

If one still remembers, the configuration weight $\det(I+B(\beta,0)) = \det(I+B(t,0)B(\beta,t))$ is just the inverse determinant of the equal-time Green's function matrix. To compute the ratio between the proposed new configuration and the configuration now, the information in equal-time Green's function matrices is enough. Since we can compute the Green's function stably, in principle we are already able to implement DQMC stably. However, if one computes Green's function in this way frequently, the time cost will be expensive. I will introduce a widely used economical process for configuration update below.

2.2.4 Configuration update

Everything is hard at the beginning. After generalizing a random configuration $\{l_{|q|,t}\}$, one needs to prepare a memory block to store B_t and $U(t), D(t), V(t), U'(t), D'(t), V'(t)$ accordingly at each imaginary time slice. Now, we have $B(\beta,0) = U(\beta)D(\beta)V(\beta)$ and $G(0,0) = (I+B(\beta,0))^{-1}$. We want to update the auxiliary field within the first imaginary time slice $B(1,0) = e^{-\Delta t H_0}\prod_{|q|\neq 0} e^{i\eta(l_{|q_1|,1})\sqrt{\frac{\Delta t V(q)}{4\Omega}}(\delta\rho_q+\delta\rho_{-q})} e^{\eta(l_{|q_2|,1})\sqrt{\frac{\Delta t V(q)}{4\Omega}}(\delta\rho_q-\delta\rho_{-q})}$ and define the updating matrix as $M_{|q_2|,1} = e^{\eta(l_{|q_2|,1})\sqrt{\frac{\Delta t V(q)}{4\Omega}}(\delta\rho_q-\delta\rho_{-q})}$. Then we move the updating matrix to the left without changing the determinant of the Greens' function by

$$G_b(1,1) = M_{|q_2|,1}G(0,0)M^{-1}_{|q_2|,1}. \tag{2.53}$$

Here $G_b(1,1)$ is just an auxiliary matrix and does not correspond to any observable since it comes from Trotter decomposition. If we try updating $l_{|q_2|,1}$ to $l'_{|q_2|,1}$, we need to compute the weight

$$\begin{aligned}
\frac{\det(I+B'(\beta,0))}{\det(I+B(\beta,0))} &= \det\left[\frac{I+(I+\Delta)M_{|q_2|,1}B(\beta,0)M^{-1}_{|q_2|,1}}{I+M_{|q_2|,1}B(\beta,0)M^{-1}_{|q_2|,1}}\right] \\
&= \det\left[I+\Delta\frac{M_{|q_2|,1}B(\beta,0)M^{-1}_{|q_2|,1}}{I+M_{|q_2|,1}B(\beta,0)M^{-1}_{|q_2|,1}}\right] \\
&= \det\left[I+\Delta(I-G_b(1,1))\right]
\end{aligned} \tag{2.54}$$

Here we define matrix $\Delta \equiv M'_{|q_2|,1}M^{-1}_{|q_2|,1} - I$ for convenience. One can see the update ratio can be derived easily from $G_b(1,1)$ and Δ. If this configuration is unaccepted, we keep $G_b(1,1)$ unchanged and move the next updating matrix $M_{|q_1|,1}$ in $G_b(1,1)$ from right to the left and repeat the process. If the proposed configuration is accepted, we need one more step to update $G_b(1,1)$ before moving the next updating matrix, i.e.

$$\begin{aligned}
G'_b(1,1) &= \left[I+(I+\Delta)((G_b(1,1))^{-1}-I)\right]^{-1} \\
&= G_b(1,1)\left[I+\Delta(I-G_b(1,1))\right]^{-1}
\end{aligned} \tag{2.55}$$

One can see the same matrix $I+\Delta(I-G_b(1,1))$ is used both for computing the weight and the updated $G'_b(1,1)$, we can compute it once for determinant and the inverse

since this will be the most time consuming step in our update process. Now everything goes smoothly until we updated all the $M_{|q|}$ in $B(1,0)$ and finally move $e^{-\Delta t H_0}$ from right to the left. However, as we mentioned in the last section this process can be numerically unstable after lots of matrix product and inverse operation. We would like to use a numerically stable Green's function to replace the one coming from iteration. The idea is recomputing $B(1,0)$ and the corresponding $U(1), D(1), V(1)$. Since $B(\beta,1)$ is not changed for now, $U'(1), D'(1), V'(1)$ keep the same. We use the time consuming numerical stabilization formula introduced in the last section to recompute $G(1,1) = [I + U(1)D(1)V(1)V'(1)D'(1)U'(1)]^{-1}$ and make sure this one is nearly the same with the one from iteration (e.g., the maximum matrix element error is smaller than 10^{-6} or one has to do this stabilization step more frequently). Then we can start the next time slice update similarly from the stabilized $G(1,1)$.

After finishing sweeping from right to left, we move $e^{-\Delta t H_0}$ from left to right, update in the same way for the exposed $M_{|q|,\beta}$ and move it from left to right. In this process $U(\beta-1), D(\beta-1), V(\beta-1)$ keep the same and one needs to recompute $U'(\beta-1), D'(\beta-1), V'(\beta-1)$ for stabilizing $G(\beta-1,\beta-1)$. After several sweeps, the Markov chain may achieve detailed balance and then one can sample the observable with stabilized Green's function. One can run many Markov chains parallel and sample within every chain. The direct average of all samples will give the ensemble averaged value we want.

Before we finish introducing the update section, I will introduce some useful formulas when the rank of Δ is much smaller than N (These formulas are widely used in real space lattice models since one auxiliary field only couples few sites). The first idea comes from the determinant $\det(I + UV) = \det(I_n + VU)$ where U, V are $N \times n$ $(N > n)$ rectangular matrices, I_n is the $n \times n$ identity matrix. The second idea comes from Sherman–Morrison formula for computing inverse

$$(A + UV)^{-1} = A^{-1} - A^{-1}U(I_n + VU)^{-1}VA^{-1}. \tag{2.56}$$

Here A is invertible $N \times N$ square matrix whose inverse is already known or can be computed easily so that the complexity reduces to compute the inverse of a smaller matrix. In our case let's focus on the matrix $I + \Delta(I - G_b)$. For example, the Δ, G_b and $I - G_b$ are

$$\Delta = \begin{pmatrix} 0 & 0 & 0 \\ \mathrm{X}_{2,1} & \mathrm{X}_{2,2} & 0 \\ \mathrm{X}_{3,1} & \mathrm{X}_{3,2} & 0 \end{pmatrix}, G_b = \begin{pmatrix} \mathrm{X}_{1,1} & \mathrm{X}_{1,2} & \mathrm{X}_{1,3} \\ \mathrm{X}_{2,1} & \mathrm{X}_{2,2} & \mathrm{X}_{2,3} \\ \mathrm{X}_{3,1} & \mathrm{X}_{3,2} & \mathrm{X}_{3,3} \end{pmatrix}, I - G_b = \begin{pmatrix} 1 - \mathrm{X}_{1,1} & -\mathrm{X}_{1,2} & -\mathrm{X}_{1,3} \\ -\mathrm{X}_{2,1} & 1 - \mathrm{X}_{2,2} & -\mathrm{X}_{2,3} \\ -\mathrm{X}_{3,1} & -\mathrm{X}_{3,2} & 1 - \mathrm{X}_{3,3} \end{pmatrix} \tag{2.57}$$

We can define the $\tilde{\Delta}$, $\tilde{G}_b$, $\tilde{G}_b^{\Delta}$ and $\tilde{G}_b^I$ as

$$\tilde{\Delta} = \begin{pmatrix} \mathrm{X}_{2,1} & \mathrm{X}_{2,2} \\ \mathrm{X}_{3,1} & \mathrm{X}_{3,2} \end{pmatrix}, \tilde{G}_b = \begin{pmatrix} \mathrm{X}_{1,2} & \mathrm{X}_{1,3} \\ \mathrm{X}_{2,2} & \mathrm{X}_{2,3} \\ \mathrm{X}_{3,2} & \mathrm{X}_{3,3} \end{pmatrix},$$
$$\tilde{G}_b^{\Delta} = \begin{pmatrix} -\mathrm{X}_{1,2} & -\mathrm{X}_{1,3} \\ 1-\mathrm{X}_{2,2} & -\mathrm{X}_{2,3} \end{pmatrix}, \tilde{G}_b^I = \begin{pmatrix} 1-\mathrm{X}_{1,1} & -\mathrm{X}_{1,2} & -\mathrm{X}_{1,3} \\ -\mathrm{X}_{2,1} & 1-\mathrm{X}_{2,2} & -\mathrm{X}_{2,3} \end{pmatrix} \tag{2.58}$$

where empty columns and rows in Δ and the corresponding columns and rows in G_b and $I - G_b$ are erased. With these new matrices, the determinant $\det(I + \Delta(I - G_b))$ and $G_b \left[I + \Delta(I - G_b)\right]^{-1}$ can be computed in a cheaper way

$$\begin{aligned} \det(I + \Delta(I - G_b)) &= \det(I_n + \tilde{G}_b^{\Delta}\tilde{\Delta}) \\ G_b \left[I + \Delta(I - G_b)\right]^{-1} &= G_b - \tilde{G}_b\tilde{\Delta}(I_n + \tilde{G}_b^{\Delta}\tilde{\Delta})^{-1}\tilde{G}_b^I \end{aligned} \tag{2.59}$$

One can see the key matrix becomes $I_n + \tilde{G}_b^{\Delta}\tilde{\Delta}$ where determinant and inverse are needed and the time complexity for this computation should be $O(r^3)$ where r is the rank of Δ. If r is independent with system size, the threshold complexity will be $O(N^2)$ for computing each matrix element. Considering the amount of all configuration field $N_\beta N_q$, our algorithm will have $O(N_\beta N_q N^2)$ time complexity. While this is not the case for the momentum space DQMC where $r = N$, so that complexity for momentum space algorithm will be $O(N_\beta N_q N^3)$.

Actually, this complexity reducing process can also apply on nonequal-time Green's function as shown explicitly in Ref [34]. While the formulas will not be used in general observable measurement since the nonequal-time Green's function can be computed within numerical stabilization step and is independent with the update weight. However, in the measurement of exponential observable Rényi entanglement entropy the update weight will be dependent on the nonequal-time Green's function and those formulas will become useful for a quicker update [3, 34, 35]. For completeness, we list those formulas below

$$\begin{aligned} G'_b(t,t) &= G_b(t,t)\left[I + \Delta(I - G_b(t,t))\right]^{-1} = G_b(t,t) - G_b(t,t)\Delta(I + G_b^I(t,t)\Delta)^{-1}G_b^I(t,t) \\ G'_b(t,0) &= G'_b(t,t)(I+\Delta)B_b(t,0) = G_b(t,0) + G_b(t,t)\Delta(I + G_b^I(t,t)\Delta)^{-1}G_b(t,0) \\ G'_b(0,0) &= (I + B_b(\beta,t)(I+\Delta)B_b(t,0))^{-1} = G_b(0,0) + G_b(0,t)\Delta(I + G_b^I(t,t)\Delta)^{-1}G_b(t,0) \\ G'_b(0,t) &= -G'_b(0,0)B_b(\beta,t) = G_b(0,t) - G_b(0,t)\Delta(I + G_b^I(t,t)\Delta)^{-1}G_b^I(t,t) \end{aligned} \tag{2.60}$$

Here we use B_b, G_b to label B and G matrix after moving $M_{|q|}$ matrix and $G_b^I \equiv I - G_b$. Considering Δ may not be full rank, one can replace the corresponding matrix with its tilde version (by erasing columns and rows).

2.3 Sign problem and sign bounds theory

2.3.1 Introduction to sign problem

As one can notice that there is no promise the weight $\mathrm{Tr}(\prod_t \hat{B}_t(\{l_{|q|,t}\}))$ is positive for all auxiliary field $\{l_{|q|,t}\}$ so that it is generally an ill-defined PMF. There are some sufficient conditions proving the weight is positive for all auxiliary fields [36–40]. The spirit is to prove the decoupled matrix $\prod_t B_t(\{l_{|q|,t}\})$ has complex conjugate paired eigenvalues such that $\det(I + \prod_t B_t(\{l_{|q|,t}\}))$ is just some mode square product which is always positive. However, when this is not the case, one can also simulate the system by a reweight trick [41].

$$\begin{aligned} \langle \hat{O} \rangle &\approx \frac{\sum_l W_l \langle \hat{O} \rangle_l}{\sum_{l'} W_{l'}} \\ &= \frac{\sum_l |\Re(W_l)| \frac{W_l \langle \hat{O} \rangle_l}{|\Re(W_l)|}}{\sum_{l'} |\Re(W_{l'})|} \\ &\equiv \frac{\frac{\sum_l |\Re(W_l)| \frac{W_l}{|\Re(W_l)|}}{\sum_{l'} |\Re(W_{l'})|}}{\langle sign \rangle} \\ &\equiv \frac{\langle \hat{O} \rangle_{|\Re(W_l)|}}{\langle sign \rangle} \end{aligned} \tag{2.61}$$

Here we define $W_l \equiv P(\{l_{|q|,t}\}) \,\mathrm{Tr}(\prod_t \hat{B}_t(\{l_{|q|,t}\}))$ for shorthand. One can see the numerator can be seen as a new observable $\frac{W_l \langle \hat{O} \rangle_l}{|\Re(W_l)|}$ with a new weight labeled by the red part. The denominator is the weighted average based on the same weight and the observable there is basically the sign of $\Re(W_l)$. It seems this routine can already avoid the ill-defined PMF problem. However, if one looks carefully for the $\langle sign \rangle \equiv \frac{\sum_l W_l}{\sum_{l'} |\Re(W_{l'})|}$, one will find its numerator is just the partition function Z and its denominator can be seen as some kind of fiction partition function Z_f so that $\langle sign \rangle \propto e^{-\beta N \delta f}$, where N is the system size and δf is the free energy density difference between Z and Z_f. Since δf can be a finite number, $\langle sign \rangle$ may decay exponentially with β and N. Remember $\langle \hat{O} \rangle$ such as Green's function is a $O(1)$ number, the numerator $\langle \hat{O} \rangle_{|\Re(W_l)|}$ should also be exponentially small at large size and low temperature limit. In a word, this computation process will cause exponentially large relative error which is the so-called sign problem.

2.3.2 Sign bounds theory

As one may already notice in the derivation above, this exponential decay behavior comes from finite δf. If we can find a case $\delta f = 0$, we will give a sufficient condition where $\langle sign \rangle$ cannot be exponentially small [1, 42, 43]. However, since we can only see $\sum_l |\Re(W_l)|$ as a fiction partition function, we have no idea about the corresponding

fiction free energy. An interesting observation comes below,

$$\sum_l |\Re(W_l)| = \sum_l P(l)|\Re(\mathrm{Tr}(\prod_t \hat{B}_t(l)))| \leqslant \sum_l P(l)|\,\mathrm{Tr}(\prod_t \hat{B}_t(l))| \leqslant \sqrt{\sum_l P(l)|\,\mathrm{Tr}(\prod_t \hat{B}_t(l))|^2}. \tag{2.62}$$

Here $P(l)$ can be seen as PMF so that we have these inequalities above. This interesting observation tells us we can enlarge the unknown numerator $\sum_l |\Re(W_l)|$ to derive the lower bound of $\langle sign\rangle$ if the expression on the right side of the inequality can be easily derived.

$$\langle sign\rangle \geqslant \frac{\sum_l W_l}{\sum_l P(l)|\,\mathrm{Tr}(\prod_t \hat{B}_t(l))|}, \langle sign\rangle \geqslant \frac{\sum_l W_l}{\sqrt{\sum_l P(l)|\,\mathrm{Tr}(\prod_t \hat{B}_t(l))|^2}} \tag{2.63}$$

This is the spirit of our sign bound theory, i.e. one can enlarge the denominator of $\langle sign\rangle$ to some quantity easily understood to estimate a lower bound of $\langle sign\rangle$. Corresponding to two enlarge ways shown above, two quick corollaries come below.

Corollary I: If $\mathrm{Tr}(\prod_t \hat{B}_t(l))$ is promised real for every configuration (e.g., decoupled Hamiltonian is real), $|\,\mathrm{Tr}(\prod_t \hat{B}_t(l))|^2 = (\mathrm{Tr}(\prod_t \hat{B}_t(l)))^2$. The corresponding Hamiltonian of enlarged denominator H_R is just the one introducing an extra $SU(2)$ symmetry on H (i.e., replacing every $c^\dagger_\alpha c_\beta$ by $\sum_{s=\pm 1} c^\dagger_{\alpha,s} c_{\beta,s}$). At low temperature limit, the sign bound in this case is

$$\langle sign\rangle \geqslant \frac{g_O e^{-\beta(E_O - E_R/2)}}{\sqrt{g_R}}. \tag{2.64}$$

Here $g_O, E_O(g_R, E_R)$ are ground state degeneracy and energy of original(reference) Hamiltonian $H(H_R)$. One can see if $E_O - E_R/2 = 0$, this will give a sufficient condition that $\langle sign\rangle$ cannot decay exponentially.

Corollary II: The Hamiltonian is written in a form below

$$H = K + \sum_A (A - \mu_A)^2. \tag{2.65}$$

Here K, A are some fermion bilinear $c^\dagger c$ and μ_A is real constant number (e.g., all kinds of repulsive Hubbard model). If for a certain group of μ_A there is no sign problem, for computing a Hamiltonian H with a group of μ_A where there is a sign problem, one can enlarge the denominator of $\langle sign\rangle$ to $\sum_l P(l)|\,\mathrm{Tr}(\prod_t \hat{B}_t(l))|$ and the corresponding reference Hamiltonian H_R is just the one where there is no sign problem (This can be seen as μ_A only contribute a configuration dependent phase before $|\,\mathrm{Tr}(\prod_t \hat{B}_t(l))|$ after decouple). At low temperature limit, the sign bound in this case is

$$\langle sign\rangle \geqslant \frac{g_O e^{-\beta(E_O - E_R)}}{g_R}. \tag{2.66}$$

Here $g_O, E_O(g_R, E_R)$ are ground state degeneracy and energy of original(reference) Hamiltonian $H(H_R)$. One can see if $E_O - E_R = 0$, this will give a sufficient condition that $\langle sign\rangle$ cannot decay exponentially.

Though these guiding rules are kind of abstract, one will see the applications of them in Chapter 3 later and have a better understanding.

2.4 Exponential observable measurement

In traditional DQMC, the observable is Green's function which is an $O(1)$ number both for each configuration and the final ensemble average value. And the weight is exponentially large compared with observable such that our importance sampling can work well. However, in some cases (e.g., free energy, Rényi entropy and Rényi entanglement entropy), the observable can also be exponentially large or small while the final result we would like to derive is an extensive quantity. This makes our traditional dividing way for the weight and observable works badly [3, 34, 35, 44]. In Ref [3, 45, 46], a general identity is proposed

$$\log\langle e^{\hat{X}}\rangle = \int_0^1 \mathrm{d}t\langle\hat{X}\rangle_t, \tag{2.67}$$

where $\langle\ldots\rangle_t$ represents a modified average where the distribution probability gets an extra factor of $e^{t\hat{X}}$. The weight and observable there is seen in a new point of view and this is the key idea for computing exponential observable. In this section, I will introduce the definition of Rényi entropy and Rényi entanglement entropy, then give DQMC formula for computing them and finally introduce an efficient integral algorithm where a new weight-observable separation way is taken explicitly to promise the importance sampling.

2.4.1 Rényi entropy and Rényi entanglement entropy

First, I would like to introduce entanglement in quantum mechanics and how to quantize this concept by introducing Rényi entropy. Let's assume we have two sites A and B. For each site, there can be a spin up or spin down arrow. Then one can use the spin basis $\{|\uparrow_A\uparrow_B\rangle, |\uparrow_A\downarrow_B\rangle, |\downarrow_A\uparrow_B\rangle, |\downarrow_A\downarrow_B\rangle\}$ to represent a vector in Hilbert space, so that any normalized state vector can be written in this basis as $|\psi_a\rangle = a_{11}|\uparrow_A\uparrow_B\rangle + a_{12}|\uparrow_A\downarrow_B\rangle + a_{21}|\downarrow_A\uparrow_B\rangle + a_{22}|\downarrow_A\downarrow_B\rangle$. Now we assume there is a discrete random variable x following distribution function $p(x)$. And for a given $x = a$, one has the possibility $p(a)$ of sitting on $|\psi_a\rangle$ state. Then we can define a density matrix operator $\hat{\rho}$ describing the system.

$$\hat{\rho} \equiv \sum_x p(x)|\psi_x\rangle\langle\psi_x| \tag{2.68}$$

One can easily check $\mathrm{Tr}(\hat{\rho}) = \sum_x p(x)(|x_{11}|^2 + |x_{12}|^2 + |x_{21}|^2 + |x_{22}|^2) = \sum_x p(x) = 1$ and $\langle\uparrow_A\uparrow_B|\hat{\rho}|\uparrow_A\uparrow_B\rangle = \sum_x p(x)|x_{11}|^2$ which gives the correct physical interpreting that the possibility of observing all kinds of states should be normalized and the possibility of observing a certain state is equal to the possibility of this state sitting in x times the possibility of observing it for a given x. Since we have an operator behaving like PMF very much, we can naturally use it to define the Rényi entropy to describe the

randomness of this PMF.

$$S^{(n)} \equiv \frac{1}{1-n}\log \mathrm{Tr}(\hat{\rho}^n) \tag{2.69}$$

The advantage of defining $S^{(n)}$ in this way is when taking $n \to 1$ we can recover the traditional von Neumann entropy $S^{(n)} \to -\mathrm{Tr}(\hat{\rho}\log(\hat{\rho}))$ and in Rényi form the tricky non-polynomial term $\log(\hat{\rho})$ is absent. For now, we have not encountered the concept of entanglement. The entropy comes totally from the randomness of thermodynamic weight $p(x)$ (The precise form is $p(x) \equiv \frac{e^{-\beta E_x}}{\sum_y e^{-\beta E_y}}$ where β is inverse of temperature and E_x is the eigen energy for eigenstate $|\psi_x\rangle$). But how can we describe the randomness from quantum superposition or how can we describe the entanglement property between different parts of whole system? The answer is we use reduced density matrix $\hat{\rho}_A$ by partially tracing one part as environment (Hilbert space of site B for example) in density matrix so that $\hat{\rho}_A \equiv \mathrm{Tr}_B(\hat{\rho})$ and replace $\hat{\rho}$ by this $\hat{\rho}_A$ operator in Rényi entropy to define Rényi entanglement entropy.

$$S_A^{(n)} \equiv \frac{1}{1-n}\log \mathrm{Tr}_A(\hat{\rho}_A^n) \tag{2.70}$$

Let's check the behavior of this quantity by looking at some examples below. First, we would like to compute $S_A^{(n)}$ for $\hat{\rho} = |\uparrow_A\uparrow_B\rangle\langle\uparrow_A\uparrow_B|$. Since $\hat{\rho}_A = \mathrm{Tr}_B(\hat{\rho}) = |\uparrow_A\rangle\langle\uparrow_A|$ and $\hat{\rho}_A^n = \hat{\rho}_A$, we can derive $S_A^{(n)} = 0$ for any n easily. This means when we have measured B site, there is no randomness for A site (A site must be $|\uparrow_A\rangle$ in this case). Another quick example is for pure superposition state density matrix $\hat{\rho} = \frac{1}{2}(|\uparrow_A\uparrow_B\rangle + |\downarrow_A\downarrow_B\rangle)(\langle\uparrow_A\uparrow_B| + \langle\downarrow_A\downarrow_B|)$. Since this is a pure state ($p(x) = 1$ only for one case $x = a$), one can check $\hat{\rho}^n = \hat{\rho}$ and entropy $S^{(n)} = 0$. This indicates quantum superposition (entanglement) cannot be measured in entropy $S^{(n)}$. However, one notices $\hat{\rho}_A = \frac{1}{2}(|\uparrow_A\rangle\langle\uparrow_A| + |\downarrow_A\rangle\langle\downarrow_A|)$ becomes a mixed state after partially tracing site B and $\hat{\rho}_A^n = \frac{1}{2^n}(|\uparrow_A\rangle\langle\uparrow_A| + |\downarrow_A\rangle\langle\downarrow_A|)$ so that $S_A^{(n)} = \frac{1}{1-n}\log 2^{1-n} = \log 2$ indicating finite entanglement between site A and B (i.e., after measuring B we still have a finite possibility for A sitting in different states even though there is no randomness for the whole original system!). One may also want to check $\hat{\rho} = \frac{1}{2}(|\uparrow_A\uparrow_B\rangle + |\downarrow_A\uparrow_B\rangle)(\langle\uparrow_A\uparrow_B| + \langle\downarrow_A\uparrow_B|)$ where it seems site A choosing up or down has nothing do to with site B, and the reduced density matrix $\hat{\rho}_A = \frac{1}{2}(|\uparrow_A\rangle + |\downarrow_A\rangle)(\langle\uparrow_A| + \langle\downarrow_A|)$ indeed is a pure state so that $S_A^{(n)} = 0$ (One may notice that in this case density matrix can be written as a product state $\hat{\rho} = \frac{1}{2}(|\uparrow_A\rangle + |\downarrow_A\rangle)(\langle\uparrow_A| + \langle\downarrow_A|) \otimes |\uparrow_B\rangle\langle\uparrow_B|$ so that both A and B parts are pure). In our final example, one can see the whole mixed state system can also have zero entanglement entropy. To see that, one just use $\hat{\rho} = \frac{1}{2}(|\uparrow_A\uparrow_B\rangle\langle\uparrow_A\uparrow_B| + |\downarrow_A\uparrow_B\rangle\langle\downarrow_A\uparrow_B|) = \frac{1}{2}(|\uparrow_A\rangle\langle\uparrow_A| + |\downarrow_A\rangle\langle\downarrow_A|) \otimes |\uparrow_B\rangle\langle\uparrow_B|$. Partially trace B site will derive a mixed state which has finite entropy while partially trace A site will give a pure state without entanglement. After checking those examples above, we can conclude that *for a system whose density matrix cannot be written as a single product of two separated parts, there will be a finite entanglement no matter it is pure or mixed state. While for a system whose density matrix can be written as a product, the total entanglement entropy of two parts is equal to its entropy.*

2.4.2 Entanglement Entropy in DQMC language

We have already obtained enough tools for computing many-fermion entropy by DQMC from sections before. Let's introduce how to derive a reduced density matrix in DQMC first so that we can compute the entanglement entropy. Then I will show the integral algorithm for computing entanglement entropy without suffering the badly sampling issue.

The reduced density matrix formula is thanks to Grover's work [47], where the reduced density matrix is expressed as

$$\hat{\rho}_A = \frac{\sum_l \det(I + \prod_t B_t(l)) \det\{\left[(I + \prod_t B_t(l))^{-1}\right]_A\} e^{c_A^\dagger \log\{\left[(I+\prod_t B_t(l))^{-1}\right]_A^{-1} - I_A\} c_A}}{\sum_{l'} \det(I + \prod_t B_t(l'))}. \tag{2.71}$$

Here $\left[(I + \prod_t B_t(l))^{-1}\right]_A$ means taking rows and columns labeled by A region sites from $N \times N$ matrix $(I + \prod_t B_t(l))^{-1}$ to form a new $N_A \times N_A$ matrix. Then the corresponding I_A, $c_A^\dagger$ and c_A also only take parts with A region label. Since the red part in above formula is just the PMF, let's focus on the left part $\hat{\rho}_{A;l} \equiv \frac{e^{c_A^\dagger \log\{\left[(I+\prod_t B_t(l))^{-1}\right]_A^{-1} - I_A\} c_A}}{\mathrm{Tr}_A(e^{c_A^\dagger \log\{\left[(I+\prod_t B_t(l))^{-1}\right]_A^{-1} - I_A\} c_A})}$ to see it indeed has all the properties needed for a reduced density matrix. First, it is easy to check the normalization requirement

$$\mathrm{Tr}_A \left(\det\{ \left[(I + \prod_t B_t(l))^{-1} \right]_A \} e^{c_A^\dagger \log\{\left[(I+\prod_t B_t(l))^{-1}\right]_A^{-1} - I_A\} c_A} \right) = 1. \tag{2.72}$$

Then, we would like to prove

$$\mathrm{Tr}_A(\hat{\rho}_A c_i^\dagger c_j) = \mathrm{Tr}(\hat{\rho} c_i^\dagger c_j) \tag{2.73}$$

for any $i, j \in A$ so that $\hat{\rho}_A$ works as a density matrix for $c_i^\dagger c_j$ operator in A region (This is the definition of the reduced density matrix). Except for the same PMF part, trace the RHS ($\hat{\rho}_l \equiv \frac{\prod_t \hat{B}_t(l)}{\mathrm{Tr}(\prod_t \hat{B}_t(l))}$) is

$$\frac{\mathrm{Tr}(\prod_t \hat{B}_t(l) c_i^\dagger c_j)}{\mathrm{Tr}(\prod_t \hat{B}_t(l))} = \left[I - (I + \prod_t B_t(l))^{-1} \right]_{j,i} \tag{2.74}$$

Similarly except for the same PMF part, trace the LHS will derive (remember the definition $\hat{\rho}_{A;l} \equiv \frac{e^{c_A^\dagger \log\{\left[(I+\prod_t B_t(l))^{-1}\right]_A^{-1} - I_A\} c_A}}{\mathrm{Tr}_A(e^{c_A^\dagger \log\{\left[(I+\prod_t B_t(l))^{-1}\right]_A^{-1} - I_A\} c_A})}$)

$$\begin{aligned}
&\frac{\mathrm{Tr}_A(e^{c_A^\dagger \log\{\left[(I+\prod_t B_t(l))^{-1}\right]_A^{-1} - I_A\} c_A} c_i^\dagger c_j)}{\mathrm{Tr}_A(e^{c_A^\dagger \log\{\left[(I+\prod_t B_t(l))^{-1}\right]_A^{-1} - I_A\} c_A})} \\
&= \mathrm{Tr}_{N_A}(\left[(I+\prod_t B_t(l))^{-1}\right]_A \{\left[(I+\prod_t B_t(l))^{-1}\right]_A^{-1} - I_A\} \delta_{r=i,c=j}) \\
&= \left[I - (I+\prod_t B_t(l))^{-1}\right]_{j,i}
\end{aligned} \tag{2.75}$$

This equals to the RHS and the proof is finished for $c_i^\dagger c_j$ case. To prove for any operator chain it always works, one just needs to use Wick's theorem to expand both $\mathrm{Tr}_A(\hat{\rho}_{A;l} c_i^\dagger c_j c_{i'}^\dagger c_{j'} ...)$ and $\mathrm{Tr}(\hat{\rho}_l c_i^\dagger c_j c_{i'}^\dagger c_{j'} ...)$ into product of $\mathrm{Tr}_A(\hat{\rho}_{A;l} c^\dagger c)$ and $\mathrm{Tr}(\hat{\rho}_l c^\dagger c)$ to see it is correct (see Appendix A). Then we can write down the direct formula for computing the second Rényi entanglement entropy

$$S_A^{(2)} = -\log \mathrm{Tr}(\hat{\rho}^2) = -\log\left[\frac{\sum_{\{l,l'\}} \det\left[G(\{l\})G(\{l'\})\right] \det\left[g(\{l,l'\})\right]}{\sum_{\{l,l'\}=\{\pm 1\}} \det\left[G(\{l\})G(\{l'\})\right]}\right] \tag{2.76}$$

Here we define $G(\{l\}) = I + \prod_t B_t(l)$ and $g(\{l,l'\}) = \left[G^{-1}(\{l\})\right]_A \left[G^{-1}(\{l'\})\right]_A + (I_A - \left[G^{-1}(\{l\})\right]_A)(I_A - \left[G^{-1}(\{l'\})\right]_A)$ for shorthand. Now one can directly compute the Rényi entanglement entropy based Monte Carlo sampling over red part PMF. But this will suffer the exponential fluctuation of samples [44]. An intuitive interpretation for this is entropy is an extensive quantity proportional to size of system so that the mean value in $-\log[...]$ has to be exponentially small with system size and the relative error for this average is exponentially large. We solve this problem by write the formula above in an integral form, where the integrand at each point can be computed by Monte Carlo routine and numerically integrating will give the final result [3]. Below, we will illustrate those steps. $S_A^{(2)}$ can be decomposed as

$$\begin{aligned}
S_A^{(2)} &= -\sum_{i=1}^{N_k} \log(\frac{\lambda_i}{\lambda_{i-1}}), \\
\frac{\lambda_i}{\lambda_{i-1}} &= \frac{\sum_{\{l,l'\}} \det\left[G(\{l\})G(\{l'\})\right] \det\left[g(\{l,l'\})\right]^{(i-1)/N_k} \det\left[g(\{l,l'\})\right]^{1/N_k}}{\sum_{\{l,l'\}} \det\left[G(\{l\})G(\{l'\})\right] \det\left[g(\{l,l'\})\right]^{(i-1)/N_k}} \\
&\equiv \left\langle \det\left[g(\{l,l'\})\right]^{1/N_k} \right\rangle_i
\end{aligned} \tag{2.77}$$

The computation for each piece $\log(\frac{\lambda_i}{\lambda_{i-1}})$ can be done in parallel and adding them together will derive the final result (This is the incremental idea shown in Ref [35]). When N_k is large enough, the exponential fluctuation can be suppressed by $1/N_k$ power. However, in this method we have no idea about how large this N_k should be enough.

Let's focus on the large N_k limit below. Since x^{1/N_k} for $x > 0$ approaches to uniform value when taking $N_k \to \infty$, taking the equality case of Jensen's inequality when we set $N_k \to \infty$ limit gives

$$\begin{aligned} S_A^{(2)} &= -\sum_{i=1}^{N_k} \log(\left\langle \det\left[g(\{l,l'\})\right]^{1/N_k}\right\rangle_i) \\ &\leqslant -\frac{1}{N_k}\sum_{i=1}^{N_k} \left\langle \log(\det\left[g(\{l,l'\})\right])\right\rangle_i \\ &\to -\int_0^1 dt \frac{\sum_{\{l,l'\}} \det\left[G(\{l\})G(\{l'\})\right] \det\left[g(\{l,l'\})\right]^t \log(\det\left[g(\{l,l'\})\right])}{\sum_{\{l,l'\}} \det\left[G(\{l\})G(\{l'\})\right] \det\left[g(\{l,l'\})\right]^t} \\ &\equiv -\int_0^1 dt \left\langle \log(\det\left[g(\{l,l'\})\right])\right\rangle_t \end{aligned} \tag{2.78}$$

Since we take $N_k \to \infty$ limit for integral, the final line above for $S_A^{(2)}$ is exact. Here, our observable becomes $\log(\det\left[g(\{l,l'\})\right])$ which is not exponentially small and the integral over continuous field $t \in [0,1]$ can be realized by numerical integral. This formula can also be easily generalized to $S_A^{(n)}$ and we show $S_A^{(2)}$, $S_A^{(3)}$ results for 4×4 dichotomy half-filled square lattice Hubbard model in the Fig 2.2 below. Besides, one can notice the derivative $\frac{\partial\langle\log(\det[g(\{l,l'\})])\rangle_t}{\partial t} = \left\langle \log(\det\left[g(\{l,l'\})\right])^2\right\rangle_t - \langle\log(\det\left[g(\{l,l'\})\right])\rangle_t^2 \geqslant 0$ indicates the fluctuation for $\langle\log(\det\left[g(\{l,l'\})\right])\rangle_t$. As long as the slope is not sharp (i.e., indicating mild fluctuation which is indeed the case in our computation), we can compute $\langle\log(\det\left[g(\{l,l'\})\right])\rangle_t$ accurately at given t points and integrating them within $[0,1]$ will give us the 2nd Rényi entropy. The idea works the same for the computation of free energy and entropy. For completeness, we list all the formulas below.

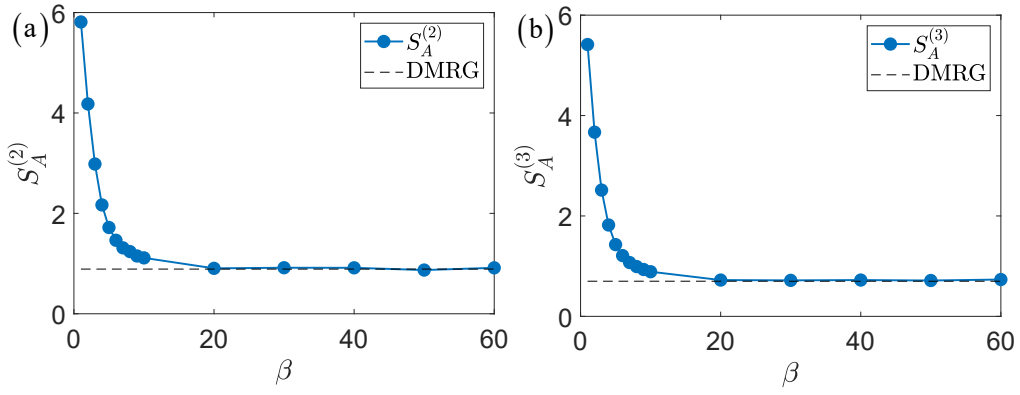


Figure 2.2: The 2nd and 3rd Rényi entropy for 4×4 dichotomy half-filled square lattice Hubbard model. Blue dots in (a), (b) indicates $S_A^{(2)}$, $S_A^{(3)}$ from DQMC integral algorithm and the dark dashed line is result of density matrix renormalization group (DMRG) at zero temperature. This figure comes from Ref [3].

$$
\begin{aligned}
S_A^{(n)} &\equiv -\frac{1}{n-1}\log(\mathrm{Tr}(\hat{\rho}_A^n)) \\
&= \frac{1}{1-n}\int_0^1 dt \frac{\sum_l [P(l)]^n \,\mathrm{Tr}(\hat{\rho}_{A;l}^n)^t \log(\mathrm{Tr}(\hat{\rho}_{A;l}^n))}{\sum_{l'} [P(l')]^n \,\mathrm{Tr}(\hat{\rho}_{A;l'}^n)^t} \\
&\equiv -\int_0^1 dt \left\langle \log(\mathrm{Tr}(\hat{\rho}_{A;l}^n)) \right\rangle_t , \\
S^{(n)} &\equiv -\frac{1}{n-1}\log(\mathrm{Tr}(\hat{\rho}^n)) \\
&= \frac{1}{1-n}\int_0^1 dt \frac{\sum_l [P(l)]^n \,\mathrm{Tr}(\hat{\rho}_l^n)^t \log(\mathrm{Tr}(\hat{\rho}_l^n))}{\sum_{l'} [P(l')]^n \,\mathrm{Tr}(\hat{\rho}_{l'}^n)^t} \\
&\equiv -\int_0^1 dt \left\langle \log(\mathrm{Tr}(\hat{\rho}_l^n)) \right\rangle_t , \\
F &\equiv -\frac{1}{\beta}\log(Z) \\
&= -\frac{1}{\beta}\int_0^1 dt \frac{\sum_l W_l P_l^t \log(P_l)}{\sum_{l'} W_{l'} P_{l'}^t} \\
&\equiv -\frac{1}{\beta}\int_0^1 dt \left\langle \log(P_l) \right\rangle_t . \qquad (2.79)
\end{aligned}
$$

Here $[P(l)]^n \equiv \prod_{i=1}^n P(l_i), \rho_{A;l}^n \equiv \prod_{i=1}^n \rho_{A;l_i}, \rho_l^n \equiv \prod_{i=1}^n \rho_{l_i}$, W_l is the decouple coefficient independent with Hamiltonian and P_l is the determinant contribution from Hamiltonian (e.g., if we decouple the interaction term like $e^{\alpha\hat{O}^2} = \frac{1}{4}\sum_{l=\pm1,\pm2}\gamma(l)e^{\sqrt{\alpha}\eta(l)\hat{o}} + O\left(\alpha^4\right)$, where $\gamma(\pm1) = 1+\frac{\sqrt{6}}{3}, \gamma(\pm2) = 1-\frac{\sqrt{6}}{3}, \eta(\pm1) = \pm\sqrt{2(3-\sqrt{6})}$ and $\eta(\pm2) = \pm\sqrt{2(3+\sqrt{6})}$, then the $\frac{\gamma(l)}{4}$ part contributes the W_l, and after tracing the fermion degree of freedom the determinant part is the P_l term).

One can see by introducing an additional integral and reallocating the weight and observable in a new point of view, the exponential observable becomes a traditional polynomial observable and the importance sampling idea can work again.

2.5 Further discussion

As the development of the numerical method, lots of interesting projects become possible for study. I will give some directions for the future simulation based on the developed numerical methods in this chapter.

According to the sign bounds theory, sign problem of DQMC at low temperature limit can be locked with the ground state property. Some near exactly solvable model like fractional quantum hall with near Haldane pseudo potential can become candidate for study with DQMC. The topological property can also be detected with the entanglement measurement of the developed integral algorithm.

Besides the entanglement, integral algorithm also provides an efficient and low-error way for computing free energy. By considering the free energy change with involved

perturbation in the Hamiltonian, one can study the stability with the perturbation as well as the possible phase transition after differential.

Finally, with the fashion of quantum circuit, DQMC can also be a potential tool for studying fermionic quantum circuit. By noticing the random evolution of traceless free fermion Hamiltonian will at most involve real sign, such evolution for any $SU(2)$ fermions will have no sign problem for simulation.

Chapter 3

Twisted bilayer graphene (TBG)

3.1 Outline

In this chapter, I will begin from the tight-binding model of graphene, derive the Dirac dispersion and solve the low-energy Hamiltonian involving inter-layer tunneling to give the band dispersion for TBG. By considering the twisted angle with dispersive bands, I will introduce the gate-tunable nonlinear Hall effect induced by the Berry curvature sliding. At magic angle with flat bands, I will discuss the ground state and excitation at charge neutrality by taking flat-band limit and DQMC simulation results with finite band width. Also at magic angle but at the other integer fillings, I will discuss the connection between ground state degeneracy and the polynomial sign problem of DQMC at all kinds of chiral and non-chiral cases. As an example, finite-temperature topological phase transition is identified at $\nu = \pm 1$. Finally, I will give some future directions along the way I have studied in the discussion section.

3.2 Graphene and Dirac dispersion

In this section, I will introduce the tight-binding model describing low-energy physics of graphene, derive the Dirac dispersion and discuss the symmetries protecting the gapless Dirac cone here [10].

By assuming the p-electron wavefunction is localized at the carbon atom center and ignoring the oscillation of carbon atoms, we can describe electrons in graphene approximately by a nearest-neighbor-hopping tight-binding Hamiltonian on a honeycomb lattice H_h.

$$H_h = \sum_{\langle i,j \rangle} t_{i,j} c_i^\dagger c_j \tag{3.1}$$

Here $t_{i,j}$ comes from the overlap of the wavefunction localized at the nearest neighbor carbon atoms for the single particle operator (i.e., kinetic term and mean field potential term). Because of the C_6 symmetry, $t_{i,j} = t_1$ is a constant number in graphene. By

labeling A, B sublattices explicitly and defining the lattice vector R_1, R_2 as shown in Fig 3.1, we use the real space Hamiltonian below to describe graphene.

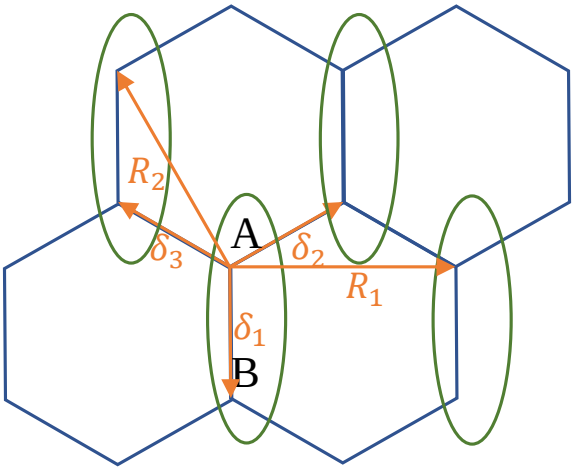


Figure 3.1: The schematic plot of honeycomb lattice with A, B sublattice. Green circles label unit cells and orange arrows define vectors.

$$H_g = t_1 \sum_{R_i} (c^\dagger_{R_i,A} c_{R_i,B} + c^\dagger_{R_i,A} c_{R_i+R_1+R_2,B} + c^\dagger_{R_i,A} c_{R_i+R_2,B} + h.c.) \tag{3.2}$$

According to Fourier transformation

$$\begin{cases} c^\dagger_{R_i,A} = \dfrac{1}{\sqrt{N}} \sum\limits_{k_1} e^{ik_1 \cdot R_i} c^\dagger_{k_1,A} \\ c^\dagger_{R_i,B} = \dfrac{1}{\sqrt{N}} \sum\limits_{k_2} e^{ik_2 \cdot (R_i+\delta_1)} c^\dagger_{k_2,B} \end{cases}, \begin{cases} c_{R_i,A} = \dfrac{1}{\sqrt{N}} \sum\limits_{k_1} e^{-ik_1 \cdot R_i} c_{k_1,A} \\ c_{R_i,B} = \dfrac{1}{\sqrt{N}} \sum\limits_{k_2} e^{-ik_2 \cdot (R_i+\delta_1)} c_{k_2,B} \end{cases}, \tag{3.3}$$

and orthogonal relation $\sum_{R_i} e^{i(k-k_0)\cdot R_i} = N\delta_{k,k_0}$, we rewrite H_g in plane-wave basis

$$H_g = t_1 \sum_{k} (e^{-k\cdot\delta_1} + e^{-ik\cdot(R_1+R_2+\delta_1)} + e^{-ik\cdot(R_2+\delta_1)}) c^\dagger_{k,A} c_{k,B} + h.c. \tag{3.4}$$

This is a block diagonalized Hamiltonian labeled by k because of the discrete transition symmetry. Within each block, there are two sublattices degree of freedom so that one can express Hamiltonian at each k point by a 2×2 matrix as

$$H_k = t_1 \begin{pmatrix} 0 & e^{-ik\cdot\delta_1} + e^{-ik\cdot\delta_2} + e^{-ik\cdot\delta_3} \\ e^{ik\cdot\delta_1} + e^{ik\cdot\delta_2} + e^{ik\cdot\delta_3} & 0 \end{pmatrix}. \tag{3.5}$$

The definition of δ_i, R_i is shown in Fig 3.1 and I set $R_1 = (\sqrt{3}a, 0), R_2 = (-\frac{\sqrt{3}}{2}a, \frac{3}{2}a)$ where a is the lattice constant. The eigenvalues are $E_k = \pm t_1 |e^{ik\cdot\delta_1} + e^{ik\cdot\delta_2} + e^{ik\cdot\delta_3}|$. Since $t_1 \neq 0$, one can find two degenerate points in the first Brillouin zone coming from

the solution of $e^{ik\cdot(\delta_1-\delta_3)}+e^{ik\cdot(\delta_2-\delta_3)}+1=0$,

$$\begin{cases} k\cdot R_2=\dfrac{2\pi}{3} \\ k\cdot R_1=\dfrac{2\pi}{3} \end{cases} \text{or} \begin{cases} k\cdot R_2=-\dfrac{2\pi}{3} \\ k\cdot R_1=-\dfrac{2\pi}{3} \end{cases} \Rightarrow \begin{cases} K^+=\dfrac{2\pi}{3\sqrt{3}a}(1,\sqrt{3}) \\ K^-=-\dfrac{2\pi}{3\sqrt{3}a}(1,\sqrt{3}) \end{cases}. \tag{3.6}$$

The natural filling for graphene is charge neutrality point (CNP) where Fermi surface reduces to two points K^+, K^-. Considering low-energy physics we can expand the Hamiltonian H_k to linear order around, for example, K^+ as

$$\begin{aligned} H_{K^++k} &= t_1 \begin{pmatrix} 0 & e^{i\frac{2\pi}{3}}e^{-ik\cdot\delta_1}+e^{-i\frac{2\pi}{3}}e^{-ik\cdot\delta_2}+e^{-ik\cdot\delta_3} \\ e^{-i\frac{2\pi}{3}}e^{ik\cdot\delta_1}+e^{i\frac{2\pi}{3}}e^{ik\cdot\delta_2}+e^{ik\cdot\delta_3} & 0 \end{pmatrix} \\ &\approx t_1 \begin{pmatrix} 0 & -e^{i\frac{2\pi}{3}}\delta_1-e^{-i\frac{2\pi}{3}}\delta_2-\delta_3 \\ e^{-i\frac{2\pi}{3}}\delta_1+e^{i\frac{2\pi}{3}}\delta_2+\delta_3 & 0 \end{pmatrix}\cdot ik \\ &= \begin{pmatrix} 0 & (1,i) \\ (1,-i) & 0 \end{pmatrix}\cdot\tilde{k} \\ &= \tilde{k}_x\sigma_x-\tilde{k}_y\sigma_y \end{aligned} \tag{3.7}$$

Here we have absorbed the constant number in $\tilde{k}$ and one can see the shape of energy dispersion is a cone $E_{\tilde{k}}=\pm\sqrt{\tilde{k}_x^2+\tilde{k}_y^2}$. The similar cone-shape Hamiltonian can also be found as $H_{K^-+k}=-\tilde{k}_x\sigma_x-\tilde{k}_y\sigma_y$ near K^- point. Actually one can derive this H_{K^-+k} by time reversal symmetry $H^*_{K^+-k}=H_{K^-+k}$. Time reversal alone cannot protect the Dirac cone from gapping since one can see adding a mass term σ_z can easily gap the degenerate points without breaking time reversal.

$$\begin{cases} H_{K^++k}=\tilde{k}_x\sigma_x-\tilde{k}_y\sigma_y+m\sigma_z \\ H_{K^-+k}=-\tilde{k}_x\sigma_x-\tilde{k}_y\sigma_y+m\sigma_z \end{cases}. \tag{3.8}$$

One can check there is still $H^*_{K^+-k}=H_{K^-+k}$ while the eigenvalues at K^+, K^- become non-degenerate $\pm m$. For shorthand, let's name those two cones as two valleys labeled by $\tau=\pm1$. One may notice another inversion transformation (or C_2 rotation which is the same as inversion in 2D) can also connect the low-energy Hamiltonian between two valleys $\sigma_x H_{K^+-k}\sigma_x=H_{K^-+k}$. Again, inversion alone also cannot protect the Dirac cone from gapping and one can check this by adding different mass terms σ_z at two valleys without breaking inversion.

$$\begin{cases} H_{K^++k}=\tilde{k}_x\sigma_x-\tilde{k}_y\sigma_y+m\sigma_z \\ H_{K^-+k}=-\tilde{k}_x\sigma_x-\tilde{k}_y\sigma_y-m\sigma_z \end{cases}. \tag{3.9}$$

However, if one restricts the system has both time reversal and inversion symmetries, one can derive a constrain for the Hamiltonian within one valley $\sigma_x H^*_{K^++k}\sigma_x=H_{K^++k}$. Since our Hamiltonian is a 2×2 Hermitian matrix at a given k point, one can use σ

matrices and identity matrix σ_0 to express it, i.e. $H_k = a\sigma_x + b\sigma_y + c\sigma_z + d\sigma_0$. Without considering trivial energy shift by setting $d = 0$, the symmetry constrain becomes $a = a^*, b = b^*, c = -c^*$. The Hermitian constrain requires $c = c^*$ so that $c = 0$. Assuming any perturbation controlled by the parameters a, b, the perturbative Hamiltonian should be $H_{\tilde{k}} = \tilde{k}_x\sigma_x - \tilde{k}_y\sigma_y + a\sigma_x + b\sigma_y = (\tilde{k}_x + a)\sigma_x - (\tilde{k}_y - b)\sigma_y$. One can see this perturbation just shift the Dirac point to $K^+ + (-a, b)$. We say this Dirac cone is locally protected by time reversal-inversion symmetry. One can also prove C_3 rotation symmetry will prohibit this shift departing from K^+, K^- where we call C_3 globally protect this Dirac cone.

This is the story about primitive graphene. In experiments, one can stack multilayer graphene (with or without relative twist) to give more Dirac cones (e.g., AA stacking bilayer preserving inversion) or a quadratic band touching (e.g., AB stacking bilayer breaking inversion) near K^+, K^- points and make the story more interesting. I will focus on the near AA stacking twisted bilayer graphene case in the rest part of this chapter, where at a certain twist angle the energy band can be tuned flat (i.e., the slope of the Dirac cone becomes zero) so that interaction terms play significant roles and all kinds of correlation effects are observed in experiments [48–70].

3.3 Bistritzer-MacDonald (BM) model for small angle TBG

There are tight binding model and continuous model for theoretical study of TBG [71–76]. In this section, I will introduce the continuous BM model for describing small angle twisted bilayer graphene which gives the band dispersion and wavefunction serving as starting point for interaction involved computation later.

First, one puts two graphene Brillouin zones with a small twist together and will see near a K point of one valley two Dirac cones have a relative shift. For now, we have not considered the inter-layer hopping yet and the nearest Dirac cone just comes from the other layer. If one considers the inter-layer hopping up to the leading order, one should consider the hopping from two nearest Dirac cone low-energy fermions in momentum space. I would like to use the matrix form of Hamiltonian involving additional layer degree of freedom to describe this consideration.

$$H_{k,k'} = \delta_{k,k'} \begin{pmatrix} -\hbar v_F (k - K_1)\cdot\sigma & 0 \\ 0 & -\hbar v_F (k - K_2)\cdot\sigma \end{pmatrix} + \begin{pmatrix} 0 & U \\ U^\dagger & 0 \end{pmatrix} \tag{3.10}$$

Now the explicit 2×2 labels two layers. One can see the first term comes from two identical Dirac cones located at different momentum points K_1, K_2 and the second term coming from Fourier transformation for inter-layer hopping. If we label the momentum linking two nearest Dirac cones with q_1, q_2, q_3 as shown in Fig 3.2. The hopping matrix should be written as

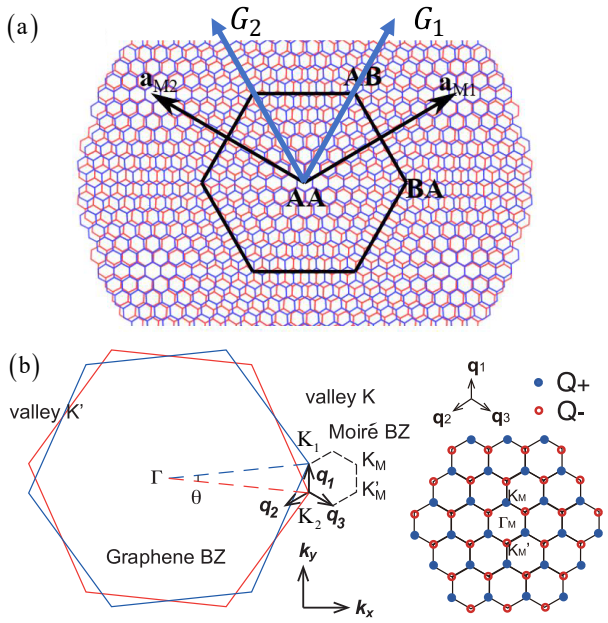


Figure 3.2: Illustration of real space AA,AB,BA region and reciprocal lattice vectors G_1, G_2 in (a) and momentum space graphene Brillouin zone (BZ), moiré BZ and q_1, q_2, q_3 definition in (b). These figures come from Ref [77, 78]

$$T^{\alpha,\beta}(r) = \sum_{j=1}^{3} e^{-iq_j \cdot r} T_j^{\alpha,\beta} \tag{3.11}$$

Here I use α, β to label sublattices. One can see momentum space nearest neighbor hopping becomes real space local tunneling. By identifying AA, AB, BA tunneling should have the property that AA and BB tunneling reaches the largest value in AA region and only AB, BA tunneling exist in AB, BA region separately, I put AA region at $r = 0$ and then $T_j^{\alpha,\beta}$ has the matrix form below.

$$T_j = \begin{pmatrix} u_0 & u_1 e^{-i\frac{2\pi(j-1)}{3}} \\ u_1 e^{i\frac{2\pi(j-1)}{3}} & u_0 \end{pmatrix} \tag{3.12}$$

Here I use u_0, u_1 to label different magnitude of intra-sublattice and inter-sublattice tunneling. This difference comes from the wrinkle of TBG where the inter-layer distance is smaller in AB region than AA so that $u_1 > u_0$ [79, 80]. To express the whole Hamiltonian in the same basis, one needs to Fourier transform the real space part of

$T^{\alpha,\beta}(r)$.

$$\begin{aligned}\sum_{j=1}^{3} e^{-iq_j\cdot r} &\rightarrow \frac{1}{N\Omega}\sum_{j=1}^{3}\sum_{k_1}\sum_{k_2}\int d^2 r e^{i(k_1-k_2-q_j)\cdot r} \\ &= \frac{1}{N}\sum_{j=1}^{3}\sum_{k_1}\sum_{k_2}\delta_{k_1,k_2+q_j} \\ &= \sum_{j=1}^{3}\sum_{k_1}\delta_{k_1,k_1'-q_1+q_j} \\ &= \sum_{k_1}(\delta_{k_1,k_1'}+\delta_{k_1,k_1'-G_1}+\delta_{k_1,k_1'-G_2}) \end{aligned} \tag{3.13}$$

Here Ω is the area of the system and I use G_1, G_2 to label moiré reciprocal lattice vectors with the definition $q_1 = \frac{G_1+G_2}{3}, q_2 = \frac{G_2-2G_1}{3}, q_3 = \frac{G_1-2G_2}{3}$. Finally, in the same basis (plane wave basis), we can write down the inter-layer hopping U term in BM model Hamiltonian for $+$ valley as

$$U = \begin{pmatrix} u_0 & u_1 \\ u_1 & u_0 \end{pmatrix}\delta_{k,k'} + \begin{pmatrix} u_0 & u_1 e^{-i\frac{2\pi}{3}} \\ u_1 e^{i\frac{2\pi}{3}} & u_0 \end{pmatrix}\delta_{k,k'-G_1} + \begin{pmatrix} u_0 & u_1 e^{i\frac{2\pi}{3}} \\ u_1 e^{-i\frac{2\pi}{3}} & u_0 \end{pmatrix}\delta_{k,k'-G_2} \tag{3.14}$$

The Hamiltonian in the other $-$ valley can be derived by time reversal transformation (move the element from $\delta_{k,k'}$ to $\delta_{-k,-k'}$ with a complex conjugate). In a word, we write down BM Hamiltonian for two valleys $\tau, -\tau$ as

$$\begin{aligned} H^{\tau}_{k,k'} &= \delta_{k,k'}\begin{pmatrix} -\hbar v_F(k-K_1)\cdot\sigma & 0 \\ 0 & -\hbar v_F(k-K_2)\cdot\sigma \end{pmatrix} + \begin{pmatrix} 0 & U^{\tau} \\ U^{\tau\dagger} & 0 \end{pmatrix} \\ U^{\tau} &= \begin{pmatrix} u_0 & u_1 \\ u_1 & u_0 \end{pmatrix}\delta_{k,k'} + \begin{pmatrix} u_0 & u_1 e^{-i\frac{2\pi}{3}} \\ u_1 e^{i\frac{2\pi}{3}} & u_0 \end{pmatrix}\delta_{k,k'-G_1} + \begin{pmatrix} u_0 & u_1 e^{i\frac{2\pi}{3}} \\ u_1 e^{-i\frac{2\pi}{3}} & u_0 \end{pmatrix}\delta_{k,k'-G_2} \\ H^{-\tau}_{k,k'} &= \delta_{k,k'}\begin{pmatrix} -\hbar v_F(-k-K_1)\cdot\sigma^* & 0 \\ 0 & -\hbar v_F(-k-K_2)\cdot\sigma^* \end{pmatrix} + \begin{pmatrix} 0 & U^{-\tau} \\ U^{-\tau\dagger} & 0 \end{pmatrix} \\ U^{-\tau} &= \begin{pmatrix} u_0 & u_1 \\ u_1 & u_0 \end{pmatrix}\delta_{k,k'} + \begin{pmatrix} u_0 & u_1 e^{i\frac{2\pi}{3}} \\ u_1 e^{-i\frac{2\pi}{3}} & u_0 \end{pmatrix}\delta_{k,k'+G_1} + \begin{pmatrix} u_0 & u_1 e^{-i\frac{2\pi}{3}} \\ u_1 e^{i\frac{2\pi}{3}} & u_0 \end{pmatrix}\delta_{k,k'+G_2}. \end{aligned} \tag{3.15}$$

According to first principle parameter near the first magic angle flat band (slope of final Dirac dispersion approaches zero), we set $(\theta, \hbar v_F/a_0, u_0, u_1) = (1.08^\circ, 2.38eV, 0.06eV, 0.11eV)$, where θ is the relative twist angle and $a_0 = 0.246nm$ is the graphene lattice constant. One can see this is a infinite hopping model in momentum space (i.e., the Hilbert space is infinite) with low-energy diagonal elements near K_1, K_2 points. But by taking a $|G_c| = 6|G_0|$ Brillouin zone momentum cut near $k - K_1 = 0, k - K_2 = 0$, one can derive the converged low-energy band dispersion (as shown in Fig 2.1) and corresponding wavefunction.

3.4 Gate-tunable nonlinear Hall effect in topological flat bands

As mentioned in Chapter 2 where the nonlinear Hall effect connects directly with the Berry curvature dipole, I would like to discuss the nonlinear Hall effect in TBG flat bands. According to Onsager reciprocal relations, TBG with time reversal symmetry should have symmetric conductivity tensor so that linear Hall conductance should always be zero. By breaking C_3 rotational symmetry with strain, the second order Hall conductance is allowed to exist and becomes the leading order effect [13, 51, 81–85]. The nonlinear Hall effect in TBG flat bands can be even more interesting because the hexagonal boron nitride (hbn)-aligned potential breaks inversion symmetry and gaps the Dirac cone, which prohibits the trivial Berry curvature redistribution from band close-reopen topological phase transition process [4, 86, 87]. However, the flat band shape can be easily tuned by relatively small gate voltage such that Berry curvature hotspots can slide within flat band and lead to significant changes in the direction and amplitude of the nonlinear Hall signal. We give the theoretical analysis and computation results below.

Following Ref [86–88], we first discuss how to include strain in BM model in our calculation. A small amount of strain field is introduced to break the three-fold rotational symmetry. In the theoretical model, we scanned different strain field at different orientations and picked the one where the simulated nonlinear Hall data best resembles the experimental results.

Imagine there is a two components vector x, then with a small strain ϵ the new vector x' can be seen as a coordinate transformation matrix S applying on x

$$x' = \begin{pmatrix} \frac{1}{1+\epsilon} & 0 \\ 0 & \frac{1}{1-\delta\epsilon} \end{pmatrix} x \approx \begin{pmatrix} 1-\epsilon & 0 \\ 0 & 1+\delta\epsilon \end{pmatrix} x \tag{3.16}$$

Here $\delta = 0.16$ is the Poisson ratio for graphene. We can rotate the direction of strain with an angle α by applying rotation matrixes on S

$$\begin{aligned} S(\epsilon,\alpha) &= \begin{pmatrix} \cos(\alpha) & \sin(\alpha) \\ -\sin(\alpha) & \cos(\alpha) \end{pmatrix} \begin{pmatrix} 1-\epsilon & 0 \\ 0 & 1+\delta\epsilon \end{pmatrix} \begin{pmatrix} \cos(\alpha) & -\sin(\alpha) \\ \sin(\alpha) & \cos(\alpha) \end{pmatrix} \\ &= I + \epsilon \begin{pmatrix} -\cos^2(\alpha) + \delta\sin^2(\alpha) & (1+\delta)\cos(\alpha)\sin(\alpha) \\ (1+\delta)\cos(\alpha)\sin(\alpha) & -\sin^2(\alpha) + \delta\cos^2(\alpha) \end{pmatrix} \\ &\equiv I + E(\epsilon,\alpha) \end{aligned} \tag{3.17}$$

Here I is the 2×2 identity matrix. Because of the relation $a_M \cdot G = 2\pi$, where a_M is moiré lattice vector and G is moiré reciprocal vector, the vector in momentum space p should transform as

$$p' = S^{-1}(\epsilon,\alpha)p \tag{3.18}$$

Keep it up to the first order of ϵ

$$S^{-1}(\epsilon,\alpha) \approx I - \epsilon \begin{pmatrix} -\cos^2(\alpha) + \delta \sin^2(\alpha) & (1+\delta)\cos(\alpha)\sin(\alpha) \\ (1+\delta)\cos(\alpha)\sin(\alpha) & -\sin^2(\alpha) + \delta\cos^2(\alpha) \end{pmatrix} \equiv I - E(\epsilon,\alpha) \quad (3.19)$$

According to Ref [80], strain will also introduce a fictitious gauge field A for one Dirac cone and $-A$ for the other

$$A = -\frac{\sqrt{3}}{2\theta a_M}\beta\epsilon(1+\delta)\begin{pmatrix}\cos(2\alpha)\\ \sin(2\alpha)\end{pmatrix} \quad (3.20)$$

Here $\beta = 3.14$ is estimated by the first principle calculation for graphene and $\theta = 1.3°$ is the twisted angle between two graphene layers in our experiment [4] so that moiré lattice constant $a_M \approx \frac{a_0}{\theta}$. Without strain, the K points from two twisted layers for valley $\pm$ are labeled by $K_1^{\pm}$, $K_2^{\pm}$ as shown in Fig 3.3. We will only focus on valley $+$ below, and valley $-$ can be obtained by time reversal (as illustrated in the last section). Considering uniaxial strain $\epsilon_1 = -0.15\%$ for layer 1, $\epsilon_2 = 0.15\%$ for layer 2 and the induced fictitious gauge field A, the coordinates for K_1^+, K_2^+ are

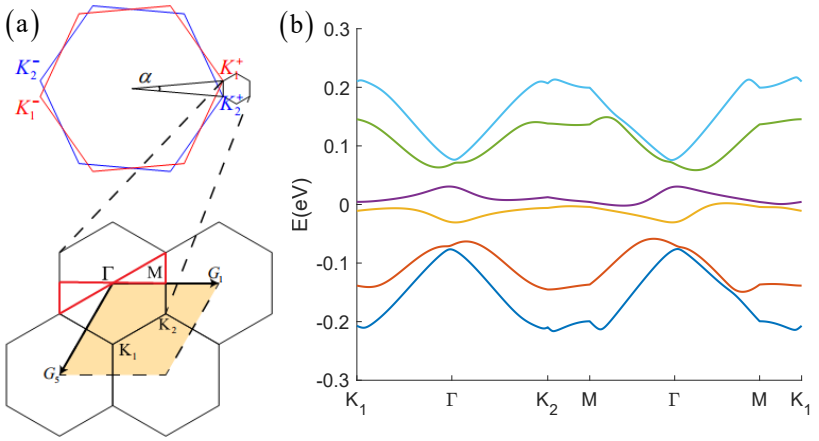


Figure 3.3: Schematic moiré BZ without strain and the high symmetry red lines are shown in (a). The band structure with strain along the red lines is shown in (b). This figure comes from supplemental material of Ref [4].

$$K_1^+ \approx S^{-1}(\epsilon_1,\alpha)\frac{G_0}{\sqrt{3}}\begin{pmatrix}1\\ \frac{\theta}{2}\end{pmatrix} + A_1$$
$$K_2^+ \approx S^{-1}(\epsilon_2,\alpha)\frac{G_0}{\sqrt{3}}\begin{pmatrix}1\\ -\frac{\theta}{2}\end{pmatrix} + A_2 \quad (3.21)$$

Here G_0 is the graphene reciprocal vector length. Keep them up to the first order of ϵ and θ and shift a constant vector $-\frac{G_0}{\sqrt{3}}\begin{pmatrix}1\\0\end{pmatrix}$

$$\begin{aligned} K_1^+ &\approx \frac{G_0}{\sqrt{3}}\begin{pmatrix}0\\\frac{\theta}{2}\end{pmatrix} - E(\epsilon_1,\alpha)\frac{G_0}{\sqrt{3}}\begin{pmatrix}1\\0\end{pmatrix} + A_1 \\ K_2^+ &\approx -\frac{G_0}{\sqrt{3}}\begin{pmatrix}0\\\frac{\theta}{2}\end{pmatrix} - E(\epsilon_2,\alpha)\frac{G_0}{\sqrt{3}}\begin{pmatrix}1\\0\end{pmatrix} + A_2 \end{aligned} \tag{3.22}$$

The second and third terms are contributions from strains. One can see the relative position $K_1^+ - K_2^+$ will not be affected by allocation of total strain $\epsilon = \epsilon_1 - \epsilon_2$, so does any physical result after a momentum shift. Besides, we also derive 6 new moiré reciprocal vectors with strain

$$G_i' = S^{-1}(\epsilon,\alpha)\begin{pmatrix}1 & -\theta\\ \theta & 1\end{pmatrix} G_i - G_i \tag{3.23}$$

, where $\begin{pmatrix}1 & -\theta\\ \theta & 1\end{pmatrix}$ represents the inter-layer rotation. Keep it up to the first order of ϵ and θ, we list all G_i and correspond G_i' explicitly

$$\begin{aligned} [G_1,G_2,G_3,G_4,G_5,G_6] &= G_0\left[\begin{pmatrix}0\\-1\end{pmatrix},\begin{pmatrix}\frac{\sqrt{3}}{2}\\-\frac{1}{2}\end{pmatrix},\begin{pmatrix}\frac{\sqrt{3}}{2}\\\frac{1}{2}\end{pmatrix},\begin{pmatrix}0\\1\end{pmatrix},\begin{pmatrix}-\frac{\sqrt{3}}{2}\\\frac{1}{2}\end{pmatrix},\begin{pmatrix}-\frac{\sqrt{3}}{2}\\-\frac{1}{2}\end{pmatrix}\right] \\ [G_1',G_2',G_3',G_4',G_5',G_6'] &= G_0\theta\left[\begin{pmatrix}1\\0\end{pmatrix},\begin{pmatrix}\frac{1}{2}\\\frac{\sqrt{3}}{2}\end{pmatrix},\begin{pmatrix}-\frac{1}{2}\\\frac{\sqrt{3}}{2}\end{pmatrix},\begin{pmatrix}-1\\0\end{pmatrix},\begin{pmatrix}-\frac{1}{2}\\-\frac{\sqrt{3}}{2}\end{pmatrix},\begin{pmatrix}\frac{1}{2}\\-\frac{\sqrt{3}}{2}\end{pmatrix}\right] \\ &- G_0E(\epsilon,\alpha)\left[\begin{pmatrix}0\\-1\end{pmatrix},\begin{pmatrix}\frac{\sqrt{3}}{2}\\-\frac{1}{2}\end{pmatrix},\begin{pmatrix}\frac{\sqrt{3}}{2}\\\frac{1}{2}\end{pmatrix},\begin{pmatrix}0\\1\end{pmatrix},\begin{pmatrix}-\frac{\sqrt{3}}{2}\\\frac{1}{2}\end{pmatrix},\begin{pmatrix}-\frac{\sqrt{3}}{2}\\-\frac{1}{2}\end{pmatrix}\right] \end{aligned} \tag{3.24}$$

The second term in G_i' comes from contribution of relative strain. The BM model without strain is written in the last section. Now considering the BM model with strain, one just needs to replace all momentum with the vector after the transformation $S^{-1}(\epsilon,\alpha)$ and keep the scalar $k\cdot\sigma$ unchanged.

$$\begin{aligned} H^\tau_{k,k'} &= \delta_{k,k'}\begin{pmatrix}-\hbar v_F S(\epsilon,\alpha)\left(k-K_1^+\right)\cdot\sigma & 0\\ 0 & -\hbar v_F S(\epsilon,\alpha)\left(k-K_2^+\right)\cdot\sigma\end{pmatrix} + \begin{pmatrix}0 & U^\tau\\ U^{\tau\dagger} & 0\end{pmatrix} \\ U^\tau &= \begin{pmatrix}u_0 & u_1\\ u_1 & u_0\end{pmatrix}\delta_{k,k'} + \begin{pmatrix}u_0 & u_1e^{-i\frac{2\pi}{3}}\\ u_1e^{i\frac{2\pi}{3}} & u_0\end{pmatrix}\delta_{k,k'-G_1'} + \begin{pmatrix}u_0 & u_1e^{i\frac{2\pi}{3}}\\ u_1e^{-i\frac{2\pi}{3}} & u_0\end{pmatrix}\delta_{k,k'-G_2'} \end{aligned} \tag{3.25}$$

Since ϵ is small, and the leading order comes from I in $S(\epsilon,\alpha) = I + E(\epsilon,\alpha)$. BM model we use with small strain can be written as

$$\begin{aligned} H^{\tau}_{k,k'} &= \delta_{k,k'} \begin{pmatrix} -\hbar v_F \left(k - K_1^+\right)\cdot\sigma & 0 \\ 0 & -\hbar v_F \left(k - K_2^+\right)\cdot\sigma \end{pmatrix} + \begin{pmatrix} 0 & U^{\tau} \\ U^{\tau\dagger} & 0 \end{pmatrix} \\ U^{\tau} &= \begin{pmatrix} u_0 & u_1 \\ u_1 & u_0 \end{pmatrix} \delta_{k,k'} + \begin{pmatrix} u_0 & u_1 e^{-i\frac{2\pi}{3}} \\ u_1 e^{i\frac{2\pi}{3}} & u_0 \end{pmatrix} \delta_{k,k'-G_1'} + \begin{pmatrix} u_0 & u_1 e^{i\frac{2\pi}{3}} \\ u_1 e^{-i\frac{2\pi}{3}} & u_0 \end{pmatrix} \delta_{k,k'-G_2'} \end{aligned} \tag{3.26}$$

Here we take $\frac{\hbar v_F}{a_0} = 2.377eV$ and lattice constant for monolayer graphene $a_0 = 0.246nm$ so that $a_M \approx \frac{a_0}{\theta} = 10.84nm$. In the computation, we take hbn-aligned potential $\Delta = 0.017eV$ [86, 89] which is a $\Delta\sigma_z$ between AB sublattices for one layer to break inversion symmetry and open a gap between flat bands. The contribution from hbn-aligned potential in Hamiltonian is

$$H^{\tau}_{\Delta} = \delta_{k,k'} \begin{pmatrix} 0 & 0 \\ 0 & \Delta\sigma_z \end{pmatrix}. \tag{3.27}$$

We can also introduce vertical electric field by considering an electrostatic energy difference V between two layers

$$H^{\tau}_{E} = \delta_{k,k'} \begin{pmatrix} \frac{V}{2}\sigma_0 & 0 \\ 0 & -\frac{V}{2}\sigma_0 \end{pmatrix} \tag{3.28}$$

Here σ_0 is identity matrix and V changes between $\pm 0.4eV$. The displacement field D is related to the applied electric field, $D = \varepsilon E$, through the out-of-plane dielectric constant ε of the twisted graphene. Here we suppose weak screen environment between graphene bilayer, therefore $\varepsilon = 1$ is used. The inter-layer potential difference V is then determined by $V = Ed$, where $d = 0.35nm$ is the inter-layer separation. Now we are ready to diagonalize the total Hamiltonian $H^{\tau} = H^{\tau}_{k,k'} + H^{\tau}_{\Delta} + H^{\tau}_{E}$. The band structure without electric field for 6 nearest zero-energy bands along red line in Fig 3.3(a) is shown in Fig 3.3(b).

For computing Berry curvature Ω, we take 100×100 momentum points in the parallelogram first moiré Brillouin zone as the orange region in Fig 3.3(a) and use the numerical method proposed in Ref [16]. The band structure and Berry curvature Ω for flat valence band with electrostatic energy difference V from $-0.2eV$ to $0.18eV$ are shown in Fig 3.4(a) and Fig 3.4(b) from top left to bottom right with interval $0.02eV$. One can see there is no band close-reopen during this tuning process while the Berry curvature hotspots can slide within BZ.

For computing contribution for nonlinear hall conductance near charge neutrality from berry curvature dipole [13], we consider 6 bands closest to zero-energy, because

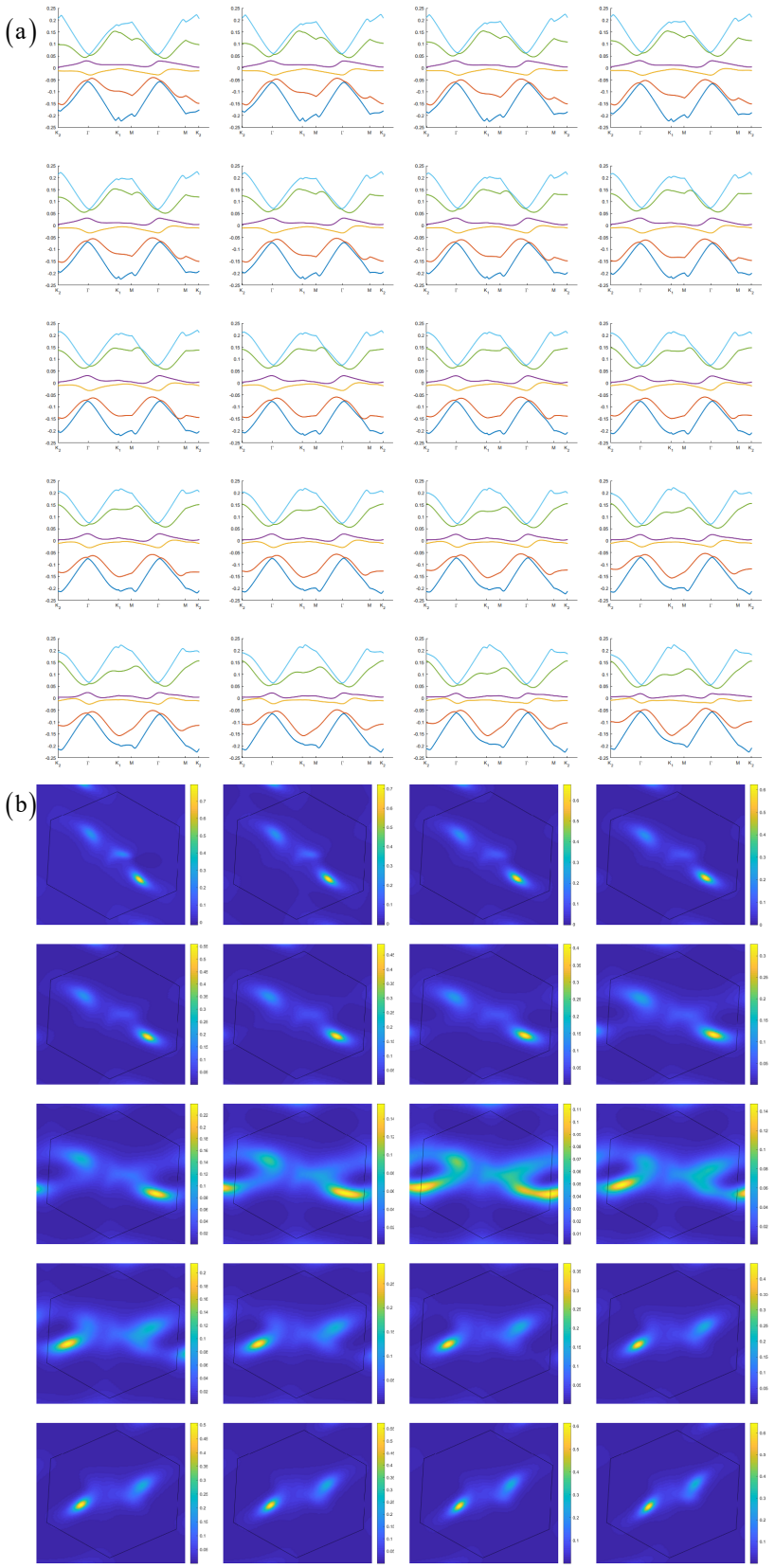


Figure 3.4: Band structure and Berry curvature $\mathbf{\Omega}$ for flat valence band with electrostatic energy difference V from $-0.2eV$ to $0.18eV$ are shown in (a) and (b) from top left to bottom right with interval $0.02eV$.

only bands near fermi surface contribute according to $\partial_b f_0$ in the expression below

$$\Lambda_b = \sum_{n=1}^{6} \int_k (\partial_b f_0)\, \Omega_n. \tag{3.29}$$

This formula is proportional to the geometrical contribution of Hall conductance derived in Chapter 2.

$$\chi_{xyy} = \frac{q^3 \tau}{1 + iw\tau} \int \frac{d^D k}{(2\pi)^D} (\partial_{k_y} f^{(0)}(k)) \Omega_z(k) \tag{3.30}$$

In our computation, we tune different strain's angle α (the angle between the strain axis and the zigzag direction of graphene) from $0° \sim 180°$ with interval $15°$ and measure dipole Λ_1, Λ_5 along direction G_1' and G_5'. We also derived $\Lambda(\varphi)$ along the angular directions φ (the angle between the measurement direction and the zigzag direction of graphene) by

$$\begin{aligned} \partial_\varphi &= \cos(\varphi)\partial_x + \sin(\varphi)\partial_y \\ \partial_1 &= \partial_x \\ \partial_5 &= \cos(\theta)\partial_x + \sin(\theta)\partial_y \end{aligned} \tag{3.31}$$

so that $\partial_\varphi = \cos(\varphi)\partial_1 + \sin(\varphi)\frac{\partial_5 - \cos(\theta)\partial_1}{\sin(\theta)}$ and $\Lambda_\varphi = \cos(\varphi)\Lambda_1 + \sin(\varphi)\frac{\Lambda_5 - \cos(\theta)\Lambda_1}{\sin(\theta)}$. Here θ is the angle between G_5' and G_1' which approaches to $-120°$ with strain.

In our experimental TBG heterostructures [4], a dual gate geometry is used to independently control the total carrier density n and the displacement field D. The scheme of longitudinal and transverse measurement is illustrated in Fig 3.5(b). We first characterize the TBG device by measuring the longitudinal resistance R_{xx} and the Hall carrier density n_H as a function of the gate voltage (or equivalently, the filling factor ν of the bands) at a temperature of $T = 1.5K$. The sharp peak of R_{xx} near the CNP indicates the mobility $\sim 110,000 cm^2 V^{-1} s^{-1}$. In TBG, single-particle gaps form at CNP and at a superlattice density of $n = \pm n_s = \pm\frac{4}{A}$, where A is the moiré unit cell area and the factor 4 accounts for the spin and valley degeneracies. These fillings with single-particle gaps ($\nu = 0$ and ± 4) can be identified in Fig 3.5(c) (vertical dashed lines) by peaks of R_{xx} and the sharp sign change in n_H, indicating the switching between electron-like to hole-like pockets as the Fermi energy swap through a band gap. While additional R_{xx} peaks can be observed near the half filling and the quarter filling, n_H at these positions shows no anomalies and follows $n_H = n$, suggesting that correlation effect is relatively small in this device and a BM type of the flat-bands model, which we adapt in the theoretical calculation, offers a good description of such a system. This behavior is also consistent with the observation of additional sign changes in n_H at $3 < |\nu| < 4$ that indicates electron-hole charge carrier interface in the single-particle band structure. From the superlattice density $n_s = 4 \times 10^{12} cm^{-2}$, the twist angle of this device is determined to be $1.3°$. It is worthwhile to highlight that by utilizing this twisting angle away from the magic angle, complicated many-body effects, such as the anomalous enhancement of the nonlinear Hall signal from divergence effective mass, are avoided so that a clean

platform where semi-classical description for nonlinear Hall effect from band anomalous velocity can be used is obtained to study the Berry curvature dipole of intrinsic band structures. The advantage of such a flat band is that the distribution of Berry curvature is diffused in band so that there will be significant signal from Berry curvature detected within band.

As shown in the bottom panel of Fig 3.5(c), where the second harmonic Hall voltage $V_{\perp}^{2\omega}$ at $I^{\omega} = 100nA$ versus ν is plotted, non-zero responses are indeed observed. First of all, in agreement with the sign changes of Berry curvature dipole Λ at band gaps, $V_{\perp}^{2\omega}$ changes signs at CNP and full fillings. In addition, $V_{\perp}^{2\omega}$ show two peaks with opposite signs near the band gaps, which can be understood by the Berry curvature hotspots near the edges of the gap.

We then systematically study the dependence of nonlinear Hall effect with an out-of-plane displacement D field which induces charge and voltage differences between the layers. Fig 3.6(a) shows the map of $V_{\perp}^{2\omega}$ in the space of filling factor-displacement field $(\nu - D)$. $V_{\perp}^{2\omega}$ at $\nu = -1.5$ and at $\nu = +1$ are marked by the dashed line labeled with p and n in Fig 3.6(a) respectively. The magnitude and direction of $V_{\perp}^{2\omega}$ changes when we tune D while keeping ν unchanged. To be more specific, $V_{\perp}^{2\omega}$ at $\nu = -1.5$ at various D is plotted in Fig 3.6(b). A region with small negative values of $V_{\perp}^{2\omega}$ is observed between two positive $V_{\perp}^{2\omega}$ peaks. Moreover, $V_{\perp}^{2\omega}$ shows a clear quadratic current–voltage $(I - V)$ characteristic for all D (Fig 3.6(c)), which, combined with the 2ω frequency, indicates a robust nonlinear Hall effect. Similar D switchable $V_{\perp}^{2\omega}$ is observed in the conduction band (Fig 3.6(d),(e)). These observations show that D can effectively modulate the low-energy bands as well as the sign and the amplitude of the Berry curvature dipole Λ.

To understand the experimental observation, I compute Λ_b with strain's angle $\alpha = 45°$ and dipole's angle $\varphi = 10°$. One can see the result matches well with the experiment observation in Fig 3.7 and confirm the theoretical picture I introduced at the beginning of this section. At the same time, skew scattering can also be a possible origin of nonlinear Hall effect, while there is no mechanism promising the gate-tunable behavior in the TBG experiment so that the Berry curvature should be the main contribution.

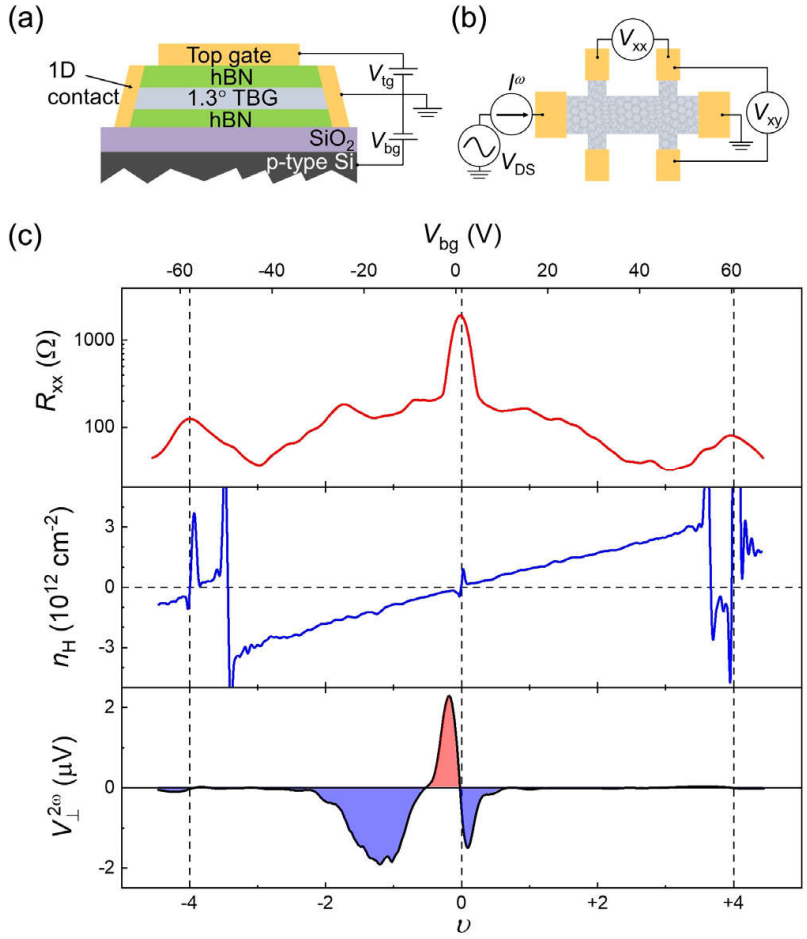


Figure 3.5: Basic characterization of the TBG device. (a) Schematic structure of the 1.30° TBG device. The carrier density n and the displacement field D are controlled by the top and bottom gates with gate voltage V_{tg} and V_{bg}, respectively. (b) The four-probe measurement scheme. Here, we measure the longitudinal voltage V_{xx} and Hall voltage V_{xy} in the presence of an AC longitudinal current I^{ω}. (c) The longitudinal resistance $R_{xx} = V_{xx}/I^{\omega}$ (top panel) and the carrier density measured via the Hall effect n_H (middle panel) as functions of ν and V_{bg} ($V_{tg} = 0V$). The vertical dashed lines denote the CNP and fully filled moiré bands. The second harmonic Hall voltage $V_{\perp}^{2\omega}$ as a function of filling factor ν measured at $I^{\omega} = 100nA$ and $T = 1.5K$ is shown in bottom panel. These figures come from Ref [4].

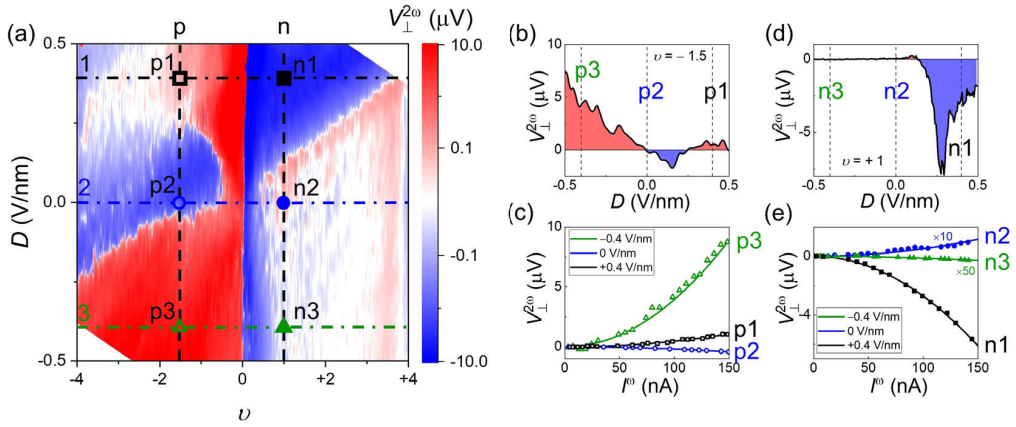


Figure 3.6: Electric field tunable nonlinear Hall effect. (a) Filling and displacement field mapping of $V_{\perp}^{2\omega}$ measured at $T = 1.5K$. Dashed lines marked with p and n indicate $\nu = -1.5$ and $\nu = +1$, respectively. Dash dotted lines marked with 1, 2 and 3 indicate three different fields: $D = +0.4,\ 0,\ -0.4V/nm$. Their intersection points are named as shown in the figure. (b) $V_{\perp}^{2\omega}$ versus D measured at $\nu = -1.5$ at $I^{\omega} = 100nA$. (c) $V_{\perp}^{2\omega}$ versus I^{ω} at various displacement fields at $\nu = -1.5$. Dots are the experimental data and the solid lines are parabolic fittings. (d),(e) Same as (b) and (c) for $\nu = +1$. These figures come from Ref [4].

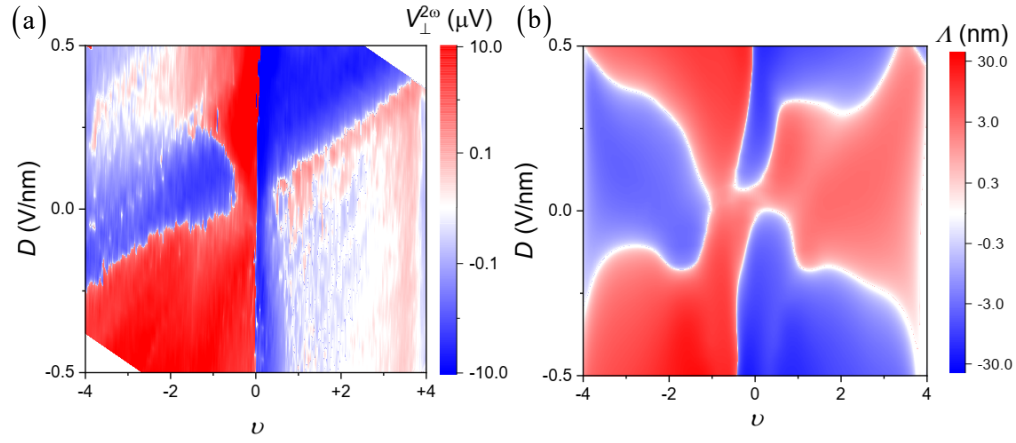


Figure 3.7: Electric field tunable nonlinear Hall effect signal from experiment and simulation. Filling and displacement field mapping of $V_{\perp}^{2\omega}$ and Λ at $T = 1.5K$ from experiment and simulation are shown in (a) and (b) respectively.

3.5 Projected Coulomb interaction and half filling ground state

One of the earliest proposals from BM model is that the emergence of gapped flat bands should induce strong correlation phenomena [73]. And the exciting results follow soon [48, 49], triggering a fashion in the condensed matter and 2D quantum material communities. As experiments have discovered the correlated insulating phases at various integer fillings, the proximate superconductivity (SC) phases and many other correlation features [48–70], a key question arises that how to model and understand the properties of the insulating phases, both for their own sake and that could eventually provide a clue for the understanding of the mechanism of the SC and other properties in TBG systems.

Many experimental and theoretical works have indicated the interplay between the nontrivial topology and strong interaction as the essential ingredients for the understanding of the electronic correlations in such materials, therefore pointing out a proper model for TBG system shall be significantly different from the typical Hubbard-type Hamiltonian with on-site interactions [90–97]. Besides, the nature of the insulating states discovered in the material is also under debate. On the one hand, the analytical and the Hartree-Fock calculations at various integer fillings have found the quantum anomalous hall (QAH) and the inter-valley coherent (IVC) states as the ground states without breaking the translation symmetry, suggesting that the physics is similar to the quantum Hall ferromagnetism at the lowest Landau level (LL) [98–108]. Such similarity also led to the proposal of the skyrmion SC for the mechanism of SC discovered near the insulating phases at $\nu = \pm 2$ [109, 110]. On the other hand, numerical calculations based on the density matrix renormalization group (DMRG) [109, 111–113] and exact diagonalization (ED) [114–117] have discovered a larger manifold of nearly degenerate states strongly competing with each other even in the strong coupling regime, hinting that such systems could contain much more complicated physics than that of the LL.

According to experiments that the correlated physics emerges only when the chemical potential lies inside the flat bands [48–50] and the large band gap that separates the flat bands and remote bands allows one to focus on the flat bands only to study the electronic correlations [54], the effective Hamiltonian is given by the BM model in momentum space [118] with the projected Coulomb interactions onto the flat bands, which has significantly simplified the system for realistic analytical and numerical calculations [77, 78, 99, 104, 111, 114, 119–122].

In this section, I will introduce the momentum space DQMC method [5, 25] for the aforementioned TBG models. I first introduce the model Hamiltonian we use and prove the absence of the sign problem for DQMC simulation at integer fillings when either the two valley or the two spin degrees of freedom are considered. Then, by taking the realistic parameters of the twist angle and inter-layer tunnelings into account, we benchmark the DQMC data with the band gap derived by exact solution and reveal

the insulating ground states at CNP. Finally, by combining the DQMC simulation with the stochastic analytic continuation (SAC), we obtain single-particle and IVC excitation spectra at chiral limit and realistic parameter at CNP.

3.5.1 DQMC for TBG Hamiltonian with Coulomb Interaction

Combining the DQMC for momentum space introduced in Chapter 2 with the BM model introduce above. We derive the TBG Hamiltonian with Coulomb interaction below.

$$
\begin{aligned}
H &= \sum_{k,n,s,\tau} \epsilon_{\tau;k,n} c^{\dagger}_{k,n,s,\tau} c_{k,n,s,\tau} \\
&+ \frac{1}{4\Omega} \sum_{|q+G|\neq 0} V(q+G) \left[(\delta\rho_{q+G} + \delta\rho_{-q-G})^2 - (\delta\rho_{q+G} - \delta\rho_{-q-G})^2 \right] \\
V(q+G) &= \frac{e^2}{4\pi\varepsilon} \int d^2r (\frac{1}{r} - \frac{1}{\sqrt{r^2+d^2}}) e^{iq\cdot r} = \frac{e^2}{2\varepsilon}\frac{1}{q}(1-e^{-qd}) \\
\delta\rho_{q+G} &= \sum_{k,m,n,s,\tau} \lambda_{\tau;m,n}(k, k+q+G)(c^{\dagger}_{k,m,s,\tau} c_{k+q,n,s,\tau} - \frac{1}{2}\delta_{q,0}\delta_{m,n}) = (\delta\rho_{-q-G})^{\dagger} \\
\lambda_{\tau;m,n}(k, k+q+G) &= \sum_{G',l,a} u^{*}_{\tau;m;G',l,a}(k) u_{\tau;n;G'+G,l,a}(k+q)
\end{aligned}
\tag{3.32}
$$

Here the moiré lattice vector $L_M = \frac{a_0}{2\sin(\frac{\theta}{2})}$, and the system area $\Omega = N_k \frac{\sqrt{3}}{2} L_M^2$ with N_k momentum points in moiré Brillouin zone. We adopt single-gate screened Coulomb potential $V(r) \propto (\frac{1}{r} - \frac{1}{\sqrt{r^2+d^2}})$ with the gate distance $\frac{d}{2} = 20nm$ and dielectric constant $\varepsilon = 7\varepsilon_0$. We use $s, \tau = \pm 1$ to label spin and valley, l, a to label layer and sublattice degree of freedom. $u_{\tau;n;G',l,a}(k)$ is the unitary transformation diagonalizing BM model Hamiltonian at valley τ, momentum k from plane wave basis labeled by G', l, a to band basis labeled by $n = \pm 1$. One should be careful that k is constrained within first Brillouin zone and for BM model Hamiltonian with momentum $k + mG$, one should diagonalize the Hamiltonian at k and move the elements to mG accordingly in $u_{\tau;n;G',l,a}(k)$ to make sure the gauge choice consistency so that form factor $\lambda_{\tau;m,n}(k, k+q+G)$ is well defined. If there is no cut off for infinite band summation m, n, everything should be exact after this unitary transformation. But the huge degree of freedom will ruin any computation. We take a hard cut off and constrain the degree of freedom up to two flat bands and $\frac{1}{2}\delta_{q,0}\delta_{m,n}$ is the half filling tuning term where Hartree-Fock contribution from remote bands is involved as justified in [78]. Another cut off should also included for $V(q+G)$. According to Ref [123], this interaction combining with form factor $\lambda_{\tau;m,n}(k, k+q+G)$ will decay exponentially with $|q+G|$, we keep $q+G$ points within three Brillouin zones as shown in Fig 3.8(a). Now we have discussed all the setting and we are ready to write down the DQMC formula following the routine introduced in Chapter 2.

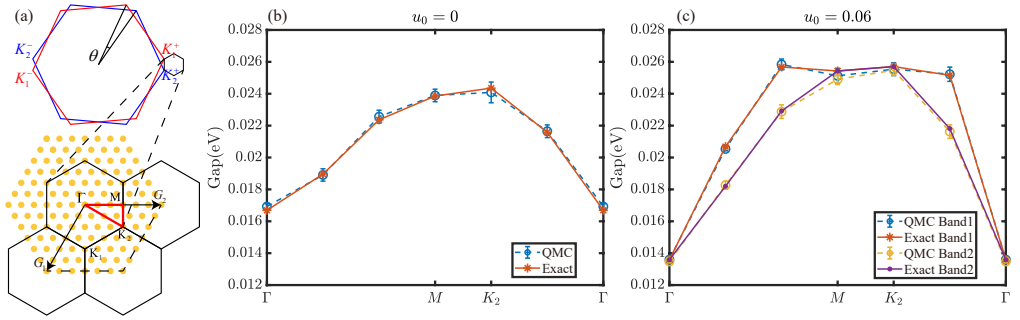


Figure 3.8: (a) Upper panel shows the BZ folding in TBG, with the small hexagon representing the moiré BZ. $K^{\pm}_{1,2}$ are the Dirac points for valley $\pm$ and layer 1 and 2, θ is the rotating angle. In lower panel, G_1 and G_2 are the reciprocal lattice vectors of the moiré BZ. The yellow dots are the allowed momentum transfer $q + G$ points in DQMC. Here we consider momentum transfer up to G, which means for a 6×6 mesh in moiré BZ, the allowed number of $q + G$ is 126. (b) and (c) show the comparison at the CNP of the single-particle excitation gap at the chiral limit ($u_0 = 0$) and realistic case ($u_0 = 0.06$) between exact solution and the DQMC results. The DQMC gaps are obtained from fitting the imaginary time decay of the fermion Green's function. These figures come from Ref [5].

$$
\begin{aligned}
Z &\approx \mathrm{Tr}\Big(\prod_{t=1}^{N_\beta} e^{-\Delta t H_0} e^{-\Delta t H_I(t)}\Big) \\
&\approx \mathrm{Tr}\Big(\prod_t \Big\{ e^{-\Delta t H_0} \prod_{|q|\neq 0} e^{-\frac{\Delta t V(q)}{4\Omega}\left[(\delta\rho_q+\delta\rho_{-q})^2-(\delta\rho_q-\delta\rho_{-q})^2\right]} \Big\}\Big) \\
&\approx \sum_{\{l_{|q|,t}\}} \prod_t \left[\frac{1}{16}\gamma(l_{|q_1|,t})\gamma(l_{|q_2|,t})\right] \\
&\quad \cdot \mathrm{Tr}\Big(\prod_t \Big\{ e^{-\Delta t H_0} \prod_{|q|\neq 0} e^{i\eta(l_{|q_1|,t})\sqrt{\frac{\Delta t V(q)}{4\Omega}}(\delta\rho_q+\delta\rho_{-q})} e^{\eta(l_{|q_2|,t})\sqrt{\frac{\Delta t V(q)}{4\Omega}}(\delta\rho_q-\delta\rho_{-q})} \Big\}\Big)
\end{aligned}
\tag{3.33}
$$

Here we replace all the $q + G$ by q to keep consistent with the formula in Chapter 2. As one has seen before, whether the PMF is positive definite is determined by $\mathrm{Tr}\Big(\prod_t \Big\{ e^{-\Delta t H_0} \prod_{|q|\neq 0} e^{i\eta(l_{|q_1|,t})\sqrt{\frac{\Delta t V(q)}{4\Omega}}(\delta\rho_q+\delta\rho_{-q})} e^{\eta(l_{|q_2|,t})\sqrt{\frac{\Delta t V(q)}{4\Omega}}(\delta\rho_q-\delta\rho_{-q})} \Big\}\Big)$. We note if one sets $H_0 = 0$ (flat band limit), the exponential parts of decoupled interaction are anti-Hermitian, the following three statements about the sign structure of the DQMC fermion determinants are listed in order:

Statement 1 Considering single valley and single spin without kinetic terms at half filling, the sign of the determinant is always real.

Proof In our decoupled Hamiltonian, the probability of accepting a configuration is proportional to $e^{-\frac{1}{2}\sum_j \mathrm{Tr}(M_j)} \det\left(I + e^{M_1} e^{M_2} ... e^{M_n}\right)$. Here M_j coming from two-fermion coefficients in $i(\delta\rho_q + \delta\rho_{-q})$ and $(\delta\rho_q - \delta\rho_{-q})$ terms are anti-Hermitian matrices

in single particle basis and $e^{-\frac{1}{2}\sum_j \mathrm{Tr}(M_j)}$ comes from constant terms in $e^{i(\delta\rho_q+\delta\rho_{-q})}$. Since e^{M_j} are unitary matrixes, $U = e^{M_1}e^{M_2}...e^{M_n}$ is also unitary with eigenvalue $e^{i\lambda_j}$. Set $\det(U) = e^{\sum_j \mathrm{Tr}(M_j)} = e^{\sum_j i\lambda_j} = e^{i\Gamma}$, $e^{-i\frac{\Gamma}{2}}\det(I+U) = e^{-i\frac{\Gamma}{2}}\prod_j\left(1+e^{i\lambda_j}\right)$. For any term $e^{i(\Sigma_{k\in A}\lambda_k-\frac{\Gamma}{2})}$, $A \subseteq \{1,2,...,n\}$, there is always a term $e^{i(\Sigma_{k\notin A}\lambda_k-\frac{\Gamma}{2})} = e^{-i(\Sigma_{k\in A}\lambda_k-\frac{\Gamma}{2})}$, so add all terms together will always be real.

Statement 2 Considering single valley and double spin without kinetic terms at half filling, there is no sign problem.

Proof It is straightforward to see this result according to **Statement 1** by noticing the other spin just gives a copy so that real sign will become non-negative sign. But kinetic terms could change this result.

Statement 3 Considering single spin and double valley with flat band kinetic terms at half filling, there is no sign problem.

Proof Here we will use the particle-hole transformation and the symmetry of TBG for proving this statement. Following the discussion in band basis as in Ref [78], the Hermiticity condition for λ is

$$\lambda_{\tau;m,n}(k,k+q+G) = \lambda^*_{\tau;n,m}(k+q+G,k). \tag{3.34}$$

The $C_{2z}T$ symmetry operates on λ as

$$\lambda_{\tau;m,n}(k,k+q+G) = \lambda^*_{\tau;m,n}(k,k+q+G), \tag{3.35}$$

which means λ is real in this gauge choice. The $C_{2z}P$ symmetry operates on λ as

$$\lambda_{\tau;m,n}(k,k+q+G) = m\times n\times\lambda_{-\tau;-m,-n}(k,k+q+G). \tag{3.36}$$

Based on these relations, we can derive the **Statement 3** as:

$$\begin{aligned}
\delta\rho_{-\tau;q+G} &= \sum_{k,m,n}\lambda_{-\tau;m,n}(k,k+q+G)(c^\dagger_{k,m,-\tau}c_{k+q,n,-\tau}-\frac{1}{2}\delta_{q,0}\delta_{m,n}) \\
&= \sum_{k,m,n}-m\times n\times\lambda_{\tau;m,n}(k,k+q+G)(c_{k+q,-n,-\tau}c^\dagger_{k,-m,-\tau}-\frac{1}{2}\delta_{q,0}\delta_{m,n}) \\
&= \sum_{k,m,n}-\lambda_{\tau;m,n}(k,k+q+G)(\tilde{c}^\dagger_{k+q,n,-\tau}\tilde{c}_{k,m,-\tau}-\frac{1}{2}\delta_{q,0}\delta_{m,n}) \\
&= \sum_{k,m,n}-\lambda_{\tau;n,m}(k,k-q-G)(\tilde{c}^\dagger_{k,n,-\tau}\tilde{c}_{k-q,m,-\tau}-\frac{1}{2}\delta_{q,0}\delta_{m,n})
\end{aligned} \tag{3.37}$$

Here $\tilde{c}_{k,m,-\tau} = mc^{\dagger}_{k,-m,-\tau}$, $m,n \in \{\pm 1\}$. According to the last line, single-particle matrixes between two valleys satisfy $\delta\rho_{-\tau;q+G} = -\delta\rho_{\tau;-q-G}$. This directly means

$$\begin{aligned} D_\tau &\equiv \mathrm{Tr}(\prod_t \left\{ \prod_{|q|\neq 0} e^{i\eta(l_{|q_1|,t})\sqrt{\frac{\Delta t V(q)}{4\Omega}}(\delta\rho_{\tau;q}+\delta\rho_{\tau;-q})} e^{\eta(l_{|q_2|,t})\sqrt{\frac{\Delta t V(q)}{4\Omega}}(\delta\rho_{\tau;q}-\delta\rho_{\tau,-q})} \right\}) \\ &= \mathrm{Tr}(\prod_t \left\{ \prod_{|q|\neq 0} e^{-i\eta(l_{|q_1|,t})\sqrt{\frac{\Delta t V(q)}{4\Omega}}(\delta\rho_{-\tau;q}+\delta\rho_{-\tau;-q})} e^{\eta(l_{|q_2|,t})\sqrt{\frac{\Delta t V(q)}{4\Omega}}(\delta\rho_{-\tau;q}-\delta\rho_{-\tau,-q})} \right\}) \\ &= D^*_{-\tau}. \end{aligned} \tag{3.38}$$

Then we have $\mathrm{Tr}(\prod_t \left\{ e^{-\Delta t H_0} \prod_{|q|\neq 0} e^{i\eta(l_{|q_1|,t})\sqrt{\frac{\Delta t V(q)}{4\Omega}}(\delta\rho_q+\delta\rho_{-q})} e^{\eta(l_{|q_2|,t})\sqrt{\frac{\Delta t V(q)}{4\Omega}}(\delta\rho_q-\delta\rho_{-q})} \right\}) = D_\tau D_{-\tau} = |D_\tau|^2$. Besides, this transformation does not change kinetic terms. Since

$$\epsilon_{\tau;k,m} = -\epsilon_{\tau;-k,-m} = \epsilon_{-\tau;-k,m}, \tag{3.39}$$

so that

$$\begin{aligned} & \epsilon_{\tau;k,m} c^{\dagger}_{k,m,\tau} c_{k,m,\tau} + \epsilon_{\tau;-k,-m} c^{\dagger}_{-k,-m,\tau} c_{-k,-m,\tau} \\ = \; & \epsilon_{\tau;k,m}(c^{\dagger}_{k,m,\tau} c_{k,m,\tau} - c^{\dagger}_{-k,-m,\tau} c_{-k,-m,\tau}), \\ & \epsilon_{-\tau;k,-m} c^{\dagger}_{k,-m,-\tau} c_{k,-m,-\tau} + \epsilon_{-\tau;-k,m} c^{\dagger}_{-k,m,-\tau} c_{-k,m,-\tau} \\ = \; & \epsilon_{\tau;k,m}(c_{k,-m,-\tau} c^{\dagger}_{k,-m,-\tau} - c_{-k,m,-\tau} c^{\dagger}_{-k,m,-\tau}) \\ = \; & \epsilon_{\tau;k,m}(\tilde{c}^{\dagger}_{k,m,-\tau} \tilde{c}_{k,m,-\tau} - \tilde{c}^{\dagger}_{-k,-m,-\tau} \tilde{c}_{-k,-m,-\tau}). \end{aligned} \tag{3.40}$$

One can see kinetic terms can be viewed as complex conjugated between two valleys since the dispersion $\epsilon_{\tau;k,m}$ is real. The similar observation, that the TBG Hamiltonian at CNP after DQMC decoupling is invariant under anti-unitary particle-hole symmetry, is also pointed out in Ref [25].

We organize these statements in Tab 3.1.

Table 3.1: List of the sign structure for TBG Hamiltonian [5].

Degrees of freedom	Kinetic terms	Sign Structure
Single valley single spin	No	Real
Single valley double spin	No	Non-negative
Double valley single spin	Flat bands	Non-negative
Double valley double spin	Flat bands	Non-negative

3.5.2 Exact solution and DQMC results for ground state and excitation

At half filling, there is a great advantage for considering flat band limit which has exact solution for ground state and low-energy single-particle and two-particle charge-neutral

excitations [2, 99, 120]. We will introduce those results and benchmark with spectra derived from our DQMC simulation. Departing from the exact solution case, we will show the IVC state will be favored for small band dispersion case and display the low-energy excitation spectra of it.

Let's consider the Hamiltonian at flat band limit

$$H = \frac{1}{2\Omega}\sum_{q,G} V(q+G)(\delta\rho_{q+G}\delta\rho_{-q-G}). \tag{3.41}$$

Since $\delta\rho_{q+G} = (\delta\rho_{-q-G})^\dagger$ and $V(q+G) > 0$, this Hamiltonian is positive semi-definite (For positive semi-definite Hamiltonian $H = \sum_i A_i^\dagger A_i$ with any operator A_i and any wavefunction $|\psi\rangle$, $\langle\psi|H|\psi\rangle = \sum_i \langle A_i\psi|A_i\psi\rangle \geqslant 0$ is always true), if we find a zero-energy eigenstate it must be a ground state. By requiring $\delta\rho_{q+G}|\psi\rangle = \sum_{k,m,n,s,\tau}\lambda_{\tau;m,n}(k,k+q+G)(c^\dagger_{k,m,s,\tau}c_{k+q,n,s,\tau} - \frac{1}{2}\delta_{q,0}\delta_{m,n}) = \sum_{k,m,n}\lambda_{\tau;m,n}(k,k+q+G)(c^\dagger_{k,m,s,\tau}c_{k+q,n,s,\tau} + c^\dagger_{k,m,-s,\tau}c_{k+q,n,-s,\tau} + \tilde{c}^\dagger_{k,m,s,-\tau}\tilde{c}_{k+q,n,s,-\tau} + \tilde{c}^\dagger_{k,m,-s,-\tau}\tilde{c}_{k+q,n,-s,-\tau} - 2\delta_{q,0}\delta_{m,n}) = 0$ for any $q+G$, we find fully fill two of four spin-valley bands will be eigenstates with zero energy (e.g., fill $[(s,\tau),(-s,\tau)]$ bands in $[(s,\tau),(-s,\tau),(s,-\tau),(-s,-\tau)]$). Besides, by looking at $\delta\rho_{q+G}$ carefully

$$\begin{aligned}\delta\rho_{q+G} &= \sum_{k,m,n}\lambda_{\tau;m,n}(k,k+q+G)(c^\dagger_{k,m,s,\tau}c_{k+q,n,s,\tau} + c^\dagger_{k,m,-s,\tau}c_{k+q,n,-s,\tau} \\ &+ \tilde{c}^\dagger_{k,m,s,-\tau}\tilde{c}_{k+q,n,s,-\tau} + \tilde{c}^\dagger_{k,m,-s,-\tau}\tilde{c}_{k+q,n,-s,-\tau} - 2\delta_{q,0}\delta_{m,n})\end{aligned} \tag{3.42}$$

One can notice it is a block diagonalized identity in spin-valley space such that any unitary transformation in spin-valley space with identity in k,m space as

$$U_{s,\tau;s',\tau'} = u_{s,\tau;s',\tau'}\sum_{k,m} c^\dagger_{k,m,s,\tau}c_{k,m,s',\tau'} \tag{3.43}$$

will commute with $\delta\rho_{q+G}$ (i.e., $[U_{s,\tau;s',\tau'}, \delta\rho_{q+G}] = 0$) as well as the Hamiltonian. Since this unitary transformation parameter $u_{s,\tau;s',\tau'}$ lives in 4×4 spin-valley space, we say this Hamiltonian has spin-valley $U(4)$ symmetry. This knowledge is useful for discussing ground state degeneracy and the polynomial sign problem at other integer fillings which we will introduce in the next section. For now, we will focus on computing excitations above the ground state.

Following the method in Ref [2, 121], we first prove the single particle excitation states and charge neutral excitation states form closed orthogonal subspaces separately. Then, we derive the eigen excitation states by diagonalizing the Hamiltonian in the subspace.

We choose one full-filling spin-valley bands ground state as $|\psi_0\rangle$ where filled bands labeled by σ and empty bands labeled by σ'. By defining raising operators and their

Hermitian conjugate linking filled spin-valley bands and empty spin-valley bands as

$$\begin{aligned}\Delta^{\dagger}_{\sigma',\sigma} &= \sum_{k,m} c^{\dagger}_{k,m,\sigma'} c_{k,m,\sigma} \\ \Delta_{\sigma',\sigma} &= \sum_{k,m} c^{\dagger}_{k,m,\sigma} c_{k,m,\sigma'}\end{aligned} \tag{3.44}$$

we can check these operators commute with $\delta\rho_{q+G}$ and also with the Hamiltonian (They belong to $U_{s,\tau;s',\tau'}$). The commutation relations between these operators are

$$\begin{aligned}\left[\Delta^{\dagger}_{\sigma'_1,\sigma_1}, \Delta^{\dagger}_{\sigma'_2,\sigma_2}\right] &= \left[\Delta_{\sigma'_1,\sigma_1}, \Delta_{\sigma'_2,\sigma_2}\right] = 0 \\ \left[\Delta^{\dagger}_{\sigma'_1,\sigma_1}, \Delta_{\sigma'_2,\sigma_2}\right] &= \sum_{k,m} c^{\dagger}_{k,m,\sigma'_1} c_{k,m,\sigma'_2} \delta_{\sigma_1,\sigma_2} - c^{\dagger}_{k,m,\sigma_1} c_{k,m,\sigma_2} \delta_{\sigma'_1,\sigma'_2}\end{aligned} \tag{3.45}$$

For raising between empty bands ($\Delta^{\dagger}_{\sigma'_1,\sigma'_2} = \sum_{k,m} c^{\dagger}_{k,m,\sigma'_1} c_{k,m,\sigma'_2}$) or full bands ($\Delta^{\dagger}_{\sigma_1,\sigma_2} = \sum_{k,m} c^{\dagger}_{k,m,\sigma_1} c_{k,m,\sigma_2}$), those operators will not change the state and only give a constant $\Delta^{\dagger}_{\sigma'_1,\sigma'_2} |\psi_0\rangle = 0 |\psi_0\rangle$ and $\Delta^{\dagger}_{\sigma_1,\sigma_2} |\psi_0\rangle = 2N_k \delta_{\sigma_1,\sigma_2} |\psi_0\rangle$. We can conclude all orthogonal ground states $|\psi_g\rangle$ can be expressed based on $|\psi_0\rangle$ and raising operators in a form below

$$|\psi_g\rangle = \prod_{\sigma',\sigma} (\Delta^{\dagger}_{\sigma',\sigma})^{m_{\sigma',\sigma}} |\psi_0\rangle \tag{3.46}$$

Here $m_{\sigma',\sigma}$ are non-negative integers. The reason follows that if one inserts $\Delta^{\dagger}_{\sigma'_1,\sigma'_2}$ or $\Delta^{\dagger}_{\sigma_1,\sigma_2}$ (which also belongs to $U_{s,\tau;s',\tau'}$ and together with $\Delta^{\dagger}_{\sigma',\sigma}$, $\Delta_{\sigma',\sigma}$ form all the possibility of $U_{s,\tau;s',\tau'}$) in this product, commutation between $\Delta^{\dagger}_{\sigma'_1,\sigma'_2}$ and $\Delta^{\dagger}_{\sigma'_3,\sigma_4}$ will be $\Delta^{\dagger}_{\sigma'_1,\sigma_4} \delta_{\sigma'_2,\sigma'_3}$ which belongs to $\Delta^{\dagger}_{\sigma',\sigma}$ and the rest part after all the commutations driving $\Delta^{\dagger}_{\sigma'_1,\sigma'_2}$ to the rightmost will be $\Delta^{\dagger}_{\sigma'_1,\sigma'_2} |\psi_0\rangle = 0 |\psi_0\rangle$. This means any ground state generated by $U_{s,\tau;s',\tau'}$ can be expressed by the linear combination of wavefunctions in the form above. On the other hand, each $\Delta^{\dagger}_{\sigma',\sigma}$ will change the particle number while keeping momentum conservation in two bands so that different particle number distribution or different momentum conservation way states are orthogonal.

Now, we would like to check the orthogonal and close property for single particle excitation subspace $c^{\dagger}_{k_1,m_1,\sigma_1} |\psi_g\rangle$ by computing $\langle\psi_g| c_{k'_1,m'_1,\sigma'_1} c^{\dagger}_{k_1,m_1,\sigma_1} |\psi_g\rangle$ or equivalently $\langle\psi_0| [\prod_{\sigma',\sigma} (\Delta^{\dagger}_{\sigma',\sigma})^{m_{\sigma',\sigma}}]^{\dagger} c_{k'_1,m'_1,\sigma'_1} c^{\dagger}_{k_1,m_1,\sigma_1} \prod_{\sigma',\sigma} (\Delta^{\dagger}_{\sigma',\sigma})^{m_{\sigma',\sigma}} |\psi_0\rangle$. Here σ_1 is not necessarily full-filled bands because bands can be partially filled in $|\psi_g\rangle$. Noticing $|\psi_0\rangle$ is single particle Kronecker product state, orthogonality can be easily checked by Wick's theorem (see Appendix A). To be specific by noticing the contraction will transfer momentum and band conservation, only full contraction can give non-zero result $A\delta_{k_1,k'_1} \delta_{m_1,m'_1} \delta_{\sigma_1,\sigma'_1}$ where A is a constant from contraction. This proves the orthogonal property and the

close property can also be checked according to

$$\begin{aligned}
& Hc^{\dagger}_{k_1,m_1,\sigma_1}|\psi_g\rangle = \left[H, c^{\dagger}_{k_1,m_1,\sigma_1}\right]|\psi_g\rangle \\
= & \frac{1}{2\Omega}\sum_{q,G} V(q+G)\delta\rho_{q+G}\left[\delta\rho_{-q-G}, c^{\dagger}_{k_1,m_1,\sigma_1}\right]|\psi_g\rangle \\
= & \frac{1}{2\Omega}\sum_{q,G} V(q+G)\left[\delta\rho_{q+G}, \left[\delta\rho_{-q-G}, c^{\dagger}_{k_1,m_1,\sigma_1}\right]\right]|\psi_g\rangle \\
= & \sum_{m_2,m}\left[\frac{1}{2\Omega}\sum_{q,G} V(q+G)\lambda_{\sigma_1;m_2,m}(k_1,k_1+q+G)\lambda_{\sigma_1;m,m_1}(k_1+q+G,k_1)\right] c^{\dagger}_{k_1,m_2,\sigma_1}|\psi_g\rangle
\end{aligned} \tag{3.47}$$

This means H only projects such a single-particle excitation state to linear combination of single particle excitation states. Then one can diagonalize H in each k_1, σ_1 subspace (2×2 matrix in band space) to derive eigen single-particle excitation. The single hole excitation is exactly the same with particle due to many-body particle-hole symmetry. This gives the star lines labeled by "Exact" in Fig 3.8(b),(c).

For charge-neutral two-particle excitation $c^{\dagger}_{k_1,m_1,\sigma_1}c_{k_2,m_2,\sigma_2}|\psi_g\rangle$, one needs to exclude self-contraction within one side for $\langle\psi_g| c^{\dagger}_{k_2',m_2',\sigma_2'}c_{k_1',m_1',\sigma_1'}c^{\dagger}_{k_1,m_1,\sigma_1}c_{k_2,m_2,\sigma_2}|\psi_g\rangle$ which gives $\delta_{k_1,k_2}\delta_{k_1',k_2'}$ but not $\delta_{k_1,k_1'}\delta_{k_2,k_2'}$ as we want. This can be excluded automatically by requiring the momentum of this excitation non-zero (i.e., $k_1-k_2\neq 0$). If we ignore the zero excitation momentum point, then the left states again form an orthogonal and close subspace

$$\begin{aligned}
& Hc^{\dagger}_{k,m_1,\sigma_1}c_{k+p,m_2,\sigma_2}|\psi_g\rangle = \left[H, c^{\dagger}_{k,m_1,\sigma_1}c_{k+p,m_2,\sigma_2}\right]|\psi_g\rangle \\
= & \frac{1}{2\Omega}\sum_{q,G} V(q+G)\left[\delta\rho_{q+G}, \left[\delta\rho_{-q-G}, c^{\dagger}_{k,m_1,\sigma_1}c_{k+p,m_2,\sigma_2}\right]\right]|\psi_g\rangle \\
= & \frac{1}{2\Omega}\sum_{q,G} V(q+G)\sum_{m,n}[\lambda_{\sigma_1;n,m}(k,k+q+G)\lambda_{\sigma_1;m,m_1}(k+q+G,k)c^{\dagger}_{k,n,\sigma_1}c_{k+p,m_2,\sigma_2} \\
& -2\lambda_{\sigma_2;m_2,n}(k+p,k+p+q+G)\lambda_{\sigma_1;m,m_1}(k+q+G,k)c^{\dagger}_{k+q,m,\sigma_1}c_{k+q+p,n,\sigma_2} \\
& +\lambda_{\sigma_2;n,m}(k+p+q+G,k+p)\lambda_{\sigma_2;m_2,n}(k+p,k+p+q+G)c^{\dagger}_{k,m_1,\sigma_1}c_{k+p,m,\sigma_2}]|\psi_g\rangle
\end{aligned} \tag{3.48}$$

Within each total momentum fixed excitation subspace, one can diagonalize this Hamiltonian and this gives the red dashed lines labeled by "Analytic Goldstone modes" in Fig 3.9(b). This finishes the discussion of exact solution. And I will introduce how to derive those excitation from Green's function in DQMC below.

In the simulation of DQMC, the sign problem is absent no matter whether band dispersion is involved so that we discuss the general setting with finite H_0 below. $H_0=0$ case can be used to benchmark our DQMC result and we will discuss the ground state

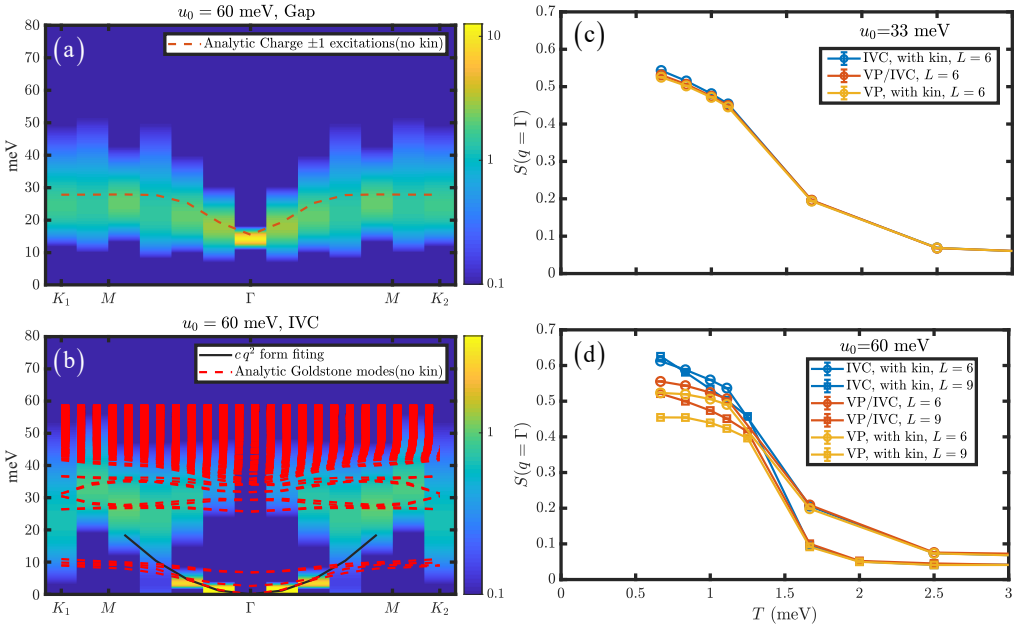


Figure 3.9: (a) Single-particle spectra at $T = 0.667meV$, $u_0 = 60meV$ and $L = 9$, which shows an insulating gap $\sim 10meV$. The dashed lines are the analytic computation of the lowest single-particle excitation at the flat-band limit. (b) Dynamical spectra of IVC with the same parameters. Sharp and ferromagnetic-like valley waves are observed near $q = \Gamma$ and a fit of $c\,q^2$ gives rise to $c = 31.32 \pm 0.03$ (black solid line in (b)). At the energy scale of twice the single-particle gap, $\sim 20meV$, valley waves are over-damped into the particle-hole continuum. The dashed lines are the analytic computation of the Goldstone mode at the flat-band limit. (c) $S(q = \Gamma)$, the correlation of order parameters, for VP and IVC at $u_0 = 33$ meV and $L = 6$, as a function of temperature. (b) The same quantity at $u_0 = 60$ meV with both $L = 6$ and $L = 9$. When kinetic energy is ignored, the two order parameters are almost degenerate. When the kinetic energy is taken into account ("with kin"), this degeneracy is lifted. At $u_0 = 33$ meV, the splitting between VP and IVC is weak. This splitting becomes more pronounced at $u_0 = 60$ meV, indicating that IVC is more favored at low temperatures in comparison to VP, although the competition between these two symmetry-breaking channels remains. These figures come from Ref [6].

for $H_0 \neq 0$. First, let's focus on imaginary-time single-particle Green's function

$$\begin{aligned} G_{m,m'}(t,0) &\equiv \frac{\mathrm{Tr}(e^{-(\beta-t)H}c_{k,m,\sigma}e^{-tH}c^{\dagger}_{k,m',\sigma})}{\mathrm{Tr}(e^{-\beta H})} \\ &= e^{\beta F}\sum_{i,j}\langle i|c_{k,m,\sigma}|j\rangle\left\langle j|c^{\dagger}_{k,m',\sigma}|i\right\rangle e^{-(\beta-t)\epsilon_i - t\epsilon_j} \end{aligned} \tag{3.49}$$

Here, $F \equiv -\frac{1}{\beta}\log(\mathrm{Tr}(e^{-\beta H}))$ is the free energy and i,j labels different eigenstates of H. By a unitary transformation diagonalizing $G_{m,m'}(t,0)$, we derive

$$G_{\alpha}(t,0) = e^{\beta F}\sum_{i,j}\left|\left\langle j|c^{\dagger}_{k,\alpha,\sigma}i\right\rangle\right|^2 e^{-(\beta-t)\epsilon_i - t\epsilon_j} \tag{3.50}$$

Now assuming low-temperature limit $\beta \to \infty$, there are two dominant cases that $t \ll \beta$ and $t \to \beta$. For each case only ground state term $e^{-(\beta-t)\epsilon_0}$ or $e^{-t\epsilon_0}$ in the summation gives dominant contribution so that

$$G_{\alpha}(t,0) \approx e^{\beta F-\beta\epsilon_0}\sum_{g,j}\left|\left\langle j|c^{\dagger}_{k,\alpha,\sigma}\psi_g\right\rangle\right|^2 e^{-t(\epsilon_j-\epsilon_0)} + e^{\beta F-\beta\epsilon_0}\sum_{g,i}\left|\langle i|c_{k,\alpha,\sigma}\psi_g\rangle\right|^2 e^{-(\beta-t)(\epsilon_i-\epsilon_0)} \tag{3.51}$$

where g labels all the degenerate ground states. Now one can read from the expression that $G_{\alpha}(t,0)$ is proportional to the summation of all the single-particle (single-hole) excitation weighted by the overlap with excitation eigenstates and an exponential decay with excitation energy. Further more for a single-particle (single-hole) gapped system $\epsilon_j - \epsilon_0 \neq 0$ ($\epsilon_i - \epsilon_0 \neq 0$), one should observe $G_{\alpha}(t,0)$ decays to zero for large t ($\beta - t$) which is a direct justification from DQMC data for identifying a single-particle gapped system and the smallest slope with t ($\beta - t$) for $\log(G_{\alpha}(t,0))$ indicates the magnitude of the smallest single-particle (single-hole) gap $\epsilon_j - \epsilon_0$ ($\epsilon_i - \epsilon_0 \neq 0$). This argument can go far away from single-particle (single-hole) excitation and apply for all kinds of excitation defined by $O^{\dagger}$.

$$\begin{aligned} C_{m,m'}(t,0) &\equiv \frac{\mathrm{Tr}(e^{-(\beta-t)H}O_m e^{-tH}O^{\dagger}_{m'})}{\mathrm{Tr}(e^{-\beta H})} \\ &= e^{\beta F}\sum_{i,j}\langle i|O_m|j\rangle\left\langle j|O^{\dagger}_{m'}|i\right\rangle e^{-(\beta-t)\epsilon_i - t\epsilon_j} \end{aligned} \tag{3.52}$$

In the similar way, one can identify all kinds of excitation energy in different excitation channels from DQMC correlation measurement, e.g, two-particle charge-neutral excitations. I will show analytical derivation examples for those Green's function in Chapter 4. Besides the intuitive understanding, one can also derive the spectral function $A(k,\omega)$ from stochastic analytic continuation method as introduced in Appendix D.

Return back to TBG system, at $H_0 = 0$ one can see there are only two single-particle excitations in exact solution (by diagonalizing 2×2 matrix at each k point) and we confirm this result by extrapolating the slope of $G_{\alpha}(t,0)$ at large β. The result is

shown as "QMC" lines with error bars in Fig 3.8(b),(c) and dashed line in Fig 3.9(a). When $H_0 \neq 0$ but small due to flat bands, we confirm the ground state is also single-particle gapped by single-particle spectra as shown Fig 3.9(a). Here spin-valley $U(4)$ is broken while spin $SU(2)$ is conserved. Because of Mermin–Wagner theorem there is no spin order at finite temperature for 2D system. And we would like to detect valley order, i.e., valley polarization (VP) or inter-valley coherence (IVC) by defining two-particle charge-neutral order parameters. For VP and IVC, we define the order parameter structure with momentum q in projection band basis as

$$\begin{aligned} O_{VP}(q) &\equiv \frac{1}{N_k}\sum_{k,m,s}(c^\dagger_{k+q,m,+,s}c_{k,m,+,s} - c^\dagger_{k+q,m,-,s}c_{k,m,-,s}) \\ O_{IVC}(q) &\equiv \frac{1}{N_k}\sum_{k,m,s}(imc^\dagger_{k+q,m,+,s}c_{k,-m,-,s} - imc^\dagger_{k+q,-m,-,s}c_{k,m,+,s}). \end{aligned} \quad (3.53)$$

Then for finite momentum excitation, one just computes correlation

$$\begin{aligned} S_{VP}(q) &\equiv \langle O_{VP}(q)O_{VP}(-q)\rangle_l \\ &= \frac{1}{N_k^2}\sum_{k,m,s;k',m',s'}(\left\langle c^\dagger_{k+q,m,+,s}c_{k,m,+,s}c^\dagger_{k',m',+,s'}c_{k'+q,m',+,s'}\right\rangle_l \\ &- \left\langle c^\dagger_{k+q,m,+,s}c_{k,m,+,s}c^\dagger_{k',m',-,s'}c_{k'+q,m',-,s'}\right\rangle_l \\ &- \left\langle c^\dagger_{k+q,m,-,s}c_{k,m,-,s}c^\dagger_{k',m',+,s'}c_{k'+q,m',+,s'}\right\rangle_l \\ &+ \left\langle c^\dagger_{k+q,m,-,s}c_{k,m,-,s}c^\dagger_{k',m',-,s'}c_{k'+q,m',-,s'}\right\rangle_l) \\ &= \frac{1}{N_k^2}\sum_{k,m;k',m'}(4G^I_{k,m;k+q,m}(\tau)G^I_{k'+q,m';k',m'}(\tau) + 2G^I_{k'+q,m';k+q,m}(\tau)G_{k,m;k',m'}(\tau) \\ &- 4G^I_{k,m;k+q,m}(\tau)G^I_{k'+q,m';k',m'}(-\tau) - 4G^I_{k,m;k+q,m}(-\tau)G^I_{k'+q,m';k',m'}(\tau) \\ &+ 4G^I_{k,m;k+q,m}(-\tau)G^I_{k'+q,m';k',m'}(-\tau) + 2G^I_{k'+q,m';k+q,m}(-\tau)G_{k,m;k',m'}(-\tau) \\ &= \frac{1}{N_k^2}\sum_{k,m;k',m'}(4G^I_{k,m;k+q,m}(\tau)G^I_{k'+q,m';k',m'}(\tau) + 2G^I_{k'+q,m';k+q,m}(\tau)G_{k,m;k',m'}(\tau) \\ &- 4G^I_{k,m;k+q,m}(\tau)G^*_{k',m';k'+q,m'}(\tau) - 4G^*_{k+q,m;k,m}(\tau)G^I_{k'+q,m';k',m'}(\tau) \\ &+ 4G^*_{k+q,m;k,m}(\tau)G^*_{k',m';k'+q,m'}(\tau) + 2G^*_{k+q,m;k'+q,m'}(\tau)(G^I_{k',m';k,m}(\tau))^* \end{aligned} \quad (3.54)$$

Here $\langle\cdots\rangle_l$ labels average for a given auxiliary field l in DQMC measurement and one can compute the correlation according to Wick's theorem as introduced in Chapter 2. We use k, m labels to form a row or column in Green's function matrix at valley τ block, i.e. $G_{k,m;k',m'}(\tau)$. And as the same convention used in Chapter 2, we define $G^I_{k,m;k',m'}(\tau) \equiv I - G_{k,m;k',m'}(\tau)$ where I is identity matrix. The Green's function in the other valley $-\tau$ can be expressed by the one in valley τ if one use this transformation

$\tilde{c}_{k,m,-\tau} = mc^{\dagger}_{k,-m,-\tau}$

$$\begin{aligned} G_{k,m;k',m'}(-\tau) &\equiv \frac{\mathrm{Tr}(B_{-\tau}(\beta,0)c_{k,m,-\tau}c^{\dagger}_{k',m',-\tau})}{\mathrm{Tr}(B_{-\tau}(\beta,0))} \\ &= mm'\frac{\mathrm{Tr}(B^{*}_{\tau}(\beta,0)\tilde{c}^{\dagger}_{k,-m,-\tau}\tilde{c}_{k',-m',-\tau})}{\mathrm{Tr}(B^{*}_{\tau}(\beta,0))} \\ &= mm'(G^{I}_{k',-m';k,-m}(\tau))^{*} \end{aligned} \tag{3.55}$$

Here we use $B_{-\tau}$ or B_{τ} to identify $\lambda_{-\tau}$ or λ_{τ} in B operator while this subscript has nothing do to with $c^{\dagger}_{\pm\tau}$ or $c_{\pm\tau}$ used within B. With this formula, one can simulate only one spin-valley section in DQMC and use the mapping to transform the Green's function in other valley as shown in the final expression of $S_{VP}(q)$. Now let's look at $S_{IVC}(q)$

$$\begin{aligned} S_{IVC}(q) &\equiv \langle O_{IVC}(q)O_{IVC}(-q)\rangle_{l} \\ &= \frac{1}{N_k^2}\sum_{k,m,s;k',m',s'} mm'(\left\langle c^{\dagger}_{k+q,m,+,s}c_{k,-m,-,s}c^{\dagger}_{k',-m',-,s'}c_{k'+q,m',+,s'}\right\rangle_{l} \\ &+ \left\langle c^{\dagger}_{k+q,-m,-,s}c_{k,m,+,s}c^{\dagger}_{k',m',+,s'}c_{k'+q,-m',-,s'}\right\rangle_{l}) \\ &= \frac{1}{N_k^2}\sum_{k,m;k',m'} mm'(2G^{I}_{k'+q,m';k+q,m}(\tau)G_{k,-m;k',-m'}(-\tau) \\ &+ 2G^{I}_{k'+q,-m';k+q,-m}(-\tau)G_{k,m;k',m'}(\tau)) \\ &= \frac{1}{N_k^2}\sum_{k,m;k',m'} (2G^{I}_{k'+q,m';k+q,m}(\tau)(G^{I}_{k',m';k,m}(\tau))^{*} \\ &+ 2G^{*}_{k+q,m;k'+q,m'}(\tau)G_{k,m;k',m'}(\tau)) \end{aligned} \tag{3.56}$$

These are the observable we use in DQMC implementation. One can prove at flat band limit $H_0 = 0$, we have $S_{VP}(q) = S_{IVC}(q)$ as it should be from valley $SU(2)$. This proof has used the condition that when $H_0 = 0$, B matrix is unitary as discussed in the proof of **Statement 1**. Then by definition $G = (I + B)^{-1}$, we derive

$$G + G^{\dagger} = (I + B)^{-1} + B(I + B)^{-1} = I \tag{3.57}$$

By replacing all the G^I by $G^{\dagger}$ in $S_{VP}(q)$ and $S_{IVC}(q)$, one can easily check

$$S_{VP}(q) = \frac{1}{N_k^2}\sum_{k,m;k',m'} 4G^{*}_{k+q,m;k'+q,m'}(\tau)G_{k,m;k',m'}(\tau) = S_{IVC}(q) \tag{3.58}$$

The simulation results without and with H_0 are shown in Fig 3.9(c),(d), where an IVC order shapes faster than VP at finite temperature indicating the ground state is IVC order. The difference of dynamic spectrum of the finite momentum excitation from those two orders derived from imaginary time correlation and SAC is small and the IVC result is shown in Fig 3.9(b).

3.6 Polynomial sign problem and topological insulators at chiral integer fillings

Besides the CNP flat-band limit spin-valley $U(4)$ solution introduced in the last section, exact analytical solution of the TBG model has also been obtained at other limits with the similar spirit [2, 99, 120]. On the numerical side, we have discussed the CNP by using sign-problem-free momentum-space DQMC simulations. Away from the CNP, the sign problem arises but at certain limit it will decay in a polynomial form with system size at low temperature limit according to the sign bounds theory introduced in Chapter 2 **Corollary II**. In this section, we introduce the sign problem in TBG at the flat-band limit (interaction effect will be overestimated which will cause quantitative difference for a gaped insulator ground state). Utilizing the sign bounds theory [1], we prove that TBG flat bands at even integer fillings, or arbitrary integer fillings in the chiral limit, exhibit (at most) polynomial sign problem. This observation allows us to utilize DQMC methods to study TBG systems with fillings away from charge neutrality, away from the chiral limit, and/or in the presence of extra attractive interactions with phonon or topological origins [93, 109, 110, 116, 124–137] on top of the Coulomb repulsion. As the gentlest sign problem case, we examine the chiral limit at filling $\nu = 1$ (we denote the fully empty/filled flat bands as $\nu = -4/+4$ and charge neutrality as $\nu = 0$). At $T = 0$, this model can be solved exactly, and the exact solution reveals that at $T \to 0$, the system is a correlated Chern insulator – a topological Mott insulator (TMI) [2, 138] – with Chern number $C = 1$. Upon raising the temperature, our DQMC simulations observe three different phases/states (1) a metal phase with time-reversal symmetry at high temperature $T > T^\star$, (2) a time-reversal invariant pseudo-gap phase at intermediate temperature $T_c < T < T^\star$ and (3) a low-temperature TMI phase at $T < T_c$. Here, $T^\star$ is a crossover temperature scale and T_c is the critical temperature below which the time-reversal symmetry is spontaneously broken.

3.6.1 Ground state energy, degeneracy and sign bounds

First of all, let's introduce the Hamiltonian we use to describe both repulsion and possible inter-valley attraction.

$$\begin{aligned}
H_I &= \frac{1}{2\Omega}\sum_{q,G}\left(V_1(q+G)\delta\rho_{1,q+G}\delta\rho_{1,-q-G} + V_2(q+G)\delta\rho_{2,q+G}\delta\rho_{2,-q-G}\right) \\
\delta\rho_{1,q+G} &= \sum_{k,m,n,\tau,s}\lambda_{\tau;m,n}(k,k+q+G)\left(c^\dagger_{k,m,\tau,s}c_{k+q,n,\tau,s} - \frac{\nu+4}{8}\delta_{q,0}\delta_{m,n}\right) \\
\delta\rho_{2,q+G} &= \sum_{k,m,n,s}\left[\lambda_{\tau;m,n}(k,k+q+G)c^\dagger_{k,m,\tau,s}c_{k+q,n,\tau,s}\right. \\
&- \left.\lambda_{-\tau;m,n}(k,k+q+G)c^\dagger_{k,m,-\tau,s}c_{k+q,n,-\tau,s}\right]
\end{aligned} \tag{3.59}$$

Here $V_1 > 0$ is the same as the Coulomb repulsion used in the last section and we use $V_2 \geqslant 0$ to label the possible inter-valley attraction. One can check this inter-valley attraction by expanding the density-density interaction. Here ν is used to tune the chemical potential and $\nu = 0$ indicates the CNP case. We would like to introduce the chiral limit for BM model below, where the band becomes exact flat so that $H = H_I$ with $H_0 = 0$ [94]. Focusing on BM model

$$\begin{aligned}
H^{\tau}_{k,k'} &= \delta_{k,k'}\begin{pmatrix} -\hbar v_F(k-K_1)\cdot\sigma & 0 \\ 0 & -\hbar v_F(k-K_2)\cdot\sigma \end{pmatrix} + \begin{pmatrix} 0 & U^{\tau} \\ U^{\tau\dagger} & 0 \end{pmatrix} \\
U^{\tau} &= \begin{pmatrix} u_0 & u_1 \\ u_1 & u_0 \end{pmatrix}\delta_{k,k'} + \begin{pmatrix} u_0 & u_1 e^{-i\frac{2\pi}{3}} \\ u_1 e^{i\frac{2\pi}{3}} & u_0 \end{pmatrix}\delta_{k,k'-G_1} + \begin{pmatrix} u_0 & u_1 e^{i\frac{2\pi}{3}} \\ u_1 e^{-i\frac{2\pi}{3}} & u_0 \end{pmatrix}\delta_{k,k'-G_2} \\
H^{-\tau}_{k,k'} &= \delta_{k,k'}\begin{pmatrix} -\hbar v_F(-k-K_1)\cdot\sigma^* & 0 \\ 0 & -\hbar v_F(-k-K_2)\cdot\sigma^* \end{pmatrix} + \begin{pmatrix} 0 & U^{-\tau} \\ U^{-\tau\dagger} & 0 \end{pmatrix} \\
U^{-\tau} &= \begin{pmatrix} u_0 & u_1 \\ u_1 & u_0 \end{pmatrix}\delta_{k,k'} + \begin{pmatrix} u_0 & u_1 e^{i\frac{2\pi}{3}} \\ u_1 e^{-i\frac{2\pi}{3}} & u_0 \end{pmatrix}\delta_{k,k'+G_1} + \begin{pmatrix} u_0 & u_1 e^{-i\frac{2\pi}{3}} \\ u_1 e^{i\frac{2\pi}{3}} & u_0 \end{pmatrix}\delta_{k,k'+G_2}.
\end{aligned} \tag{3.60}$$

One can see if we set $u_0 = 0$, this Hamiltonian will have no diagonal elements in sublattice subspace so that it must be linear combination of σ_x, σ_y which anti-commutes with σ_z. Then σ_z becomes the chiral symmetry operator of this Hamiltonian, i.e. $\sigma_z H^{\tau}_{k,k'}\sigma_z = -H^{\tau}_{k,k'}$. Since two flat bands are degenerate, one can use eigenvalues of σ_z to label the degenerate bands which gives two topological nontrivial bands with ± 1 Chern number. This basis is called Chern basis where the form factor coming from the overlap of wavefunction $\lambda_{\tau,m,n}(k, k+q+G) \to \lambda_{\tau,m,m}(k, k+q+G)\delta_{m,n}$ since the overlap between two eigenfunctions with different eigenvalues is zero. Based on this, we can expand spin-valley subspace similarly as we do in CNP $U(4)$ case.

$$\begin{aligned}
\delta\rho_{q+G} &= \sum_{k,m} \lambda_{\tau;m,m}(k, k+q+G)(c^{\dagger}_{k,m,s,\tau}c_{k+q,m,s,\tau} + c^{\dagger}_{k,m,-s,\tau}c_{k+q,m,-s,\tau} \\
&+ \tilde{c}^{\dagger}_{k,m,s,-\tau}\tilde{c}_{k+q,m,s,-\tau} + \tilde{c}^{\dagger}_{k,m,-s,-\tau}\tilde{c}_{k+q,m,-s,-\tau} - \frac{\nu+4}{2}\delta_{q,0})
\end{aligned} \tag{3.61}$$

One can see Chern band label forms two closed subspace where there is $U(4)$ symmetry within each, so that the symmetry now for the V_1 term is $U(4) \times U(4)$. This analysis is important for computing ground state degeneracy and we will turn back to it later. Now, we will introduce what is the sufficient conditions for zero ground state energy and exact ground state below.

At chiral limit in Chern basis, form factor $\lambda_{\tau;m,n}(k, k+q+G)$ is diagonal about Chern bands and $\sum_k \lambda_{+,+,\tau}(k, k+G) = \sum_k \lambda_{-,-,\tau'}(k, k+G)$. If there is no attraction

($V_2 = 0$), in Chern basis

$$\begin{aligned} H_I &= \frac{1}{2\Omega}\sum_{q,G} V_1(q+G)\delta\rho_{1,q+G}\delta\rho_{1,-q-G} \\ \delta\rho_{1,q+G} &= \sum_{k,m,\tau,s} \lambda_{\tau;m,m}(k,k+q+G)(c^\dagger_{k,m,\tau,s}c_{k+q,m,\tau,s} - \frac{\mu}{8}\delta_{q,0}) \end{aligned} \tag{3.62}$$

We define $\mu \equiv \nu + 4$ for convenience here. For a certain integer filling tuned by μ, we can find a ground state $|\psi_0\rangle$ with whole Chern bands occupied by noticing a state satisfying $\delta\rho_{1,q+G}|\psi_0\rangle = 0$ for any $q+G$ must be the ground state for this positive semi-definite Hamiltonian.

$$\sum_{k,m',\tau',s'} \lambda_{\tau';m',m'}(k,k+G) - \mu\sum_{k} \lambda_{\tau;m,m,}(k,k+G) = 0 \tag{3.63}$$

Here m', τ', s' mean filled Chern band, valley and spin indexes. One just requires the amount of filled bands is equal to μ to acquire zero energy ground state. This means *all integer filling μ from 0 to 8 have zero energy ground state when $V_2 = 0$.*

With finite attraction $V_2 > 0$, we need one more satisfied restriction $\delta\rho_{2,q+G}|\psi_0\rangle = 0$ to obtain zero energy ground state. Explicitly, this requirement is

$$\sum_{k,m',s'} \lambda_{\tau;m',m'}(k,k+G) - \sum_{k,m'',s''} \lambda_{-\tau;m'',m''}(k,k+G) = 0 \tag{3.64}$$

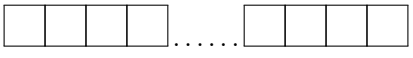
Here m', s' mean filled Chern band, spin indexes in valley τ and m'', s'' are filled Chern band, spin indexes in valley $-\tau$. This restriction actually requires *the same amount of filling bands in opposite valleys*, which rules out odd integer filling cases at $V_2 = 0$.

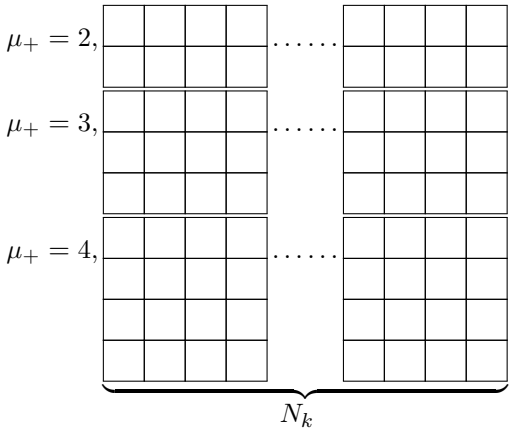
For non-chiral $V_2 = 0$ case, $\sum_k \lambda_{\tau;+,+}(k,k+G) = \sum_k \lambda_{\tau';-,-}(k,k+G)$ cannot be promised. The zero energy ground state requirement becomes

$$\sum_{k,m',\tau',s'} \lambda_{\tau';m',m'}(k,k+G) - \frac{\mu}{2}\sum_{k,m} \lambda_{\tau;m,m}(k,k+G) = 0 \tag{3.65}$$

This means one needs to *fully fill even opposite Chern bands*, which corresponds to even integer fillings. These zero ground state energy states will be the necessary condition for sign bounds analysis below.

Symmetry for no attraction ($V_2 = 0$) chiral system is $U(4) \times U(4)$ according to our discussion before, where each $U(4)$ corresponds to spin-valley freedom within the same Chern number bands sector. We use Young diagram, as introduced briefly in Appendix C, for $SU(4)$ to compute ground state degeneracy of different integer fillings. The ground state wave function irreducible representation for filling μ_+ from 0 to 4 corresponding to 2 spins, 2 valleys within + Chern bands sector can be expressed as Young diagram below respectively

$\mu_+ = 1,$  $\ldots\ldots$



The amount of normal Young tableau for $SU(4)$ symmetry calculated by hook length formula (see Appendix C) are

$$\begin{aligned}
d_{\mu_+=0}(SU(4)) &= 1 \\
d_{\mu_+=1}(SU(4)) &= \prod_j \frac{4+j-1}{j} = \frac{\frac{(N_k+3)!}{3!}}{N_k!} = \frac{(N_k+3)(N_k+2)(N_k+1)}{3!} \\
d_{\mu_+=2}(SU(4)) &= \prod_{i,j} \frac{4+j-i}{h_{i,j}} = \frac{\frac{(N_k+3)!(N_k+2)!}{3!2!}}{(N_k+1)!N_k!} = \frac{(N_k+3)(N_k+2)^2(N_k+1)}{3!2!} \\
d_{\mu_+=3}(SU(4)) &= \frac{\frac{(N_k+3)!(N_k+2)!(N_k+1)!}{3!2!}}{\frac{(N_k+2)!(N_k+1)!N_k!}{2!}} = \frac{(N_k+3)(N_k+2)(N_k+1)}{3!} \\
d_{\mu_+=4}(SU(4)) &= 1
\end{aligned} \tag{3.66}$$

By the way, the $SU(2)$ Young diagram for $\mu_+ = 0, \mu_+ = 1, \mu_+ = 2$ have the same shape with the $SU(4)$ above, but the amounts of normal Young tableau are different

$$\begin{aligned}
d_{\mu_+=0}(SU(2)) &= 1 \\
d_{\mu_+=1}(SU(2)) &= \prod_j \frac{2+j-1}{j} = N_k+1 \\
d_{\mu_+=2}(SU(2)) &= 1
\end{aligned} \tag{3.67}$$

Now we are ready to count the total degeneracy for all integer filling μ from 0 to 8 (corresponding to ν from -4 to 4) for chiral no attraction ($V_2 = 0$) TBG model by using

$SU(4)$ Young diagram.

$$
\begin{aligned}
d_{\mu=0} &= d_{\{\mu_+=0,\mu_-=0\}} = 1 \\
d_{\mu=1} &= d_{\{\mu+=1,\mu_-=0\}} + d_{\{\mu_+=0,\mu_-=1\}} = \frac{(N_k+3)(N_k+2)(N_k+1)}{3} \\
d_{\mu=2} &= 2d_{\{\mu_+=2,\mu_-=0\}} + d_{\{\mu_+=1,\mu_-=1\}} \\
&= \frac{(N_k+3)(N_k+2)^2(N_k+1)}{3!} + \frac{(N_k+3)^2(N_k+2)^2(N_k+1)^2}{3!3!} \\
d_{\mu=3} &= 2d_{\{\mu_+=3,\mu_-=0\}} + 2d_{\{\mu_+=2,\mu_-=1\}} \\
&= \frac{(N_k+3)(N_k+2)(N_k+1)}{3} + \frac{(N_k+3)^2(N_k+2)^3(N_k+1)^2}{3!3!} \\
d_{\mu=4} &= 2d_{\{\mu_+=4,\mu_-=0\}} + 2d_{\{\mu_+=3,\mu_-=1\}} + d_{\{\mu_+=2,\mu_-=2\}} \\
&= 2 + \frac{(N_k+3)^2(N_k+2)^2(N_k+1)^2}{3!3} + \frac{(N_k+3)^2(N_k+2)^4(N_k+1)^2}{3!3!2!2!} \\
d_{\mu=5} &= 2d_{\{\mu_+=4,\mu_-=1\}} + 2d_{\{\mu_+=3,\mu_-=2\}} \\
&= \frac{(N_k+3)(N_k+2)(N_k+1)}{3} + \frac{(N_k+3)^2(N_k+2)^3(N_k+1)^2}{3!3!} \\
d_{\mu=6} &= 2d_{\{\mu_+=4,\mu_-=2\}} + d_{\{\mu_+=3,\mu_-=3\}} \\
&= \frac{(N_k+3)(N_k+2)^2(N_k+1)}{3!} + \frac{(N_k+3)^2(N_k+2)^2(N_k+1)^2}{3!3!} \\
d_{\mu=7} &= 2d_{\{\mu_+=4,\mu_-=3\}} = \frac{(N_k+3)(N_k+2)(N_k+1)}{3} \\
d_{\mu=8} &= d_{\{\mu_+=4,\mu_-=4\}} = 1
\end{aligned}
\tag{3.68}
$$

When we consider $N_k \to \infty$, the degeneracy with power of N_k for different fillings can be seen as $d_{\mu=0} \propto N_k^0, d_{\mu=1} \propto N_k^3, d_{\mu=2} \propto N_k^6, d_{\mu=3} \propto N_k^7, d_{\mu=4} \propto N_k^8, d_{\mu=5} \propto N_k^7, d_{\mu=6} \propto N_k^6, d_{\mu=7} \propto N_k^3, d_{\mu=8} \propto N_k^0$. Because the degeneracy for our reference system ($\mu = 4$ case where there is no sign problem) is $d_{\mu=4} \propto N_k^8$, we can see the other integer filling have different polynomial sign bounds decay according to $\langle sign \rangle_b \equiv b_\mu = d_\mu / d_{\mu=4}$ as $b_{\mu=3,\mu=5} \propto N_k^{-1}, b_{\mu=2,\mu=6} \propto N_k^{-2}, b_{\mu=1,\mu=7} \propto N_k^{-5}, b_{\mu=0,\mu=8} \propto N_k^{-8}$. This is the second column result in Tab 3.2. One can verify the involving attraction case ($V_2 > 0$) will break the $U(4) \times U(4)$ to $U(2) \times U(2) \times U(2) \times U(2)$, where original spin-valley $U(4)$ is broken into two spin $U(2)$. By introducing *filling the same amount of bands in opposite valleys* restriction for zero energy ground states, we can write valley label τ explicitly for a given μ and use the $SU(2)$ Young diagram results above to count the degeneracy of even integer fillings now

$$
\begin{aligned}
d_{\mu=0} &= d_{\{\mu_\tau=0,\mu_{-\tau}=0\}} = 1 \\
d_{\mu=2} &= 4d_{\{\mu_\tau=1,\mu_{-\tau}=1\}} = 4(N_k+1)^2 \\
d_{\mu=4} &= 4d_{\{\mu_{+,\tau}=2,\mu_{-,-\tau}=2\}} + 4d_{\{\mu_{+,\tau}=2,\mu_{-,-\tau}=1,\mu_{+,-\tau}=1\}} + d_{\{\mu_{+,\tau}=1,\mu_{+,-\tau}=1,\mu_{-,\tau}=1,\mu_{-,-\tau}=1\}} \\
&= 4 + 4(N_k+1)^2 + (N_k+1)^4 \\
d_{\mu=6} &= 4d_{\{\mu_\tau=3,\mu_{-\tau}=3\}} = 4(N_k+1)^2 \\
d_{\mu=8} &= d_{\{\mu_\tau=4,\mu_{-\tau}=4\}} = 1
\end{aligned}
\tag{3.69}
$$

At large N_k, sign bounds with attraction ($V_2 > 0$) at chiral even integer filling are written as $b_{\mu=2,\mu=6} \propto N_k^{-2}, b_{\mu=0,\mu=8} \propto N_k^{-4}$, which is the result of the fourth column in Tab 3.2. It is shown before that non-chiral condition breaks $U(4) \times U(4)$ into one $U(4)$. We can count the ground state degeneracy of $V_2 = 0$ case by $SU(4)$ Young diagram

$$\begin{aligned} d_{\mu=0} &= 1 \\ d_{\mu=2} &= d_{\{\mu_{s,\tau}=2\}} = \frac{(2N_k+3)(2N_k+2)(2N_k+1)}{3!} \\ d_{\mu=4} &= d_{\{\mu_{s,\tau}=4\}} = \frac{(2N_k+3)(2N_k+2)^2(2N_k+1)}{3!2!} \\ d_{\mu=6} &= d_{\{\mu_{s,\tau}=6\}} = \frac{(2N_k+3)(2N_k+2)(2N_k+1)}{3!} \\ d_{\mu=8} &= 1 \end{aligned} \tag{3.70}$$

This gives the third column result of Tab 3.2, which are sign bounds $b_{\mu=2,\mu=6} \propto N_k^{-1}, b_{\mu=0,\mu=8} \propto N_k^{-4}$ for non-chiral $V_2 = 0$ large N_k case (still assuming $H_0 = 0$).

Table 3.2: Scaling of the sign bound $\langle sign \rangle_b$ at low temperature and large moiré lattice size $N_k = L^2$ [2]. A power-law function of N_k indicates that the sign problem is (at most) polynomial. ✗ indicates the sign bound decays to zero exponentially.

Filling(ν)	Chiral($\gamma = 0$)	Non-chiral($\gamma = 0$)	Chiral($\gamma > 0$)
0	1	1	1
± 1	N_k^{-1}	✗	✗
± 2	N_k^{-2}	N_k^{-1}	N_k^{-2}
± 3	N_k^{-5}	✗	✗
± 4	N_k^{-8}	N_k^{-4}	N_k^{-4}

3.6.2 DQMC results for sign bounds and $\nu = \pm 1$ case

As shown in Chapter 2, in DQMC simulations the expectation value of a physical observable O is measured as $\langle \hat{O} \rangle = \sum_l W_l \langle \hat{O} \rangle_l$, where W_l and $\langle \hat{O} \rangle_l$ are the weight and the expectation value for the configuration l. Instead of summing over all configurations, a DQMC simulation samples the configuration space using the probability W_l. In sign-problem-free DQMC simulations, $W_l \geq 0$ for all l and an accurate expectation value can be obtained by only sampling a small number of configurations – the importance sampling, and this number scales as a power-law function of the system size (see Appendix A). However, for many quantum systems, W_l can be negative or even complex, and thus to obtain an accurate expectation value, it requires to sample a large number of configurations, which usually scales as an exponential function of the system size [41].

It is worthwhile to emphasize that the sign problem doesn't always lead to an exponentially high computational cost as discussed in detail in Chapter 2. To measure the severity of the sign problem, we use the average sign $\langle sign \rangle = \sum_l W_l / \sum_l |\Re(W_l)|$, where $|\Re(W_l)|$ is the absolute value of the real part of W_l. For physical partition function

$Z = \sum_l W_l = \sum_l \Re(W_l)$, this average sign is between 0 and 1, and $\langle sign \rangle = 1$ means that the system is sign problem free, while smaller $\langle sign \rangle$ means severer sign problem. Although the average sign can be easily measured in DQMC simulations, it usually doesn't have a simple analytic formula. To estimate the numerical cost to overcome the sign problem, we utilize the sign bound $\langle sign \rangle_b$ defined in [1]. As proved in Chapter 2, $\langle sign \rangle_b$ is the lower bound of $\langle sign \rangle$ (i.e., $\langle sign \rangle_b \leqslant \langle sign \rangle$). Thus, if the sign bound scale is a power-law function of the system size, the sign problem is (at most) polynomial. In the last section, we have computed the low temperature sign bound by counting ground state degeneracy, which can be obtained using $SU(4)$ and $SU(2)$ Young diagram and the analytical results are summarized in Tab 3.2. For Coulomb repulsion ($V_2 = 0$), the sign problem is polynomial at any (even) integer fillings at (away from) the chiral limit. When inter-valley attractions are introduced ($V_2 > 0$), even integer fillings at the chiral limit also have polynomial sign bound.

To further verify the result, we directly calculate $\langle sign \rangle$ and $\langle sign \rangle_b$ in DQMC simulations at various filling ν, and compare them with the exact formula of the sign bound obtained at integer fillings. As shown in Fig 3.10, $\langle sign \rangle$ is always larger or equal to $\langle sign \rangle_b$ as expected, and the sign bound at integer filling indeed converges to the exact solution. The peak in $\langle sign \rangle$ at integer (or even integer) fillings indicates that the sign problem is less severe and DQMC simulations have a faster convergence at these fillings. The location of these peaks are fully consistent with the polynomial sign problem summarized in Tab 3.2. The only exceptions are $\nu = 3$ and 4 of Fig 3.10(a), where the sign problem is polynomial but the figure doesn't exhibit visible peaks. This is because the power-law function here has high powers N_k^{-5} and N_k^{-8}, which requires higher resolution (longer simulation time) to show clear distinction from exponential functions.

With the polynomial sign bound obtained, we discuss the DQMC results as a function of temperature for the chiral limit $\nu = 1$ filling case. In the DQMC simulation, we observe a thermal phase transition with pseudogap spectrum and spontaneous time reversal symmetry breaking, which is of immediate relevance to the experimental finding of correlated Chern insulators at zero-field and $\nu = 1$ filling in hbn nonaligned TBG devices and its relatively high Curie temperature of $T_c \sim 4.5K$ [139].

At low temperature limit for $\nu = 1$, exact solution at $T = 0$ expects degenerate ground states with Chern number $C = \pm 1$, and ± 3. In the large system size limit $N_k \to \infty$, the number of ground states scales as $\propto N_k^7$ for $C = \pm 1$ and N_k^3 for $C = \pm 3$ as discussed in the last section. Due to the higher amount of ground state degeneracy, thermal fluctuations shall stabilize the $C = \pm 1$ state as the thermal equilibrium state at low temperature via the order by disorder mechanism [140, 141]. This low-temperature state breaks spontaneously the time-reversal symmetry, but this symmetry breaking process as a function of temperature is unknown from exact solution and our DQMC simulation at finite temperature reveals this process. To probe the time-reversal symmetry breaking, we use the Chern band polarization as the order parameter, $\langle \hat{N}_+ - \hat{N}_- \rangle / N_k$, where

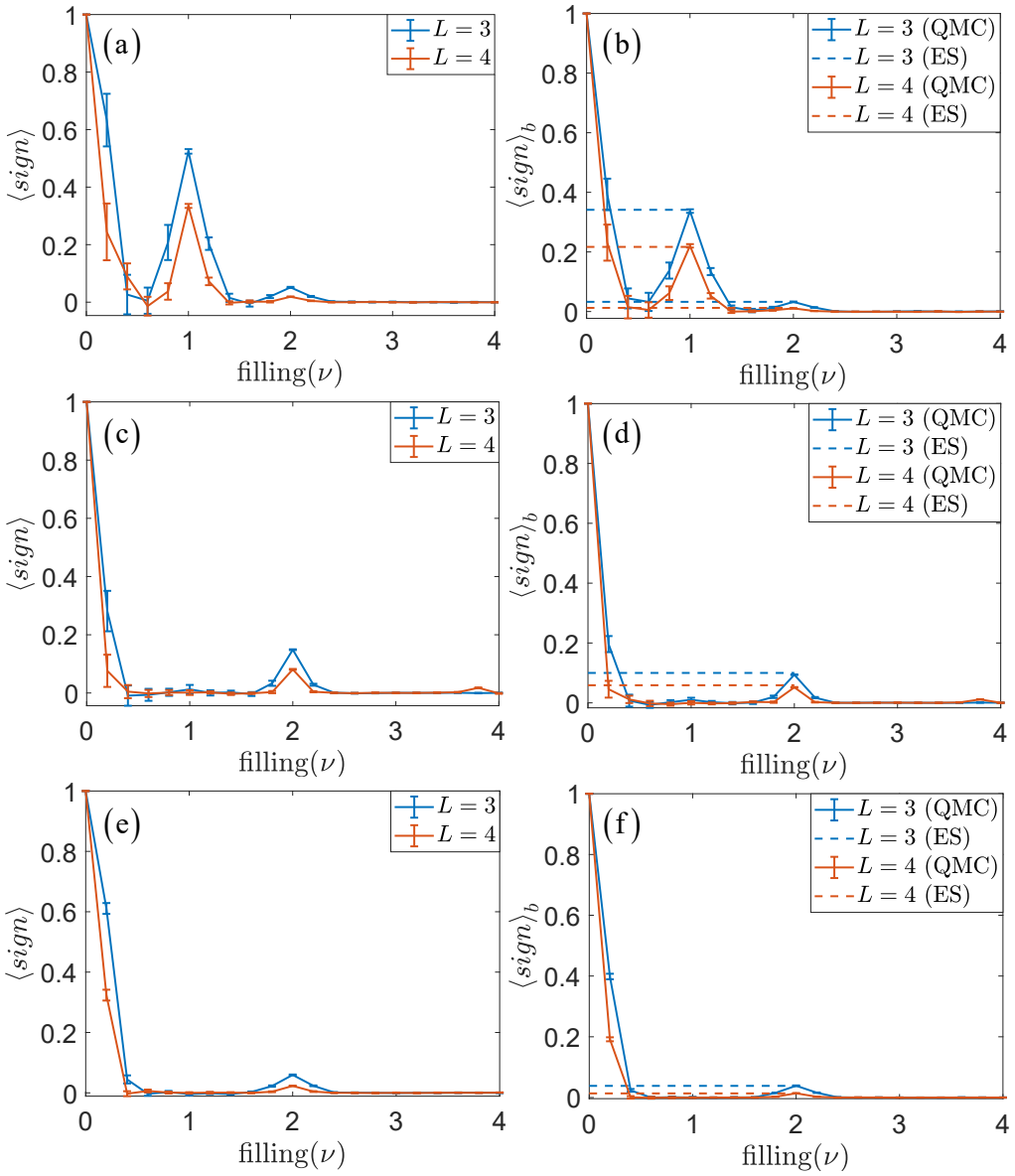


Figure 3.10: $\langle sign \rangle$ versus filling ν (a,c,e) and $\langle sign \rangle_b$ versus filling ν (b,d,f) at low temperature $T = 1meV$. The fillings of $\nu < 0$ are symmetric with respect to $\nu = 0$ via the particle-hole symmetry. (a-b) are the chiral limit $\gamma = 0$ cases, (c-d) are the non-chiral $\gamma = 0$ cases where we take $u_0 = 0.06eV$ and (e-f) are the chiral limit $\gamma = 4$ cases. (a,c,d) are the average sign $\langle sign \rangle$ for $L = 3(N_k = 9)$ and $L = 4(N_k = 16)$ measured from DQMC for filling from $\nu = 0$ to $\nu = 4$. (b,d,f) are the sign bounds $\langle sign \rangle_b$ for $L = 3(N_k = 9)$ and $L = 4(N_k = 16)$ measured from DQMC (solid line) and derived from exact solution (ES) at the low temperature limit for filling $\nu = 1, 2$ (dash line values). The ES values in (b) are 1119/3278, 3630/111493 for $L = 3$ at $\nu = 1, 2$ and 945/4357, 183/14912 for $L = 4$ at $\nu = 1, 2$. The ES values are 1/10 for $L = 3$, 1/17 for $L = 4$ at $\nu = 2$ in (d) and 100/2601 for $L = 3$, 71/5201 for $L = 4$ at $\nu = 2$ in (f). These figures come from Ref [2].

$\hat{N}_\pm$ are the fermion occupation number operators of $\pm$ Chern bands. The correlation function of this order parameter is plotted in Fig 3.11, $S \equiv \langle(\hat{N}_+ - \hat{N}_-)^2\rangle / N_k^2$, and scaling analysis reveals a second order phase transition at $T_c \sim 1.8meV$, below which the time-reversal symmetry is spontaneously broken, similar to what was observed at $\nu = 3$ effective models [19, 142, 143]. At low temperature, S approaches 1, indicating that the Chern number is $C = \pm 1$, instead of ± 3. In Fig 3.11(b), we rescale the y axis as $S \times L^{2\beta/\nu}$ using the 2D Ising exponents $\beta = 1/8$ and $\nu = 1$, and the cross point at $T_c \sim 1.8meV$ marks the critical temperature (see Appendix B).

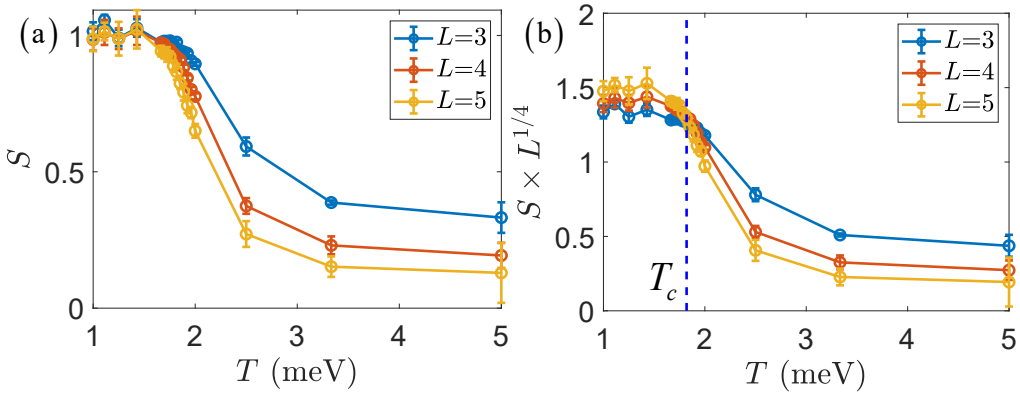


Figure 3.11: (a) Chern band polarization correlation function S versus T. At low temperature, the Chern number approaches to 1. (b) 2D Ising universality class crossing to determine the phase transition point at $T_c \sim 1.8meV$, denoted by the dashed line. These figures come from Ref [2].

Such a spontaneously generated Chern insulator is of both theoretical and experimental interesting as in the temperature range of $0 < T < T_c$, it only breaks the time reversal symmetry but not the spin-valley $U(4)$ continuous symmetry. In contrast to quantum Hall states, where fermion spins are polarized due to Zeeman splitting, spin degrees of freedom doesn't form any order in this TMI phase and the spin $SU(2)$ symmetry is preserved. To better demonstrate this point, we use the method introduced in the CNP case for computing excitation spectrum and analytically derive the results for single-particle and two-particle charge-neutral exciton excitations at $T = 0$. As shown in Fig 3.12(a), single particle excitations (red stars) are fully gaped, indicating an insulating state. To restore the time-reversal symmetry, it requires to move fermions from + Chern bands to - Chern bands (or vice versa). However, such particle-hole excitations are fully gapped (yellow stars in Fig 3.12(a)), and thus thermal fluctuations at low T cannot restore the time-reversal symmetry. In contrast, particle-hole excitations between spin-valley bands with the same Chern number (blue starts) are gapless. These excitons describe spin $SU(2)$ and spin-valley $SU(4)$ fluctuations, and any spin or spin-valley order would be destroyed by these gapless excitations at any finite temperature.

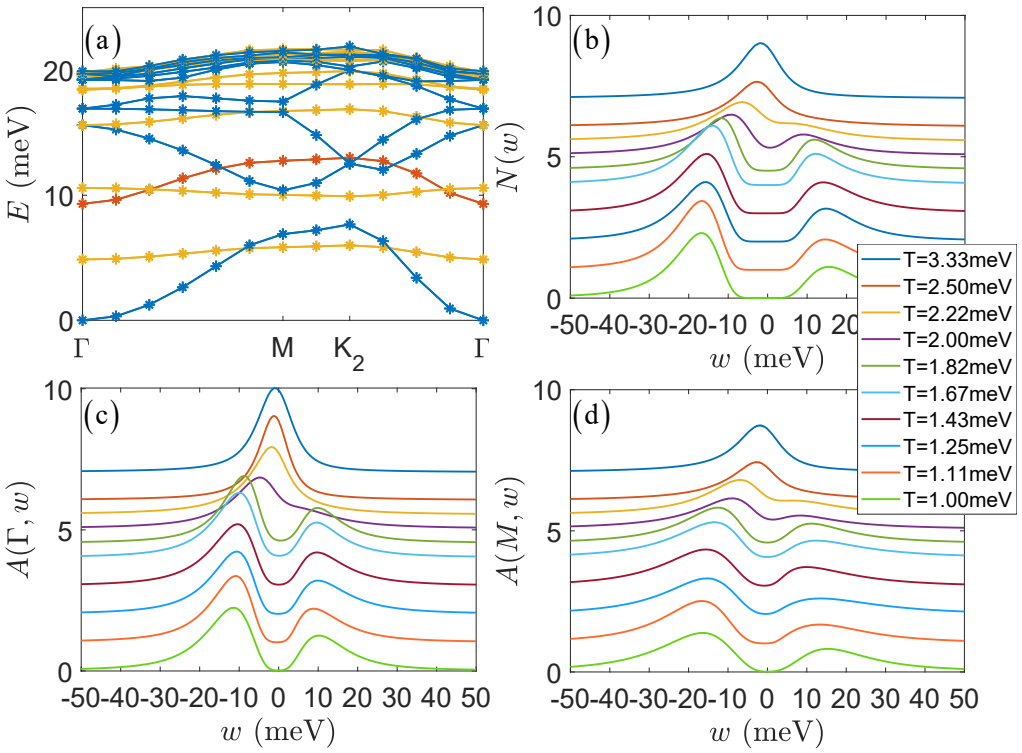


Figure 3.12: (a) Analytical excitation spectra along a high symmetry path in moiré BZ. The red line labels the single particle excitations. Blue lines show the 10 lowest charge neutral excitons between bands with the same Chern number. The yellow lines label the 10 lowest charge neutral excitons between opposite Chern bands, which are responsible to the restoration of time reversal symmetry. (b-d) Local density of states $N(\omega)$, the single particle spectra $A(\Gamma, \omega)$ and $A(M, \omega)$ obtained from the DQMC-SAC scheme as a function of T. Different lines are lifted in y direction with the amount of $\Delta\beta = \Delta(1/T)$ for clarity. Between the high temperature metal-like phase and the low temperature TMI phase, pseudogap behavior can be found at $T^\star \sim 2meV$ above $T_c = 1.8meV$. These figures come from Ref [2].

3.7 Further discussion

Finally, as the close of this chapter, I would like to mention some effort and development keep going on for this TBG system. For example, DQMC simulation on non-chiral non-CNP case [33], heavy-fermion picture interpretation [144–158] and strong magnetic field study [159–166]. While along the direction of the model I have studied, there is also some interesting directions.

As one can see, the derivation of sign structure at CNP has nothing to do with the twist angle or the C_3 breaking strain. This promises a numerical study of TBG with strain and twist angle perturbation near magic angle. By studying free energy or order parameter, one can identify the stability and possible phase transition there.

Another obvious possible project is to study the other cases listed in Tab 3.2 with all kinds of perturbations (e.g., finite temperature, non-chiral, non-flat bands). Though polynomial sign problem will also increase the complexity of simulation, this polynomial hard problem is considered to be much easier compared with the general exponential time costing sign problem cases.

One can see inspired by the amazing results in TBG system, some experiments on other twisted 2D materials are emerging such as the twisted transition metal dichalcogenides (TTMD) where fractional quantum anomalous Hall effect is reported [167–170]. As a starting point for TTMD study, I will introduce the TTMD system in the next chapter by using the similar methodology discussed in this chapter.

Chapter 4

Twisted transition metal dichalcogenides (TTMD)

4.1 Outline

In this chapter, I will introduce the similarity and difference between K valley and Γ valley TTMD. At flat-band limit and half filling, ground states and excitations are discussed with the method used in the last chapter. Besides, single-particle and gapless two-particle Green's function are also derived exactly. By assuming inter-valley attraction and $SU(2)$ limit, I have derived the bosonic fluid phase and its excitation spectra for K valley TTMD. DQMC is also used to identify the superconductor departing from $SU(2)$ limit by involving finite band dispersion. Finally, some recent developments about fractional quantum anomalous Hall observed in TTMD and further research directions are discussed.

4.2 K valley and Γ valley flat bands and half filling insulators

Besides the K valley flat bands in TBG, there are also K valley and Γ valley flat bands proposed for TTMD [171] based on the position of valence band top. For example, the twisted double layer WS_2 has the band top near Γ point [171] so that it has the Γ valley flat bands as shown in Fig 4.1(a). And the twisted double layer $MoTe_2$ has the band top near K points [172] so that it has the K valley flat bands as shown in Fig 4.1(b). Since there are two K points and one Γ in the Brillouin zone, there is an additional valley Z_2 for K valley TTMD. Different with TBG where spin-orbital coupling is small and spin is almost degenerate, K valley TTMD has spin-valley locking, i.e. spin $\uparrow$ electron band is on the top at one valley K then spin $\downarrow$ electron band must be the top band of the other valley. Γ valley TTMD also has weak spin-orbital coupling so that spin $SU(2)$ is there but the absence of Dirac dispersion also can make the story different.

In this section, I will introduce the continuous models describing Γ valley twisted double layer WS_2 and K valley twisted double layer $MoTe_2$. By identifying the flat

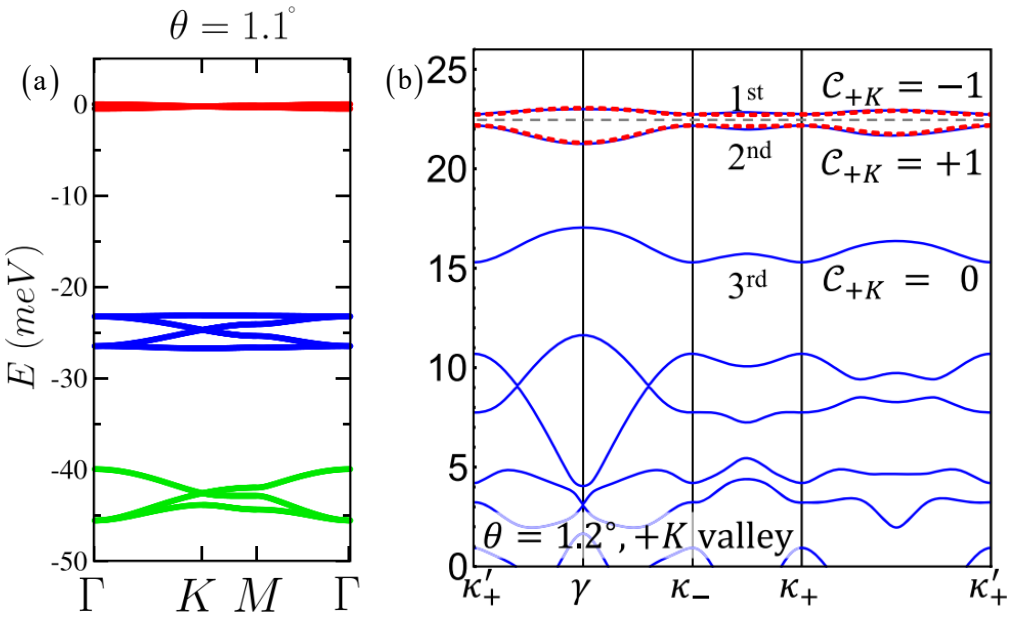


Figure 4.1: (a) Band structure of Γ valley TTMD 1.1° twisted WS_2. (b) Band structure of K valley 1.2° twisted $MoTe_2$. These figures come from Ref [171, 172].

band and band gap similarly as the TBG case, I will project the repulsive Coulomb interaction there at half filling and discuss the flat band limit ground state and the excitation above it. One step forward from the discussion in Chapter 3, I will also introduce how to derive the exact expression for single-particle and two-particle Green's function at low temperature limit.

4.2.1 Γ valley twisted double layer WS_2

First, let's consider Γ valley twisted double layer WS_2 model. Here the starting point is the quadratic dispersion with a C_6 moiré potential [171]

$$H = -\frac{\hbar^2 k^2}{2m^*} - \sum_s V_s \sum_{j=1}^{6} e^{ig_j^s \cdot r}. \tag{4.1}$$

Write it explicitly in plane wave basis after Fourier transformation

$$H(k) = -\sum_G \frac{\hbar^2 (k+G)^2}{2m^*} c_{k+G}^\dagger c_{k+G} - \sum_G \sum_s V_s \sum_{j=1}^{6} c_{k+G}^\dagger c_{k+G+g_j^s}. \tag{4.2}$$

Here we use parameter rotation angle $\theta = 1.2°$, scattering magnitude of moiré potential $V_1 = 33.5, V_2 = 4, V_3 = 5.5$, effective mass $m^* = 0.87m_e$ and lattice constant $a_0 = 0.318nm$ [171]. In the expression, s is used to label the scattering from sth nearest neighbor BZ [123], G, g_j^s mean reciprocal lattice vectors and s, j in g_j^s label s shell j direction moiré potential scattering.

After diagonalization the band dispersion is similar with 1.1° case in Fig 4.1. One can see there are two flat valence bands separated with remote bands. After projecting the same Coulomb interaction used in Chapter 3, keeping only flat band degree of freedom and ignore band dispersion, our interaction Hamiltonian is written as

$$\begin{aligned} H &= \frac{1}{2\Omega}\sum_{q,G} V(q+G)(\delta\rho_{q+G}\delta\rho_{-q-G}) \\ \delta\rho_{q+G} &= \sum_{k,m,n} \lambda_{m,n}\left(k,k+q+G\right)\left(c^{\dagger}_{k,m,s}c_{k+q,n,s}+c^{\dagger}_{k,m,-s}c_{k+q,n,-s}-\delta_{q,0}\delta_{m,n}\right) \\ &= \delta\rho^{\dagger}_{-q-G}. \end{aligned} \tag{4.3}$$

One can see there is no valley degree of freedom here and the coefficients before two spin terms are the same in $\delta\rho_{q+G}$ so that it is identity 2×2 matrix in spin subspace and there is an exact spin $SU(2)$. Again since the Hamiltonian is positive semi-definite, fully filling two flat bands within a single spin sector will be one of the zero energy ground state at half filling. Then one can compute the single-particle and two-particle charge-neutral excitation as discussed in Chapter 3. Alternatively, we would like to compute the exact form of single-particle and two-particle Green's function at low temperature limit by normalizing all ground states, single-particle excitation states and two-particle charge-neutral excitation states. The Green's function results can compare directly with the data from DQMC simulation and the same technique will be applied to K valley TTMD and attractive interaction induced inter-valley pairing superconductor later.

As the first step, we need to identify all the ground states and normalize them. One notices spin polarization (SP) is one of degenerated ground states since $\lambda_{m,m}(k,k)=1$ (the overlap of the same wavefunction is normalized) and $\delta\rho_{q+G}\left|\psi^{Full}_{-s}\right\rangle=0$. Then we can define a raising operator $\Delta^{\dagger}=\sum_{k,m}c^{\dagger}_{k,m,s}c_{k,m,-s}$ commutating with $\delta\rho_{q+G}$ as well as the Hamiltonian H so that $\left(\Delta^{\dagger}\right)^{n}\left|\psi^{Full}_{-s}\right\rangle$ is also a ground state ($n=0,1,2,\ldots,2N$). Now we derive all the $2N+1$ degenerate ground states coming from spin $SU(2)$ (we assume there are N momentum points with the Brillouin zone for a single band).

Single-particle Green's function at low temperature limit can be achieved by normalizing all ground states and single-particle states. First, $\left\langle\psi^{Full}_{-s}|\psi^{Full}_{-s}\right\rangle=1$ so that $\left|\psi^{Full}_{-s}\right\rangle$ is already normalized. Since

$$\begin{aligned} \left[\Delta,\Delta^{\dagger}\right] &= \sum_{k,m}\left(c^{\dagger}_{k,m,-s}c_{k,m,-s}-c^{\dagger}_{k,m,s}c_{k,m,s}\right)\equiv\hat{N}_{-s}-\hat{N}_{s} \\ &\quad \left\langle\psi^{Full}_{-s}\left|\Delta^{n}\left(\Delta^{\dagger}\right)^{n}\right|\psi^{Full}_{-s}\right\rangle \\ &= n(2N-n+1)\left\langle\psi^{Full}_{-s}\left|\Delta^{n-1}\left(\Delta^{\dagger}\right)^{n-1}\right|\psi^{Full}_{-s}\right\rangle \\ &= \frac{n!(2N)!}{(2N-n)!}, \end{aligned} \tag{4.4}$$

we can define normalized ground states

$$|\psi_n\rangle \equiv \sqrt{\frac{(2N-n)!}{n!(2N)!}} \left(\Delta^\dagger\right)^n \left|\psi_{-s}^{Full}\right\rangle . \tag{4.5}$$

For normalizing $c_{k,1,s}^\dagger \left(\Delta^\dagger\right)^n \left|\psi_{-s}^{Full}\right\rangle$, one notices $\Delta c_{k,1,s}^\dagger \left|\psi_{-s}^{Full}\right\rangle = 0$ so that

$$\begin{aligned} & \left\langle \psi_{-s}^{Full} \left| c_{k,1,s} \Delta^n \left(\Delta^\dagger\right)^n c_{k,1,s}^\dagger \right| \psi_{-s}^{Full} \right\rangle \\ = \; & n(2N-n) \left\langle \psi_{-s}^{Full} \left| c_{k,1,s} \Delta^{n-1} \left(\Delta^\dagger\right)^{n-1} c_{k,1,s}^\dagger \right| \psi_{-s}^{Full} \right\rangle \\ = \; & \frac{n!(2N-1)!}{(2N-1-n)!}. \end{aligned} \tag{4.6}$$

Then we can define normalized single-particle excitation states

$$\left|\psi_{n,k,1}\right\rangle \equiv \sqrt{\frac{(2N-1-n)!}{n!(2N-1)!}} c_{k,1,s}^\dagger \left(\Delta^\dagger\right)^n \left|\psi_{-s}^{Full}\right\rangle = \sqrt{\frac{2N}{2N-n}} c_{k,1,s}^\dagger \left|\psi_n\right\rangle . \tag{4.7}$$

At the same time, one also has the single-hole excitation states

$$\begin{aligned} & \left\langle \psi_{-s}^{Full} \left| \Delta^n c_{k,1,s}^\dagger c_{k,1,s} \left(\Delta^\dagger\right)^n \right| \psi_{-s}^{Full} \right\rangle \\ = \; & \left\langle \psi_{-s}^{Full} \left| \Delta^n \left(\Delta^\dagger\right)^n \right| \psi_{-s}^{Full} \right\rangle - \left\langle \psi_{-s}^{Full} \left| c_{k,1,s} \Delta^n \left(\Delta^\dagger\right)^n c_{k,1,s}^\dagger \right| \psi_{-s}^{Full} \right\rangle \\ = \; & \frac{n!(2N)!}{(2N-n)!} - \frac{n!(2N-1)!}{(2N-1-n)!} = \frac{n!(2N-1)!}{(2N-1-n)!} \left(\frac{n}{2N-n}\right) \end{aligned} \tag{4.8}$$

so that we can define normalized single-hole excitation states

$$\left|\psi_{n,k,-1}\right\rangle \equiv \sqrt{\frac{(2N-1-n)!(2N-n)}{n!(2N-1)!n}} c_{k,1,s} \left(\Delta^\dagger\right)^n \left|\psi_{-s}^{Full}\right\rangle = \sqrt{\frac{2N}{n}} c_{k,1,s} \left|\psi_n\right\rangle . \tag{4.9}$$

Now we are ready to derive single-particle Green's function at low temperature limit

$$\begin{aligned} G_{k,1,s}(t) = \left\langle c_{k,1,s}(t) c_{k,1,s}^\dagger(0) \right\rangle &= \frac{\mathrm{Tr}\left(e^{-(\beta-t)H} c_{k,1,s} e^{-tH} c_{k,1,s}^\dagger\right)}{\mathrm{Tr}\left(e^{-\beta H}\right)} \\ \overset{\lim}{\beta\to\infty} \; & \frac{1}{2N+1} \left[\sum_n e^{-t\varepsilon_{k,1}} \left|\left\langle c_{k,1,s}^\dagger \psi_n \middle| \psi_{n,k,1} \right\rangle\right|^2 + \sum_n e^{-(\beta-t)\varepsilon_{k,-1}} \left|\left\langle \psi_{n,k,-1} \middle| c_{k,1,s} \psi_n \right\rangle\right|^2\right] \\ = \; & \frac{1}{2N+1} \left[e^{-t\varepsilon_{k,1}} \sum_n \frac{2N-n}{2N} + e^{-(\beta-t)\varepsilon_{k,-1}} \sum_n \frac{n}{2N}\right] \\ = \; & \frac{1}{2} e^{-t\varepsilon_{k,1}} + \frac{1}{2} e^{-(\beta-t)\varepsilon_{k,-1}}. \end{aligned} \tag{4.10}$$

Here $\varepsilon_{k,1}, \varepsilon_{k,-1}$ label single-particle and single-hole excitation energy above ground state. One can see the result is just two branches of exponential decay from $t = 0$ and $t = \beta$ with the exponents corresponding to single-particle and single-hole excitation energy.

Then we turn to two-particle Green's function for the Goldstone mode detection. For 2D system, we know spin $SU(2)$ symmetry cannot spontaneously break so that there should be no magnetism, but magnet susceptibility can be finite at finite temperature and diverge at $\beta \to \infty$. According to spin $SU(2)$ symmetry, we define order parameters $O_{x,q}, O_{z,q}$ as below to detect the susceptibility and Goldstone modes

$$\begin{aligned} O_{x,q} &\equiv \sum_{k,m} \left(c^{\dagger}_{k,m,s} c_{k+q,m,-s} + c^{\dagger}_{k,m,-s} c_{k+q,m,s} \right) \\ O_{z,q} &\equiv \sum_{k,m} \left(c^{\dagger}_{k,m,s} c_{k+q,m,s} - c^{\dagger}_{k,m,-s} c_{k+q,m,-s} \right) \end{aligned} \tag{4.11}$$

We discuss this part according to $q \neq 0$ and $q = 0$ two cases.

For $q \neq 0$, the excitation spectra can be computed by the commutation with Hamiltonian H as discussed in Chapter 3, and one can compute the momentum dispersion as shown in Fig 4.2 where $O_{x,q}, O_{z,q}$ excitation spectra are the same as they should be. Here the blue line represents the lowest 10 $c^{\dagger}_{k,m_1,s_1} c_{k+p,n_1,s_2}$ excitations with momentum p and red line represents single-particle excitations with momentum p. Contrast with TBG at chiral limit with neutral filling, one can see different p all have almost zero-energy excitations (Fig 4.2(b)). This result comes from $\lambda_{m,n}(k+p, k+p+q+G) \approx \lambda_{m,n}(k, k+q+G)$, which is the result we only fold one band to form moiré flat band and wavefunctions of this band are very similar at small moiré dispersion region.

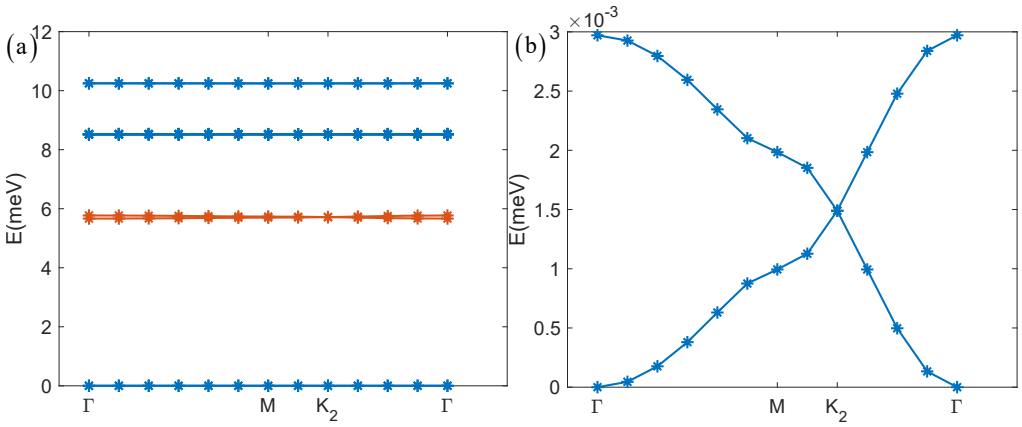


Figure 4.2: (a) Excitation spectra of Γ valley TTMD 1.2° twisted WS_2 where red lines label single-particle excitations and blue lines label two-particle charge-neutral excitations. (b) Zoom in for the two lowest lines in (a) where a soft Goldstone mode can be observed.

When $q = 0$, one can check $[O_{x,0}, H] = [O_{z,0}, H] = 0$ so that there is no imaginary-time decay for $O_{x,0}, O_{z,0}$ excitation. By noticing commutation relation $\left[O_{x,0}, \Delta^{\dagger}\right] = -O_{z,0} = \hat{N}_{-s} - \hat{N}_s$, we can normalize state $O_{x,0} \left(\Delta^{\dagger}\right)^n \left|\psi^{Full}_{-s}\right\rangle = n(2N-n+1) \left(\Delta^{\dagger}\right)^{n-1} \left|\psi^{Full}_{-s}\right\rangle + \left(\Delta^{\dagger}\right)^{n+1} \left|\psi^{Full}_{-s}\right\rangle$. That will be $O_{x,0} \left|\psi_n\right\rangle = \sqrt{n(2N-n+1)} \left|\psi_{n-1}\right\rangle + \sqrt{(n+1)(2N-n)} \left|\psi_{n+1}\right\rangle$. Combine all results above, we can see the excitation defined by $O_{x,0}$ at low temperature

limit should be

$$\begin{aligned} & \langle O_{x,0}(t)O_{x,0}(0)\rangle \\ = \quad & \langle O_{x,0}(0)O_{x,0}(0)\rangle \\ = \quad & \frac{\mathrm{Tr}\left(e^{-\beta H}O_{x,0}O_{x,0}\right)}{\mathrm{Tr}\left(e^{-\beta H}\right)} \\ \overset{\lim}{=} \quad & \frac{1}{2N+1}\sum_n \langle\psi_n|O_{x,0}O_{x,0}|\psi_n\rangle \\ = \quad & \frac{2}{2N+1}\sum_n n(2N-n+1) \\ = \quad & \frac{2N(2N+2)}{3} \end{aligned} \tag{4.12}$$

At the same time, $\langle O_{z,0}(t)O_{z,0}(0)\rangle$ at low temperature limit can also be easily calculated

$$\begin{aligned} & \langle O_{z,0}(t)O_{z,0}(0)\rangle \\ = \quad & \langle O_{z,0}(0)O_{z,0}(0)\rangle \\ = \quad & \frac{\mathrm{Tr}\left(e^{-\beta H}O_{z,0}O_{z,0}\right)}{\mathrm{Tr}\left(e^{-\beta H}\right)} \\ \overset{\lim}{=} \quad & \frac{1}{2N+1}\sum_n (2N-2n)^2 \\ = \quad & \frac{2N(2N+2)}{3} \end{aligned} \tag{4.13}$$

One can see $\langle O_{x,0}(t)O_{x,0}(0)\rangle = \langle O_{z,0}(t)O_{z,0}(0)\rangle$ and both do not decay with t, which should be a natural result from $SU(2)$ symmetry.

4.2.2 K valley twisted double layer $MoTe_2$

We consider twisted double layer $MoTe_2$ model as the example of K valley. Here the starting point is the quadratic dispersion with a C_3 moiré potential at valley + [172, 173].

$$\begin{aligned} H^+(k,r) &= \begin{pmatrix} -\frac{\hbar^2(k-K_b)^2}{2m^*}+\Delta_b(r) & \Delta_T(r) \\ \Delta_T^\dagger(r) & -\frac{\hbar^2(k-K_t)^2}{2m^*}+\Delta_t(r) \end{pmatrix} \\ \Delta_l(r) &= 2w_z\sum_{j=1,3,5}\cos\left(G_j\cdot r+l\psi\right),\ l\in\{b,t\}=\{+1,-1\} \\ \Delta_T(r) &= w\left(1+e^{-iG_2\cdot r}+e^{-iG_3\cdot r}\right) \end{aligned} \tag{4.14}$$

Here, we use the same G_j as the TBG case in Chapter 3. Subscript t, b are used to identify top and bottom layer $MoTe_2$. Contrast to TBG case, there is no sublattice label and the dispersion becomes quadratic. We take parameters $\left(\frac{\hbar^2}{2m^*a_0^2},\ w_z, w, \psi, \theta\right) = (495meV,\ 8meV,\ -8.5meV,\ -89.6°, 1.2°)$. After Fourier transformation, the energy

dispersion is plotted as Fig 4.1(b).

Next, we project Coulomb interaction on the top-most two bands and assume flat band limit at half filling. The Hamiltonian now is

$$\begin{aligned} H &= \frac{1}{2\Omega}\sum_{q,G} V(q+G)\delta\rho_{q+G}\delta\rho_{-q-G} \\ \delta\rho_{q+G} &= \sum_{k,m,n,\tau} \lambda_{\tau;m,n}(k,k+q+G)\left(c^\dagger_{k,m,\tau}c_{k+q,n,\tau} - \frac{1}{2}\delta_{q,0}\delta_{m,n}\right) = \delta\rho^\dagger_{-q-G} \end{aligned} \tag{4.15}$$

By noticing a particle-hole symmetry, we can rewrite particle operator at valley $-\tau$ as hole operator

$$\begin{aligned} \delta\rho_{-\tau;q+G} &= \sum_{k,m,n} \lambda_{-\tau;m,n}(k,k+q+G)\left(c^\dagger_{k,m,-\tau}c_{k+q,n,-\tau} - \frac{1}{2}\delta_{q,0}\delta_{m,n}\right) \\ &= -\sum_{k,m,n} \lambda_{\tau;n,m}(k,k+q+G)\left(c_{-k,n,-\tau}c^\dagger_{-k-q,m,-\tau} - \frac{1}{2}\delta_{q,0}\delta_{m,n}\right) \\ &= -\sum_{k,m,n} \lambda_{\tau;n,m}(k,k+q+G)\left(\tilde{c}^\dagger_{k,n,-\tau}\tilde{c}_{k+q,m,-\tau} - \frac{1}{2}\delta_{q,0}\delta_{m,n}\right) \end{aligned} \tag{4.16}$$

Here we redefine $\tilde{c}^\dagger_{k,n,-\tau} = c_{-k,n,-\tau}$ so that

$$\delta\rho_{q+G} = \sum_{k,m,n} \lambda_{\tau;m,n}(k,k+q+G)\left(c^\dagger_{k,m,\tau}c_{k+q,n,\tau} - \tilde{c}^\dagger_{k,m,-\tau}\tilde{c}_{k+q,n,-\tau}\right) \tag{4.17}$$

One can see contrast with the case for Γ valley where there is a spin $SU(2)$ symmetry, K valley degree of freedom forms a valley σ_z but not σ_0 so that there is only a valley Z_2 symmetry here. From $\delta\rho_{q+G} = \sum_{k,m,n} \lambda_{\tau;m,n}(k,k+q+G)\left(c^\dagger_{k,m,\tau}c_{k+q,n,\tau} - \tilde{c}^\dagger_{k,m,-\tau}\tilde{c}_{k+q,n,-\tau}\right)$, we can easily find these two degenerate zero-energy eigenstates $\left|\psi^{Full}_\tau\right\rangle \bigotimes \left|\tilde{\psi}^{Full}_{-\tau}\right\rangle$ and $\left|\psi^{Empty}_\tau\right\rangle \bigotimes \left|\tilde{\psi}^{Empty}_{-\tau}\right\rangle$. If one translates $\tilde{c}^\dagger_{k,n,-\tau}$ back to $c_{-k,n,-\tau}$, these are two valley-polarized (and also spin-polarized because of spin-valley locking) ground states $\left|\psi^{Full}_\tau\right\rangle \bigotimes \left|\psi^{Empty}_{-\tau}\right\rangle$ and $\left|\psi^{Empty}_\tau\right\rangle \bigotimes \left|\psi^{Full}_{-\tau}\right\rangle$. One can see the energy for exciting a particle at valley τ on state $\left|\psi^{Empty}_\tau\right\rangle \bigotimes \left|\psi^{Full}_{-\tau}\right\rangle$ is equal to the energy for exciting a particle from empty, which can be achieved by diagonalizing H_τ in single-particle basis

$$H_\tau = \frac{1}{2\Omega}\sum_{q,G} V(q+G) \sum_{k,m,n,n'} \lambda_{\tau;m,n'}(k,k+q+G)\lambda_{\tau;n',n}(k+q+G,k)c^\dagger_{k,m,\tau}c_{k,n,\tau}. \tag{4.18}$$

While excite a particle at valley $-\tau$ on state $\left|\psi_{\tau}^{Full}\right\rangle \bigotimes \left|\psi_{-\tau}^{Empty}\right\rangle$ can be achieved by diagonalizing $H_{-\tau}$

$$\begin{aligned} H_{-\tau} &= \frac{1}{2\Omega}\sum_{q,G} V(q+G) \sum_{k,m,n,n'} \lambda_{-\tau;m,n'}(k,k+q+G)\lambda_{-\tau;n',n}(k+q+G,k)c^{\dagger}_{k,m,-\tau}c_{k,n,-\tau} \\ &= \frac{1}{2\Omega}\sum_{q,G} V(q+G) \sum_{k,m,n,n'} \lambda_{\tau;n,n'}(k,k+q+G)\lambda_{\tau;n',m}(k+q+G,k)c^{\dagger}_{-k,m,-\tau}c_{-k,n,-\tau}. \end{aligned} \tag{4.19}$$

This means single-particle excitation $\varepsilon_{k,\tau,1} = \varepsilon_{-k,-\tau,1}$. Besides, one should notice there is another local C_{2z} rotation symmetry for $H^{+}(k,r)$. This rotation center is at middle point between K_b and K_t and one should also interchange two layers $H^{+}(k,r) = \sigma_x H^{+}(-k,-r)\sigma_x$. According to this rotation, $\lambda_{\tau;m,n}(k,k+q+G) = \lambda_{\tau;m,n}(-k,-k-q-G)$ after choosing a homogenous gauge. Finally, we conclude single particle excitation energy $\varepsilon_{k,\tau,1} = \varepsilon_{-k,\tau,1} = \varepsilon_{k,-\tau,1} = \varepsilon_{-k,-\tau,1} \equiv \varepsilon_{k,1}$. We plot $\varepsilon_{k,1}$ $\varepsilon_{k,2}$ for different momentum point k in Fig 4.3(a).

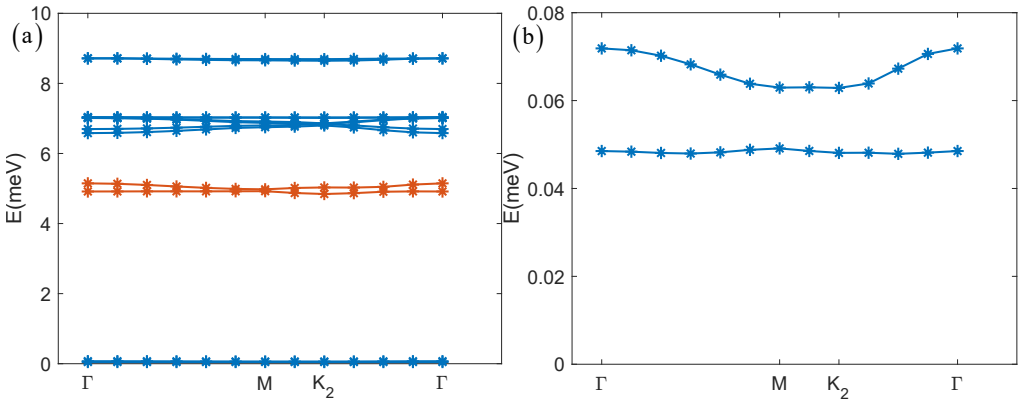


Figure 4.3: (a) Excitation spectra of K valley TTMD 1.2° twisted $MoTe_2$ where red lines label single-particle excitations and blue lines label two-particle charge-neutral excitations. (b) Zoom in for the two lowest lines in (a) where a gap can be observed.

Similar with the discussion in Γ valley section, single-particle Green's function at low temperature limit is easy to achieve

$$\begin{aligned} G_{k,1,\tau}(t) &= \left\langle c_{k,1,\tau}(t)c^{\dagger}_{k,1,\tau}(0)\right\rangle = \frac{\mathrm{Tr}\left(e^{-(\beta-t)H}c_{k,1,\tau}e^{-tH}c^{\dagger}_{k,1,\tau}\right)}{\mathrm{Tr}\left(e^{-\beta H}\right)} \\ &\overset{\lim}{\beta\to\infty} \frac{1}{2}\left[e^{-t\varepsilon_{k,1}}\left|\left\langle c^{\dagger}_{k,1,\tau}\psi^{Empty}_{\tau}\middle|\psi_{\tau,k,1}\right\rangle\right|^2 + e^{-(\beta-t)\varepsilon_{k,1}}\left|\left\langle \psi_{\tau,k,-1}\middle|c_{k,1,s}\psi^{Full}_{\tau}\right\rangle\right|^2\right] \\ &= \frac{1}{2}e^{-t\varepsilon_{k,1}} + \frac{1}{2}e^{-(\beta-t)\varepsilon_{k,1}} \end{aligned} \tag{4.20}$$

One can see even though the symmetry and ground state degeneracy are different, the form of single-particle Green's function for K valley is the same with the Γ valley case.

Different with Γ valley, this Z_2 discrete symmetry can be spontaneously broken with finite temperature fluctuation (e.g., 2D Ising) so that VP (or SP) should be the true long-range order at finite temperature. And $O_{x,q}, O_{z,q}$ defined below will give totally different results because of lacking $SU(2)$.

$$\begin{aligned} O_{x,q} &= \sum_{k,m} \left(c^{\dagger}_{k,m,\tau} c_{k+q,m,-\tau} + c^{\dagger}_{k,m,-\tau} c_{k+q,m,\tau} \right) \\ O_{z,q} &= \sum_{k,m} \left(c^{\dagger}_{k,m,\tau} c_{k+q,m,\tau} - c^{\dagger}_{k,m,-\tau} c_{k+q,m,-\tau} \right) \end{aligned} \tag{4.21}$$

We also discuss this part according to $q = 0$ and $q \neq 0$ two cases.

For $q = 0$, $[O_{z,0}, \delta\rho_{q+G}] = 0$ so that

$$\begin{aligned} & \langle O_{z,0}(t) O_{z,0}(0) \rangle \\ = \; & \langle O_{z,0}(0) O_{z,0}(0) \rangle \\ = \; & \frac{\mathrm{Tr}\left(e^{-\beta H} O_{z,0} O_{z,0} \right)}{\mathrm{Tr}\left(e^{-\beta H} \right)} \\ \overset{\lim}{\underset{\beta\to\infty}{=}} \; & \frac{1}{2} \, 2(2N)^2 \\ = \; & 4N^2 \end{aligned} \tag{4.22}$$

This value has N^2 power means the spectrum for $O_{z,q}$ excitation should have zero point at momentum $q = 0$ and the absence of Goldstone mode indicates it is gapped elsewhere for $q \neq 0$. While $[O_{x,0}, \delta\rho_{q+G}] \neq 0$ and $\langle O_{x,0}(t) O_{x,0}(0) \rangle$ is gapped everywhere and will decay exponentially with t or $\beta - t$.

For $q \neq 0$, one can compute the commutation relation with the Hamiltonian and derive the corresponding excitation spectra as I introduced in Chapter 3. The result is shown in Fig 4.3. Here the blue line represents the lowest 10 $c^{\dagger}_{k,m_1,\tau} c_{k+p,n_1,-\tau}$ excitations with momentum p and red line represents single-particle excitations with momentum p. One can see two-particle charge-neutral excitation is gapped and the gap is much smaller than single-particle gap.

As the conclusion of this K valley and Γ valley TTMD with half filling two top valence bands and taking flat band limit discussion, I will list their differences below.

For Γ valley case, there is a spin $SU(2)$ symmetry and ground states are $2N + 1$ ferromagnetic spin degenerate states. Single-particle excitation is gapped and there is no charge-gapless excitation so that it is an insulator. Because of $SU(2)$ continuous symmetry it has gapless Goldstone mode while it will not form an order at finite temperature.

For K valley case, there is a valley (or spin) Z_2 symmetry and ground states are 2 ferromagnetic degenerate states. Single-particle excitation is gapped and there is no charge-gapless excitation so that it is an insulator. Because of Z_2 discrete symmetry it

has no gapless Goldstone mode. However, the Z_2-breaking excitation energy is much smaller than single-particle gap so that the Ising-ferromagnetic ground state can only be realized in very low temperature which means this ferromagnetism is not stable under perturbation.

4.3 Inter-valley attraction and superconductor near $SU(2)$ limit

Since in the model above, pure Coulomb cannot induce superconductor, we turn to what universal principles/properties that flat-band moiré superconductors shall obey/exhibit, by introducing an artificial inter-valley attractive interaction in K valley TTMD and study its nontrivial consequence. By matching inter-valley attraction strength with intra-valley repulsion, we find that at the flat band limit, such systems have pair-density $SU(2)$ symmetry and can be solved exactly. Away from the flat-band limit, although an exact solution is absent, the model can be simulated via the momentum-space DQMC as I introduced in Chapter 2 and Chapter 3 without suffering the sign problem at any fillings, with a similar reason of attractive Hubbard model [174–178]. By combining exact analytic solution and momentum-space DQMC, we show that moiré flat-band superconductors exhibit a rich phase diagram, in sharply contrast to conventional BCS superconductors. As shown in Fig 4.4(a-b), at the temperature above the superconducting dome, the system doesn't directly transform into a Fermi liquid. Instead, it first turns into a super-compressible bosonic fluid (SCBF) phase, where fermionic excitations are fully gapped but the compressibility is high and increases/diverges upon cooling. This physics is analogy to the flat-band attractive Hubbard model [179, 180], but also with clear differences. In the flat-band Hubbard model, the same type of physics only arises when the interactions are strictly on-site, and non-onsite interactions, such as nearest-neighbor, quickly leads to other physics, e.g., phase separation [180]. In contrast, for moiré flat bands, our studies indicate that the exactly solution and related phenomena are extremely robust and fully insensitive to such microscopic details. No matter the interaction is short-range or longe-range and no matter spin-orbit coupling is weak (e.g. TBG) or strong (TTMD), our exact solution and all qualitative features remain the same. This robustness is of crucial important for experimental study of moiré lattices, where on-site interaction are not expected to be dominant and spin-orbit effect may or may not be strong depending on the materials. As one further increases the temperature, this bosonic fluid gives its way to a pseudogap (PG) phase, where fermion states start to emerge inside the gap and gradually fill it up upon increasing the temperature. These nontrivial sequence of phase transitions/crossovers arise at filling range larger than superconducting dome and survive to temperature much higher than the superconducting transition T_c.

The bosonic fluid phase can be viewed as a liquid of Cooper pairs, where although the Cooper pairs have fully formed, (quasi)-long-range phase coherence has not yet been developed due to strong fluctuations. Experimentally, key signature of this phase is

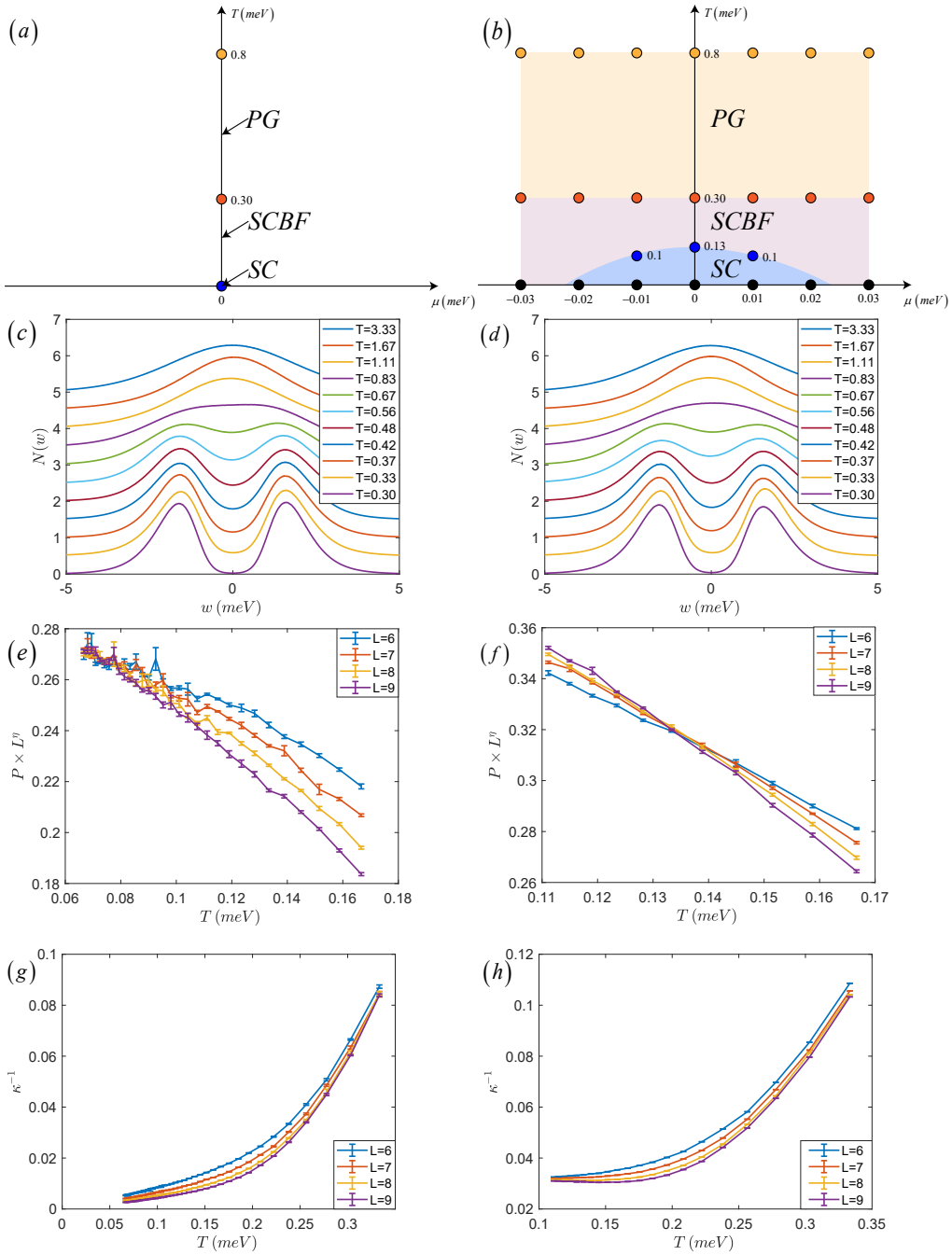


Figure 4.4: DQMC simulations of the flat-band limit (left column) and away from the flat-band limit (right column). The bandwidths of non-interacting band structures are set to 0 and $0.8meV$ respectively. (a-b) Phase diagrams. In the flat-band limit (a), a finite chemical potential drives the system into a trivial insulator with either empty ($\mu \ll 0$) or complete filled ($\mu \gg 0$) bands. In (b), the yellow/purple region is the pseudogap (PG)/ super-compressible bosonic fluid (SCBF) phase, and the blue region marks the superconducting (SC) dome. (c-d) Density of states for a 9×9 system at $\mu = 0$. The Cooper gap survives above the superconducting transition temperature and turns into a pseudogap above $T \sim 0.3$ for both flat-band limit (c) and finite band dispersion (d). The single-particle spectrum is almost determined by the strength of interaction since the band dispersion is small. (e-f) Critical scaling of $P \times L^{\eta}$ versus T with BKT anomalous dimension $\eta = 1/4$. The crossing point of different system sizes ($L = 6, 7, 8, 9$) marks the superconducting transition temperature: $T_c \sim 0$ in (e) and ~ 0.13 in (f). (g-h) Inverse of compressibility κ for $L = 6, 7, 8, 9$ at $\mu = 0$. At low temperature, diverged compressibility κ in (g) converges in superconducting phase as shown in (h). These figures come from Ref [7].

a large single-particle gap around the Fermi energy, combined with a high/diverging compressibility. The pseudogap phase is a partially melted boson liquid, where thermal fluctuations start to tear apart some Cooper pairs , feeding single fermion spectral weight into the energy gap.

Simulations and analytic theory also indicate that the crossover temperatures between normal fluid and the pseudogap phase (or between the pseudogap and the bosonic fluid phases) are dictated by the energy scale of the inter-valley attractions, and is nearly independent of filling levels or flat-band band width. In contrast, the superconducting transition temperature depends strongly on the bandwidth of the flat band, as well as filling fractions. In the DQMC simulations, a superconducting dome is observed, qualitatively consistent with the experimental observations in TBG and TTMD systems with chemical potential partially filling all flat bands [53, 181–183].

To begin our discussion, we consider a generic system with two valleys, labeled by the valley index τ and $-\tau$. In the flat-band limit, kinetic energy can be dropped once other bands are projected out. For interactions, we define it in the momentum space as

$$H_I = \frac{1}{2\Omega}\sum_{q,G} V(q+G)\delta\rho_{q+G}\delta\rho_{-q-G}, \tag{4.23}$$

We set the interaction strength $V(q+G)$ to be an arbitrary positive function (e.g., the same screened Coulomb repulsion used in Chapter 3) and $\delta\rho_{q+G}$ is the density difference between two valleys

$$\delta\rho_{q+G} = \rho_{\tau;q+G} - \rho_{-\tau;q+G}. \tag{4.24}$$

where ρ_τ and $\rho_{-\tau}$ are the fermion density from the two valleys. In band basis, $\delta\rho$ can be projected to the flat band

$$\begin{aligned}\delta\rho_{q+G} &= \sum_{k,m,n} [\lambda_{\tau;m,n}(k,k+q+G)c^\dagger_{k,m,\tau}c_{k+q,n,\tau} \\ &- \lambda_{-\tau;m,n}(k,k+q+G)c^\dagger_{k,m,-\tau}c_{k+q,n,-\tau}]\end{aligned} \tag{4.25}$$

This interaction contains inter-valley attraction and intra-valley repulsion with the same strength V, and this is how inter-valley attractions are introduced in our model. With this interaction, this model is exactly solvable in the flat-band limit, while away from the exactly-solvable limit (i.e. with finite band width and chemical potential), it can be simulated via DQMC without sign problem.

Here we introduce the exact solution result. The idea is the same as the $SU(2)$ and raising operator trick for Green's function in last Γ valley TTMD section. After dropping the trivial kinetic energy, the flat-band limit of our Hamiltonian is reduced to $H = H_I$, which can be solved according to an emergent $SU(2)$ symmetry with generators

$$\sigma_x = \Delta + \Delta^\dagger, \sigma_y = i(\Delta - \Delta^\dagger), \sigma_z = \hat{N}_p - N_d, \tag{4.26}$$

where $\Delta^\dagger = \sum_{k,m} c^\dagger_{k,m,\tau} c^\dagger_{-k,m,-\tau}$ and $\Delta = \sum_{k,m} c_{-k,m,-\tau} c_{k,m,\tau}$ creates/annihilates one inter-valley Cooper pair and $\hat{N}_p$ is the particle number operator of flat bands. The constant N_d is the max electron number that these flat bands can host in one valley. It is easy to verify that these three operators obey the su(2) algebra $[\sigma_i, \sigma_j] = 2i\epsilon_{ijk}\sigma_k$ and they all commute with $\delta\rho$ and H_I, $[\sigma_i, H_I] = 0$. In other words, these three operators generate an $SU(2)$ symmetry group.

Because our Hamiltonian is semi-positive definite, two obvious zero-energy ground states can be immediately identified: the empty and fully filled states labeled by $|\psi_0\rangle$ and $|\psi_{2N_d}\rangle$, where $\delta\rho\,|\psi_0\rangle = \delta\rho\,|\psi_{2N_d}\rangle = 0$. In terms of the $SU(2)$ symmetry group, these two states are fully polarized states of the σ_z operator, known as the highest weight states, where the eigenvalues of σ_z reach the highest/lowest possible values $\pm N_d$. Due to the $SU(2)$ symmetry, any $SU(2)$ rotation of these two ground states must also be a degenerate ground state. Here, we use $\Delta^\dagger$ and Δ as raising and lowering operators of the su(2) algebra, and generate all the normalized degenerate ground states from the empty state $|0\rangle \equiv |\psi_0\rangle$

$$|\psi_{2n}\rangle \equiv \sqrt{\frac{(N_d-n)!}{n!(N_d)!}}(\Delta^\dagger)^n\,|0\rangle\,, \tag{4.27}$$

where $0 \le n \le N_d$ and $|\psi_{2n}\rangle$ is the degenerate ground state with $2n$ fermions. Another way to understand these degenerate ground states is to realize $[H_I, \Delta^\dagger] = 0$ implies that it costs no energy to create a Cooper pair. Thus, we can introduce arbitrary number of Cooper pairs to the empty state, and obtain a degenerate ground state $|\psi_{2n}\rangle$ with n Cooper pairs. It is worthwhile to highlight that the BCS wavefunction $\psi_{BCS} = \frac{1}{\mathcal{N}}\exp(\frac{v}{u}\Delta^\dagger)\,|0\rangle$ is also an exact ground state of this model. But this state is nothing special and just one of N_d+1 degenerate ground states. The BCS wavefunction may not be favored when kinetic term and chemical potential is introduced, since chemical potential term will favor a certain filling but not mixing states with different particle number.

In the exact solution, single-particle and Cooper pair Green's function can be computed by noticing $|\psi_{2n}\rangle = \sqrt{\frac{(N_d-n)!}{n!N_d!}}(\Delta^\dagger)^n\,|0\rangle$, $|\psi_{2n+1,k,\tau}\rangle = \sqrt{\frac{(N_d-n-1)!}{n!(N_d-1)!}}(\Delta^\dagger)^n c^\dagger_{k,\tau}\,|0\rangle$, and $c^\dagger_{k,\tau}\,|\psi_{2n}\rangle = \sqrt{\frac{N_d-n}{N_d}}\,|\psi_{2n+1,k,\tau}\rangle$, $c_{k,\tau}\,|\psi_{2n}\rangle = \sqrt{\frac{n}{N_d}}\,|\psi_{2n-1,-k,-\tau}\rangle$, and $\Delta^\dagger\,|\psi_{2n}\rangle = \sqrt{(N_d-n)(n+1)}\,|\psi_{2n+2}\rangle$. Here $|\psi_{2n}\rangle$ and $|\psi_{2n\pm1,k,\tau}\rangle$ are normalized eigenstates with $2n$ and $2n\pm1$ electrons. According to those normalization relations, we can derive

single-particle Green's function at zero temperature limit

$$\begin{aligned} G_{k,\tau}(t) &= \frac{\mathrm{Tr}(e^{-(\beta-t)H_I}c_{k,\tau}e^{-tH_I}c_{k,\tau}^\dagger)}{\mathrm{Tr}(e^{-\beta H_I})} \\ &\overset{\lim}{\underset{\beta\to\infty}{=}} \frac{1}{N_d+1}\Big[\sum_{n=0}^{N_d-1} e^{-t\varepsilon_{k,\tau}}\left|\left\langle c_{k,\tau}^\dagger\psi_{2n}|\psi_{2n+1,k,\tau}\right\rangle\right|^2 \\ &\quad + \sum_{n=1}^{N_d} e^{-(\beta-t)\varepsilon_{k,\tau}}\left|\left\langle\psi_{2n-1,-k,-\tau}|c_{k,\tau}\psi_{2n}\right\rangle\right|^2\Big] \\ &= \frac{1}{2}\left[e^{-t\varepsilon_{k,\tau}}+e^{-(\beta-t)\varepsilon_{k,\tau}}\right]. \end{aligned} \tag{4.28}$$

Besides, we can also exactly derive Green's function of Cooper pair excitation at zero temperature.

$$\begin{aligned} \left\langle\Delta(t)\Delta^\dagger(0)\right\rangle &= \frac{\mathrm{Tr}(e^{-(\beta-t)H_I}\Delta e^{-tH_I}\Delta^\dagger)}{\mathrm{Tr}(e^{-\beta H_I})} \\ &\overset{\lim}{\underset{\beta\to\infty}{=}} \frac{1}{N_d+1}\sum_{n=0}^{N_d-1}\left|\left\langle\Delta^\dagger\psi_{2n}|\psi_{2n+2}\right\rangle\right|^2 \\ &= \frac{N_d(N_d+2)}{6}. \end{aligned} \tag{4.29}$$

Since pairing correlation function P is defined as $P=\frac{1}{2N_d^2}\left\langle\Delta\Delta^\dagger+\Delta^\dagger\Delta\right\rangle$, we actually achieve P at zero temperature. It is also worthwhile to point out that in the thermodynamic limit, this N_d^2 scaling diverges faster than the system size, indicating an instability towards superconductivity at $T=0$.

According to $SU(2)$ symmetry $\langle\sigma_z^2\rangle=\langle\sigma_x^2\rangle$, there should be a relation linking density fluctuation with Cooper pair correlation $\langle\hat{N}_p^2\rangle-\langle\hat{N}_p\rangle^2=2\langle\Delta\Delta^\dagger\rangle$ when there is no kinetic term in our Hamiltonian. One can also prove this formula explicitly in DQMC's setting.

Remember $\hat{B}_{t,\tau}\left(\left\{l_{|q|,t}\right\}\right)$ is a unitary operator for any configuration $\left\{l_{|q|,t}\right\}$. In single-particle basis, we write the matrix form of $\prod_t\hat{B}_{t,\tau}\left(\left\{l_{|q|,t}\right\}\right)$ as $U=e^{M_1}e^{M_2}\cdots e^{M_n}$. According to DQMC's formula, Green's function for this configuration is defined as

$$G_{i,j}(\tau)=\frac{\mathrm{Tr}\left[c_{i,\tau}c_{j,\tau}^\dagger\prod_t\hat{B}_{t,\tau}\left(\left\{l_{|q|,t}\right\}\right)\right]}{\mathrm{Tr}\left[\prod_t\hat{B}_{t,\tau}\left(\left\{l_{|q|,t}\right\}\right)\right]}=[(I+U)^{-1}]_{i,j} \tag{4.30}$$

By noticing $G(\tau)+G^\dagger(\tau)=(I+U)^{-1}+(I+U^{-1})^{-1}=(I+U)^{-1}+U(I+U)^{-1}=I$, we have $G_{i,j}(\tau)+G_{j,i}^*(\tau)=\delta_{i,j}$. To confirm $\langle\hat{N}_p^2\rangle-\langle\hat{N}_p\rangle^2=2\langle\Delta\Delta^\dagger\rangle$, one can write the

observable at given configuration field l $\langle \hat{N}_p^2 \rangle_l$ and $\langle \Delta\Delta^\dagger \rangle_l$ as

$$\begin{aligned}
\langle \Delta\Delta^\dagger \rangle_l &= \langle \sum_{k_1,m_1} c_{-k_1,m_1,-\tau} c_{k_1,m_1,\tau} \sum_{k_2,m_2} c^\dagger_{k_2,m_2,\tau} c^\dagger_{-k_2,m_2,-\tau} \rangle_l \\
&= \sum_{k_1,m_1} \sum_{k_2,m_2} \langle c_{-k_1,m_1,-\tau} c^\dagger_{-k_2,m_2,-\tau} \rangle_l \langle c_{k_1,m_1,\tau} c^\dagger_{k_2,m_2,\tau} \rangle_l \\
&= \sum_{k_1,m_1} \sum_{k_2,m_2} \left| G_{k_1 m_1, k_2 m_2} \right|^2, \qquad (4.31)
\end{aligned}$$

$$\begin{aligned}
\langle \hat{N}_p^2 \rangle_l &= \langle \sum_{k_1,m_1,\tau_1} c^\dagger_{k_1,m_1,\tau_1} c_{k_1,m_1,\tau_1} \sum_{k_2,m_2,\tau_2} c^\dagger_{k_2,m_2,\tau_2} c_{k_2,m_2,\tau_2} \rangle_l \\
&= \sum_{k_1,m_1,\tau_1} \sum_{k_2,m_2,\tau_2} \langle c^\dagger_{k_1,m_1,\tau_1} c_{k_1,m_1,\tau_1} \rangle_l \langle c^\dagger_{k_2,m_2,\tau_2} c_{k_2,m_2,\tau_2} \rangle_l \\
&+ \langle c^\dagger_{k_1,m_1,\tau_1} c_{k_2,m_2,\tau_2} \rangle_l \langle c_{k_1,m_1,\tau_1} c^\dagger_{k_2,m_2,\tau_2} \rangle_l \\
&= \left(\sum_{k_1,m_1} 2 - \left[G_{k_1,m_1}(\tau) + G^*_{k_1,m_1}(\tau) \right] \right)^2 \\
&+ \sum_{k_1,m_1} \sum_{k_2,m_2} \sum_{\tau} \left[\delta_{k_1,k_2} \delta_{m_1,m_2} - G_{k_2 m_2, k_1 m_1}(\tau) \right] G_{k_1 m_1, k_2 m_2}(\tau) \\
&= N_d^2 + 2 \sum_{k_1,m_1} \sum_{k_2,m_2} \left| G_{k_1 m_1, k_2 m_2} \right|^2 \\
&= N_d^2 + 2 \left\langle \Delta\Delta^\dagger \right\rangle_l . \qquad (4.32)
\end{aligned}$$

Since we can also easily see $\langle \hat{N}_p \rangle = N_d$ (average particle filling should be half), after averaging all configurations, one will derive $\langle \hat{N}_p^2 \rangle - \langle \hat{N}_p \rangle^2 = 2\langle \Delta\Delta^\dagger \rangle$. Because superconductivity fluctuations diverge as $\propto N_d^2$ at $T = 0$, particle-number fluctuations must also diverge as $\propto N_d^2$. This scaling violates one fundamental assumption of statistical physics, the central limit theorem, which requires square fluctuations to scale linearly with system sizes. Such violation is a consequence of the infinite ground-state degeneracy. From the fluctuation-dissipation theorem, this divergence in particle-number fluctuations implies a diverging compressibility at low T: $\kappa = \frac{1}{N_d} \frac{d\langle \hat{N}_p \rangle}{d\mu} = \beta \frac{\langle \hat{N}_p^2 \rangle - \langle \hat{N}_p \rangle^2}{N_d} = \frac{2\beta}{N_d} \left\langle \Delta\Delta^\dagger \right\rangle$. When temperature is reduced, κ increases. In the low temperature limit, because $\left\langle \Delta\Delta^\dagger \right\rangle \propto N_d^2$, κ diverges as $\kappa \propto \beta N_d$. This divergence is also seen in DQMC simulations in Fig 4.4(g).

Next, we would like to derive two-fermion charge-2e excitations. For $p \neq 0$, it is easy to check $\left\langle 0 \left| \Delta^n c_{-k_2-p,-\tau} c_{k_2,\tau} c^\dagger_{k_1,\tau} c^\dagger_{-k_1-p,-\tau} (\Delta^\dagger)^n \right| 0 \right\rangle = \delta_{k_1,k_2} A$ as well as $\left\langle 0 \left| \Delta^n c^\dagger_{k_2+p,\tau} c_{k_2,\tau} c^\dagger_{k_1,\tau} c_{k_1+p,\tau} (\Delta^\dagger)^n \right| 0 \right\rangle = \delta_{k_1,k_2} A$ where A is a normalization constant. This means two-fermion excitations on a given ground state $c^\dagger_{k_1,\tau} c^\dagger_{-k_1-p,-\tau} (\Delta^\dagger)^n |0\rangle$ or $c^\dagger_{k_1,\tau} c_{k_1+p,\tau} (\Delta^\dagger)^n |0\rangle$ are orthogonal so that they can be seen as well-defined basis. According to $SU(2)$ symmetry, they should have the same excitation spectrum. By using the formula introduced for TBG in Chapter 3, one can compute the single-particle and two-particle excitation spectra in Fig 4.5. As shown by red line in Fig 4.5, single-particle

excitation is fully gapped and independent with inter-valley interaction (no matter repulsion or attraction). For repulsive interactions, the gap is an insulating gap without other charged excitation inside [99, 118, 119, 121, 124]. In our model, this gap is the Cooper gap, i.e., the energy cost to break a Cooper pair. The Cooper gap scales linearly with interaction energy V and there are continuous charged excitations within the gap as the blue line in Fig 4.5. Thus, at low temperature $T \ll V$, all electrons are paired into Cooper pairs, i.e., the system is a fluid of Cooper pairs without unpaired fermions.

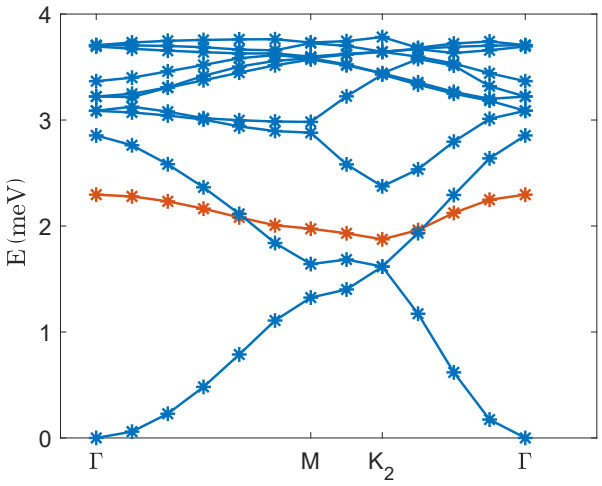


Figure 4.5: Excitation spectrum for inter-valley attractive model where the system size is 12×12. Red line and blue lines are used to label single-particle excitation and charge-2e excitation along high symmetry lines. This figure comes from Ref [7].

Despite the finite Cooper gap and diverging superconducting correlation function, Cooper pairs in this boson fluid don't lead to superconduct at any finite temperature. This is because the superconducting order parameter is part of a $SU(2)$ generator. Therefore, a superconducting state would spontaneously break the $SU(2)$ symmetry, instead of just the $U(1)$ charge symmetry. In other words, the symmetry breaking pattern here is in the Heisenberg universality class, instead of XY. For 2D systems at finite T, it has long been known that thermal fluctuations will destroy any order that spontaneously breaks an $SU(2)$ symmetry (i.e., there is no finite temperature order for Heisenberg spins in 2D). Thus, although Cooper pairs have formed at $T \sim V$, long-range or quasi-long range phase coherence cannot be developed at any finite temperature. This conclusion is verified in DQMC simulations, where we observe a fully-developed Cooper gap at finite T, but the phase coherence remains disordered even down to lowest accessible temperature (Fig 4.4(a,c,e,g)).

In DQMC, we simulated both Hamiltonian without and with band dispersion. With the imaginary-time correlation functions obtained in DQMC, we further employ the SAC method (see Appendix D) to extract the real-frequency spectra [184–194]. In Fig 4.4(c-d), we plot the fermion DOS at different temperature for a 9×9 system. At $T < 0.3$, a

full gap is observed, which is the Cooper gap discussed above. For $0.3 < T < 0.8$, fermion spectral weight start to emerge inside the gap, i.e., a pseudogap (PG) is formed. Defining $P = \frac{1}{2N_d^2}\left\langle \Delta\Delta^\dagger + \Delta^\dagger\Delta \right\rangle$, we also try to determine the superconducting phase transition temperature T_c by probing the onset of quasi-long range order. This is achieved via data cross of $P \times L^\eta$ versus T as shown in Fig 4.4(e-f) with the 2D XY critical anomalous dimension exponent $\eta = \frac{1}{4}$ [178, 195–197], using $P = L^{-\eta} f(L \cdot \exp(-\frac{A}{(T-T_c)^{1/2}}))$ (see Appendix B). In Fig 4.4(e) for the case of flat band limit, the cross point is indeed approaching $T_c \to 0$, confirming the absence of finite temperature phase transition, in full agreement with the exact solution. Besides, one can also check the superfluid density criterion [198–200] by computing current-current correlation by noticing $j_\alpha(q) = \frac{[H_I, n_q]}{q_\alpha}$ where α indicates the direction of the current and $n_q = \rho_{\tau;q} + \rho_{-\tau;q}$.

$$
\begin{aligned}
& \langle j_\alpha(q,t) j_\alpha(-q,0)\rangle \\
= \quad & \frac{\mathrm{Tr}(e^{-(\beta-t)H_I}[H_I,n_q]e^{-tH_I}[H_I,n_{-q}])}{-\mathrm{Tr}(e^{-\beta H_I})q_\alpha q_\alpha} \\
\overset{\lim}{\underset{\beta\to\infty}{=}} \quad & \frac{\sum_{g,m}\langle g|n_q H_I|m\rangle\langle m|e^{-tH_I}H_I n_{-q}|g\rangle}{\sum_g q_\alpha q_\alpha} + \frac{\sum_{g,m}\langle m|e^{-(\beta-t)H_I}H_I n_q|g\rangle\langle g|n_{-q}H_I|m\rangle}{\sum_g q_\alpha q_\alpha} \\
\overset{\lim}{\underset{q\to 0}{\approx}} \quad & \left(\frac{\epsilon_q}{q_\alpha}\right)^2 \left(\frac{\sum_g \langle g|n_q|q\rangle\langle q|n_{-q}|g\rangle}{\sum_g 1} + \frac{\sum_g \langle -q|n_q|g\rangle\langle g|n_{-q}|-q\rangle}{\sum_g 1}\right)
\end{aligned}
\tag{4.33}
$$

Here we use g to label all the degenerate ground states and in the last line we only take the state with the minimum excitation energy ϵ_q and with finite momentum q,$-q$ from the summation over m. Since the dispersion of ferromagnetic-like spectrum is quadratic with slope equal to zero, $\frac{\epsilon_q}{q_\alpha} = 0$ tells us the superfluid density has to be zero.

With the exactly solvable limit understood, a kinetic energy term with finite (but small) bandwidth is introduced, which explicitly breaks the $SU(2)$ symmetry. Here, again, the band width we take is near $0.8meV$. Same qualitative features are expected for other more complicated setups, such as TBGs. Without the $SU(2)$ symmetry, a BKT superconducting phase becomes allowed, and in DQMC simulations, we indeed observe a superconducting dome with chemical potential partially filling flat bands, in analogy to experiments reported in TBGs. Above the superconducting dome, the pseudogap and SCBF phases remain. Because the band width is still smaller than interaction energy scale, the temperature scales for the pseudogap and SCBF phases, which are dominated by interactions, are almost invariant for different band fillings, consistent with the STM experiment in TBG between different integer fillings [51]. Another observation in TBG experiment is $d\mu/dn$ reduces towards 0 at superconducting doping [158], which implies a large compressibility κ. This is also seen in our simulation results Fig 4.4(g-h).

4.4 Further discussion

Except for those Mott insulator phase and possible superconductor phase, there is another amazing strong correlating feature, fractional quantum anomalous Hall (FQAH),

observed in both TTMD and multilayer graphene recently [167–170, 201, 202]. Up to date, theories predict there is emerged flat bands and repulsive interaction projected on it forces fractional filling to favor FQAH state [173, 203–224]. Charge density wave (CDW) order is also a possible candidate in this case, and some discussions on the influence of remote non-flat bands indicate the two-particle charge-neutral roton mode is necessary for understanding of CDW and FQAH [220, 221, 225–232]. Other discussions about the effect of quantum metric give a guiding principle for finding a FQAH state. However, for now, a specific identifying rule is still absent for a given system before one makes his hands dirty to solves it numerically or conducts an experiment.

Chapter 5

Landau level with moiré potential

5.1 Landau level basis of Dirac fermion in magnetic field

Besides electric field, another convenient and frequently-used tuning method for 2D materials is magnetic field. I have introduced a recently developed fancy way that twisting layers inducing flat band in Chapter 3 and Chapter 4. Actually before this recent development, there is a more traditional way that using strong magnetic field for realizing flat bands. As one has learned from quantum mechanics textbooks, free electron gas with quadratic momentum dispersion $\frac{p^2}{2m}$ will form Landau level after introducing a magnetic field and replacing p by $p + eA$. I will not review this part and just give the Landau level eigen energy result for free electron gas as

$$E_n = (n + \frac{1}{2})\frac{\hbar eB}{m}. \tag{5.1}$$

Here $n = 0, 1, 2, \ldots$ labels different Landau level and $B = |\nabla \times A|$ is the strength of the magnetic field. One can see for a given Landau level, the energy is linearly dependent on the strength of the magnetic field. The Landau level for linear momentum dispersion $v_F \sigma \cdot p$ (where v_F is the Fermi velocity and σ is Dirac matrix) also has an exact solution and the Landau level there has a square root dependence on magnetic field

$$E_n = \pm v_F \sqrt{2n\hbar eB}. \tag{5.2}$$

Since I will consider 2D material graphene and its family with moiré potential in this chapter later, I will introduce the derivation of this Dirac fermion Landau level below in detail as the beginning of this chapter [160, 233–239]. The Hamiltonian with a Dirac dispersion is written as

$$v_F \sigma \cdot p \left|\psi\right\rangle = \epsilon \left|\psi\right\rangle. \tag{5.3}$$

When introducing magnetic field, we take Landau gauge and have $A = (0, Bx, 0)$, $p + eA = (-i\hbar\partial_x, -i\hbar\partial_y + eBx, 0)$. By defining mechanical momentum $\pi = p + eA$, we can write the Hamiltonian in 2×2 matrix form

$$v_F \begin{pmatrix} 0 & \pi_x - i\pi_y \\ \pi_x + i\pi_y & 0 \end{pmatrix} \begin{pmatrix} \psi_1 \\ \psi_2 \end{pmatrix} = \epsilon \begin{pmatrix} \psi_1 \\ \psi_2 \end{pmatrix}. \tag{5.4}$$

Let's define the operator $L^- = \pi_x - i\pi_y$ and $L^+ = \pi_x + i\pi_y$. One can see the matrix form above is equal to solving two equations

$$\begin{cases} v_F L^- \psi_2 = \epsilon \psi_1 \\ v_F L^+ \psi_1 = \epsilon \psi_2 \end{cases}. \tag{5.5}$$

This can be solved by applying operator $L^\pm$ again and decoupling two components

$$\begin{aligned} L^+ L^- \psi_2 &= \left(\frac{\epsilon}{v_F}\right)^2 \psi_2 \\ L^- L^+ \psi_1 &= \left(\frac{\epsilon}{v_F}\right)^2 \psi_1. \end{aligned} \tag{5.6}$$

Noticing the commutation relation

$$\left[L^-, L^+\right] = 2i\left[\pi_x, \pi_y\right] = 2\hbar eB, \tag{5.7}$$

One can define bosonic operators by dividing $L^\pm$ with $\sqrt{2\hbar eB}$

$$\begin{aligned} a^\dagger &= \frac{L^+}{\sqrt{2\hbar eB}} \\ a &= \frac{L^-}{\sqrt{2\hbar eB}}. \end{aligned} \tag{5.8}$$

By noticing the bosonic vacuum $\psi_{2,0}$ should be one of the eigenstates with zero energy, one can apply $a^\dagger$ on it n times to derive all the eigenstates with

$$2n\hbar eB = \left(\frac{\epsilon}{v_F}\right)^2. \tag{5.9}$$

Here $n = 0, 1, 2, \ldots$. The solution for ϵ is

$$\epsilon = \pm v_F \sqrt{2n\hbar eB}. \tag{5.10}$$

Now we are trying to derive the corresponding wavefunctions. Notice we require $a\psi_{2,0} = 0$ so that explicitly we have

$$\left(-i\hbar\partial_x - i\left(-i\hbar\partial_y + eBx\right)\right)\psi_{2,0} = 0 \tag{5.11}$$

It is easy to solve the y component wavefunction $e^{ik_y y}$ with eigenvalue k_y and the equation for the left x component will be

$$\left(\partial_x + \left(k_y + \frac{eBx}{\hbar}\right)\right)\psi_{2,0}(x) = 0 \tag{5.12}$$

This can be solved easily

$$\psi_{2,0}(x) = Ce^{-\frac{1}{2}\frac{eB}{\hbar}x^2 - k_y x} = \left(\frac{eB}{\pi\hbar}\right)^{\frac{1}{4}} e^{-\frac{1}{2}\frac{eB}{\hbar}\left(x+\frac{k_y\hbar}{eB}\right)^2} \tag{5.13}$$

Here the constant $\left(\frac{eB}{\pi\hbar}\right)^{\frac{1}{4}}$ is used to normalize the wavefunction. Other eigenstates can be derived by $\psi_{2,n} = \frac{1}{\sqrt{n!}}\left(a^\dagger\right)^n\psi_{2,0}$

$$\psi_{2,n}(x) = \left(\sqrt{\frac{\hbar}{2eB}}\right)^n \frac{(-i)^n}{\sqrt{n!}}\left(\partial_x - \left(k_y + \frac{eBx}{\hbar}\right)\right)^n \psi_{2,0}(x) \tag{5.14}$$

By defining $z = \sqrt{\frac{eB}{\hbar}}\left(x + \frac{k_y\hbar}{eB}\right)$, we have

$$\psi_{2,n}(z) = \left(\frac{eB}{\pi\hbar}\right)^{\frac{1}{4}} \frac{(-i)^n}{\sqrt{2^n n!}}\left(\partial_z - z\right)^n e^{-\frac{1}{2}z^2} = \left(\frac{eB}{\pi\hbar}\right)^{\frac{1}{4}} \frac{i^n}{\sqrt{2^n n!}} e^{-\frac{1}{2}z^2} H_n(z). \tag{5.15}$$

Here $H_n(z)$ is Hermite polynomial. One may notice this solution just has an additional phase i^n compared with general Hermite functions which seems contribute nothing. But one will see this will be the phase difference between ψ_1 and ψ_2 as $v_F L^- \psi_2 = \epsilon\psi_1$

$$\epsilon_n\psi_{1,n} = v_F\sqrt{2\hbar eB}\,a\psi_{2,n} = v_F\sqrt{2n\hbar eB}\,\psi_{2,n-1} \tag{5.16}$$

Then the two components solution will be

$$\psi_n = \begin{pmatrix}\psi_{1,n}\\ \psi_{2,n}\end{pmatrix} = \begin{pmatrix}\psi_{2,n-1}\\ \psi_{2,n}\end{pmatrix} = C_n e^{ik_y y}\begin{pmatrix}-i\phi_{n-1}(z)\\ \phi_n(z)\end{pmatrix} \tag{5.17}$$

Here $n \geq 0, \epsilon_n \geq 0$ and $\psi_{1,0} = 0$. C_n is the normalization constant which is $1/\sqrt{2}$ for $n \neq 0$ and 1 for $n = 0$. $\phi_n(z)$ is the normal Hermite functions without the additional phase i^n. While for $n < 0$, one notices the wavefunction will be the same as $|n|$ so that

$$\begin{aligned}\epsilon_n\psi_{1,n} &= v_F\sqrt{2\hbar eB}\,a\psi_{2,|n|} = v_F\sqrt{2|n|\hbar eB}\,\psi_{2,|n|-1}\\ \psi_n &= \begin{pmatrix}-\psi_{2,|n|-1}\\ \psi_{2,|n|}\end{pmatrix} = C_n e^{ik_y y}\begin{pmatrix}i\phi_{|n|-1}(z)\\ \phi_{|n|}(z)\end{pmatrix}\end{aligned} \tag{5.18}$$

In summary, we have wave function for all possible $n = 0, \pm1, \pm2, \ldots$

$$\psi_n = C_n e^{ik_y y}\begin{pmatrix}-i\,\mathrm{sgn}(n)\phi_{|n|-1}(z)\\ \phi_{|n|}(z)\end{pmatrix}. \tag{5.19}$$

For the other valley (transforming with the inversion and exchanging sublattices) the basis is similar. One just needs to exchange sublattices and give a minus sign before i (which comes from inversion $z \to -z$).

$$\psi'_n = C_n e^{ik_y y} \begin{pmatrix} \phi_{|n|}(z) \\ i\,\mathrm{sgn}(n)\phi_{|n|-1}(z) \end{pmatrix} \tag{5.20}$$

Now, we have all the primitive components which can already be used to describe graphene electrons in magnetic field. One can see the system is degenerate over different choosing of k_y so that for each Landau level the system is also highly degenerate with tuning k_y (just as the flat band induced by moiré potential). One interesting feature for those degenerate bands is under periodic lattice potential, they will form fractal structures [160, 234–239] (also known as Hofstadter's butterfly). And this periodic lattice potential can just be realized by moiré potential naturally. In the next section, I will introduce the analytical process for computing this fractal energy spectrum which is directly corresponding to the moiré graphene electrons in the strong magnetic field.

5.2 Hofstadter's butterfly in super-Moiré of graphene

Hofstadter's butterfly is originally introduced in lattice tight binding model with magnetic field by Peierls substitution [240]. However, it requires the lattice constant up to several tens of nanometer (which is impossible for natural atom distance) to observe within affordable magnetic field (several Tesla). The recently developed moiré system makes this huge unit cell possible but the periodicity can be poor for a small twist angle. In this section, I would like to propose another way to enlarge the moiré unit cell that use two moiré potential to form a moiré super cell (i.e., super-moiré) and study the electromagnetic response there.

For graphene with moiré potential, one can write either a tight binding model or a continuous model. There has been shown that the tight binding model with Peierls phase has the similar energy spectrum with transforming the continuous model to Landau level basis and diagonalizing it [235]. And there is also other methods by constructing the model with open momentum space with a boundary cutoff [239]. To avoid the possible Wannier obstruction of writing a tight binding model and cutoff edge states, I will take continuous model in the Landau level basis method below and introduce how it can be used to solve the super-moiré lattice potential graphene system in magnetic field [160, 234–237].

Here we consider the super-moiré lattice formed by matching two twist angles. One is the twist angle between graphene and the nearly aligned hbn and the other is the electric potential from twisted hbn substrate [241, 242]. The schematic is shown in Fig 5.1 where the dashed lines label x and y axis from aligned hbn, the blue arrows label the reciprocal vectors from graphene/hbn moiré, the orange arrow labels the reciprocal vector from twisted hbn/hbn and the yellow arrows label the super-moiré reciprocal vectors. When fixing graphene/hbn moiré G_i and tuning hbn/hbn moiré G'_i, one can

see the length of vector G_i' will increase linearly with twist angle at small twist case. If one wants to realize super-moiré, the final reciprocal vectors g_i should match with G_i and G_i' (i.e., Both G_i and G_i' can be written as the linear combination of g_i).

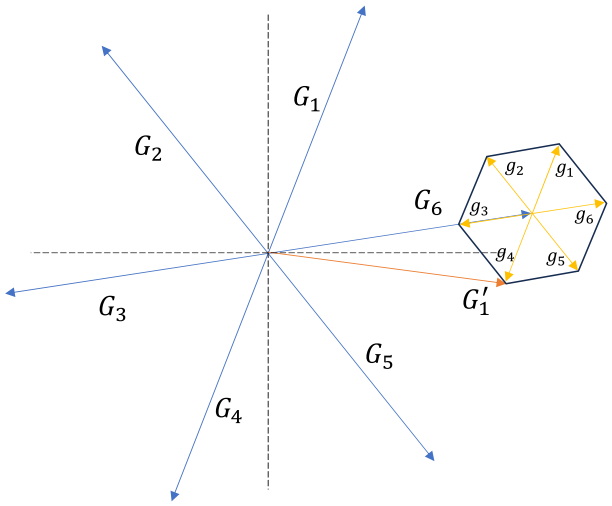


Figure 5.1: Schematic plot of deriving super-moiré reciprocal vectors. Dashed lines label x and y axis from aligned hbn, the blue arrows label the reciprocal vectors from graphene/hbn moiré, the orange arrow labels the reciprocal vector from twisted hbn/hbn and the yellow arrows label the super-moiré reciprocal vectors.

Here, we assume graphene with lattice constant $a_g \approx 0.244nm$ has a $\sim 0.378°$ twist relative to aligned hbn which gives the moiré lattice constant $L_{g/h} \approx 12.943nm$, moiré pattern rotation angle $\phi \approx 20.1°$ [241] and reciprocal vector $G_0 = |G_i| = \frac{4\pi}{\sqrt{3}L_{g/h}} \approx 0.56nm^{-1}$. The triangular relationships give

$$\begin{cases} \frac{\sin(60°)}{G_0'} = \frac{\sin(30°-\phi+\theta)}{g_0} \\ \cos(30° - \phi + \theta) = \frac{{G_0'}^2+3G_0^2-g_0^2}{2\sqrt{3}G_0G_0'} \end{cases} \tag{5.21}$$

Here $G_0' = |G_i'| = \frac{4\pi}{\sqrt{3}L_{h/h}} \approx \frac{4\pi\theta}{\sqrt{3}a_{hbn}}$ is the moiré reciprocal vector length from twisted hbn with twist angle θ and lattice constant $a_{hbn} \approx 0.2504nm$. Solve the equations and the solution gives $\theta \approx 1.016°$, $G_0' \approx 0.5137nm^{-1}$, $g_0 \approx 0.1126nm^{-1} \approx \frac{G_0}{5}, L_s \approx 64.63nm$. This means with this group of parameters, super-moiré unit cell is composed of 5×5 graphene/hbn moiré unit cells.

Then we define the coordinate in our computation according to super-moiré reciprocal vector g_i, where $g_0 = \frac{4\pi}{\sqrt{3}L_s}$ and

$$[g_1, g_2, g_3, g_4, g_5, g_6] = g_0 \left[\begin{pmatrix} 0 \\ 1 \end{pmatrix}, \begin{pmatrix} -\frac{\sqrt{3}}{2} \\ \frac{1}{2} \end{pmatrix}, \begin{pmatrix} -\frac{\sqrt{3}}{2} \\ -\frac{1}{2} \end{pmatrix}, \begin{pmatrix} 0 \\ -1 \end{pmatrix}, \begin{pmatrix} \frac{\sqrt{3}}{2} \\ -\frac{1}{2} \end{pmatrix}, \begin{pmatrix} \frac{\sqrt{3}}{2} \\ \frac{1}{2} \end{pmatrix} \right]. \tag{5.22}$$

It is easy to derive G_i and G'_i respectively

$$\begin{aligned}[G_1, G_2, G_3, G_4, G_5, G_6] &= 5\,[g_1, g_2, g_3, g_4, g_5, g_6] \\ \left[G'_1, G'_2, G'_3, G'_4, G'_5, G'_6\right] &= [5g_6 + g_4, 5g_1 + g_5, 5g_2 + g_6, 5g_3 + g_1, 5g_4 + g_2, 5g_5 + g_3]\,.\end{aligned} \tag{5.23}$$

According to [243–245], the electric potential from twist hbn is written as

$$V(r,z) = \mathrm{sgn}(z)\frac{P_0\sqrt{3}}{9\epsilon_0}e^{-G'|z|}\sum_{j=1,3,5}\cos\left(G'_j\cdot r - \frac{\pi}{2}\right). \tag{5.24}$$

Here z is the distance between the graphene plane and the twisted hbn plane and r labels position in 2D graphene plane. The magnitude of $V(r,z)$ is about $0 \sim 200meV$. Since z should be fixed in experiment, we set $V(r+\delta R) = V_{h/h}\sum_{j=1,3,5}\cos\left(G'_j\cdot(r+\delta R) - \frac{\pi}{2}\right)$ and $V_{h/h} \leqslant 200meV$ where constant vector δR indicates the displacement from hbn/hbn AA stacking center. Use Fourier transformation to rewrite this potential in momentum space with plane wave basis

$$\begin{aligned}H_{h/h} &= \frac{1}{S}\int dr V(r+\delta R)c^\dagger(r)c(r) \\ &= \frac{V_{h/h}}{2NS}\int dr\left(\sum_{j=1,3,5}e^{i\left(G'_j\cdot(r+\delta R)-\frac{\pi}{2}\right)} + e^{-i\left(G'_j\cdot(r+\delta R)-\frac{\pi}{2}\right)}\right)\sum_{k_1,k_2}e^{ik_1\cdot r - ik_2\cdot r}c^\dagger_{k_1}c_{k_2} \\ &= \sum_k V(k)\end{aligned} \tag{5.25}$$

Here S and N are area and amount of moiré unit cells, the integral of r covers whole real space and $V(k) = \frac{V_{h/h}}{2}\sum_{j=1,3,5}e^{i\left(G'_j\cdot\delta R-\frac{\pi}{2}\right)}c^\dagger_k c_{k+G'_j} + e^{-i\left(G'_j\cdot\delta R-\frac{\pi}{2}\right)}c^\dagger_k c_{k-G'_j}$. One can see δR only changes a gauge phase and we can just replace $e^{i\left(G'_j\cdot\delta R\right)}c_{k+G'_j}$ by $c_{k+G'_j}$ to remove it.

Next I will introduce how to compute the effective graphene/hbn Hamiltonian $H_{g/hbn}$ based on [235, 242]. I assume the bare graphene and hbn Hamiltonian is H_g and H_{hbn} and the tunneling is described by U.

$$\begin{aligned}H_{g/hbn} &= \begin{pmatrix}H_g & U^\dagger \\ U & H_{hbn}\end{pmatrix} \\ U &= \begin{pmatrix}u_N & u_B \\ u_N & u_B\end{pmatrix} + \begin{pmatrix}u_N & e^{-i\frac{2\pi}{3}}u_B \\ e^{i\frac{2\pi}{3}}u_N & u_B\end{pmatrix}e^{iG_5\cdot r} + \begin{pmatrix}u_N & e^{i\frac{2\pi}{3}}u_B \\ e^{-i\frac{2\pi}{3}}u_N & u_B\end{pmatrix}e^{iG_6\cdot r} \\ H_{hbn} &= \begin{pmatrix}V_N & 0 \\ 0 & V_B\end{pmatrix}\end{aligned} \tag{5.26}$$

Here we take tunneling parameters $u_N \approx 0.097eV,\ u_B \approx 0.144eV, V_B \approx 3.332eV,\ V_N \approx -1.493eV$ in our computation [235, 242]. According to the second order perturbation

$$H_{g/hbn} \approx H_g - U^\dagger H_{hbn}^{-1} U \equiv H_g + V_{hbn}, \tag{5.27}$$

here

$$\begin{aligned}
V_{hbn} = & -\left[\begin{pmatrix} u_N & u_N \\ u_B & u_B \end{pmatrix} + \begin{pmatrix} u_N & e^{-i\frac{2\pi}{3}}u_N \\ e^{i\frac{2\pi}{3}}u_B & u_B \end{pmatrix} e^{-iG_5\cdot r} + \begin{pmatrix} u_N & e^{i\frac{2\pi}{3}}u_N \\ e^{-i\frac{2\pi}{3}}u_B & u_B \end{pmatrix} e^{-iG_6\cdot r}\right] \\
& \begin{pmatrix} \frac{1}{V_N} & 0 \\ 0 & \frac{1}{V_B} \end{pmatrix} \left[\begin{pmatrix} u_N & u_B \\ u_N & u_B \end{pmatrix} + \begin{pmatrix} u_N & e^{-i\frac{2\pi}{3}}u_B \\ e^{i\frac{2\pi}{3}}u_N & u_B \end{pmatrix} e^{iG_5\cdot r} + \begin{pmatrix} u_N & e^{i\frac{2\pi}{3}}u_B \\ e^{-i\frac{2\pi}{3}}u_N & u_B \end{pmatrix} e^{iG_6\cdot r}\right] \\
= & -3\left(\frac{1}{V_N} - \frac{1}{V_B}\right)\begin{pmatrix} u_N^2 & 0 \\ 0 & u_B^2 \end{pmatrix} \\
& - e^{iG_2\cdot r}\begin{pmatrix} \left(\frac{1}{V_N} + e^{-i\frac{2\pi}{3}}\frac{1}{V_B}\right)u_N^2 & \left(\frac{1}{V_N} + e^{-i\frac{2\pi}{3}}\frac{1}{V_B}\right)u_N u_B \\ \left(e^{i\frac{2\pi}{3}}\frac{1}{V_N} + \frac{1}{V_B}\right)u_N u_B & \left(e^{i\frac{2\pi}{3}}\frac{1}{V_N} + \frac{1}{V_B}\right)u_B^2 \end{pmatrix} \\
& - e^{iG_5\cdot r}\begin{pmatrix} \left(\frac{1}{V_N} + e^{i\frac{2\pi}{3}}\frac{1}{V_B}\right)u_N^2 & \left(e^{-i\frac{2\pi}{3}}\frac{1}{V_N} + \frac{1}{V_B}\right)u_N u_B \\ \left(\frac{1}{V_N} + e^{i\frac{2\pi}{3}}\frac{1}{V_B}\right)u_N u_B & \left(e^{-i\frac{2\pi}{3}}\frac{1}{V_N} + \frac{1}{V_B}\right)u_B^2 \end{pmatrix} \\
& - e^{iG_3\cdot r}\begin{pmatrix} \left(\frac{1}{V_N} + e^{i\frac{2\pi}{3}}\frac{1}{V_B}\right)u_N^2 & \left(\frac{1}{V_N} + e^{i\frac{2\pi}{3}}\frac{1}{V_B}\right)u_N u_B \\ \left(e^{-i\frac{2\pi}{3}}\frac{1}{V_N} + \frac{1}{V_B}\right)u_N u_B & \left(e^{-i\frac{2\pi}{3}}\frac{1}{V_N} + \frac{1}{V_B}\right)u_B^2 \end{pmatrix} \\
& - e^{iG_6\cdot r}\begin{pmatrix} \left(\frac{1}{V_N} + e^{-i\frac{2\pi}{3}}\frac{1}{V_B}\right)u_N^2 & \left(e^{i\frac{2\pi}{3}}\frac{1}{V_N} + \frac{1}{V_B}\right)u_N u_B \\ \left(\frac{1}{V_N} + e^{-i\frac{2\pi}{3}}\frac{1}{V_B}\right)u_N u_B & \left(e^{i\frac{2\pi}{3}}\frac{1}{V_N} + \frac{1}{V_B}\right)u_B^2 \end{pmatrix} \\
& - e^{iG_1\cdot r}\begin{pmatrix} \left(\frac{1}{V_N} + e^{i\frac{2\pi}{3}}\frac{1}{V_B}\right)u_N^2 & \left(e^{i\frac{2\pi}{3}}\frac{1}{V_N} + e^{-i\frac{2\pi}{3}}\frac{1}{V_B}\right)u_N u_B \\ \left(e^{i\frac{2\pi}{3}}\frac{1}{V_N} + e^{-i\frac{2\pi}{3}}\frac{1}{V_B}\right)u_N u_B & \left(e^{-i\frac{2\pi}{3}}\frac{1}{V_N} + \frac{1}{V_B}\right)u_B^2 \end{pmatrix} \\
& - e^{iG_4\cdot r}\begin{pmatrix} \left(\frac{1}{V_N} + e^{-i\frac{2\pi}{3}}\frac{1}{V_B}\right)u_N^2 & \left(e^{-i\frac{2\pi}{3}}\frac{1}{V_N} + e^{i\frac{2\pi}{3}}\frac{1}{V_B}\right)u_N u_B \\ \left(e^{-i\frac{2\pi}{3}}\frac{1}{V_N} + e^{i\frac{2\pi}{3}}\frac{1}{V_B}\right)u_N u_B & \left(e^{i\frac{2\pi}{3}}\frac{1}{V_N} + \frac{1}{V_B}\right)u_B^2 \end{pmatrix}.
\end{aligned} \tag{5.28}$$

From now on, we are ready to express the super-moiré Hamiltonian according to two sets of perturbation moiré fields. For valley τ in plane wave basis,

$$\begin{aligned}
H_\tau(k) &= H_g + V_{hbn} + H_{h/h} \\
&= c_k^\dagger\left[-\hbar v_F\begin{pmatrix} 0 & k_x - ik_y \\ k_x + ik_y & 0 \end{pmatrix} - 3\left(\frac{1}{V_N} + \frac{1}{V_B}\right)\begin{pmatrix} u_N^2 & 0 \\ 0 & u_B^2 \end{pmatrix}\right]c_k \\
&- \sum_{j=1}^{6} c_{k+G_j}^\dagger\left[\begin{pmatrix} w_{11}^j & w_{12}^j \\ w_{21}^j & w_{22}^j \end{pmatrix}\right]c_k + \frac{V_{h/h}}{2}\sum_{j=1,3,5} e^{i\frac{\pi}{2}}c_{k+G_j'}^\dagger c_k + e^{-i\frac{\pi}{2}}c_{k-G_j'}^\dagger c_k.
\end{aligned} \tag{5.29}$$

Here we take Fermi velocity $v_F \approx 0.8 \times 10^6 m/s$ and w^j matrix can be read from V_{hbn}. The Hamiltonian in the other valley can be derived directly by time reversal $H_{-\tau}(k) = H_\tau^*(-k)$ (there is no magnetic field for now). One can express G_j and G_j' by g_j and

cut off the matrix dimension to include all g_j which satisfies $|g_j| \leq 10g_0$ and this will include $2G_0$ and $2G_0'$ meshes. When we set $V_{h/h} = 0$, we can compute density of states to compare our result from g_j mesh with G_j mesh, where there should be no difference since we trivially fold bands into a smaller Brillouin zone and do not change the density of states. After we turn on $V_{h/h} \sim 100meV$, the main feature of the density of states keeps the same since V_{hbn} has a larger magnitude, while there will be tiny dips emerge because of the folded bands open gaps as shown in Fig 5.2(a). Here we use a finite temperature broadening Fermi-Dirac distribution for computing density of states

$$\partial_\epsilon f^0 = \frac{1}{2kT[\cosh(\frac{\epsilon-\mu}{kT}) + 1]}. \tag{5.30}$$

Here we set $kT = 2meV$ for plotting Fig 5.2(a) and a gap from graphene/hbn moiré potential at hole doping $\nu_{g/h} = -1$ is observed as expected. By relaxation time approximation, we can also compute the relative shape of Drude conductance $\sigma_{xx} \propto \int d^2k\ \partial_\epsilon f^0\ (\partial_{k_x}\epsilon)^2$. At the same temperature $kT = 2meV$, the result is shown in Fig 5.2(b). One can see twisted hbn potential reduces the conductance and gives tiny dips features because of the super-moiré.

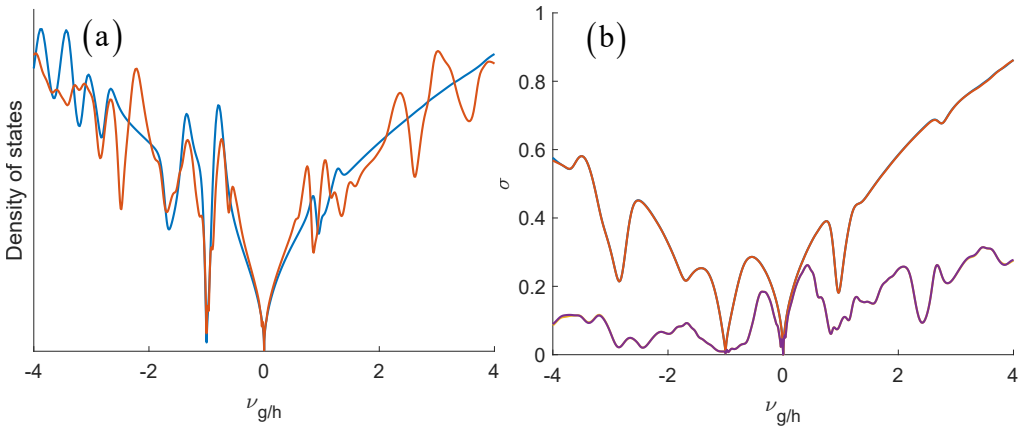


Figure 5.2: Density of states and Drude conductance versus filling $\nu_{g/h}$ of graphene/hbn moiré bands. (a) Density of states (without normalization) versus filling with $V_{h/h} = 0$ (blue line) and $V_{h/h} = 100meV$ (red line). (b) Drude conductance along G_1 and G_2 directions with $V_{h/h} = 0$ (blue and red lines) and with $V_{h/h} = 100meV$ (purple and yellow lines) versus filling.

Then we would like to compute the case with magnetic field which achieves several quantum fluxes for super-moiré unit cell so that a periodic oscillation with B can be observed. To write down the Hamiltonian in Dirac fermion Landau level basis, we need to compute each matrix element with the overlap of Landau level wavefunctions [160, 234–237]. First, it is straightforward to write down the Dirac dispersion within every layer, which is already diagonalized since this is just the definition of this basis.

$$H_g \to \epsilon_n \delta_{n,n'} \delta_{m,m'} \tag{5.31}$$

Here we use n to label the Landau level and use m to label the degenerate k_y label. And the AB sublattice difference term can also be computed according to

$$\begin{aligned}
&\int dydz\ \psi^{\dagger}_{n,m}\left[-3\left(\frac{1}{V_N}+\frac{1}{V_B}\right)\begin{pmatrix}u_N^2 & 0\\ 0 & u_B^2\end{pmatrix}\right]\psi_{n',m'}\\
=\ & C_n^2\delta_{n,n'}\delta_{m,m'}\left[-3\left(\frac{1}{V_N}+\frac{1}{V_B}\right)\left(\mathrm{sgn}(n)^2u_N^2+u_B^2\right)\right]
\end{aligned}\tag{5.32}$$

Then it comes to compute the moiré scattering elements $\left\langle \phi_{n,k_y}e^{ik_yy}\middle|e^{iG\cdot r}\middle|e^{ik'_yy}\phi_{n',k'_y}\right\rangle$. There is an explicit expression for this step and the idea is expanding Hermite polynomials. The expansion center can be seen from

$$e^{-\frac{1}{2}a\left(x+\frac{k_y}{a}\right)^2}e^{-\frac{1}{2}a\left(x+\frac{k'_y}{a}\right)^2}e^{iG_xx}=e^{-a\left(x+\frac{k_y+k'_y-iG_x}{2a}\right)^2}e^{\frac{\left(k_y+k'_y-iG_x\right)^2}{4a}}e^{-\left(\frac{k_y^2+{k'_y}^2}{2a}\right)}\tag{5.33}$$

Here we define $a=eB/\hbar$ and use $z=\sqrt{a}(x+\frac{k_y+k'_y-iG_x}{2a})$ to label the expansion center. Define $\Delta_y=k'_y-k_y$ so that the Hermite polynomials can be written as

$$\begin{aligned}
H_{n'}\left(\sqrt{a}\left(x+\frac{k'_y}{a}\right)\right) &= \sum_{k'=0}^{n'}\frac{n'!}{k'!\,(n'-k')!}H_{k'}(z)\left(\frac{\Delta_y+iG_x}{\sqrt{a}}\right)^{n'-k'}\\
H_{n}\left(\sqrt{a}\left(x+\frac{k_y}{a}\right)\right) &= \sum_{k=0}^{n}\frac{n!}{k!(n-k)!}H_{k}(z)\left(\frac{-\Delta_y+iG_x}{\sqrt{a}}\right)^{n-k}
\end{aligned}\tag{5.34}$$

According to orthogonal relation of Hermite polynomials

$$\int_{-\infty}^{\infty}H_m(z)H_n(z)e^{-z^2}dz=\sqrt{\pi}2^nn!\delta_{n,m},\tag{5.35}$$

remember the integral in $\left\langle \phi_{n,k_y}e^{ik_yy}\middle|e^{iG\cdot r}\middle|e^{ik'_yy}\phi_{n',k'_y}\right\rangle$ is for $dx=\frac{dz}{\sqrt{a}}$ and dy. We can compute $\left\langle \phi_{n,k_y}e^{ik_yy}\middle|e^{iG\cdot r}\middle|e^{ik'_yy}\phi_{n',k'_y}\right\rangle$ as

$$\begin{aligned}
&\delta_{k_y,k'_y+G_y}e^{\frac{\left(k_y+k'_y-iG_x\right)^2}{4a}}e^{-\left(\frac{k_y^2+{k'_y}^2}{2a}\right)}\frac{1}{\sqrt{2^nn!2^{n'}n'!}}\\
\times\ &\sum_{k=0}^{\min(n,n')}\frac{n'!}{k!\,(n'-k)!}\frac{n!}{k!(n-k)!}2^kk!\left(\frac{\Delta_y+iG_x}{\sqrt{a}}\right)^{n'-k}\left(\frac{-\Delta_y+iG_x}{\sqrt{a}}\right)^{n-k}
\end{aligned}\tag{5.36}$$

Let's focus on the k-dependent part first and define $m = \min(n, n')$, $M = \max(n, n')$

$$\begin{aligned}
&\sum_{k=0}^{\min(n,n')} \frac{n'!}{k!\,(n'-k)!}\frac{n!}{k!(n-k)!}2^k k!\left(\frac{\Delta_y+iG_x}{\sqrt{a}}\right)^{n'-k}\left(\frac{-\Delta_y+iG_x}{\sqrt{a}}\right)^{n-k}\\
=\;&\left(\frac{\Delta_y+iG_x}{\sqrt{a}}\right)^{n'-m}\left(\frac{-\Delta_y+iG_x}{\sqrt{a}}\right)^{n-m}\sum_{k=0}^{m}\frac{n'!}{k!\,(n'-k)!}\frac{n!}{(n-k)!}2^m\left(-\frac{\Delta_y^2+G_x^2}{2a}\right)^{m-k}\\
=\;&\left(\frac{\Delta_y+iG_x}{\sqrt{a}}\right)^{n'-m}\left(\frac{-\Delta_y+iG_x}{\sqrt{a}}\right)^{n-m}\sum_{k=0}^{m}\frac{M!}{(m-k)!k!}\frac{m!}{(M-m+k)!}2^m\left(-\frac{\Delta_y^2+G_x^2}{2a}\right)^{k}\\
=\;&\left(\frac{\Delta_y+iG_x}{\sqrt{a}}\right)^{n'-m}\left(\frac{-\Delta_y+iG_x}{\sqrt{a}}\right)^{n-m}2^m m!L_m^{(M-m)}\left(\frac{\Delta_y^2+G_x^2}{2a}\right)
\end{aligned}\tag{5.37}$$

Here $L_m^{(M-m)}\left(\frac{\Delta_y^2+G_x^2}{2a}\right)$ is associated Laguerre polynomial. Combine the coefficients with the k-independent part before

$$\begin{aligned}
&\delta_{k_y,k_y'+G_y}e^{\frac{\left(k_y+k_y'-iG_x\right)^2}{4a}}e^{-\left(\frac{k_y^2+{k_y'}^2}{2a}\right)}\frac{2^m m!}{\sqrt{2^n n!2^{n'}n'!}}\left(\frac{\Delta_y+iG_x}{\sqrt{a}}\right)^{n'-m}\left(\frac{-\Delta_y+iG_x}{\sqrt{a}}\right)^{n-m}\\
=\;&\delta_{k_y,k_y'+G_y}\sqrt{\frac{m!}{M!}}e^{\frac{\left(k_y+k_y'-iG_x\right)^2}{4a}}e^{-\left(\frac{k_y^2+{k_y'}^2}{2a}\right)}\left(\frac{G_x+i\Delta_y}{\sqrt{\Delta_y^2+G_x^2}}\right)^{n-n'}\left(\frac{i\sqrt{\Delta_y^2+G_x^2}}{\sqrt{2a}}\right)^{|n-n'|}\\
=\;&\delta_{k_y,k_y'+G_y}\sqrt{\frac{m!}{M!}}e^{-\frac{i\left(k_y+k_y'\right)G_x}{2a}}e^{-\frac{\Delta_y^2+G_x^2}{4a}}\left(\frac{G_x+i\Delta_y}{\sqrt{\Delta_y^2+G_x^2}}\right)^{n-n'}\left(\frac{i\sqrt{\Delta_y^2+G_x^2}}{\sqrt{2a}}\right)^{|n-n'|}
\end{aligned}\tag{5.38}$$

Since $\Delta_y = k_y' - k_y = -G_y$, we finally derive the same expression as in Ref [160, 235]

$$\begin{aligned}
&\left\langle\phi_{n,k_y}e^{ik_y y}\middle|e^{iG\cdot r}\middle|e^{ik_y' y}\phi_{n',k_y'}\right\rangle\\
=\;&\delta_{k_y,k_y'+G_y}\sqrt{\frac{m!}{M!}}e^{-\frac{i\left(k_y+k_y'\right)G_x}{2a}}e^{-\frac{G_y^2+G_x^2}{4a}}\\
\cdot\;&\left(\frac{G_x-iG_y}{\sqrt{G_y^2+G_x^2}}\right)^{n-n'}\left(\frac{i\sqrt{G_y^2+G_x^2}}{\sqrt{2a}}\right)^{|n-n'|}L_m^{(M-m)}\left(\frac{G_y^2+G_x^2}{2a}\right)
\end{aligned}\tag{5.39}$$

For now, we have not used the magnetic translation symmetry of lattice, which will loosen the constriction $\delta_{k_y,k_y'+G_y}$ to $\delta_{k_y,k_y'+G_y+T_y}$ where T_y corresponds to translation-invariant reciprocal vector. To utilize this, we define magnetic flux as $BS = \frac{p}{q}\frac{h}{e}$ so that $\frac{eB}{h} = \frac{2\pi p}{qS}$ and use three variables k_0, j, m to relabel $k_y \equiv k_0 + (jp+m)G_y = k_0 + \frac{2\pi}{L_M}(jp+m)$. Here k_0 is continuum and $0 < k_0 < G_y$, m corresponds to the unit moiré translation and $0 < m < p-1$, and j controls the magnetism translation $-\infty < j < +\infty$. Let's assume $L_1 = (0, L_M)$, $L_2 = \left(\frac{\sqrt{3}}{2}, \frac{1}{2}\right)L_M$ are two moiré lattice vectors. The property of this magnetism translation can be checked by adding mL_1 on

the Landau level wavefunction

$$\begin{aligned} & \phi_{n,k_y}(x)e^{ik_y(y+mL_M)} \\ = \; & \phi_{n,k_0,j,m'}(x)e^{i\left(k_0+\frac{2\pi}{L_M}(jp+m')\right)(y+mL_M)} \\ = \; & \phi_{n,k_0,j,m'}(x)e^{i\left(k_0+\frac{2\pi}{L_M}(jp+m')\right)y}e^{ik_0mL_M} \end{aligned} \tag{5.40}$$

Here we replace the label k_y with k_0, j, m. The wavefunction after translation is the same except for a phase shift $e^{ik_0mL_M}$. This should be obvious since we choose k_y as good quantum number and we are translating along y direction. At the same time, one can check the translation along the other direction jqL_2,

$$\begin{aligned} & \phi_{n,k_y}\left(x+\frac{jq\sqrt{3}L_M}{2}\right)e^{ik_y\left(y+\frac{jqL_M}{2}\right)} \\ = \; & \phi_{n,k_0,j'+j,m'}(x)e^{i\left(k_0+\frac{2\pi}{L_M}(j'p+m')\right)\left(y+\frac{jqL_M}{2}\right)} \end{aligned} \tag{5.41}$$

If there is a translation symmetry, there should be at most a phase different between $\phi_{n,k_y}\left(x+\frac{jq\sqrt{3}L_M}{2}\right)e^{ik_y\left(y+\frac{jqL_M}{2}\right)}$ and $\phi_{n,k_y}(x)e^{ik_y(y)}$ while this is not the case for the basis now. We would like to combine wavefunctions at different j' by a Fourier transformation to z

$$\Phi_{n,k_0,z,m'}(r) \equiv \frac{1}{\sqrt{N}}\sum_{j'=-\infty}^{\infty}\phi_{n,k_0,j',m'}(x)e^{i\left(k_0+\frac{2\pi}{L_M}(j'p+m')\right)y}e^{i\frac{2\pi}{L_M}(j'p+m')z} \tag{5.42}$$

Now we can check this transformation keeps mL_1 translation invariant property

$$\begin{aligned} & \Phi_{n,k_0,z,m'}\left(r+mL_1\right) \\ = \; & \frac{1}{\sqrt{N}}\sum_{j'=-\infty}^{\infty}\phi_{n,k_0,j',m'}(x)e^{i\left(k_0+\frac{2\pi}{L_M}(j'p+m')\right)(y+mL_M)}e^{i\frac{2\pi}{L_M}(j'p+m')z} \\ = \; & e^{ik_0mL_M}\Phi_{n,k_0,z,m'}(r) \end{aligned} \tag{5.43}$$

And if we require q is even (this will not cause any trouble since $\frac{p}{q}$ can approach any rational number), we will have

$$\begin{aligned}
&\Phi_{n,k_0,z,m'}\left(r+jqL_2\right)\\
=\;&\frac{1}{\sqrt{N}}\sum_{j'=-\infty}^{\infty}\phi_{n,k_0,j'+j,m'}(x)e^{i\left(k_0+\frac{2\pi}{L_M}(j'p+m')\right)\left(y+\frac{jqL_M}{2}\right)}e^{i\frac{2\pi}{L_M}(j'p+m')z}\\
=\;&\frac{1}{\sqrt{N}}\sum_{j'=-\infty}^{\infty}\phi_{n,k_0,j',m'}(x)e^{i\left(k_0+\frac{2\pi}{L_M}((j'-j)p+m')\right)\left(y+\frac{jqL_M}{2}\right)}e^{i\frac{2\pi}{L_M}((j'-j)p+m')z}\\
=\;&e^{-i\frac{2\pi}{L_M}jp(y+z)}\frac{1}{\sqrt{N}}\sum_{j'=-\infty}^{\infty}\phi_{n,k_0,j',m'}(x)e^{i\left(k_0+\frac{2\pi}{L_M}(j'p+m')\right)\left(y+\frac{jqL_M}{2}\right)}e^{i\frac{2\pi}{L_M}(j'p+m')z}\\
=\;&e^{-i\frac{2\pi}{L_M}jp(y+z)}e^{ik_0\frac{jqL_M}{2}}\Phi_{n,k_0,z,m'}(r)
\end{aligned}\tag{5.44}$$

Under this new basis where translation symmetry along the other direction is also involved, we can rewrite the elements of Hamiltonian matrix. For $\delta_{m_i,m_i'}$, it is straightforward by replacing it with $\delta_{k_i,k_i'}\delta_{z_i,z_i'}\delta_{m_i,m_i'}$. For matrix element $\left\langle\phi_{n,k_y}e^{ik_yy}\middle|e^{iG\cdot r}\middle|e^{ik_y'y}\phi_{n',k_y'}\right\rangle$, it should be replaced by

$$\begin{aligned}
&\left\langle\Phi_{n,k_0,z,l}(r)\middle|e^{iG\cdot r}\middle|\Phi_{n',k_0',z',l'}(r)\right\rangle\\
=\;&\frac{\delta_{k_0,k_0'}\delta_{l,l'+1}}{\sqrt{N}}e^{i\frac{2\pi}{L_M}(l'z'-lz)}\sum_{j'=-\infty}^{\infty}e^{-\frac{i\left(2k_0+\frac{2\pi}{L_M}(2j'p+2l'+1)\right)G_x}{2a}}e^{i\frac{2\pi}{L_M}j'p(z'-z)}\\
&\sqrt{\frac{m!}{M!}}e^{-\frac{G_y^2+G_x^2}{4a}}\left(\frac{G_x-iG_y}{\sqrt{G_y^2+G_x^2}}\right)^{n-n'}\left(\frac{i\sqrt{G_y^2+G_x^2}}{\sqrt{2a}}\right)^{|n-n'|}L_m^{(M-m)}\left(\frac{G_y^2+G_x^2}{2a}\right)\\
=\;&\delta_{k_0,k_0'}\delta_{l,l'+1}\delta_{z',z}e^{-i\frac{2\pi}{L_M}z}e^{-\frac{i\left(2k_0+\frac{2\pi}{L_M}(2l'+1)\right)G_x}{2a}}\\
&\sqrt{\frac{m!}{M!}}e^{-\frac{G_y^2+G_x^2}{4a}}\left(\frac{G_x-iG_y}{\sqrt{G_y^2+G_x^2}}\right)^{n-n'}\left(\frac{i\sqrt{G_y^2+G_x^2}}{\sqrt{2a}}\right)^{|n-n'|}L_m^{(M-m)}\left(\frac{G_y^2+G_x^2}{2a}\right)
\end{aligned}\tag{5.45}$$

One can see the variables k_0, z will at most contribute a trivial global phase to the Hamiltonian so that one can just take $k_0=0$ and $z=0$ to compute the spectrum. Similarly, when we consider $L_1=\left(-\frac{1}{2},\frac{\sqrt{3}}{2}\right)L_s, L_2=(1,\ 0)L_s$ which matches the mesh of our G_j and g_j. We replace the L_M in above formula with $\sqrt{3}L_s$. The matrix elements for G_1,G_2,G_3,G_4,G_5,G_6 are the similar as before except for we should use $\delta_{l,l'+10},\delta_{l,l'+5},\delta_{l,l'-5},\delta_{l,l'-10},\delta_{l,l'-5},\delta_{l,l'+5}$ to match the graphene/hbn scattering along k_y direction. The matrix elements for $G_1',G_2',G_3',G_4',G_5',G_6'$ are similar with $\delta_{l,l'+3},\delta_{l,l'+9},\delta_{l,l'+6},\delta_{l,l'-3},\delta_{l,l'-9},\delta_{l,l'-6}$.

In a word, for G_α we have

$$\begin{aligned}
&\left\langle \Phi_{n,k_0,z,l}(r)\middle| e^{iG\cdot r}\middle|\Phi_{n',k_0',z',l'}(r)\right\rangle \\
= \;& \delta_{k_0,k_0'}\delta_{l,l_\alpha'}\delta_{z',z} e^{-\frac{i\frac{2\pi}{\sqrt{3}L_s}(l'+l_\alpha')G_x}{2a}} \\
& \sqrt{\frac{m!}{M!}} e^{-\frac{G_y^2+G_x^2}{4a}} \left(\frac{G_x-iG_y}{\sqrt{G_y^2+G_x^2}}\right)^{n-n'} \left(\frac{i\sqrt{G_y^2+G_x^2}}{\sqrt{2a}}\right)^{|n-n'|} L_m^{(M-m)}\left(\frac{G_y^2+G_x^2}{2a}\right)
\end{aligned} \tag{5.46}$$

For G_α', we have the same formula except for replacing $G \to G'$. Now we have collected all the formulas needed for writing the Hamiltonian in Dirac Landau level basis. The dimension of the final Hamiltonian we would like to diagonalize is $4N(p,\theta)\times p$. Here $N(p,\theta)$ is the amount of cut off Landau levels at magnetic flux $\frac{p}{q}$ and twist angle θ. Since the energy scale of Landau level scales as $\epsilon_n = \hbar v_F\sqrt{2n\frac{2\pi p}{qS}}$, we keep the amount of $N(p,\theta)$ to make sure $N(p,\theta)\times p \approx const\ integer$ when continuously tuning integer p at a fixed twist angle θ. From this expression, one can also see when twist angle is deduced which enlarges the area of the moiré unit cell S, the required $N(p,\theta)$ should also be enlarged to observe converged spectrum at the low energy region. The energy spectra for $V_{h/h}=0$ and $V_{h/h}=100meV$ are shown in Fig 5.3.

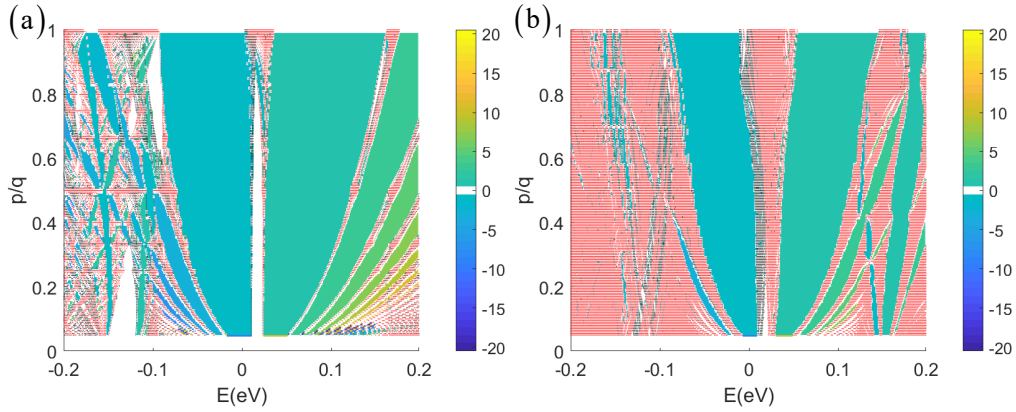


Figure 5.3: Energy spectra versus magnetic flux p/q for $V_{h/h}=0$ (a) and $V_{h/h}=100meV$ (b). The dark dots and red dots label states from different valleys and the colored gaps are identified with quantized Hall conductance by Diophantine equation. Only [-20,20] quantized Hall conductance are plotted and we take a cutoff for $N(p,\theta)\times p\approx 2200$ for (a) and $N(p,\theta)\times p\approx 22000$ for (b).

After deriving the energy spectrum, we are ready to compute the Hall conductance and plot the Wannier diagram [246](transform the $p/q-E$ spectrum to $p/q-\nu$ diagram where ν directly corresponds to charge/hole density in experiments). Computing the Hall conductance is basically solving the Diophantine equation [10, 11, 14]

$$r = pt + qs \tag{5.47}$$

Here r is the number of filled states, t is the quantized Hall conductance and s is the integer independent with magnetic field. Within a gap, integers t, s will not change so that the quantized Hall conductivity is

$$\frac{r'-r}{p'-p} = t. \tag{5.48}$$

For the nearest two magnetic flux we take $p'-p=1$, the quantized Hall conductivity is just the difference of filled states between two nearest p. For the continuous model we discuss, the filled states (by particles or holes) should be counted from half filling. We set the axis as $p/q-\nu_{g/h}$ and plot density of states with a finite temperature broadening to show the Wannier diagram. The results for $V_{h/h}=0$ and $V_{h/h}=100meV$ are shown in Fig 5.4. It is obviously that when we turn on $V_{h/h}$, there are some branches coming from non-integer $\nu_{g/h}$ especially near $p=0, \nu_{g/h}=-4$ (it is still the integer filling of super-moiré bands). This will be one feature of forming super-moiré.

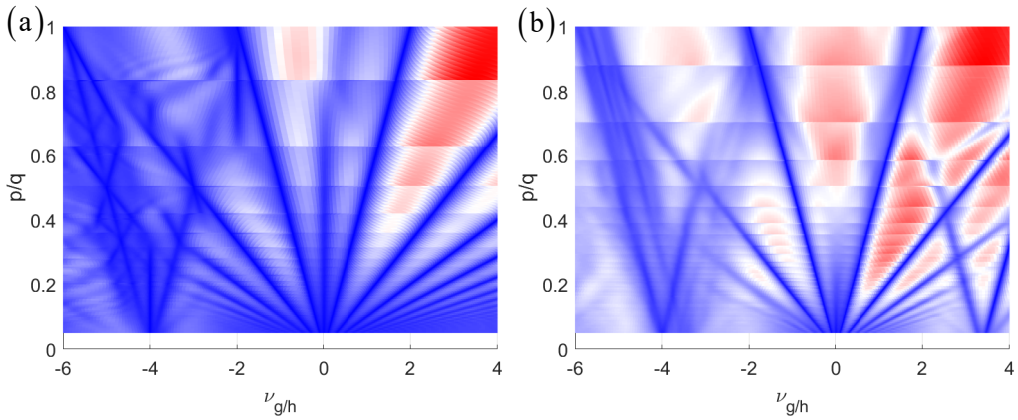


Figure 5.4: Density of states map with filling of graphene/hbn bands $\nu_{g/h}$ and magnetic flux p/q for $V_{h/h}=0$ (a) and $V_{h/h}=100meV$ (b). The cutoff setting is the same as used in Fig 5.3 and we take $kT=2meV$ for plotting broadening density of states where deep blue indicates low density of states corresponding a gap. One can read the quantized Hall conductivity from the slop of blue lines directly.

Besides the Hall response, one can also detect super-moiré forming from the Drude conductance oscillation with magnetic field as observed in experiments [247–249]. Since we are not working in plane wave basis but in modified Landau level basis, one needs to transform the velocity operator from plane wave basis to the one in the same basis diagonalizing the Hamiltonian. In Hamiltonian eigenstate $|n\rangle$ basis,

$$\begin{aligned}
\sigma_{xx} &\propto \int d^2k \sum_n \left(\left\langle n \left| \frac{\partial H}{\partial k_x} \right| n \right\rangle \right)^2 \frac{\partial f^0}{\partial \epsilon_n} \\
&= \int d^2k \ \mathrm{Tr}\left[U^\dagger \left(\frac{\partial H_g}{\partial k_x} \right) U \odot U^\dagger \left(\frac{\partial H_g}{\partial k_x} \right) U \odot \frac{\partial f^0}{\partial \epsilon} \right] \\
&\equiv \mathrm{Tr}\left[U^\dagger M U \odot U^\dagger M U \odot \frac{\partial f^0}{\partial \epsilon} \right] \frac{\sqrt{3}}{2} g_0^2
\end{aligned} \tag{5.49}$$

Here $\odot$ means the corresponding elements product (i.e., Hadamard product) and U is the unitary transformation from plane wave basis to Hamiltonian eigenstate basis. Since the plane wave basis Hamiltonian is linear with k_x, $M \equiv \frac{\partial H_g}{\partial k_x}$ is a constant matrix and the integral over Brillouin zone just gives the area $\frac{\sqrt{3}}{2}g_0^2$. In plane wave basis, M is written as

$$M = \begin{pmatrix} 0 & 1 & 0 & 0 & \\ 1 & 0 & 0 & 0 & \ddots \\ 0 & 0 & 0 & 1 & \\ 0 & 0 & 1 & 0 & \\ & \ddots & & & \ddots \end{pmatrix} \tag{5.50}$$

Here, the moiré potential is dependent on G, G' and independent with k_x. Because the unitary transformation will not change the eigenvalues and the trace, one can conclude the matrix after transformation also consists of half eigenvalues 1 and half -1 and a trivial trace gives $\mathrm{Tr}\left[U^\dagger M U\right] = 0$. Ignoring the finite density of states weight $\frac{\partial f^0}{\partial \epsilon}$, the aim becomes to find in which case, the trace $\mathrm{Tr}\left[U^\dagger M U \odot U^\dagger M U\right]$ will give nontrivial value. This demands to understand the matrix $U^\dagger M U$. We separate the transformation in U to two parts, from plane wave to Landau level and from Landau level to Hamiltonian eigenstate. The first part is independent with the magnetic field and one can write down an effective one-dimension Hamiltonian to describe M in this Landau level basis.

$$H_M(k_y) = \frac{i}{\sqrt{2}}\left(c_1^\dagger c_0 - c_{-1}^\dagger c_0\right) + \frac{i}{2}\sum_{n>1}\left(c_n^\dagger c_{n-1} + c_n^\dagger c_{1-n}\right) - \frac{i}{2}\sum_{n<-1}\left(c_n^\dagger c_{-n-1} + c_n^\dagger c_{1+n}\right) + h.c. \tag{5.51}$$

Here $n = 0, \pm 1, \pm 2, \ldots$ is Landau level label and this Hamiltonian has amount of k_y degenerate copies. Write it in matrix form where each block matrix $H_{n,m}$ labels the hopping between n, m Landau levels and is the coefficient multiplying identity in k_y subspace.

$$H_M = \begin{pmatrix} 0 & H_{0,1} & H_{0,-1} & 0 & 0 & 0 & 0 \\ H_{1,0} & 0 & 0 & H_{1,2} & H_{1,-2} & 0 & 0 \\ H_{-1,0} & 0 & 0 & H_{-1,2} & H_{-1,-2} & 0 & 0 \\ 0 & H_{2,1} & H_{2,-1} & 0 & 0 & H_{2,3} & H_{2,-3} \\ 0 & H_{-2,1} & H_{-2,-1} & 0 & 0 & H_{-2,3} & H_{-2,-3} \\ 0 & 0 & 0 & H_{3,2} & H_{3,-2} & 0 & 0 \\ 0 & 0 & 0 & H_{-3,2} & H_{-3,-2} & 0 & 0 \end{pmatrix} \tag{5.52}$$

Now the aim reduces to what kind of the second transformation can make the norm of diagonal elements larger. A naive pure Landau level case where the transformation is identity matrix obviously cannot do this job since the diagonal elements without any transformation are zeros. Another way to look at this problem is checking the fully diagonal case, where the square of the eigenvalues reaches the maximum, i.e., any unitary transformation applying on the diagonal case will decrease the mode of diagonal

elements so that $1, 1, ...$ is the largest square of diagonal elements case

$$\lambda_i = \sum_\alpha U^\dagger_{i,\alpha}(\pm 1)_{\alpha,\alpha}U_{\alpha,i} = \sum_\alpha (\pm 1)_{\alpha,\alpha}\left|u_{\alpha,i}\right|^2 \leq \sum_\alpha \left|u_{\alpha,i}\right|^2 = 1 \tag{5.53}$$

Another conclusion one can derive is if the perturbation only hybridizes different k_y labels within the same Landau level without mixing different Landau levels, then apparently after applying this unitary transformation the diagonal blocks are still zeros. This indicates the wavefunction needs to at least hybridize two Landau levels to give a finite contribution for σ_{xx}. For the super-moiré situation, the requirement will be either original moiré can hybridize but not necessarily both. And this oscillation can still be observed even when one of the component moiré is not large compared with the Landau levels gap. The numerical results for $\mathrm{Tr}\left[U^\dagger MU \odot U^\dagger MU \odot \frac{\partial f^0}{\partial \epsilon}\right]\frac{\sqrt{3}}{2}g_0^2$ at $V_{h/h} = 0$ and $V_{h/h} = 100meV$ are shown in Fig 5.5. One can see the clear oscillation peaks near fractional and integer magnetic flux case which should directly correspond to oscillations observation in an experiment. A naive understanding for this peak behavior at fractional and integer magnetic flux is merged fractal bands at rational flux can contribute larger velocity. However, a quantitative understanding is still absent and waited for future exploring.

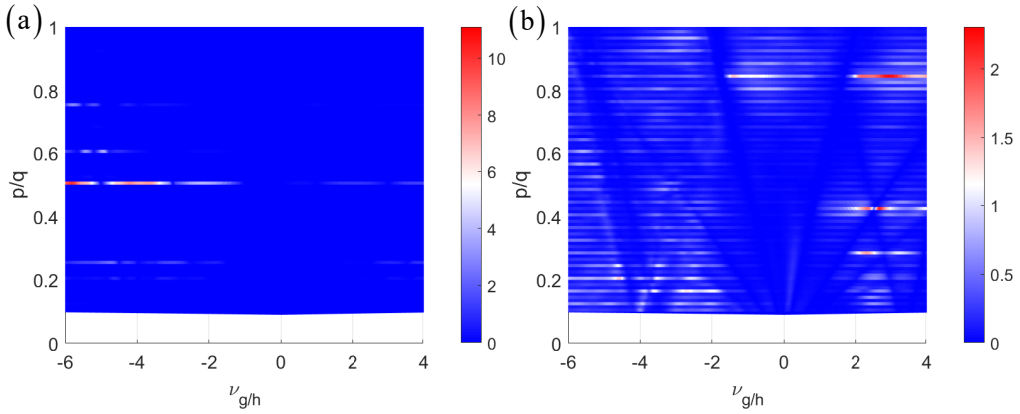


Figure 5.5: Drude conductance σ_{xx} map with filling of graphene/hbn bands $\nu_{g/h}$ and magnetic flux p/q for $V_{h/h} = 0$ (a) and $V_{h/h} = 100meV$ (b). The cutoff setting is the same as used in Fig 5.3 and we take $kT = 2meV$ for computing $\frac{\partial f^0}{\partial_{\epsilon_n}}$. One can see the small $V_{h/h} = 100meV$ can produce obvious oscillation at integer super-moiré flux while the amplitude of σ_{xx} becomes much smaller than $V_{h/h} = 0$.

5.3 Further discussion

Starting from this Landau level with moiré potential basis (which we may call Hofstadter's butterfly basis), what will be brought by putting interaction in is even more interesting. The integer-flux TBG case has been studied analytically and reentrant correlated insulators are derived [164, 165] while interesting fractional filling is still left for both numerical and possible analytical study in the future.

Appendix A

Mathematical preparation on Quantum Monte Carlo

A.1 Markov chain Monte Carlo

In this section, I would like to introduce how to generate a series of configuration according to a given probability distribution by Markov chain technique [250]. The well known classical Ising model will be adopted to indicate this idea. The Hamiltonian of Ising model is shown as

$$H = J \sum_{\langle i,j \rangle} s_i s_j. \tag{A.1}$$

Here $\langle i,j \rangle$ means the summation is over all the nearest neighbor sites i,j and s_i is a number which can only take ± 1. The partition function of this model is written as

$$Z = \mathrm{Tr}(e^{-\beta H}) = \sum_{\{s\}} \prod_{\langle i,j \rangle} e^{-\beta J s_i s_j}. \tag{A.2}$$

Here $\beta \equiv \frac{1}{T}$ is the inverse of temperature, the trace $\mathrm{Tr}(\cdots)$ means summation over all possible configuration $\{s\}$ and because of $s_i s_j$ are some numbers one can rewrite the summation on exponent as a product. Since one cares more about the ensemble average but not the partition function itself, we can see any observable $\hat{O}$ can be expressed as

$$\langle \hat{O} \rangle = \frac{\mathrm{Tr}(\hat{O} e^{-\beta H})}{\mathrm{Tr}(e^{-\beta H})} = \sum_{\{s\}} \frac{\prod_{\langle i,j \rangle} e^{-\beta J s_i s_j}}{\sum_{\{s'\}} \prod_{\langle i',j' \rangle} e^{-\beta J s'_{i'} s'_{j'}}} O_{\{s\}} \equiv \sum_{\{s\}} p_{\{s\}} O_{\{s\}}. \tag{A.3}$$

One can easily see $p_{\{s\}} \equiv \dfrac{\prod_{\langle i,j \rangle} e^{-\beta J s_i s_j}}{\sum_{\{s'\}} \prod_{\langle i',j' \rangle} e^{-\beta J s'_{i'} s'_{j'}}}$ is positive definite and normalized (i.e., $\sum_{\{s\}} p_{\{s\}} = 1$) so that it is a well defined probability mass function (PMF). We have transformed the problem computing ensemble average of an observable to deriving weighted average for a given PMF, which one can apply Markov chain Monte Carlo to solve. This is the starting point for all kinds of Monte Carlo methods.

The importance sampling idea comes from the fact that the whole configuration space $\{s\}$ is so huge (exponentially dependent on system size) that exhausting all configurations is almost impossible for a large size system. However, the good news is all of them contribute not equally. This PMF is basically an exponential function of bond energy Js_is_j, which means as long as the fluctuation of the observable between different configurations is below exponent (It is actually $O(1)$ in most of cases we care about), the (system-size) polynomial joint exponential distribution can be approximately determined by (system-size) polynomial amount of configurations. Our task next is just finding those important configurations out. We use a Markov chain to do this job.

Let's assume we start at the configuration μ, we have a transition probability $P(\mu \to \nu)$ to update our system into configuration ν. We require this probability is normalized so that $\sum_\nu P(\mu \to \nu) = 1$ for any μ. Another requirement is we hope after some steps, no matter we start from which distribution p_α, we end with the balanced distribution we want p_ν (or just $p_{\{s\}}$ in our Ising model case). A sufficient condition for achieving this is after some steps, we should always have

$$p_\nu P(\nu \to \mu) = p_\mu P(\mu \to \nu). \tag{A.4}$$

This is so-called condition of detailed balance that transition current is conserved between any two configurations. This stronger constrain is used to rule out the limit cycle case and sum over μ on both sides of the equation one can derive the condition of balance

$$p_\nu = \sum_\mu p_\mu P(\mu \to \nu). \tag{A.5}$$

In our practice, we always choose $P(\mu \to \nu)$ satisfying the stronger detailed balance constrain and make sure our update process is ergodic. Then from a random distribution p_α we can always flow to the expected single p_ν by applying $P(\alpha \to \alpha')$ enough times (The detailed balance condition and ergodic makes sure $P(\alpha \to \alpha')$ is an irreducible aperiodic matrix so that one can apply Perron–Frobenius theorem to prove 1 is its maximum single eigenvalue). Specifically, we take Metropolis algorithm to fulfill a ergodic and detailed balance constrained sampling. The $P(\{s\} \to \{s'\})$ matrix can take

$$P(\{s\} \to \{s'\}) = \min\{1, \frac{p_{\{s'\}}}{p_{\{s\}}}\}. \tag{A.6}$$

If we try flipping site one by one, the ergodic is straightforward. One can also check the detailed balance condition $\frac{P(\{s\}\to\{s'\})}{P(\{s'\}\to\{s\})} = \frac{p_{\{s'\}}}{p_{\{s\}}}$ is obvious. After determining $P(\{s\} \to \{s'\})$, the algorithm goes as generate a random configuration $\{s\}$, try updating s_i on each site with possibility $\min\{1, \frac{p_{s_i'}}{p_{s_i}}\}$ one by one (generate a random number between 0 and 1, if it is smaller than $\frac{p_{s_i'}}{p_{s_i}}$ then update the site, else keep it unchanged), measure the observable after Markov chain reaching balance (fluctuation of observable becomes Gaussian from the law of large numbers if the PMF is converged) and compute the average of the sampled observable will derive the final result.

A.2 Wick's theorem

Wick's theorem is an extremely important formula in Quantum Monte Carlo measurements as well as mean field approximation. In this section, I will go through its usually used forms under mean field wavefunction average and ensemble average for discrete degree of freedom fermion systems [8, 9].

Let's prove the simple case first, where we choose a single state in occupation basis such as $|\psi_s\rangle = |0,1,1,0,...\rangle$ where $0,1$ means there is zero or one particle on the corresponding site. Then one can arrange the sequence of $\hat{c}_i^\dagger \hat{c}_j \hat{c}_{i'}^\dagger \hat{c}_{j'}...$ with the normal order label $:\hat{c}_i^\dagger \hat{c}_j \hat{c}_{i'}^\dagger \hat{c}_{j'}...:$ so that $\hat{c}_i^\dagger/\hat{c}_i$ is always put on the right if there is $1/0$ particle on site i. The arranged sequence in this way has the property $\left\langle \psi_s| :\hat{c}_i^\dagger \hat{c}_j \hat{c}_{i'}^\dagger \hat{c}_{j'}...: |\psi_s\right\rangle = 0$ since this is just the definition of this arrangement. This gain demands a pain that during the arrangement, the anti-commutation relationship may contract two operators and replaces it with a number (e.g., an additional $\delta_{i,j}$ will appear when one want to replace $\hat{c}_i^\dagger \hat{c}_j$ by $-\hat{c}_j \hat{c}_i^\dagger$ if $\hat{c}_j \hat{c}_i^\dagger$ is the required sequence while there is no such a term if $\hat{c}_i^\dagger \hat{c}_j$ is already the correct order). All the possible ways of this contribution are equal to different ways picking $\hat{c}^\dagger$ operator from $i, i', ...$ list and picking $\hat{c}$ operator from $j, j', ...$ list. After considering one contraction, e.g., contraction between i, j, we can continuously arrange the left operators in normal order to make $\left\langle \psi_s| :\hat{c}_{i'}^\dagger \hat{c}_{j'}...: |\psi_s\right\rangle = 0$. Then the result becomes clear that when we want to compute $\left\langle \psi_s|\hat{c}_i^\dagger \hat{c}_j \hat{c}_{i'}^\dagger \hat{c}_{j'}...|\psi_s\right\rangle$, we can try arranging operators in normal order and only left fully contracted terms such as $N_{i,j}N_{i',j'}...$ can give a contribution, where $N_{i,j}$ picks $\delta_{i,j}$ if $\hat{c}_i^\dagger \hat{c}_j$ is originally not in the correct order and picks 0 if it is. According to this definition, one can see the number $N_{i,j}$ is just equal to $\left\langle \psi_s|\hat{c}_i^\dagger \hat{c}_j|\psi_s\right\rangle$. There will also be $\pm$ sign before these terms which comes from anti-commutation and is equal to $(-1)^{C(P)}$. Based on above derivation, we conclude

$$\left\langle \psi_s|\hat{c}_i^\dagger \hat{c}_j \hat{c}_{i'}^\dagger \hat{c}_{j'}...|\psi_s\right\rangle = \sum_P (-1)^{C(P)} \prod_{ij} \left\langle \psi_s|P[\hat{c}_{i(P)}^\dagger \hat{c}_{j(P)}]|\psi_s\right\rangle. \tag{A.7}$$

Here the summation is over all the possible contraction ways where one of the contracted pair from $i, i', ...$ and the other from $j, j', ...$, the product is over all ij pairs, $C(P)$ counts the times of permutation that needed to adjust the sequence from $i, j, ...$ to $i(P), j(P), ...$ and the $P[...]$ means rearrange the $\hat{c}_{i(P)}^\dagger \hat{c}_{j(P)}$ position according to the relative positions $i(P), j(P)$ in sequence $i, j, i', j', ...$ To understand this formula better, I give an example

for six-operator sequence case below

$$\begin{aligned}\left\langle\psi_s|\hat{c}_i^\dagger\hat{c}_j\hat{c}_{i'}^\dagger\hat{c}_{j'}\hat{c}_{i''}^\dagger\hat{c}_{j''}|\psi_s\right\rangle &= \left\langle\psi_s|\hat{c}_i^\dagger\hat{c}_j|\psi_s\right\rangle\left\langle\psi_s|\hat{c}_{i'}^\dagger\hat{c}_{j'}|\psi_s\right\rangle\left\langle\psi_s|\hat{c}_{i''}^\dagger\hat{c}_{j''}|\psi_s\right\rangle \\ &+ \left\langle\psi_s|\hat{c}_i^\dagger\hat{c}_{j'}|\psi_s\right\rangle\left\langle\psi_s|\hat{c}_j\hat{c}_{i'}^\dagger|\psi_s\right\rangle\left\langle\psi_s|\hat{c}_{i''}^\dagger\hat{c}_{j''}|\psi_s\right\rangle \\ &+ \left\langle\psi_s|\hat{c}_i^\dagger\hat{c}_{j''}|\psi_s\right\rangle\left\langle\psi_s|\hat{c}_{i'}^\dagger\hat{c}_{j'}|\psi_s\right\rangle\left\langle\psi_s|\hat{c}_j\hat{c}_{i''}^\dagger|\psi_s\right\rangle \\ &+ \left\langle\psi_s|\hat{c}_i^\dagger\hat{c}_j|\psi_s\right\rangle\left\langle\psi_s|\hat{c}_{i'}^\dagger\hat{c}_{j''}|\psi_s\right\rangle\left\langle\psi_s|\hat{c}_{j'}\hat{c}_{i''}^\dagger|\psi_s\right\rangle \\ &- \left\langle\psi_s|\hat{c}_i^\dagger\hat{c}_{j'}|\psi_s\right\rangle\left\langle\psi_s|\hat{c}_{i'}^\dagger\hat{c}_{j''}|\psi_s\right\rangle\left\langle\psi_s|\hat{c}_j\hat{c}_{i''}^\dagger|\psi_s\right\rangle \\ &+ \left\langle\psi_s|\hat{c}_i^\dagger\hat{c}_{j''}|\psi_s\right\rangle\left\langle\psi_s|\hat{c}_j\hat{c}_{i'}^\dagger|\psi_s\right\rangle\left\langle\psi_s|\hat{c}_{j'}\hat{c}_{i''}^\dagger|\psi_s\right\rangle \quad \text{(A.8)}\end{aligned}$$

Since there are 6 possible pairing ways from i, i', i'' to j, j', j'', we have 6 terms in total. In each pair, the operator with less prime label, which means this operator shows up in i, j, i', j', i'', j'' earlier, is listed at the front. From i, j, i', j', i'', j'' to i, j', j, i', i'', j'', we need to permute twice which contributes $(-1)^2 = +1$. While from i, j, i', j', i'', j'' to i, j', i', j'', j, i'', we need to permute 5 times so that it contributes $(-1)^5 = -1$.

The formula for wavefunction in $|\psi_s\rangle$ in ij occupation basis is kind of trivial because we actually know the result of left-hand side (LHS) can only be $0, 1, -1$. However, this form can be easily transformed to the case where single particle product state $|\psi\rangle$ is in a general mean field basis and may not be eigenstate of $\hat{c}_i^\dagger\hat{c}_i$. The derivation is straightforward by using unitary transformation $\hat{c}_i^\dagger = \sum_\alpha u_{i,\alpha}^*\hat{c}_\alpha^\dagger, \hat{c}_j = \sum_\beta u_{j,\beta}\hat{c}_\beta$.

$$\begin{aligned}\left\langle\psi|\hat{c}_i^\dagger\hat{c}_j\hat{c}_{i'}^\dagger\hat{c}_{j'}...|\psi\right\rangle &= \sum_{\alpha,\beta,\alpha',\beta',...}\left\langle\psi|u_{i,\alpha}^*\hat{c}_\alpha^\dagger u_{j,\beta}\hat{c}_\beta u_{i',\alpha'}^*\hat{c}_{\alpha'}^\dagger u_{j',\beta'}\hat{c}_{\beta'}...|\psi\right\rangle \\ &= \sum_{\alpha,\beta,\alpha',\beta',...}\sum_P(-1)^{C(P)}\prod_{\alpha\beta}\left\langle\psi|P[u_{i(P),\alpha(P)}^*\hat{c}_{\alpha(P)}^\dagger u_{j(P),\beta(P)}\hat{c}_{\beta(P)}]|\psi\right\rangle \\ &= \sum_P(-1)^{C(P)}\prod_{ij}\left\langle\psi|P[\hat{c}_{i(P)}^\dagger\hat{c}_{j(P)}]|\psi\right\rangle \quad \text{(A.9)}\end{aligned}$$

Since the coefficients $u_{i,\alpha}^*, u_{j,\beta}$ follow tightly with $\hat{c}_\alpha^\dagger, \hat{c}_\beta$, one can recover the $\hat{c}_i^\dagger, \hat{c}_j$ form after contraction in $|\psi\rangle$ basis. Now, we can conclude the Wick's theorem above works for any single particle product state average (or mean field average and mean field trace). Actually, in our derivation of Hall conductance formula assuming mean field wavefunction in Chapter 2, we have used this form to expand current-current correlation function.

Then let's look at Wick's theorem for ensemble average case. Assume we have a mean field "Hamiltonian" $\hat{H} \equiv \sum_{i,j} h_{i,j}\hat{c}_i^\dagger\hat{c}_j$ and use it to define the density matrix operator $\hat{\rho} \equiv e^{-\beta\hat{H}}$ as our ensemble weight. Explicitly, the Wick's theorem is

$$\mathrm{Tr}(\hat{\rho}\hat{c}_i^\dagger\hat{c}_j\hat{c}_{i'}^\dagger\hat{c}_{j'}...) = \sum_P(-1)^{C(P)}\prod_{ij}\mathrm{Tr}(\hat{\rho}P[\hat{c}_{i(P)}^\dagger\hat{c}_{j(P)}]) \quad \text{(A.10)}$$

The wavefunction average form gives us a hint for proving the form above. With the

similar idea, we first assume the sequence $\hat{c}^\dagger_\alpha \hat{c}_\beta \hat{c}^\dagger_{\alpha'} \hat{c}_{\beta'} ...$ is already in $-\beta\hat{H}$ diagonalized basis with eigenvalue ϵ_i and expand according to eigenstates so that

$$\begin{aligned}
\mathrm{Tr}(\hat{\rho}\hat{c}^\dagger_\alpha \hat{c}_\beta \hat{c}^\dagger_{\alpha'} \hat{c}_{\beta'} ...) &= \sum_{\gamma_1,\gamma_2,...} e^{\sum_{\{i|\gamma_i=1\}} \epsilon_i} \left\langle \gamma_1\gamma_2...|\hat{c}^\dagger_\alpha \hat{c}_\beta \hat{c}^\dagger_{\alpha'} \hat{c}_{\beta'} ...|\gamma_1\gamma_2...\right\rangle \\
&= \sum_{\gamma_1,\gamma_2,...} e^{\sum_{\{i|\gamma_i=1\}} \epsilon_i} \sum_P (-1)^{C(P)} \prod_{\alpha\beta} \left\langle \gamma|P[\hat{c}^\dagger_{\alpha(P)} \hat{c}_{\beta(P)}]|\gamma\right\rangle \\
&= \sum_P (-1)^{C(P)} \prod_{i\notin\Gamma} (1+e^{\epsilon_i}) \sum_\Gamma e^{\epsilon_\Gamma} \prod_{\alpha\beta} \left\langle \psi_\Gamma|P[\hat{c}^\dagger_{\alpha(P)} \hat{c}_{\beta(P)}]|\psi_\Gamma\right\rangle
\end{aligned} \tag{A.11}$$

Here $\gamma = 0, 1$ labels the state is empty/occupied. In the last line, we define a set Γ to label all $\alpha, \beta, \alpha', \beta', ...$ single particle orbitals so that summation over $\hat{\rho}$ applying on all those irrelevant orbitals gives $\prod_{i\notin\Gamma}(1+e^{\epsilon_i})$. The left summation is for the relevant orbitals. If the orbital is occupied it will contribute ϵ and if it is empty it contributes zero in ϵ_Γ. Remember according to the definition of the density matrix $\mathrm{Tr}(\hat{\rho}) = 1$ so that $\prod_i (1+e^{\epsilon_i}) = 1$ and $\prod_{i\neq\alpha}(1+e^{\epsilon_i}) \prod_{i\neq\alpha'}(1+e^{\epsilon_i})... = \prod_{i\notin\Gamma}(1+e^{\epsilon_i})$. Based on this understanding, we can recover the trace product form

$$\begin{aligned}
\mathrm{Tr}(\hat{\rho}\hat{c}^\dagger_\alpha \hat{c}_\beta \hat{c}^\dagger_{\alpha'} \hat{c}_{\beta'} ...) &= \sum_P (-1)^{C(P)} \prod_{i\notin\Gamma} (1+e^{\epsilon_i}) \sum_\Gamma e^{\epsilon_\Gamma} \prod_{\alpha\beta} \left\langle \psi_\Gamma|P[\hat{c}^\dagger_{\alpha(P)} \hat{c}_{\beta(P)}]|\psi_\Gamma\right\rangle \\
&= \sum_P (-1)^{C(P)} \prod_{\alpha\beta} \sum_\Gamma e^{\epsilon_{\alpha(P),\beta(P)}} \prod_{i\neq\alpha(P),\beta(P)} (1+e^{\epsilon_i}) \left\langle \psi_\Gamma|P[\hat{c}^\dagger_{\alpha(P)} \hat{c}_{\beta(P)}]|\psi_\Gamma\right\rangle \\
&= \sum_P (-1)^{C(P)} \prod_{\alpha\beta} \mathrm{Tr}(\hat{\rho}P[\hat{c}^\dagger_{\alpha(P)} \hat{c}_{\beta(P)}])
\end{aligned} \tag{A.12}$$

Similarly, for operator sequence written in another basis, the unitary transformation coefficients $u^*_{i,\alpha}, u_{j,\beta}$ follow $\hat{c}^\dagger_\alpha, \hat{c}_\beta$ tightly so that we finally prove

$$\mathrm{Tr}(\hat{\rho}\hat{c}^\dagger_i \hat{c}_j \hat{c}^\dagger_{i'} \hat{c}_{j'} ...) = \sum_P (-1)^{C(P)} \prod_{ij} \mathrm{Tr}(\hat{\rho}P[\hat{c}^\dagger_{i(P)} \hat{c}_{j(P)}]) \tag{A.13}$$

We use this formula both in the jumped derivation of finite temperature Hall conductance in Chapter 2 as well as the correlation measurement of our Determinant Quantum Monte Carlo (DQMC) simulation in Chapter 3 and Chapter 4. When those operators are written in Heisenberg picture and imaginary-time dependent, one can rewrite the imaginary-time-order operator into the form above where there are some coefficients from commutation and absorb them to recover the imaginary-time-order form in the final result.

$$\mathrm{Tr}(T\{\hat{\rho}\hat{c}^\dagger_i \hat{c}_j \hat{c}^\dagger_{i'} \hat{c}_{j'} ...\}) = \sum_P (-1)^{C(P)} \prod_{ij} \mathrm{Tr}(T\{\hat{\rho}P[\hat{c}^\dagger_{i(P)} \hat{c}_{j(P)}]\}) \tag{A.14}$$

A.3 Suzuki–Trotter expansion

In this section, we introduce the Suzuki–Trotter expansion for imaginary-time density matrix $\hat{\rho} \equiv e^{-\beta \hat{H}}$ where $\hat{H} \equiv \hat{H}_1 + \hat{H}_2 + \cdots$ and there are N terms in total for Hamiltonian $\hat{H}$. This expansion is based on the Zassenhaus formula

$$e^{t(\hat{X}+\hat{Y})} = e^{t\hat{X}} e^{t\hat{Y}} e^{-\frac{t^2}{2}[\hat{X},\hat{Y}]} e^{\frac{t^3}{6}(2[\hat{Y},[\hat{X},\hat{Y}]]+[\hat{X},[\hat{X},\hat{Y}]])} \cdots . \tag{A.15}$$

When t is small, we have Suzuki–Trotter expansion

$$e^{t(\hat{X}+\hat{Y})} = e^{t\hat{X}} e^{t\hat{Y}} + O(t^2). \tag{A.16}$$

In our application, we cut finite β into N_β pieces $\beta = \Delta t N_\beta$. For Δt is small enough, we approximately have

$$e^{-\beta \hat{H}} = \prod_{t=1}^{N_\beta} e^{-\Delta t \hat{H}} \approx \prod_{t=1}^{N_\beta} \prod_{i=1}^{N} e^{-\Delta t \hat{H}_i} \tag{A.17}$$

Considering there is no special commutation relation between $\hat{H}_i$, we have the total Trotter error $O(N(\Delta t)^2)$. Here N comes from the amount of terms in Hamiltonian which we cannot control, but we can enlarge imaginary-time pieces (reduce Δt) to systematically control this Trotter error. If there is a commutation between $\hat{H}_i, \hat{H}_j$, i.e. $[\hat{H}_i, \hat{H}_j] = 0$, one can also reduce the Trotter error by arranging $e^{-\Delta t \hat{H}_i}, e^{-\Delta t \hat{H}_j}$ as neighbors in the product.

A.4 Hubbard–Stratonovich transformation

We will see the reason why we need Suzuki–Trotter expansion in this section. In a word, we would like to transform all the $e^{\Delta t(\sum c^\dagger h c)^2}$ terms into $e^{\eta(l)\sqrt{\Delta t}\sum c^\dagger h c}$ where $\eta(l)$ is a number determined by auxiliary field l. This means after transformation we will only have fermion bilinear form on the exponent, which can be computed easily in single particle space matrix form as shown in our DQMC section. The continuous Hubbard–Stratonovich transformation basically uses Gaussian integral to do this job.

$$e^{\Delta t \hat{O}^2} = \int_{-\infty}^{\infty} dx \frac{1}{\sqrt{2\pi}} e^{-\frac{1}{2}x^2} e^{x\sqrt{2\Delta t}\hat{O}} \tag{A.18}$$

Here $\hat{O}$ can be any operator. However, simulation for a continuous variable x within a large interval is inconvenient. As mentioned in Ref [23], we generally would like to use a four-component auxiliary field in practice. This introduces the discrete Hubbard–Stratonovich transformation below.

$$e^{\Delta t \hat{O}^2} = \sum_{l=\pm 1,\pm 2} \frac{1}{4}\gamma(l) e^{\eta(l)\sqrt{\Delta t}\hat{O}} + O\left((\Delta t)^4\right) \tag{A.19}$$

There are eight parameter $\gamma(l), \eta(l)$ needed to determine. One can Taylor expand the exponent and match the coefficients before each order with the exact continuous ones to determine them. Explicitly, we require

$$\begin{aligned}
&\frac{1}{4}\sum_l \gamma(l) = 1 \\
&\frac{1}{4}\sum_l \gamma(l)\eta(l) = 0 \\
&\frac{1}{4}\sum_l \gamma(l)\frac{1}{2}(\eta(l))^2 = 1 \\
&\frac{1}{4}\sum_l \gamma(l)\frac{1}{6}(\eta(l))^3 = 0 \\
&\frac{1}{4}\sum_l \gamma(l)\frac{1}{24}(\eta(l))^4 = \frac{1}{2} \\
&\frac{1}{4}\sum_l \gamma(l)\frac{1}{120}(\eta(l))^5 = 0 \\
&\frac{1}{4}\sum_l \gamma(l)\frac{1}{720}(\eta(l))^6 = \frac{1}{6}
\end{aligned} \tag{A.20}$$

The freedom is surplus to determine all the $\gamma(l), \eta(l)$. One can see if we require $\eta(l)$ is odd and $\gamma(l)$ is even over l, the second, fourth and sixth requirements can be satisfied directly. Let's assume this case and $\gamma(1) = a_1, \gamma(2) = a_2, \eta(1) = b_1, \eta(2) = b_2$, the constrain becomes

$$\begin{aligned}
&a_1 + a_2 = 2 \\
&a_1(b_1)^2 + a_2(b_2)^2 = 4 \\
&a_1(b_1)^4 + a_2(b_2)^4 = 24 \\
&a_1(b_1)^6 + a_2(b_2)^6 = 240
\end{aligned} \tag{A.21}$$

One group of solution is $a_1 = 1 + \frac{\sqrt{6}}{3}, a_2 = 1 - \frac{\sqrt{6}}{3}, b_1 = \sqrt{(2(3-\sqrt{6}))}, b_2 = \sqrt{(2(3+\sqrt{6}))}$. This group of $\gamma(l), \eta(l)$ is just what we take in our simulation.

$$\begin{aligned}
&\gamma(\pm 1) = 1 + \frac{\sqrt{6}}{3} \\
&\gamma(\pm 2) = 1 - \frac{\sqrt{6}}{3} \\
&\eta(\pm 1) = \pm\sqrt{(2(3-\sqrt{6}))} \\
&\eta(\pm 2) = \pm\sqrt{(2(3+\sqrt{6}))}
\end{aligned} \tag{A.22}$$

Appendix B

Universality class and scaling behavior

In this section, I will briefly introduce the idea of universality class and scaling behavior [250–253], and then give the critical exponents without proof for 2D Ising and 2D XY we use in the main text.

Define a local operator $\hat{\phi}(x)$ called order parameter operator. If the correlation density of those two operators $\frac{1}{S^2}\int dxdy \left\langle \hat{\phi}(x)\hat{\phi}(y)\right\rangle$ converges to a finite value, we call this system is in the ordered phase defined by the order parameter $\hat{\phi}(x)$. From order to disorder, order parameter can change from finite value to zero continuously (e.g., second order phase transition) or with a jump (first order phase transition). Spontaneous symmetry breaking is one of many ways triggering a phase transition, where the Hamiltonian always has a certain symmetry while the symmetry-breaking operator $\hat{\phi}(x)$ can form a long range order preventing the system transforming within different symmetry branches.

If one replaces the high frequency (or local cluster) information with the averaged one, one actually is observing the system in a larger length scale where the details are replaced by the average. Since the correlation density should be independent with the length scale for a infinitely large system, one would assume identifying the order-disorder phases should have nothing to do with this scaling transformation. For a Hamiltonian with the given symmetry, the parameters will transform with scaling transformation described by beta function and the order-disorder phases correspond to two different stable fixed points where nearby renormalization group (RG) flow runs into and scaling fields are all irrelevant (or all coefficients except for the one before fixed point term in Hamiltonian go to zero after RG steps). In the parameter space for the continuous RG flows, to separate two attractive stable fixed points one assumes there should be a surface where flows go to different directions at each side. The fixed point on this critical surface is called critical fixed point and gives scale invariant phase transition Hamiltonian.

Since our Hamiltonian has only symmetry and dimension information left at the fixed point (actually also topological information which we would not discuss in this

section), it is straightforward to expect the fixed point on the critical surface describing the phase transition for a group of Hamiltonian with the same symmetry and dimension. The scaling behavior of this group of Hamiltonian on the critical fixed point should be the same and we call this group of Hamiltonian belongs to the same universality class.

When we say scaling behavior, we are saying how the observables scale with the dimensionless relevant parameters near the critical point. As we have argued before, both at stable fixed point determining a phase and at the critical fixed point determining a phase transition, the system after infinite times scaling transformation can only have the length scale $\xi = 0$ or $\xi \to \infty$. On the other hand, for translation and rotation invariant system, the correlation is determined totally by the length between two points $G(x, y) \equiv \langle\hat{\phi}(x)\hat{\phi}(y)\rangle \equiv G(\frac{|x-y|}{\xi})$. For $\xi = 0$ case, $\langle\hat{\phi}(x)\hat{\phi}(y)\rangle = \langle\hat{\phi}(\infty)\hat{\phi}(0)\rangle$ and the correlation density is determined barely by the infinite long range correlation which should be finite at ordered phase and zero at disordered phase. To link those two different behaviors with the $\xi = 0$ case, we define a connected correlation function $G_c(x, y)$ by subtracting the mean value of infinite long range correlation as $G_c(x, y) \equiv \langle\hat{\phi}(x)\hat{\phi}(y)\rangle - \langle\hat{\phi}(\infty)\hat{\phi}(0)\rangle$ so that it measures the fluctuation around the mean value close to the $\xi = 0$ fixed point and should always approach to zero. For $\xi \to \infty$ case, the same connected correlation function $G_c(x, y) \equiv \langle\hat{\phi}(x)\hat{\phi}(y)\rangle - \langle\hat{\phi}(\infty)\hat{\phi}(0)\rangle$ has a different behavior. Since in this case we assume $|x - y| \ll \xi < \infty$ so that $\langle\hat{\phi}(\infty)\hat{\phi}(0)\rangle$ is out of ξ region and $\langle\hat{\phi}(x)\hat{\phi}(y)\rangle$ is within ξ, one should expect it gives a finite value which identifies the $\xi \to \infty$ phase transition fixed point.

Now let's consider the scaling behavior for $\xi = 0$ phase-determining fixed point and $\xi \to \infty$ phase transition fixed point. Since the fluctuation $G_c(x, y)$ for $\xi = 0$ fixed point is zero, we can safely take the mean field scaling behavior here such that $G_c(x, y) \propto e^{-\frac{|x-y|}{\xi}}$. While for $\xi \to \infty$ fixed point, one should abandon the mean field estimation. As the discussion in conformal field theory lecture [254–256], for primary field $\hat{\phi}(x)$ having scaling dimension Δ_ϕ, it transforms as

$$\hat{\phi}(x) \to \hat{\phi}'(x') = \left|\frac{\partial x'}{\partial x}\right|^{\frac{\Delta_\phi}{D}} \hat{\phi}(x') \tag{B.1}$$

Here $\left|\frac{\partial x'}{\partial x}\right|$ is the Jacobian determinant determined by scaling transformation (translation or rotation has Jacobian determinant 1). For the descendant field $\partial\hat{\phi}(x)$ the conformal weight $\Delta_{\partial\phi} = \Delta_\phi + 1$. The translation, rotation and scale invariance means the correlation must take power-law dependence on the distance $|x - y|$ such that

$$\langle\hat{\phi}(x)\hat{\phi}(y)\rangle = \frac{1}{|x - y|^{2\Delta_\phi}}. \tag{B.2}$$

With the RG steps driving the system to $\xi \to \infty$ fixed point, all parameters scale in a power-law form with the length $|x - y|$. In another word, near the $\xi \to \infty$ fixed point, any observable consisting of correlation from primary fields and their descendant fields has a power-law behavior with any parameter. The fixed point property is determined totally

by the amount of primary fields and their scaling dimensions. However, identifying the connection between primary fields and the physical observable can be a tricky thing for a given general Hamiltonian. Historically, we have 7 non-independent critical exponents according to scaling behavior of different observable. For completeness we list them below.

$$
\begin{aligned}
&\alpha : \text{specific heat } C = -T\partial_T^2 F \sim |t|^{-\alpha} \\
&\beta : \text{magnetization } M = -\partial_H F|_{H\to 0} \sim (-t)^{\beta} \\
&\gamma : \text{magnetic susceptibility } \chi = \partial_H M|_{H\to 0} \sim |t|^{-\gamma} \\
&\delta : \text{field dependence of the magnetization } M \sim |h|^{\frac{1}{\delta}} \\
&\nu : \text{correlation length } \xi \sim |t|^{-\nu} \\
&\eta : \text{anomalous dimension of correlation} \\
&G(r) \sim \begin{cases} \dfrac{1}{|r|^{d-2+\eta}}, & |r| \ll \xi \\ e^{-\frac{|r|}{\xi}}, & |r| \gg \xi \end{cases} \\
&z : \text{dynamical exponent of correlation } \tau \sim \xi^z
\end{aligned}
\tag{B.3}
$$

Here T, F, H mean temperature, free energy and magnetic field, $h \equiv \frac{H-H_c}{H_c}, t \equiv \frac{T-T_c}{T_c}$ are reduced magnetic field and temperature respected to H_c, T_c at critical point, d, τ are dimension of the system and correlation length along imaginary time axis. Critical exponent z is only used in quantum phase transition where temperature takes 0 such that imaginary time axis becomes an effective additional system dimension. The other six critical exponents are not independent and we directly list their connections labeled with the finder below.

$$
\begin{aligned}
&\text{Fisher: } \nu(2-\eta) = \gamma \\
&\text{Rushbrooke: } \alpha + 2\beta + \gamma = 2 \\
&\text{Widom: } \beta(\delta - 1) = \gamma \\
&\text{Josephson: } 2 - \alpha = \nu d
\end{aligned}
\tag{B.4}
$$

In the main text, only 2D Ising and 2D XY universality classes are involved. Here I list the critical exponents for those two kinds of phase transitions for reference.

2D Ising: $G(T, L) = L^{-\eta} f((T - T_c)L^{1/\nu})$, $(\alpha = 0, \beta = \frac{1}{8}, \gamma = \frac{7}{4}, \delta = 15, \nu = 1, \eta = \frac{1}{4})$. Here $G(T, L)$ is the order parameter correlation density with variable temperature T and system size L (i.e., $G(T, L) \sim \langle M^2 \rangle \sim (-t)^{2\beta} \sim L^{-2\beta/\nu} = L^{-(d-2+\eta)}$). f can be any scaling invariant function since $t \sim L^{-1/\nu}$ near the critical point.

2D XY: $G(T, L) = L^{-\eta} f(L \cdot \exp(-\frac{A}{(T-T_c)^{1/2}}))$, $(\eta = \frac{1}{4})$. Here $G(T, L)$ is the order parameter correlation density slightly above the phase transition temperature T_{BKT} and A is a non-universal constant number. One should notice $\xi \sim \exp(\frac{A}{(T-T_c)^{1/2}}$ exponentially diverges near critical temperature other than power law because of the

nonlinear beta equation near the critical fixed point. Below T_{BKT}, the correlation density also behaves the power-law $G(T, L) \sim L^{-\eta'}, (\eta' < \frac{1}{4})$ since BKT phase is a critical phase (i.e., BKT phase is labeled by a line consists of critical fixed points in RG flow diagram).

Appendix C

Young Diagram

Young diagram is a powerful tool to classify wavefunctions having certain continuous symmetry [120, 257]. For a given Young diagram, the amount of standard Young tableaus is equal to the irreducible representation dimension. Based on this, if one can identify an eigenfunction (say one of many degenerate ground states) belonging to a certain Young diagram, the degeneracy of this sector (i.e., the amount of standard Young tableaus) due to this continuous symmetry can be computed directly by the hook length formula. In this appendix, we introduce how to build the mapping from states having $SU(N)$ symmetry to standard tensor Young tableaus. And then we introduce the hook length formula without proving it. Finally we give simple examples to indicate how to use this formula for computing the amount of standard Young tableaus.

Let's begin with considering the simplest case, one momentum point two particles case, the wavefunction is written as

$$|12\rangle = \frac{1}{\sqrt{2}}[|12\rangle - |21\rangle]. \tag{C.1}$$

Here we use $1, 2, ..., N$ to label N different flavors particles and different positions are set for states. The corresponding tensor Young diagram with standard tableau filling is

$$\begin{array}{|c|}\hline 1 \\ \hline 2 \\ \hline \end{array} \tag{C.2}$$

The standard tensor Young tableaus requires the filling numbers row-exchange symmetric, column-exchange antisymmetric and the number in each box is no smaller than above and left boxes. The column-exchange antisymmetric requires two particles must be in different flavors so that $1, 1$ or $2, 2$ are illegal tableau filling. According to this rule, the standard tableau above has a unique corresponding fermion wavefunction $|12\rangle$.

Now let's consider a little bit complex case that we have another label besides the $SU(N)$ flavor and let's just call it momentum label. The single particle space becomes the direct product of those two subspaces. The raising and lowering operators for $SU(N)$

should have an identity matrix element in momentum subspace.

$$c_2^\dagger c_1 \to \sum_k c_{k,2}^\dagger c_{k,1} \tag{C.3}$$

One can see these operators are symmetric about momentum which is commensurate with the row-exchange symmetric rule in tensor Young tableaus. Now let's try writing the wavefunction according to the standard tensor Young tableau below.

$$\begin{array}{|c|c|}\hline 1 & 1 \\ \hline 2 & 2 \\ \hline \end{array}$$

$$\begin{aligned} \to \quad & \frac{1}{4}[|(k_1,1)(k_1,2)(k_2,1)(k_2,2)\rangle - |(k_1,1)(k_1,2)(k_2,2)(k_2,1)\rangle \\ - \quad & |(k_1,2)(k_1,1)(k_2,1)(k_2,2)\rangle + |(k_1,2)(k_1,1)(k_2,2)(k_2,1)\rangle] \end{aligned} \tag{C.4}$$

One can directly check this wavefunction is indeed symmetric over exchanging $1,1$ or $2,2$ between different k labels and antisymmetric of exchanging $1,2$ within the same k label. As another example, let's focus on the wavefunction from standard tensor Young tableau below.

$$\begin{array}{|c|c|c|c|}\hline 1 & 1 & 2 & 2 \\ \hline \end{array} \tag{C.5}$$

The corresponding wavefunction above can be derived in another way, that raising from one highest weight state of this Young diagram

$$\begin{array}{|c|c|c|c|}\hline 1 & 1 & 1 & 1 \\ \hline \end{array}$$

$$\to \quad |(k_1,1)(k_2,1)(k_3,1)(k_4,1)\rangle \tag{C.6}$$

Then apply raising operator twice to derive

$$\begin{array}{|c|c|c|c|}\hline 1 & 1 & 2 & 2 \\ \hline \end{array}$$

$$\to \quad \left(\sum_k c_{k,2}^\dagger c_{k,1}\right)^2 |(k_1,1)(k_2,1)(k_3,1)(k_4,1)\rangle\,. \tag{C.7}$$

Since all the operators are symmetric over k label and the starting state is symmetric, the result state should also be symmetric. One can easily check this superposition state is the same with the one which can be directly read from Young tableau except for a normalization constant number.

Then we introduce hook length formula for $SU(N)$ below. For every box in a given Young diagram, we define the hook number $h_{ij} \equiv R_{ij} + D_{ij} + 1$ and content number $m_{ij} \equiv j - i$ for the row i column j box, where R_{ij}, D_{ij} are amounts of boxes on the right direction of row i and down direction of column j based on the (i,j) box. Then the corresponding amount of Young tableaus is given by the formula below

$$d(SU(N)) = \prod_{ij} \frac{N + m_{ij}}{h_{ij}}. \tag{C.8}$$

To understand this expression, let's assume $N = 2$ in $SU(N)$ and check the degeneracy computed by raising operator, number of standard tensor Young tableaus and hook length formula. The raising operator is unique for transforming a charge from 1 to 2 $\sum_k c^\dagger_{k,2} c_{k,1}$. The corresponding lowering operator is just $\sum_k c^\dagger_{k,1} c_{k,2}$. For the wavefunction which is determined by standard Young tableau

1	1
2	2

(C.9)

either the number of standard tensor Young tableaus or hook length formula gives the irreducible representation dimension $d(SU(2)) = \frac{(2+0)\times(2+1)\times(2-1)\times(2+0)}{3\times2\times2\times1} = 1$. One can also see any raising or lowering operator will annihilate this state. While for the wavefunction corresponding to standard Young tableau

1	1	2	2

(C.10)

One can use raising operator at most 2 times (or lowering operator 2 times) and for each time one 1 in the tableau is replaced by 2 (or for lowering operator 2 is replaced by 1). The hook length formula also tells us the irreducible representation dimension for this Young diagram should be $d(SU(2)) = \frac{2\times3\times4\times5}{4\times3\times2\times1} = 5$. Finally, let's look at a case that full fill half of N_s flavors with N_k momentum points. The Young diagram is shown below (e.g., $N_s = 4$ and $N_k = 6$)

(C.11)

It is hard to use raising or lowering operators to compute in this case, while one can compute the irreducible representation dimension of this Young diagram by hook length formula conveniently

$$d_{[N_k,N_k]}(SU(N_s)) = \prod_{ij} \frac{N_s + j - i}{h_{ij}} = \frac{\frac{(N+3)!(N+2)!}{3!2!}}{(N+1)!N!} = \frac{(N_s+N_k-1)!(N_s+N_k-2)!}{(N_s-1)!(N_s-2)!(N_k+1)!N_k!} \tag{C.12}$$

For $N_s = 4$ and $N_k = 6$ case, the result is $d_{[6,6]}(SU(4)) = \frac{9!8!}{3!2!7!6!} = 336$, which means for putting $1, 2, 3, 4$ in each box satisfying the number is no smaller than the one in above and left boxes, there are 336 different ways in total.

Appendix D

Stochastic analytic continuation (SAC)

Here I will briefly introduce the idea of deriving spectral function $A_{\hat{O}}(\omega)$ from imaginary-time correlation function $\left\langle \hat{O}(t)\hat{O}^{\dagger}(0)\right\rangle \equiv \frac{\mathrm{Tr}(e^{-(\beta-t)H}\hat{O}e^{-tH}\hat{O}^{\dagger})}{\mathrm{Tr}(e^{-\beta H})}$ [184, 185, 258]. All the excitation spectra in the main text are computed in this way. First of all, let's rewrite the imaginary-time correlation function as

$$\begin{aligned}\left\langle \hat{O}(t)\hat{O}^{\dagger}(0)\right\rangle &= e^{\beta F}\sum_{i,j}\left\langle i|\hat{O}|j\right\rangle \left\langle j|\hat{O}^{\dagger}|i\right\rangle e^{-(\beta-t)\epsilon_i-t\epsilon_j} \\ &= e^{\beta F}\sum_{i,j}\left|\left\langle i|\hat{O}|j\right\rangle\right|^2 e^{-(\beta-t)\epsilon_i-t\epsilon_j}. \end{aligned} \tag{D.1}$$

Here i,j label different eigenstates with eigenvalues ϵ_i,ϵ_j and $F\equiv-\frac{1}{\beta}\log(\mathrm{Tr}(e^{-\beta H}))$ is the free energy. Now we Fourier transform this correlation function to imaginary-frequency

$$\begin{aligned}G_{\hat{O}}(i\omega_n) &\equiv \int_0^{\beta} dt e^{i\omega_n t}\left\langle \hat{O}(t)\hat{O}^{\dagger}(0)\right\rangle \\ &= e^{\beta F}\sum_{i,j}\frac{e^{-\beta\epsilon_i}}{i\omega_n+\epsilon_i-\epsilon_j}\left|\left\langle i|\hat{O}|j\right\rangle\right|^2 e^{t(i\omega_n+\epsilon_i-\epsilon_j)}|_0^{\beta} \\ &= e^{\beta F}\sum_{i,j}\frac{\pm e^{-\beta\epsilon_j}-e^{-\beta\epsilon_i}}{i\omega_n+\epsilon_i-\epsilon_j}\left|\left\langle i|\hat{O}|j\right\rangle\right|^2 \end{aligned} \tag{D.2}$$

To derive the last line, we have used the imaginary-frequency $\omega_n=\frac{2n\pi}{\beta}$ for bosonic excitation and $\omega_n=\frac{(2n+1)\pi}{\beta}$ for fermionic excitation and $e^{i\omega_n\beta}=\pm1$ for boson/fermion. Through analytic continuation $i\omega_n\to\omega+i\delta$, real-frequency spectral function can be derived from imaginary-frequency correlation function as

$$\begin{aligned}A_{\hat{O}}(\omega) &= \frac{1}{\pi}\Im G_{\hat{O}}(\omega) \\ &= e^{\beta F}\sum_{i,j}(e^{-\beta\epsilon_i}\mp e^{-\beta\epsilon_j})\delta(\omega+\epsilon_i-\epsilon_j)\left|\left\langle i|\hat{O}|j\right\rangle\right|^2 \end{aligned} \tag{D.3}$$

Here when taking $\delta \to 0$ we have used the Sokhotsky–Weierstrass theorem

$$\lim_{\delta\to 0^+} \int \frac{f(x)}{x \pm i\delta} dx = \mp i\pi f(0) + P \int \frac{f(x)}{x} dx. \tag{D.4}$$

Here P means taking principal value of the integral. From the formula above, one can deduce Cauchy–Dirac relation

$$\lim_{\delta\to 0^+} \frac{1}{x \pm i\delta} = \mp i\pi\delta(x) + P\frac{1}{x}. \tag{D.5}$$

Based on this formula, we have $\Im \lim_{\delta\to 0^+} \frac{1}{\omega+\epsilon_i-\epsilon_j+i\delta} = -i\pi\delta(\omega+\epsilon_i-\epsilon_j)$ which is used to derive $A_{\hat{O}}(\omega)$. If the excitation is well-defined boson/fermion according to $[\hat{O}, \hat{O}^\dagger]_\mp = 1$, one can check spectral function $A_{\hat{O}}(\omega)$ is normalized $\int_{-\infty}^{\infty} d\omega A_{\hat{O}}(\omega) = 1$. Imaginary-time correlation function can be deduced from spectral function as

$$\left\langle \hat{O}(t)\hat{O}^\dagger(0) \right\rangle = \int_{-\infty}^{\infty} d\omega \frac{e^{-\omega t}}{1 \mp e^{-\beta\omega}} A_{\hat{O}}(\omega). \tag{D.6}$$

From this formula, by taking $t = 0$ one can derive $\left\langle \hat{O}^\dagger\hat{O} \right\rangle = \int_{-\infty}^{\infty} d\omega \frac{1}{e^{\beta\omega}\mp 1} A_{\hat{O}}(\omega)$. This formula gives the physical interpretation for $A_{\hat{O}}(\omega)$ that the possibility density of finding $\hat{O}$ particle states at ω (e.g., in fermion system $A_{\hat{O}_k}(0)$ is finite for some k points indicates the $\hat{O}_k$ fermions at those k points are allowed for putting on the $\omega = 0$ fermi surface). Besides, even though for a general $\hat{O} = \hat{a} + \hat{b} + \cdots$ composed of linear combination of orthogonal bosons/fermions, one can check this possibility density interpretation also works with the possibility density now contributed from each boson/fermion independently. Based on this understanding, as long as there is no boson-fermion mixing in $\hat{O}$ and $\hat{O}$ has the component of the certain boson/fermion, one can read out the spectrum of that boson/fermion from $A_{\hat{O}}(\omega)$ (maybe along with chaos from other boson/fermion components). This is why we can define a simple $\hat{O}$ (e.g., order parameter) and compute the spectrum as long as it describes the most features of that boson/fermion spectrum we want. Below I will discuss how to derive $A_{\hat{O}}(\omega)$ from DQMC data $\left\langle \hat{O}(t)\hat{O}^\dagger(0) \right\rangle$.

We know $\left\langle \hat{O}(t)\hat{O}^\dagger(0) \right\rangle$ can be computed directly with a Laplace transformation. However, in practice directly computing the inverse process has extremely uncontrolled error for a non-analytical $\left\langle \hat{O}(t)\hat{O}^\dagger(0) \right\rangle$. Below I will introduce the SAC method for doing this. Before the first step, one may notice for bosonic $\hat{O}$ there is a singular pole in $\frac{e^{-\omega t}}{1-e^{-\beta\omega}}$ at $\omega = 0$. To get avoid of this and noticing $\frac{1}{1-e^{-\beta\omega}} A_{\hat{O}}(\omega) = e^{\beta\omega} \frac{1}{1-e^{\beta\omega}} A_{\hat{O}}(-\omega)$ for Hermitian $\hat{O}$ (e.g., order parameter), one can derive

$$\begin{aligned} \left\langle \hat{O}(t)\hat{O}^\dagger(0) \right\rangle &= \int_0^{\infty} d\omega \frac{e^{-\omega t} + e^{-\omega(\beta-t)}}{1 + e^{-\beta\omega}} \frac{1 + e^{-\beta\omega}}{1 - e^{-\beta\omega}} A_{\hat{O}}(\omega) \\ &\equiv \int_0^{\infty} d\omega \frac{e^{-\omega t} + e^{-\omega(\beta-t)}}{1 + e^{-\beta\omega}} \tilde{A}_{\hat{O}}(\omega) \end{aligned} \tag{D.7}$$

Here by definition $\tilde{A}_{\hat{O}}(\omega) \equiv \frac{1+e^{-\beta\omega}}{1-e^{-\beta\omega}} A_{\hat{O}}(\omega)$ and we would like to solve $\tilde{A}_{\hat{O}}(\omega)$ below. Assuming we have N_m data from DQMC for mean value $G \equiv \frac{\sum_m \langle \hat{O}(t)\hat{O}^\dagger(0) \rangle_m}{N_m}$ and

according to Bayes' theorem $P(A(\omega)|G)P(G) = P(G|A(\omega))P(A(\omega))$, to make sure $P(A(\omega)|G)$ is large for the given G means to make sure $P(G|A(\omega))$ is large for a given $A(\omega)$. We assume the correctness of this guess $P(G|A(\omega))$ has a Gaussian distribution with least squares value χ

$$\begin{aligned} P(G|A(\omega)) &\propto e^{-\frac{\chi^2}{2\Theta}} \\ \chi^2 &= \sum_{i,j}[G'(t_i) - G(t_i)](C^{-1})_{ij}[G'(t_j) - G(t_j)] \\ C_{ij} &= \frac{1}{N_m(N_m-1)}\sum_m [\left\langle \hat{O}(t_i)\hat{O}^\dagger(0)\right\rangle_m - G(t_i)][\left\langle \hat{O}(t_j)\hat{O}^\dagger(0)\right\rangle_m - G(t_j)] \end{aligned} \tag{D.8}$$

Here Θ is a tuning parameter working as temperature in classical Monte Carlo, G' comes from computation of a given $A(\omega)$ and C_{ij} is the covariance matrix describing correlation between different imaginary-time t. In practice, we begin from a large Θ, setting $A(\omega)$ by summation of a group of delta functions with random position and random height. Then we compute χ^2 and randomly adjust those delta functions based on the weight $e^{-\frac{\chi^2}{2\Theta}}$. After equilibrium of Markov chain, we reduce Θ and continue until the fluctuation of χ reaches below $\sqrt{2\chi^2_{min}}$

$$\langle\chi^2\rangle - \chi^2_{min} \approx a\sqrt{2\chi^2_{min}}. \tag{D.9}$$

Generally we take $a = \frac{1}{2}$ empirically for controlling over-fitting.

Bibliography

[1] Xu Zhang et al. "Fermion sign bounds theory in quantum Monte Carlo simulation". In: *Phys. Rev. B* 106 (3 2022), p. 035121. DOI: 10.1103/PhysRevB.106.035121. URL: https://link.aps.org/doi/10.1103/PhysRevB.106.035121.

[2] Xu Zhang et al. "Polynomial sign problem and topological Mott insulator in twisted bilayer graphene". In: *Phys. Rev. B* 107 (24 2023), p. L241105. DOI: 10.1103/PhysRevB.107.L241105. URL: https://link.aps.org/doi/10.1103/PhysRevB.107.L241105.

[3] Xu Zhang et al. "Integral algorithm of exponential observables for interacting fermions in quantum Monte Carlo simulations". In: *Phys. Rev. B* 109 (20 2024), p. 205147. DOI: 10.1103/PhysRevB.109.205147. URL: https://link.aps.org/doi/10.1103/PhysRevB.109.205147.

[4] Meizhen Huang et al. "Intrinsic Nonlinear Hall Effect and Gate-Switchable Berry Curvature Sliding in Twisted Bilayer Graphene". In: *Phys. Rev. Lett.* 131 (6 2023), p. 066301. DOI: 10.1103/PhysRevLett.131.066301. URL: https://link.aps.org/doi/10.1103/PhysRevLett.131.066301.

[5] Xu Zhang et al. "Momentum Space Quantum Monte Carlo on Twisted Bilayer Graphene". In: *Chinese Physics Letters* 38.7 (2021), p. 077305. DOI: 10.1088/0256-307X/38/7/077305. URL: https://dx.doi.org/10.1088/0256-307X/38/7/077305.

[6] Gaopei Pan et al. "Dynamical properties of collective excitations in twisted bilayer graphene". In: *Phys. Rev. B* 105 (12 2022), p. L121110. DOI: 10.1103/PhysRevB.105.L121110. URL: https://link.aps.org/doi/10.1103/PhysRevB.105.L121110.

[7] Xu Zhang et al. "Superconductivity and bosonic fluid emerging from moiré flat bands". In: *Phys. Rev. B* 106 (18 2022), p. 184517. DOI: 10.1103/PhysRevB.106.184517. URL: https://link.aps.org/doi/10.1103/PhysRevB.106.184517.

[8] Gerald D Mahan. *Many-particle physics*. Springer Science & Business Media, 2013.

[9] Piers Coleman. *Introduction to many-body physics*. Cambridge University Press, 2015.

[10] B Andrei Bernevig. *Topological insulators and topological superconductors*. Princeton university press, 2013.

[11] D. J. Thouless et al. "Quantized Hall Conductance in a Two-Dimensional Periodic Potential". In: *Phys. Rev. Lett.* 49 (6 1982), pp. 405–408. DOI: 10.1103/

PhysRevLett.49.405. URL: https://link.aps.org/doi/10.1103/PhysRevLett.49.405.

[12] Neil W. Ashcroft and N. David Mermin. *Solid state physics*. Cengage, 1976.

[13] Inti Sodemann and Liang Fu. "Quantum Nonlinear Hall Effect Induced by Berry Curvature Dipole in Time-Reversal Invariant Materials". In: *Phys. Rev. Lett.* 115 (21 2015), p. 216806. DOI: 10.1103/PhysRevLett.115.216806. URL: https://link.aps.org/doi/10.1103/PhysRevLett.115.216806.

[14] Di Xiao, Ming-Che Chang, and Qian Niu. "Berry phase effects on electronic properties". In: *Rev. Mod. Phys.* 82 (3 2010), pp. 1959–2007. DOI: 10.1103/RevModPhys.82.1959. URL: https://link.aps.org/doi/10.1103/RevModPhys.82.1959.

[15] Kenzo Ishikawa and Toyoki Matsuyama. "A microscopic theory of the quantum Hall effect". In: *Nuclear Physics B* 280 (1987), pp. 523–548. ISSN: 0550-3213. DOI: https://doi.org/10.1016/0550-3213(87)90160-X. URL: https://www.sciencedirect.com/science/article/pii/055032138790160X.

[16] Takahiro Fukui, Yasuhiro Hatsugai, and Hiroshi Suzuki. "Chern Numbers in Discretized Brillouin Zone: Efficient Method of Computing (Spin) Hall Conductances". In: *Journal of the Physical Society of Japan* 74.6 (2005), pp. 1674–1677. DOI: 10.1143/JPSJ.74.1674. eprint: https://doi.org/10.1143/JPSJ.74.1674. URL: https://doi.org/10.1143/JPSJ.74.1674.

[17] Zhong Wang and Shou-Cheng Zhang. "Simplified Topological Invariants for Interacting Insulators". In: *Phys. Rev. X* 2 (3 2012), p. 031008. DOI: 10.1103/PhysRevX.2.031008. URL: https://link.aps.org/doi/10.1103/PhysRevX.2.031008.

[18] Hsiang-Hsuan Hung et al. "Interaction effects on topological phase transitions via numerically exact quantum Monte Carlo calculations". In: *Phys. Rev. B* 89 (23 2014), p. 235104. DOI: 10.1103/PhysRevB.89.235104. URL: https://link.aps.org/doi/10.1103/PhysRevB.89.235104.

[19] Gaopei Pan et al. "Thermodynamic Characteristic for a Correlated Flat-Band System with a Quantum Anomalous Hall Ground State". In: *Phys. Rev. Lett.* 130 (1 2023), p. 016401. DOI: 10.1103/PhysRevLett.130.016401. URL: https://link.aps.org/doi/10.1103/PhysRevLett.130.016401.

[20] Yuan-Yao He et al. "Topological invariants for interacting topological insulators. II. Breakdown of single-particle Green's function formalism". In: *Phys. Rev. B* 93 (19 2016), p. 195164. DOI: 10.1103/PhysRevB.93.195164. URL: https://link.aps.org/doi/10.1103/PhysRevB.93.195164.

[21] N. A. Sinitsyn. *Semiclassical theories of the anomalous Hall effect*. 2008. DOI: 10.1088/0953-8984/20/02/023201. arXiv: 0712.0183.

[22] Z. Z. Du, Hai Zhou Lu, and X. C. Xie. *Nonlinear Hall effects*. 2021. DOI: 10.1038/s42254-021-00359-6. arXiv: 2105.10940.

[23] FF Assaad and HG Evertz. "World-line and determinantal quantum Monte Carlo methods for spins, phonons and electrons". In: *Computational Many-Particle Physics*. Springer, 2008, pp. 277–356.

[24] Shiwei Zhang. "Quantum Monte Carlo methods for strongly correlated electron systems". In: *Theoretical Methods for Strongly Correlated Electrons*. Springer, 2004, pp. 39–74.

[25] Johannes S. Hofmann et al. "Fermionic Monte Carlo Study of a Realistic Model of Twisted Bilayer Graphene". In: *Phys. Rev. X* 12 (1 2022), p. 011061. DOI: 10.1103/PhysRevX.12.011061. URL: https://link.aps.org/doi/10.1103/PhysRevX.12.011061.

[26] R. Blankenbecler, D. J. Scalapino, and R. L. Sugar. "Monte Carlo calculations of coupled boson-fermion systems. I". In: *Phys. Rev. D* 24 (8 1981), pp. 2278–2286. DOI: 10.1103/PhysRevD.24.2278. URL: https://link.aps.org/doi/10.1103/PhysRevD.24.2278.

[27] EY Loh Jr and JE Gubernatis. "Stable numerical simulations of models of interacting electrons in condensed matter physics". In: *Electronic Phase Transitions* 32 (1992), p. 177.

[28] S.E. Koonin, D.J. Dean, and K. Langanke. "Shell model Monte Carlo methods". In: *Physics Reports* 278.1 (1997), pp. 1–77. ISSN: 0370-1573. DOI: https://doi.org/10.1016/S0370-1573(96)00017-8. URL: https://www.sciencedirect.com/science/article/pii/S0370157396000178.

[29] D. J. Scalapino and R. L. Sugar. "Monte Carlo calculations of coupled boson-fermion systems. II". In: *Phys. Rev. B* 24 (8 1981), pp. 4295–4308. DOI: 10.1103/PhysRevB.24.4295. URL: https://link.aps.org/doi/10.1103/PhysRevB.24.4295.

[30] J. E. Hirsch. "Two-dimensional Hubbard model: Numerical simulation study". In: *Phys. Rev. B* 31 (7 1985), pp. 4403–4419. DOI: 10.1103/PhysRevB.31.4403. URL: https://link.aps.org/doi/10.1103/PhysRevB.31.4403.

[31] J. E. Hirsch. "Stable monte carlo algorithm for fermion lattice systems at low temperatures". In: *Phys. Rev. B* 38 (16 1988), pp. 12023–12026. DOI: 10.1103/PhysRevB.38.12023. URL: https://link.aps.org/doi/10.1103/PhysRevB.38.12023.

[32] S. R. White et al. "Numerical study of the two-dimensional Hubbard model". In: *Phys. Rev. B* 40 (1 1989), pp. 506–516. DOI: 10.1103/PhysRevB.40.506. URL: https://link.aps.org/doi/10.1103/PhysRevB.40.506.

[33] Cheng Huang et al. "Evolution from quantum anomalous Hall insulator to heavy-fermion semimetal in magic-angle twisted bilayer graphene". In: *Phys. Rev. B* 109 (12 2024), p. 125404. DOI: 10.1103/PhysRevB.109.125404. URL: https://link.aps.org/doi/10.1103/PhysRevB.109.125404.

[34] Jonathan D'Emidio et al. "Universal Features of Entanglement Entropy in the Honeycomb Hubbard Model". In: *Phys. Rev. Lett.* 132 (7 2024), p. 076502. DOI: 10.1103/PhysRevLett.132.076502. URL: https://link.aps.org/doi/10.1103/PhysRevLett.132.076502.

[35] Yuan Da Liao. *Controllable Incremental Algorithm for Entanglement Entropy in Quantum Monte Carlo Simulations*. 2023. arXiv: 2307.10602 [cond-mat.str-el].

[36] Congjun Wu and Shou-Cheng Zhang. "Sufficient condition for absence of the sign problem in the fermionic quantum Monte Carlo algorithm". In: *Phys. Rev. B* 71 (15 2005), p. 155115. DOI: 10.1103/PhysRevB.71.155115. URL: https://link.aps.org/doi/10.1103/PhysRevB.71.155115.

[37] Z. C. Wei et al. "Majorana Positivity and the Fermion Sign Problem of Quantum Monte Carlo Simulations". In: *Phys. Rev. Lett.* 116 (25 2016), p. 250601. DOI: 10.1103/PhysRevLett.116.250601. URL: https://link.aps.org/doi/10.1103/PhysRevLett.116.250601.

[38] Zi-Xiang Li, Yi-Fan Jiang, and Hong Yao. "Majorana-Time-Reversal Symmetries: A Fundamental Principle for Sign-Problem-Free Quantum Monte Carlo Simulations". In: *Phys. Rev. Lett.* 117 (26 2016), p. 267002. DOI: 10.1103/PhysRevLett.117.267002. URL: https://link.aps.org/doi/10.1103/PhysRevLett.117.267002.

[39] Zi-Xiang Li, Yi-Fan Jiang, and Hong Yao. "Solving the fermion sign problem in quantum Monte Carlo simulations by Majorana representation". In: *Phys. Rev. B* 91 (24 2015), p. 241117. DOI: 10.1103/PhysRevB.91.241117. URL: https://link.aps.org/doi/10.1103/PhysRevB.91.241117.

[40] Lei Wang et al. "Split Orthogonal Group: A Guiding Principle for Sign-Problem-Free Fermionic Simulations". In: *Phys. Rev. Lett.* 115 (25 2015), p. 250601. DOI: 10.1103/PhysRevLett.115.250601. URL: https://link.aps.org/doi/10.1103/PhysRevLett.115.250601.

[41] E. Y. Loh et al. "Sign problem in the numerical simulation of many-electron systems". In: *Phys. Rev. B* 41 (13 1990), pp. 9301–9307. DOI: 10.1103/PhysRevB.41.9301. URL: https://link.aps.org/doi/10.1103/PhysRevB.41.9301.

[42] Stefan Wessel et al. "Thermodynamic properties of the Shastry-Sutherland model from quantum Monte Carlo simulations". In: *Phys. Rev. B* 98 (17 2018), p. 174432. DOI: 10.1103/PhysRevB.98.174432. URL: https://link.aps.org/doi/10.1103/PhysRevB.98.174432.

[43] Jonathan D'Emidio, Stefan Wessel, and Frédéric Mila. "Reduction of the sign problem near $T = 0$ in quantum Monte Carlo simulations". In: *Phys. Rev. B* 102 (6 2020), p. 064420. DOI: 10.1103/PhysRevB.102.064420. URL: https://link.aps.org/doi/10.1103/PhysRevB.102.064420.

[44] Gaopei Pan et al. "Stable computation of entanglement entropy for two-dimensional interacting fermion systems". In: *Phys. Rev. B* 108 (8 2023), p. L081123. DOI: 10.1103/PhysRevB.108.L081123. URL: https://link.aps.org/doi/10.1103/PhysRevB.108.L081123.

[45] Joaquín E. Drut and William J. Porter. "Hybrid Monte Carlo approach to the entanglement entropy of interacting fermions". In: *Phys. Rev. B* 92 (12 2015), p. 125126. DOI: 10.1103/PhysRevB.92.125126. URL: https://link.aps.org/doi/10.1103/PhysRevB.92.125126.

[46] Joaquín E. Drut and William J. Porter. "Entanglement, noise, and the cumulant expansion". In: *Phys. Rev. E* 93 (4 2016), p. 043301. DOI: 10.1103/PhysRevE.93.043301. URL: https://link.aps.org/doi/10.1103/PhysRevE.93.043301.

[47] Tarun Grover. "Entanglement of Interacting Fermions in Quantum Monte Carlo Calculations". In: *Phys. Rev. Lett.* 111 (13 2013), p. 130402. DOI: 10.1103/PhysRevLett.111.130402. URL: https://link.aps.org/doi/10.1103/PhysRevLett.111.130402.

[48] Yuan Cao et al. "Unconventional superconductivity in magic-angle graphene superlattices". In: *Nature* 556.7699 (2018), pp. 43–50. DOI: 10.1038/nature26160. URL: https://doi.org/10.1038/nature26160.

[49] Yuan Cao et al. "Correlated insulator behaviour at half-filling in magic-angle graphene superlattices". In: *Nature* 556.7699 (2018), pp. 80–84. DOI: 10.1038/nature26154. URL: https://doi.org/10.1038/nature26154.

[50] Guorui Chen et al. "Tunable correlated Chern insulator and ferromagnetism in a moiré superlattice". In: *Nature* 579.7797 (2020), pp. 56–61. DOI: 10.1038/s41586-020-2049-7. URL: https://doi.org/10.1038/s41586-020-2049-7.

[51] Alexander Kerelsky et al. "Maximized electron interactions at the magic angle in twisted bilayer graphene". In: *Nature* 572.7767 (2019), pp. 95–100. DOI: 10.1038/s41586-019-1431-9. URL: https://doi.org/10.1038/s41586-019-1431-9.

[52] S. L. Tomarken et al. "Electronic Compressibility of Magic-Angle Graphene Superlattices". In: *Phys. Rev. Lett.* 123 (4 2019), p. 046601. DOI: 10.1103/PhysRevLett.123.046601. URL: https://link.aps.org/doi/10.1103/PhysRevLett.123.046601.

[53] Xiaobo Lu et al. "Superconductors, orbital magnets and correlated states in magic-angle bilayer graphene". In: *Nature* 574.7780 (2019), pp. 653–657. DOI: 10.1038/s41586-019-1695-0. URL: https://doi.org/10.1038/s41586-019-1695-0.

[54] Yonglong Xie et al. "Spectroscopic signatures of many-body correlations in magic-angle twisted bilayer graphene". In: *Nature* 572.7767 (2019), pp. 101–105. DOI: 10.1038/s41586-019-1422-x. URL: https://doi.org/10.1038/s41586-019-1422-x.

[55] Cheng Shen et al. "Correlated states in twisted double bilayer graphene". In: *Nature Physics* (2020). DOI: 10.1038/s41567-020-0825-9. URL: https://doi.org/10.1038/s41567-020-0825-9.

[56] Kevin P. Nuckolls et al. "Strongly correlated Chern insulators in magic-angle twisted bilayer graphene". In: *Nature* 588.7839 (2020), pp. 610–615. DOI: 10.1038/s41586-020-3028-8. URL: https://doi.org/10.1038%2Fs41586-020-3028-8.

[57] Andrew T Pierce et al. "Unconventional sequence of correlated Chern insulators in magic-angle twisted bilayer graphene". In: *Nature Physics* 17.11 (2021), pp. 1210–1215. URL: https://doi.org/10.1038/s41567-021-01347-4.

[58] Satoshi Moriyama et al. "Observation of superconductivity in bilayer graphene/hexagonal boron nitride superlattices". In: *arXiv e-prints*, arXiv:1901.09356 (Jan. 2019), arXiv:1901.09356. arXiv: 1901.09356 [cond-mat.supr-con].

[59] Asaf Rozen et al. “Entropic evidence for a Pomeranchuk effect in magic-angle graphene”. In: *Nature* 592.7853 (2021), pp. 214–219. URL: https://doi.org/10.1038/s41586-021-03319-3.

[60] Xiaomeng Liu et al. “Spectroscopy of a tunable moiré system with a correlated and topological flat band”. In: *Nature communications* 12.1 (2021), p. 2732. URL: https://doi.org/10.1038/s41467-021-23031-0.

[61] Hryhoriy Polshyn et al. “Large linear-in-temperature resistivity in twisted bilayer graphene”. In: *Nature Physics* 15.10 (2019), pp. 1011–1016. URL: https://doi.org/10.1038/s41567-019-0596-3.

[62] Xiaoxue Liu et al. “Tuning electron correlation in magic-angle twisted bilayer graphene using Coulomb screening”. In: *Science* 371.6535 (2021), pp. 1261–1265. DOI: 10.1126/science.abb8754. eprint: https://www.science.org/doi/pdf/10.1126/science.abb8754. URL: https://www.science.org/doi/abs/10.1126/science.abb8754.

[63] Youngjoon Choi et al. “Electronic correlations in twisted bilayer graphene near the magic angle”. In: *Nature physics* 15.11 (2019), pp. 1174–1180. URL: https://doi-org.eproxy.lib.hku.hk/10.1038/s41567-019-0606-5.

[64] Yu Saito et al. “Hofstadter subband ferromagnetism and symmetry-broken Chern insulators in twisted bilayer graphene”. In: *Nature Physics* 17.4 (2021), pp. 478–481. URL: https://doi-org.eproxy.lib.hku.hk/10.1038/s41567-020-01129-4.

[65] Ipsita Das et al. “Symmetry-broken Chern insulators and Rashba-like Landau-level crossings in magic-angle bilayer graphene”. In: *Nature Physics* 17.6 (2021), pp. 710–714. URL: https://doi.org/10.1038/s41567-021-01186-3.

[66] Shuang Wu et al. “Chern insulators, van Hove singularities and topological flat bands in magic-angle twisted bilayer graphene”. In: *Nature materials* 20.4 (2021), pp. 488–494. URL: https://doi.org/10.1038/s41563-020-00911-2.

[67] Alexandre Jaoui et al. “Quantum critical behaviour in magic-angle twisted bilayer graphene”. In: *Nature Physics* 18.6 (2022), pp. 633–638. URL: https://doi.org/10.1038/s41567-022-01556-5.

[68] Yuan Cao et al. “Tunable correlated states and spin-polarized phases in twisted bilayer–bilayer graphene”. In: *Nature* 583.7815 (2020), pp. 215–220. URL: https://doi.org/10.1038/s41586-020-2260-6.

[69] Yuan Cao et al. “Nematicity and competing orders in superconducting magic-angle graphene”. In: *Science* 372.6539 (2021), pp. 264–271. DOI: 10.1126/science.abc2836. eprint: https://www.science.org/doi/pdf/10.1126/science.abc2836. URL: https://www.science.org/doi/abs/10.1126/science.abc2836.

[70] Matthew Yankowitz et al. “Tuning superconductivity in twisted bilayer graphene”. In: *Science* 363.6431 (2019), pp. 1059–1064. DOI: 10.1126/science.aav1910. eprint: https://www.science.org/doi/pdf/10.1126/science.aav1910. URL: https://www.science.org/doi/abs/10.1126/science.aav1910.

[71] G Trambly de Laissardière, Didier Mayou, and Laurence Magaud. "Localization of Dirac electrons in rotated graphene bilayers". In: *Nano letters* 10.3 (2010), pp. 804–808. URL: https://doi.org/10.1021/nl902948m.

[72] G. Trambly de Laissardière, D. Mayou, and L. Magaud. "Numerical studies of confined states in rotated bilayers of graphene". In: *Phys. Rev. B* 86 (12 2012), p. 125413. DOI: 10.1103/PhysRevB.86.125413. URL: https://link.aps.org/doi/10.1103/PhysRevB.86.125413.

[73] Rafi Bistritzer and Allan H. MacDonald. "Moiré bands in twisted double-layer graphene". In: *Proceedings of the National Academy of Sciences* 108.30 (2011), pp. 12233–12237. DOI: 10.1073/pnas.1108174108. eprint: https://www.pnas.org/doi/pdf/10.1073/pnas.1108174108. URL: https://www.pnas.org/doi/abs/10.1073/pnas.1108174108.

[74] J. M. B. Lopes dos Santos, N. M. R. Peres, and A. H. Castro Neto. "Graphene Bilayer with a Twist: Electronic Structure". In: *Phys. Rev. Lett.* 99 (25 2007), p. 256802. DOI: 10.1103/PhysRevLett.99.256802. URL: https://link.aps.org/doi/10.1103/PhysRevLett.99.256802.

[75] J. M. B. Lopes dos Santos, N. M. R. Peres, and A. H. Castro Neto. "Continuum model of the twisted graphene bilayer". In: *Phys. Rev. B* 86 (15 2012), p. 155449. DOI: 10.1103/PhysRevB.86.155449. URL: https://link.aps.org/doi/10.1103/PhysRevB.86.155449.

[76] A.V. Rozhkov et al. "Electronic properties of graphene-based bilayer systems". In: *Physics Reports* 648 (2016). Electronic properties of graphene-based bilayer systems, pp. 1–104. ISSN: 0370-1573. DOI: https://doi.org/10.1016/j.physrep.2016.07.003. URL: https://www.sciencedirect.com/science/article/pii/S0370157316301612.

[77] Zhi-Da Song et al. "Twisted bilayer graphene. II. Stable symmetry anomaly". In: *Phys. Rev. B* 103 (20 2021), p. 205412. DOI: 10.1103/PhysRevB.103.205412. URL: https://link.aps.org/doi/10.1103/PhysRevB.103.205412.

[78] B. Andrei Bernevig et al. "Twisted bilayer graphene. III. Interacting Hamiltonian and exact symmetries". In: *Phys. Rev. B* 103 (20 2021), p. 205413. DOI: 10.1103/PhysRevB.103.205413. URL: https://link.aps.org/doi/10.1103/PhysRevB.103.205413.

[79] Kazuyuki Uchida et al. "Atomic corrugation and electron localization due to Moiré patterns in twisted bilayer graphenes". In: *Physical Review B - Condensed Matter and Materials Physics* 90.15 (2014). ISSN: 1550235X. DOI: 10.1103/PhysRevB.90.155451.

[80] Nguyen N.T. Nam and Mikito Koshino. "Lattice relaxation and energy band modulation in twisted bilayer graphene". In: *Physical Review B* 96.7 (2017). ISSN: 24699969. DOI: 10.1103/PhysRevB.96.075311. arXiv: 1706.03908.

[81] Vitor M. Pereira and A. H. Castro Neto. "Strain Engineering of Graphene's Electronic Structure". In: *Physical Review Letters* 103.4 (2009). ISSN: 00319007. DOI: 10.1103/PhysRevLett.103.046801.

[82] Pan He et al. "Graphene moiré superlattices with giant quantum nonlinearity of chiral Bloch electrons". In: *Nature Nanotechnology* 17.4 (2022), pp. 378–383. ISSN: 17483395. DOI: 10.1038/s41565-021-01060-6.

[83] Qiong Ma et al. "Observation of the nonlinear Hall effect under time-reversal-symmetric conditions". In: *Nature* 565.7739 (2019), pp. 337–342. ISSN: 14764687. DOI: 10.1038/s41586-018-0807-6. arXiv: 1809.09279.

[84] Carmine Ortix. *Nonlinear Hall Effect with Time-Reversal Symmetry: Theory and Material Realizations*. 2021. DOI: 10.1002/qute.202100056. arXiv: 2104.06690.

[85] Cheng Ping Zhang et al. "Higher-order nonlinear anomalous Hall effects induced by Berry curvature multipoles". In: *Physical Review B* 107.11 (2023). ISSN: 24699969. DOI: 10.1103/PhysRevB.107.115142. arXiv: 2012.15628. URL: http://arxiv.org/abs/2012.15628http://dx.doi.org/10.1103/PhysRevB.107.115142.

[86] Cheng Ping Zhang et al. "Giant nonlinear Hall effect in strained twisted bilayer graphene". In: *Physical Review B* 106.4 (2022). ISSN: 24699969. DOI: 10.1103/PhysRevB.106.L041111. arXiv: 2010.08333. URL: http://arxiv.org/abs/2010.08333http://dx.doi.org/10.1103/PhysRevB.106.L041111.

[87] Pierre A. Pantaleón, Tony Low, and Francisco Guinea. "Tunable large Berry dipole in strained twisted bilayer graphene". In: *Physical Review B* 103.20 (2021). ISSN: 24699969. DOI: 10.1103/PhysRevB.103.205403. arXiv: 2010.11086.

[88] Zhen Bi, Noah F. Q. Yuan, and Liang Fu. "Designing flat bands by strain". In: *Phys. Rev. B* 100 (3 2019), p. 035448. DOI: 10.1103/PhysRevB.100.035448. URL: https://link.aps.org/doi/10.1103/PhysRevB.100.035448.

[89] Hakseong Kim et al. "Accurate gap determination in monolayer and bilayer graphene/h-BN Moiré superlattices". In: *Nano letters* 18.12 (2018), pp. 7732–7741. URL: https://doi.org/10.1021/acs.nanolett.8b03423.

[90] Hoi Chun Po, Haruki Watanabe, and Ashvin Vishwanath. "Fragile Topology and Wannier Obstructions". In: *Phys. Rev. Lett.* 121 (12 2018), p. 126402. DOI: 10.1103/PhysRevLett.121.126402. URL: https://link.aps.org/doi/10.1103/PhysRevLett.121.126402.

[91] Hoi Chun Po et al. "Faithful tight-binding models and fragile topology of magic-angle bilayer graphene". In: *Phys. Rev. B* 99 (19 2019), p. 195455. DOI: 10.1103/PhysRevB.99.195455. URL: https://link.aps.org/doi/10.1103/PhysRevB.99.195455.

[92] Nick Bultinck, Shubhayu Chatterjee, and Michael P. Zaletel. "Mechanism for Anomalous Hall Ferromagnetism in Twisted Bilayer Graphene". In: *Phys. Rev. Lett.* 124 (16 2020), p. 166601. DOI: 10.1103/PhysRevLett.124.166601. URL: https://link.aps.org/doi/10.1103/PhysRevLett.124.166601.

[93] Hoi Chun Po et al. "Origin of Mott Insulating Behavior and Superconductivity in Twisted Bilayer Graphene". In: *Phys. Rev. X* 8 (3 2018), p. 031089. DOI: 10.1103/PhysRevX.8.031089. URL: https://link.aps.org/doi/10.1103/PhysRevX.8.031089.

[94] Grigory Tarnopolsky, Alex Jura Kruchkov, and Ashvin Vishwanath. "Origin of Magic Angles in Twisted Bilayer Graphene". In: *Phys. Rev. Lett.* 122 (10 2019), p. 106405. DOI: 10.1103/PhysRevLett.122.106405. URL: https://link.aps.org/doi/10.1103/PhysRevLett.122.106405.

[95] Noah F. Q. Yuan and Liang Fu. "Model for the metal-insulator transition in graphene superlattices and beyond". In: *Phys. Rev. B* 98 (4 2018), p. 045103. DOI: 10.1103/PhysRevB.98.045103. URL: https://link.aps.org/doi/10.1103/PhysRevB.98.045103.

[96] Jian Kang and Oskar Vafek. "Symmetry, Maximally Localized Wannier States, and a Low-Energy Model for Twisted Bilayer Graphene Narrow Bands". In: *Phys. Rev. X* 8 (3 2018), p. 031088. DOI: 10.1103/PhysRevX.8.031088. URL: https://link.aps.org/doi/10.1103/PhysRevX.8.031088.

[97] Mikito Koshino et al. "Maximally Localized Wannier Orbitals and the Extended Hubbard Model for Twisted Bilayer Graphene". In: *Phys. Rev. X* 8 (3 2018), p. 031087. DOI: 10.1103/PhysRevX.8.031087. URL: https://link.aps.org/doi/10.1103/PhysRevX.8.031087.

[98] Yi Zhang et al. "Correlated insulating phases of twisted bilayer graphene at commensurate filling fractions: A Hartree-Fock study". In: *Phys. Rev. B* 102 (3 2020), p. 035136. DOI: 10.1103/PhysRevB.102.035136. URL: https://link.aps.org/doi/10.1103/PhysRevB.102.035136.

[99] Nick Bultinck et al. "Ground State and Hidden Symmetry of Magic-Angle Graphene at Even Integer Filling". In: *Phys. Rev. X* 10 (3 2020), p. 031034. DOI: 10.1103/PhysRevX.10.031034. URL: https://link.aps.org/doi/10.1103/PhysRevX.10.031034.

[100] Kasra Hejazi, Xiao Chen, and Leon Balents. "Hybrid Wannier Chern bands in magic angle twisted bilayer graphene and the quantized anomalous Hall effect". In: *Phys. Rev. Res.* 3 (1 2021), p. 013242. DOI: 10.1103/PhysRevResearch.3.013242. URL: https://link.aps.org/doi/10.1103/PhysRevResearch.3.013242.

[101] Ming Xie and A. H. MacDonald. "Nature of the Correlated Insulator States in Twisted Bilayer Graphene". In: *Phys. Rev. Lett.* 124 (9 2020), p. 097601. DOI: 10.1103/PhysRevLett.124.097601. URL: https://link.aps.org/doi/10.1103/PhysRevLett.124.097601.

[102] Jianpeng Liu, Junwei Liu, and Xi Dai. "Pseudo Landau level representation of twisted bilayer graphene: Band topology and implications on the correlated insulating phase". In: *Phys. Rev. B* 99 (15 2019), p. 155415. DOI: 10.1103/PhysRevB.99.155415. URL: https://link.aps.org/doi/10.1103/PhysRevB.99.155415.

[103] Jianpeng Liu and Xi Dai. "Anomalous Hall effect, magneto-optical properties, and nonlinear optical properties of twisted graphene systems". In: *npj Computational Materials* 6.1 (2020), p. 57. URL: https://doi.org/10.1038/s41524-020-0299-4.

[104] Jianpeng Liu and Xi Dai. "Theories for the correlated insulating states and quantum anomalous Hall effect phenomena in twisted bilayer graphene". In: *Phys.*

Rev. B 103 (3 2021), p. 035427. DOI: 10.1103/PhysRevB.103.035427. URL: https://link.aps.org/doi/10.1103/PhysRevB.103.035427.

[105] Tommaso Cea and Francisco Guinea. "Band structure and insulating states driven by Coulomb interaction in twisted bilayer graphene". In: *Phys. Rev. B* 102 (4 2020), p. 045107. DOI: 10.1103/PhysRevB.102.045107. URL: https://link.aps.org/doi/10.1103/PhysRevB.102.045107.

[106] Shang Liu et al. "Nematic topological semimetal and insulator in magic-angle bilayer graphene at charge neutrality". In: *Phys. Rev. Res.* 3 (1 2021), p. 013033. DOI: 10.1103/PhysRevResearch.3.013033. URL: https://link.aps.org/doi/10.1103/PhysRevResearch.3.013033.

[107] Stephen Carr et al. "Exact continuum model for low-energy electronic states of twisted bilayer graphene". In: *Phys. Rev. Res.* 1 (1 2019), p. 013001. DOI: 10.1103/PhysRevResearch.1.013001. URL: https://link.aps.org/doi/10.1103/PhysRevResearch.1.013001.

[108] Y. H. Kwan et al. "Kekulé Spiral Order at All Nonzero Integer Fillings in Twisted Bilayer Graphene". In: *Phys. Rev. X* 11 (4 2021), p. 041063. DOI: 10.1103/PhysRevX.11.041063. URL: https://link.aps.org/doi/10.1103/PhysRevX.11.041063.

[109] Shubhayu Chatterjee, Matteo Ippoliti, and Michael P. Zaletel. "Skyrmion superconductivity: DMRG evidence for a topological route to superconductivity". In: *Phys. Rev. B* 106 (3 2022), p. 035421. DOI: 10.1103/PhysRevB.106.035421. URL: https://link.aps.org/doi/10.1103/PhysRevB.106.035421.

[110] Eslam Khalaf et al. "Charged skyrmions and topological origin of superconductivity in magic-angle graphene". In: *Science Advances* 7.19 (2021), eabf5299. DOI: 10.1126/sciadv.abf5299. eprint: https://www.science.org/doi/pdf/10.1126/sciadv.abf5299. URL: https://www.science.org/doi/abs/10.1126/sciadv.abf5299.

[111] Jian Kang and Oskar Vafek. "Non-Abelian Dirac node braiding and near-degeneracy of correlated phases at odd integer filling in magic-angle twisted bilayer graphene". In: *Phys. Rev. B* 102 (3 2020), p. 035161. DOI: 10.1103/PhysRevB.102.035161. URL: https://link.aps.org/doi/10.1103/PhysRevB.102.035161.

[112] Tomohiro Soejima et al. "Efficient simulation of moiré materials using the density matrix renormalization group". In: *Phys. Rev. B* 102 (20 2020), p. 205111. DOI: 10.1103/PhysRevB.102.205111. URL: https://link.aps.org/doi/10.1103/PhysRevB.102.205111.

[113] Yixuan Huang, Pavan Hosur, and Hridis K. Pal. "Quasi-flat-band physics in a two-leg ladder model and its relation to magic-angle twisted bilayer graphene". In: *Phys. Rev. B* 102 (15 2020), p. 155429. DOI: 10.1103/PhysRevB.102.155429. URL: https://link.aps.org/doi/10.1103/PhysRevB.102.155429.

[114] Fang Xie et al. "Twisted bilayer graphene. VI. An exact diagonalization study at nonzero integer filling". In: *Phys. Rev. B* 103 (20 2021), p. 205416. DOI: 10.1103/PhysRevB.103.205416. URL: https://link.aps.org/doi/10.1103/PhysRevB.103.205416.

[115] Masayuki Ochi, Mikito Koshino, and Kazuhiko Kuroki. "Possible correlated insulating states in magic-angle twisted bilayer graphene under strongly competing interactions". In: *Phys. Rev. B* 98 (8 2018), p. 081102. DOI: 10.1103/PhysRevB.98.081102. URL: https://link.aps.org/doi/10.1103/PhysRevB.98.081102.

[116] J. F. Dodaro et al. "Phases of a phenomenological model of twisted bilayer graphene". In: *Phys. Rev. B* 98 (7 2018), p. 075154. DOI: 10.1103/PhysRevB.98.075154. URL: https://link.aps.org/doi/10.1103/PhysRevB.98.075154.

[117] Pawel Potasz, Ming Xie, and A. H. MacDonald. "Exact Diagonalization for Magic-Angle Twisted Bilayer Graphene". In: *Phys. Rev. Lett.* 127 (14 2021), p. 147203. DOI: 10.1103/PhysRevLett.127.147203. URL: https://link.aps.org/doi/10.1103/PhysRevLett.127.147203.

[118] Oskar Vafek and Jian Kang. "Renormalization Group Study of Hidden Symmetry in Twisted Bilayer Graphene with Coulomb Interactions". In: *Phys. Rev. Lett.* 125 (25 2020), p. 257602. DOI: 10.1103/PhysRevLett.125.257602. URL: https://link.aps.org/doi/10.1103/PhysRevLett.125.257602.

[119] Jian Kang and Oskar Vafek. "Strong Coupling Phases of Partially Filled Twisted Bilayer Graphene Narrow Bands". In: *Phys. Rev. Lett.* 122 (24 2019), p. 246401. DOI: 10.1103/PhysRevLett.122.246401. URL: https://link.aps.org/doi/10.1103/PhysRevLett.122.246401.

[120] Biao Lian et al. "Twisted bilayer graphene. IV. Exact insulator ground states and phase diagram". In: *Phys. Rev. B* 103 (20 2021), p. 205414. DOI: 10.1103/PhysRevB.103.205414. URL: https://link.aps.org/doi/10.1103/PhysRevB.103.205414.

[121] B. Andrei Bernevig et al. "Twisted bilayer graphene. V. Exact analytic many-body excitations in Coulomb Hamiltonians: Charge gap, Goldstone modes, and absence of Cooper pairing". In: *Phys. Rev. B* 103 (20 2021), p. 205415. DOI: 10.1103/PhysRevB.103.205415. URL: https://link.aps.org/doi/10.1103/PhysRevB.103.205415.

[122] Yahya Alavirad and Jay Sau. "Ferromagnetism and its stability from the one-magnon spectrum in twisted bilayer graphene". In: *Phys. Rev. B* 102 (23 2020), p. 235123. DOI: 10.1103/PhysRevB.102.235123. URL: https://link.aps.org/doi/10.1103/PhysRevB.102.235123.

[123] B. Andrei Bernevig et al. "Twisted bilayer graphene. I. Matrix elements, approximations, perturbation theory, and a $k \cdot p$ two-band model". In: *Phys. Rev. B* 103 (20 2021), p. 205411. DOI: 10.1103/PhysRevB.103.205411. URL: https://link.aps.org/doi/10.1103/PhysRevB.103.205411.

[124] Biao Lian, Zhijun Wang, and B. Andrei Bernevig. "Twisted Bilayer Graphene: A Phonon-Driven Superconductor". In: *Phys. Rev. Lett.* 122 (25 2019), p. 257002. DOI: 10.1103/PhysRevLett.122.257002. URL: https://link.aps.org/doi/10.1103/PhysRevLett.122.257002.

[125] J. González and T. Stauber. "Kohn-Luttinger Superconductivity in Twisted Bilayer Graphene". In: *Phys. Rev. Lett.* 122 (2 2019), p. 026801. DOI: 10.1103/

PhysRevLett.122.026801. URL: https://link.aps.org/doi/10.1103/PhysRevLett.122.026801.

[126] Jong Yeon Lee et al. "Theory of correlated insulating behaviour and spin-triplet superconductivity in twisted double bilayer graphene". In: *Nature communications* 10.1 (2019), p. 5333. URL: https://doi.org/10.1038/s41467-019-12981-1.

[127] Yuxuan Wang, Jian Kang, and Rafael M. Fernandes. "Topological and nematic superconductivity mediated by ferro-SU(4) fluctuations in twisted bilayer graphene". In: *Phys. Rev. B* 103 (2 2021), p. 024506. DOI: 10.1103/PhysRevB.103.024506. URL: https://link.aps.org/doi/10.1103/PhysRevB.103.024506.

[128] Cenke Xu and Leon Balents. "Topological Superconductivity in Twisted Multilayer Graphene". In: *Phys. Rev. Lett.* 121 (8 2018), p. 087001. DOI: 10.1103/PhysRevLett.121.087001. URL: https://link.aps.org/doi/10.1103/PhysRevLett.121.087001.

[129] Bitan Roy and Vladimir Juričić. "Unconventional superconductivity in nearly flat bands in twisted bilayer graphene". In: *Physical Review B* 99.12 (2019), p. 121407. URL: https://link.aps.org/doi/10.1103/PhysRevB.99.121407.

[130] Fengcheng Wu, A. H. MacDonald, and Ivar Martin. "Theory of Phonon-Mediated Superconductivity in Twisted Bilayer Graphene". In: *Phys. Rev. Lett.* 121 (25 2018), p. 257001. DOI: 10.1103/PhysRevLett.121.257001. URL: https://link.aps.org/doi/10.1103/PhysRevLett.121.257001.

[131] Hiroki Isobe, Noah F. Q. Yuan, and Liang Fu. "Unconventional Superconductivity and Density Waves in Twisted Bilayer Graphene". In: *Phys. Rev. X* 8 (4 2018), p. 041041. DOI: 10.1103/PhysRevX.8.041041. URL: https://link.aps.org/doi/10.1103/PhysRevX.8.041041.

[132] Yi-Zhuang You and Ashvin Vishwanath. "Superconductivity from valley fluctuations and approximate SO (4) symmetry in a weak coupling theory of twisted bilayer graphene". In: *npj Quantum Materials* 4.1 (2019), p. 16. URL: https://doi-org.eproxy.lib.hku.hk/10.1038/s41535-019-0153-4.

[133] Dante M. Kennes, Johannes Lischner, and Christoph Karrasch. "Strong correlations and $d + id$ superconductivity in twisted bilayer graphene". In: *Phys. Rev. B* 98 (24 2018), p. 241407. DOI: 10.1103/PhysRevB.98.241407. URL: https://link.aps.org/doi/10.1103/PhysRevB.98.241407.

[134] Francisco Guinea and Niels R. Walet. "Electrostatic effects, band distortions, and superconductivity in twisted graphene bilayers". In: *Proceedings of the National Academy of Sciences* 115.52 (2018), pp. 13174–13179. DOI: 10.1073/pnas.1810947115. eprint: https://www.pnas.org/doi/pdf/10.1073/pnas.1810947115. URL: https://www.pnas.org/doi/abs/10.1073/pnas.1810947115.

[135] M. Fidrysiak, M. Zegrodnik, and J. Spałek. "Unconventional topological superconductivity and phase diagram for an effective two-orbital model as applied to twisted bilayer graphene". In: *Phys. Rev. B* 98 (8 2018), p. 085436. DOI:

10.1103/PhysRevB.98.085436. URL: https://link.aps.org/doi/10.1103/PhysRevB.98.085436.

[136] Shubhayu Chatterjee, Nick Bultinck, and Michael P. Zaletel. "Symmetry breaking and skyrmionic transport in twisted bilayer graphene". In: *Phys. Rev. B* 101 (16 2020), p. 165141. DOI: 10.1103/PhysRevB.101.165141. URL: https://link.aps.org/doi/10.1103/PhysRevB.101.165141.

[137] Cyprian Lewandowski, Stevan Nadj-Perge, and Debanjan Chowdhury. "Does filling-dependent band renormalization aid pairing in twisted bilayer graphene?" In: *npj Quantum Materials* 6.1 (2021), p. 82. URL: https://doi.org/10.1038/s41535-021-00379-6.

[138] S. Raghu et al. "Topological Mott Insulators". In: *Phys. Rev. Lett.* 100 (15 2008), p. 156401. DOI: 10.1103/PhysRevLett.100.156401. URL: https://link.aps.org/doi/10.1103/PhysRevLett.100.156401.

[139] Petr Stepanov et al. "Competing Zero-Field Chern Insulators in Superconducting Twisted Bilayer Graphene". In: *Phys. Rev. Lett.* 127 (19 2021), p. 197701. DOI: 10.1103/PhysRevLett.127.197701. URL: https://link.aps.org/doi/10.1103/PhysRevLett.127.197701.

[140] Christopher L. Henley. "Ordering due to disorder in a frustrated vector antiferromagnet". In: *Phys. Rev. Lett.* 62 (17 1989), pp. 2056–2059. DOI: 10.1103/PhysRevLett.62.2056. URL: https://link.aps.org/doi/10.1103/PhysRevLett.62.2056.

[141] EF Shender and PCW Holdsworth. "Order by disorder and topology in frustrated magnetic systems". In: *Fluctuations and Order: The New Synthesis* (1996), pp. 259–279. DOI: 10.1007/978-1-4612-3992-5_16.

[142] Bin-Bin Chen et al. "Realization of topological Mott insulator in a twisted bilayer graphene lattice model". In: *Nature communications* 12.1 (2021), p. 5480. URL: https://doi.org/10.1038/s41467-021-25438-1.

[143] Xiyue Lin et al. "Exciton Proliferation and Fate of the Topological Mott Insulator in a Twisted Bilayer Graphene Lattice Model". In: *Phys. Rev. Lett.* 128 (15 2022), p. 157201. DOI: 10.1103/PhysRevLett.128.157201. URL: https://link.aps.org/doi/10.1103/PhysRevLett.128.157201.

[144] Zhi-Da Song and B. Andrei Bernevig. "Magic-Angle Twisted Bilayer Graphene as a Topological Heavy Fermion Problem". In: *Phys. Rev. Lett.* 129 (4 2022), p. 047601. DOI: 10.1103/PhysRevLett.129.047601. URL: https://link.aps.org/doi/10.1103/PhysRevLett.129.047601.

[145] Hao Shi and Xi Dai. "Heavy-fermion representation for twisted bilayer graphene systems". In: *Phys. Rev. B* 106 (24 2022), p. 245129. DOI: 10.1103/PhysRevB.106.245129. URL: https://link.aps.org/doi/10.1103/PhysRevB.106.245129.

[146] Jian Kang, B. Andrei Bernevig, and Oskar Vafek. "Cascades between Light and Heavy Fermions in the Normal State of Magic-Angle Twisted Bilayer Graphene". In: *Phys. Rev. Lett.* 127 (26 2021), p. 266402. DOI: 10.1103/PhysRevLett.127.266402. URL: https://link.aps.org/doi/10.1103/PhysRevLett.127.266402.

[147] Dumitru Călugăru et al. "Twisted bilayer graphene as topological heavy fermion: II. Analytical approximations of the model parameters". In: *Low Temperature Physics* 49.6 (2023), pp. 640–654. URL: https://doi.org/10.1063/10.0019421.

[148] Dumitru Călugăru et al. "The Thermoelectric Effect and Its Natural Heavy Fermion Explanation in Twisted Bilayer and Trilayer Graphene". In: *arXiv preprint arXiv:2402.14057* (2024). URL: https://doi.org/10.48550/arXiv.2402.14057.

[149] Jiabin Yu et al. "Magic-angle twisted symmetric trilayer graphene as a topological heavy-fermion problem". In: *Phys. Rev. B* 108 (3 2023), p. 035129. DOI: 10.1103/PhysRevB.108.035129. URL: https://link.aps.org/doi/10.1103/PhysRevB.108.035129.

[150] Aline Ramires and Jose L. Lado. "Emulating Heavy Fermions in Twisted Trilayer Graphene". In: *Phys. Rev. Lett.* 127 (2 2021), p. 026401. DOI: 10.1103/PhysRevLett.127.026401. URL: https://link.aps.org/doi/10.1103/PhysRevLett.127.026401.

[151] Haoyu Hu et al. "Symmetric Kondo Lattice States in Doped Strained Twisted Bilayer Graphene". In: *Phys. Rev. Lett.* 131 (16 2023), p. 166501. DOI: 10.1103/PhysRevLett.131.166501. URL: https://link.aps.org/doi/10.1103/PhysRevLett.131.166501.

[152] Rafael Luque Merino et al. "Evidence of heavy fermion physics in the thermoelectric transport of magic angle twisted bilayer graphene". In: *arXiv preprint arXiv:2402.11749* (2024). URL: https://doi.org/10.48550/arXiv.2402.11749.

[153] Geng-Dong Zhou et al. "Kondo phase in twisted bilayer graphene". In: *Phys. Rev. B* 109 (4 2024), p. 045419. DOI: 10.1103/PhysRevB.109.045419. URL: https://link.aps.org/doi/10.1103/PhysRevB.109.045419.

[154] Yang-Zhi Chou and Sankar Das Sarma. "Kondo Lattice Model in Magic-Angle Twisted Bilayer Graphene". In: *Phys. Rev. Lett.* 131 (2 2023), p. 026501. DOI: 10.1103/PhysRevLett.131.026501. URL: https://link.aps.org/doi/10.1103/PhysRevLett.131.026501.

[155] A. S. Shankar et al. "Kondo effect in twisted bilayer graphene". In: *Phys. Rev. B* 107 (24 2023), p. 245102. DOI: 10.1103/PhysRevB.107.245102. URL: https://link.aps.org/doi/10.1103/PhysRevB.107.245102.

[156] Haoyu Hu, B. Andrei Bernevig, and Alexei M. Tsvelik. "Kondo Lattice Model of Magic-Angle Twisted-Bilayer Graphene: Hund's Rule, Local-Moment Fluctuations, and Low-Energy Effective Theory". In: *Phys. Rev. Lett.* 131 (2 2023), p. 026502. DOI: 10.1103/PhysRevLett.131.026502. URL: https://link.aps.org/doi/10.1103/PhysRevLett.131.026502.

[157] Yang-Zhi Chou and Sankar Das Sarma. "Scaling theory of intrinsic Kondo and Hund's rule interactions in magic-angle twisted bilayer graphene". In: *Phys. Rev. B* 108 (12 2023), p. 125106. DOI: 10.1103/PhysRevB.108.125106. URL: https://link.aps.org/doi/10.1103/PhysRevB.108.125106.

[158] Eva Y Andrei and Allan H MacDonald. "Graphene bilayers with a twist". In: *Nature materials* 19.12 (2020), pp. 1265–1275. URL: https://doi.org/10.1038/s41563-020-00840-0.

[159] Yves H. Kwan, S. A. Parameswaran, and S. L. Sondhi. "Twisted bilayer graphene in a parallel magnetic field". In: *Phys. Rev. B* 101 (20 2020), p. 205116. DOI: 10.1103/PhysRevB.101.205116. URL: https://link.aps.org/doi/10.1103/PhysRevB.101.205116.

[160] Pilkyung Moon and Mikito Koshino. "Energy spectrum and quantum Hall effect in twisted bilayer graphene". In: *Phys. Rev. B* 85 (19 2012), p. 195458. DOI: 10.1103/PhysRevB.85.195458. URL: https://link.aps.org/doi/10.1103/PhysRevB.85.195458.

[161] Fengcheng Wu and Sankar Das Sarma. "Identification of superconducting pairing symmetry in twisted bilayer graphene using in-plane magnetic field and strain". In: *Phys. Rev. B* 99 (22 2019), p. 220507. DOI: 10.1103/PhysRevB.99.220507. URL: https://link.aps.org/doi/10.1103/PhysRevB.99.220507.

[162] Yarden Sheffer and Ady Stern. "Chiral magic-angle twisted bilayer graphene in a magnetic field: Landau level correspondence, exact wave functions, and fractional Chern insulators". In: *Phys. Rev. B* 104 (12 2021), p. L121405. DOI: 10.1103/PhysRevB.104.L121405. URL: https://link.aps.org/doi/10.1103/PhysRevB.104.L121405.

[163] ZF Wang, Feng Liu, and MY Chou. "Fractal Landau-level spectra in twisted bilayer graphene". In: *Nano letters* 12.7 (2012), pp. 3833–3838. URL: https://doi.org/10.1021/nl301794t.

[164] Jonah Herzog-Arbeitman et al. "Reentrant Correlated Insulators in Twisted Bilayer Graphene at 25 T (2π Flux)". In: *Phys. Rev. Lett.* 129 (7 2022), p. 076401. DOI: 10.1103/PhysRevLett.129.076401. URL: https://link.aps.org/doi/10.1103/PhysRevLett.129.076401.

[165] Yifei Guan, Oleg V. Yazyev, and Alexander Kruchkov. "Reentrant magic-angle phenomena in twisted bilayer graphene in integer magnetic fluxes". In: *Phys. Rev. B* 106 (12 2022), p. L121115. DOI: 10.1103/PhysRevB.106.L121115. URL: https://link.aps.org/doi/10.1103/PhysRevB.106.L121115.

[166] Jonah Herzog-Arbeitman, Aaron Chew, and B. Andrei Bernevig. "Magnetic Bloch theorem and reentrant flat bands in twisted bilayer graphene at 2π flux". In: *Phys. Rev. B* 106 (8 2022), p. 085140. DOI: 10.1103/PhysRevB.106.085140. URL: https://link.aps.org/doi/10.1103/PhysRevB.106.085140.

[167] Jiaqi Cai et al. "Signatures of fractional quantum anomalous Hall states in twisted MoTe2". In: *Nature* 622.7981 (2023), pp. 63–68. URL: https://doi.org/10.1038/s41586-023-06289-w.

[168] Yihang Zeng et al. "Thermodynamic evidence of fractional Chern insulator in moiré MoTe2". In: *Nature* 622.7981 (2023), pp. 69–73. URL: https://doi.org/10.1038/s41586-023-06452-3.

[169] Heonjoon Park et al. "Observation of fractionally quantized anomalous Hall effect". In: *Nature* 622.7981 (2023), pp. 74–79. URL: https://doi.org/10.1038/s41586-023-06536-0.

[170] Fan Xu et al. "Observation of Integer and Fractional Quantum Anomalous Hall Effects in Twisted Bilayer $MoTe_2$". In: *Phys. Rev. X* 13 (3 2023), p. 031037. DOI: 10.1103/PhysRevX.13.031037. URL: https://link.aps.org/doi/10.1103/PhysRevX.13.031037.

[171] Mattia Angeli and Allan H MacDonald. "Γ valley transition metal dichalcogenide moiré bands". In: *Proceedings of the National Academy of Sciences* 118.10 (2021), e2021826118. URL: https://doi.org/10.1073/pnas.2021826118.

[172] Fengcheng Wu et al. "Topological Insulators in Twisted Transition Metal Dichalcogenide Homobilayers". In: *Phys. Rev. Lett.* 122 (8 2019), p. 086402. DOI: 10.1103/PhysRevLett.122.086402. URL: https://link.aps.org/doi/10.1103/PhysRevLett.122.086402.

[173] Heqiu Li et al. "Spontaneous fractional Chern insulators in transition metal dichalcogenide moiré superlattices". In: *Phys. Rev. Res.* 3 (3 2021), p. L032070. DOI: 10.1103/PhysRevResearch.3.L032070. URL: https://link.aps.org/doi/10.1103/PhysRevResearch.3.L032070.

[174] J. E. Hirsch. "Discrete Hubbard-Stratonovich transformation for fermion lattice models". In: *Phys. Rev. B* 28 (7 1983), pp. 4059–4061. DOI: 10.1103/PhysRevB.28.4059. URL: https://link.aps.org/doi/10.1103/PhysRevB.28.4059.

[175] Mohit Randeria et al. "Pairing and spin gap in the normal state of short coherence length superconductors". In: *Phys. Rev. Lett.* 69 (13 1992), pp. 2001–2004. DOI: 10.1103/PhysRevLett.69.2001. URL: https://link.aps.org/doi/10.1103/PhysRevLett.69.2001.

[176] Nandini Trivedi and Mohit Randeria. "Deviations from Fermi-Liquid Behavior above T_c in 2D Short Coherence Length Superconductors". In: *Phys. Rev. Lett.* 75 (2 1995), pp. 312–315. DOI: 10.1103/PhysRevLett.75.312. URL: https://link.aps.org/doi/10.1103/PhysRevLett.75.312.

[177] J. M. Singer et al. "From BCS-like superconductivity to condensation of local pairs: A numerical study of the attractive Hubbard model". In: *Phys. Rev. B* 54 (2 1996), pp. 1286–1301. DOI: 10.1103/PhysRevB.54.1286. URL: https://link.aps.org/doi/10.1103/PhysRevB.54.1286.

[178] Thereza Paiva et al. "Critical temperature for the two-dimensional attractive Hubbard model". In: *Phys. Rev. B* 69 (18 2004), p. 184501. DOI: 10.1103/PhysRevB.69.184501. URL: https://link.aps.org/doi/10.1103/PhysRevB.69.184501.

[179] Murad Tovmasyan et al. "Effective theory and emergent SU(2) symmetry in the flat bands of attractive Hubbard models". In: *Phys. Rev. B* 94 (24 2016), p. 245149. DOI: 10.1103/PhysRevB.94.245149. URL: https://link.aps.org/doi/10.1103/PhysRevB.94.245149.

[180] Johannes S. Hofmann, Erez Berg, and Debanjan Chowdhury. "Superconductivity, pseudogap, and phase separation in topological flat bands". In: *Phys. Rev. B*

102 (20 2020), p. 201112. DOI: 10.1103/PhysRevB.102.201112. URL: https://link.aps.org/doi/10.1103/PhysRevB.102.201112.

[181] Lei Wang et al. "Correlated electronic phases in twisted bilayer transition metal dichalcogenides". In: *Nature materials* 19.8 (2020), pp. 861–866. URL: https://doi-org.eproxy.lib.hku.hk/10.1038/s41563-020-0708-6.

[182] Uri Zondiner et al. "Cascade of phase transitions and Dirac revivals in magic-angle graphene". In: *Nature* 582.7811 (2020), pp. 203–208. URL: https://doi.org/10.1038/s41586-020-2373-y.

[183] Liheng An et al. "Interaction effects and superconductivity signatures in twisted double-bilayer WSe 2". In: *Nanoscale horizons* 5.9 (2020), pp. 1309–1316. URL: https://doi.org/10.1039/D0NH00248H.

[184] Anders W. Sandvik. "Stochastic method for analytic continuation of quantum Monte Carlo data". In: *Phys. Rev. B* 57 (17 1998), pp. 10287–10290. DOI: 10.1103/PhysRevB.57.10287. URL: https://link.aps.org/doi/10.1103/PhysRevB.57.10287.

[185] KSD Beach. "Identifying the maximum entropy method as a special limit of stochastic analytic continuation". In: *arXiv preprint cond-mat/0403055* (2004). URL: https://doi.org/10.48550/arXiv.cond-mat/0403055.

[186] Anders W. Sandvik. "Constrained sampling method for analytic continuation". In: *Phys. Rev. E* 94 (6 2016), p. 063308. DOI: 10.1103/PhysRevE.94.063308. URL: https://link.aps.org/doi/10.1103/PhysRevE.94.063308.

[187] Olav F Syljuåsen. "Using the average spectrum method to extract dynamics from quantum Monte Carlo simulations". In: *Physical Review B* 78.17 (2008), p. 174429. DOI: 10.1103/PhysRevB.78.174429. URL: https://link.aps.org/doi/10.1103/PhysRevB.78.174429.

[188] Hui Shao et al. "Nearly Deconfined Spinon Excitations in the Square-Lattice Spin-1/2 Heisenberg Antiferromagnet". In: *Phys. Rev. X* 7 (4 2017), p. 041072. DOI: 10.1103/PhysRevX.7.041072. URL: https://link.aps.org/doi/10.1103/PhysRevX.7.041072.

[189] Chengkang Zhou et al. "Amplitude Mode in Quantum Magnets via Dimensional Crossover". In: *Phys. Rev. Lett.* 126 (22 2021), p. 227201. DOI: 10.1103/PhysRevLett.126.227201. URL: https://link.aps.org/doi/10.1103/PhysRevLett.126.227201.

[190] Guang-Yu Sun et al. "Dynamical Signature of Symmetry Fractionalization in Frustrated Magnets". In: *Phys. Rev. Lett.* 121 (7 2018), p. 077201. DOI: 10.1103/PhysRevLett.121.077201. URL: https://link.aps.org/doi/10.1103/PhysRevLett.121.077201.

[191] Nvsen Ma et al. "Dynamical signature of fractionalization at a deconfined quantum critical point". In: *Phys. Rev. B* 98 (17 2018), p. 174421. DOI: 10.1103/PhysRevB.98.174421. URL: https://link.aps.org/doi/10.1103/PhysRevB.98.174421.

[192] Yan-Cheng Wang et al. “Fractionalized conductivity and emergent self-duality near topological phase transitions”. In: *Nature Communications* 12.1 (2021), p. 5347. URL: https://doi.org/10.1038/s41467-021-25707-z.

[193] Han Li et al. “Kosterlitz-Thouless melting of magnetic order in the triangular quantum Ising material TmMgGaO4”. In: *Nature communications* 11.1 (2020), p. 1111. URL: https://doi.org/10.1038/s41467-020-14907-8.

[194] Ze Hu et al. “Evidence of the Berezinskii-Kosterlitz-Thouless phase in a frustrated magnet”. In: *Nature communications* 11.1 (2020), p. 5631. URL: https://doi.org/10.1038/s41467-020-19380-x.

[195] S. V. Isakov and R. Moessner. “Interplay of quantum and thermal fluctuations in a frustrated magnet”. In: *Phys. Rev. B* 68 (10 2003), p. 104409. DOI: 10.1103/PhysRevB.68.104409. URL: https://link.aps.org/doi/10.1103/PhysRevB.68.104409.

[196] Weilun Jiang et al. “Monte Carlo study of the pseudogap and superconductivity emerging from quantum magnetic fluctuations”. In: *Nature communications* 13.1 (2022), p. 2655. URL: https://doi.org/10.1038/s41467-022-30302-x.

[197] Chuang Chen et al. “Fermi arcs and pseudogap in a lattice model of a doped orthogonal metal”. In: *Phys. Rev. B* 103 (16 2021), p. 165131. DOI: 10.1103/PhysRevB.103.165131. URL: https://link.aps.org/doi/10.1103/PhysRevB.103.165131.

[198] Douglas J. Scalapino, Steven R. White, and Shoucheng Zhang. “Insulator, metal, or superconductor: The criteria”. In: *Phys. Rev. B* 47 (13 1993), pp. 7995–8007. DOI: 10.1103/PhysRevB.47.7995. URL: https://link.aps.org/doi/10.1103/PhysRevB.47.7995.

[199] E. L. Pollock and D. M. Ceperley. “Path-integral computation of superfluid densities”. In: *Phys. Rev. B* 36 (16 1987), pp. 8343–8352. DOI: 10.1103/PhysRevB.36.8343. URL: https://link.aps.org/doi/10.1103/PhysRevB.36.8343.

[200] Dan Mao and Debanjan Chowdhury. “Diamagnetic response and phase stiffness for interacting isolated narrow bands”. In: *Proceedings of the National Academy of Sciences* 120.11 (2023), e2217816120. DOI: 10.1073/pnas.2217816120. eprint: https://www.pnas.org/doi/pdf/10.1073/pnas.2217816120. URL: https://www.pnas.org/doi/abs/10.1073/pnas.2217816120.

[201] Zhengguang Lu et al. “Fractional quantum anomalous Hall effect in multilayer graphene”. In: *Nature* 626.8000 (2024), pp. 759–764. URL: https://doi.org/10.1038/s41586-023-07010-7.

[202] Kaifei Kang et al. *Observation of the fractional quantum spin Hall effect in moiré MoTe2*. 2024. arXiv: 2402.03294 [cond-mat.mes-hall].

[203] DN Sheng et al. “Fractional quantum Hall effect in the absence of Landau levels”. In: *Nature communications* 2.1 (2011), p. 389. URL: https://doi.org/10.1038/ncomms1380.

[204] Titus Neupert et al. “Fractional Quantum Hall States at Zero Magnetic Field”. In: *Phys. Rev. Lett.* 106 (23 2011), p. 236804. DOI: 10.1103/PhysRevLett.106.236804. URL: https://link.aps.org/doi/10.1103/PhysRevLett.106.236804.

[205] Patrick J. Ledwith et al. "Fractional Chern insulator states in twisted bilayer graphene: An analytical approach". In: *Phys. Rev. Res.* 2 (2 2020), p. 023237. DOI: 10.1103/PhysRevResearch.2.023237. URL: https://link.aps.org/doi/10.1103/PhysRevResearch.2.023237.

[206] Cécile Repellin and T. Senthil. "Chern bands of twisted bilayer graphene: Fractional Chern insulators and spin phase transition". In: *Phys. Rev. Res.* 2 (2 2020), p. 023238. DOI: 10.1103/PhysRevResearch.2.023238. URL: https://link.aps.org/doi/10.1103/PhysRevResearch.2.023238.

[207] Ahmed Abouelkomsan, Zhao Liu, and Emil J. Bergholtz. "Particle-Hole Duality, Emergent Fermi Liquids, and Fractional Chern Insulators in Moiré Flatbands". In: *Phys. Rev. Lett.* 124 (10 2020), p. 106803. DOI: 10.1103/PhysRevLett.124.106803. URL: https://link.aps.org/doi/10.1103/PhysRevLett.124.106803.

[208] Zhao Liu, Ahmed Abouelkomsan, and Emil J. Bergholtz. "Gate-Tunable Fractional Chern Insulators in Twisted Double Bilayer Graphene". In: *Phys. Rev. Lett.* 126 (2 2021), p. 026801. DOI: 10.1103/PhysRevLett.126.026801. URL: https://link.aps.org/doi/10.1103/PhysRevLett.126.026801.

[209] Patrick Wilhelm, Thomas C. Lang, and Andreas M. Läuchli. "Interplay of fractional Chern insulator and charge density wave phases in twisted bilayer graphene". In: *Phys. Rev. B* 103 (12 2021), p. 125406. DOI: 10.1103/PhysRevB.103.125406. URL: https://link.aps.org/doi/10.1103/PhysRevB.103.125406.

[210] Ramanjit Sohal, Luiz H. Santos, and Eduardo Fradkin. "Chern-Simons composite fermion theory of fractional Chern insulators". In: *Phys. Rev. B* 97 (12 2018), p. 125131. DOI: 10.1103/PhysRevB.97.125131. URL: https://link.aps.org/doi/10.1103/PhysRevB.97.125131.

[211] Ramanjit Sohal and Eduardo Fradkin. "Intertwined order in fractional Chern insulators from finite-momentum pairing of composite fermions". In: *Phys. Rev. B* 101 (24 2020), p. 245154. DOI: 10.1103/PhysRevB.101.245154. URL: https://link.aps.org/doi/10.1103/PhysRevB.101.245154.

[212] Evelyn Tang, Jia-Wei Mei, and Xiao-Gang Wen. "High-Temperature Fractional Quantum Hall States". In: *Phys. Rev. Lett.* 106 (23 2011), p. 236802. DOI: 10.1103/PhysRevLett.106.236802. URL: https://link.aps.org/doi/10.1103/PhysRevLett.106.236802.

[213] Kai Sun et al. "Nearly Flatbands with Nontrivial Topology". In: *Phys. Rev. Lett.* 106 (23 2011), p. 236803. DOI: 10.1103/PhysRevLett.106.236803. URL: https://link.aps.org/doi/10.1103/PhysRevLett.106.236803.

[214] N. Regnault and B. Andrei Bernevig. "Fractional Chern Insulator". In: *Phys. Rev. X* 1 (2 2011), p. 021014. DOI: 10.1103/PhysRevX.1.021014. URL: https://link.aps.org/doi/10.1103/PhysRevX.1.021014.

[215] Siddharth A. Parameswaran, Rahul Roy, and Shivaji L. Sondhi. "Fractional quantum Hall physics in topological flat bands". en. In: *Comptes Rendus. Physique* 14.9-10 (2013), pp. 816–839. DOI: 10.1016/j.crhy.2013.04.003.

[216] EMIL J. BERGHOLTZ and ZHAO LIU. "TOPOLOGICAL FLAT BAND MODELS AND FRACTIONAL CHERN INSULATORS". In: *International Journal of*

Modern Physics B 27.24 (2013), p. 1330017. DOI: 10.1142/S021797921330017X. URL: https://doi.org/10.1142/S021797921330017X.

[217] Yang-Le Wu, B. Andrei Bernevig, and N. Regnault. "Zoology of fractional Chern insulators". In: *Phys. Rev. B* 85 (7 2012), p. 075116. DOI: 10.1103/PhysRevB.85.075116. URL: https://link.aps.org/doi/10.1103/PhysRevB.85.075116.

[218] Michael Levin and Ady Stern. "Fractional Topological Insulators". In: *Phys. Rev. Lett.* 103 (19 2009), p. 196803. DOI: 10.1103/PhysRevLett.103.196803. URL: https://link.aps.org/doi/10.1103/PhysRevLett.103.196803.

[219] Hongyu Lu et al. *Thermodynamic Response and Neutral Excitations in Integer and Fractional Quantum Anomalous Hall States Emerging from Correlated Flat Bands*. 2023. arXiv: 2311.15246 [cond-mat.str-el].

[220] Hongyu Lu et al. *From Fractional Quantum Anomalous Hall Smectics to Polar Smectic Metals: Nontrivial Interplay Between Electronic Liquid Crystal Order and Topological Order in Correlated Topological Flat Bands*. 2024. arXiv: 2401.00363 [cond-mat.str-el].

[221] Hongyu Lu et al. *Interaction-driven Roton Condensation in C = 2/3 Fractional Quantum Anomalous Hall State*. 2024. arXiv: 2403.03258 [cond-mat.str-el].

[222] Trithep Devakul et al. "Magic in twisted transition metal dichalcogenide bilayers". In: *Nature communications* 12.1 (2021), p. 6730. URL: https://doi.org/10.1038/s41467-021-27042-9.

[223] Jie Wang, Semyon Klevtsov, and Zhao Liu. "Origin of model fractional Chern insulators in all topological ideal flatbands: Explicit color-entangled wave function and exact density algebra". In: *Phys. Rev. Res.* 5 (2 2023), p. 023167. DOI: 10.1103/PhysRevResearch.5.023167. URL: https://link.aps.org/doi/10.1103/PhysRevResearch.5.023167.

[224] Junkai Dong et al. "Composite Fermi Liquid at Zero Magnetic Field in Twisted $MoTe_2$". In: *Phys. Rev. Lett.* 131 (13 2023), p. 136502. DOI: 10.1103/PhysRevLett.131.136502. URL: https://link.aps.org/doi/10.1103/PhysRevLett.131.136502.

[225] Valentin Crépel and Liang Fu. "Anomalous Hall metal and fractional Chern insulator in twisted transition metal dichalcogenides". In: *Phys. Rev. B* 107 (20 2023), p. L201109. DOI: 10.1103/PhysRevB.107.L201109. URL: https://link.aps.org/doi/10.1103/PhysRevB.107.L201109.

[226] Xue-Yang Song, Ya-Hui Zhang, and T. Senthil. "Phase transitions out of quantum Hall states in moiré materials". In: *Phys. Rev. B* 109 (8 2024), p. 085143. DOI: 10.1103/PhysRevB.109.085143. URL: https://link.aps.org/doi/10.1103/PhysRevB.109.085143.

[227] Xue-Yang Song et al. "Intertwined fractional quantum anomalous Hall states and charge density waves". In: *Phys. Rev. B* 109 (11 2024), p. 115116. DOI: 10.1103/PhysRevB.109.115116. URL: https://link.aps.org/doi/10.1103/PhysRevB.109.115116.

[228] Aidan P. Reddy et al. "Fractional quantum anomalous Hall states in twisted bilayer $MoTe_2$ and WSe_2". In: *Phys. Rev. B* 108 (8 2023), p. 085117. DOI: 10.

1103/PhysRevB.108.085117. URL: https://link.aps.org/doi/10.1103/PhysRevB.108.085117.

[229] Nicolás Morales-Durán et al. "Pressure-enhanced fractional Chern insulators along a magic line in moiré transition metal dichalcogenides". In: *Phys. Rev. Res.* 5 (3 2023), p. L032022. DOI: 10.1103/PhysRevResearch.5.L032022. URL: https://link.aps.org/doi/10.1103/PhysRevResearch.5.L032022.

[230] D. N. Sheng et al. *Quantum anomalous Hall crystal at fractional filling of moiré superlattices*. 2024. arXiv: 2402.17832 [cond-mat.mes-hall].

[231] Cheng Xu et al. "Maximally localized Wannier functions, interaction models, and fractional quantum anomalous Hall effect in twisted bilayer MoTe₂". In: *Proceedings of the National Academy of Sciences* 121.8 (2024), e2316749121. DOI: 10.1073/pnas.2316749121. eprint: https://www.pnas.org/doi/pdf/10.1073/pnas.2316749121. URL: https://www.pnas.org/doi/abs/10.1073/pnas.2316749121.

[232] Jiabin Yu et al. *Fractional Chern Insulators vs. Non-Magnetic States in Twisted Bilayer $MoTe_2$*. 2023. arXiv: 2309.14429 [cond-mat.mes-hall].

[233] Vladimir Borisovich Berestetskii, Evgenii Mikhailovich Lifshitz, and Lev Petrovich Pitaevskii. *Quantum Electrodynamics: Volume 4*. Vol. 4. Butterworth-Heinemann, 1982.

[234] J. A. Crosse et al. "Hofstadter butterfly and the quantum Hall effect in twisted double bilayer graphene". In: *Phys. Rev. B* 102 (3 2020), p. 035421. DOI: 10.1103/PhysRevB.102.035421. URL: https://link.aps.org/doi/10.1103/PhysRevB.102.035421.

[235] Pilkyung Moon and Mikito Koshino. "Electronic properties of graphene/hexagonal-boron-nitride moiré superlattice". In: *Phys. Rev. B* 90 (15 2014), p. 155406. DOI: 10.1103/PhysRevB.90.155406. URL: https://link.aps.org/doi/10.1103/PhysRevB.90.155406.

[236] R. Bistritzer and A. H. MacDonald. "Moiré butterflies in twisted bilayer graphene". In: *Phys. Rev. B* 84 (3 2011), p. 035440. DOI: 10.1103/PhysRevB.84.035440. URL: https://link.aps.org/doi/10.1103/PhysRevB.84.035440.

[237] Kasra Hejazi, Chunxiao Liu, and Leon Balents. "Landau levels in twisted bilayer graphene and semiclassical orbits". In: *Phys. Rev. B* 100 (3 2019), p. 035115. DOI: 10.1103/PhysRevB.100.035115. URL: https://link.aps.org/doi/10.1103/PhysRevB.100.035115.

[238] Biao Lian, Fang Xie, and B. Andrei Bernevig. "Landau level of fragile topology". In: *Physical Review B* 102.4 (2020). ISSN: 24699969. DOI: 10.1103/PhysRevB.102.041402.

[239] Biao Lian, Fang Xie, and B. Andrei Bernevig. "Open momentum space method for the Hofstadter butterfly and the quantized Lorentz susceptibility". In: *Physical Review B* 103.16 (2021). ISSN: 24699969. DOI: 10.1103/PhysRevB.103.L161405. arXiv: 2102.04479.

[240] Douglas R. Hofstadter. "Energy levels and wave functions of Bloch electrons in rational and irrational magnetic fields". In: *Phys. Rev. B* 14 (6 1976), pp. 2239–

2249. DOI: 10.1103/PhysRevB.14.2239. URL: https://link.aps.org/doi/10.1103/PhysRevB.14.2239.

[241] Matthew Yankowitz et al. "Emergence of superlattice Dirac points in graphene on hexagonal boron nitride". In: *Nature physics* 8.5 (2012), pp. 382–386. URL: https://doi.org/10.1038/nphys2272.

[242] Jeil Jung et al. "Ab initio theory of moiré superlattice bands in layered two-dimensional materials". In: *Phys. Rev. B* 89 (20 2014), p. 205414. DOI: 10.1103/PhysRevB.89.205414. URL: https://link.aps.org/doi/10.1103/PhysRevB.89.205414.

[243] Pei Zhao, Chengxin Xiao, and Wang Yao. "Universal superlattice potential for 2D materials from twisted interface inside h-BN substrate". In: *npj 2D Materials and Applications* 5.1 (2021), p. 38. URL: https://doi.org/10.1038/s41699-021-00221-4.

[244] Dong Seob Kim et al. "Electrostatic moiré potential from twisted hexagonal boron nitride layers". In: *Nature materials* 23.1 (2024), pp. 65–70. URL: https://doi-org.eproxy.lib.hku.hk/10.1038/s41563-023-01637-7.

[245] SL Moore et al. "Nanoscale lattice dynamics in hexagonal boron nitride moiré superlattices". In: *Nature Communications* 12.1 (2021), p. 5741. URL: https://doi-org.eproxy.lib.hku.hk/10.1038/s41467-021-26072-7.

[246] GH Wannier. "A result not dependent on rationality for Bloch electrons in a magnetic field". In: *physica status solidi (b)* 88.2 (1978), pp. 757–765. URL: https://doi.org/10.1002/pssb.2220880243.

[247] SG Xu et al. "Giant oscillations in a triangular network of one-dimensional states in marginally twisted graphene". In: *Nature communications* 10.1 (2019), p. 4008. URL: https://doi.org/10.1038/s41467-019-11971-7.

[248] Fanrong Lin et al. "Heteromoiré engineering on magnetic Bloch transport in twisted graphene superlattices". In: *Nano Letters* 20.10 (2020), pp. 7572–7579. URL: https://doi.org/10.1021/acs.nanolett.0c03062.

[249] Robin Huber et al. "Band conductivity oscillations in a gate-tunable graphene superlattice". In: *Nature Communications* 13.1 (2022), p. 2856. URL: https://doi.org/10.1038/s41467-022-30334-3.

[250] Mark EJ Newman and Gerard T Barkema. *Monte Carlo methods in statistical physics*. Clarendon Press, 1999.

[251] Ramamurti Shankar. *Quantum field theory and condensed matter: an introduction*. Cambridge University Press, 2017.

[252] Eduardo Fradkin. *Field theories of condensed matter physics*. Cambridge University Press, 2013.

[253] Alexander Altland and Ben D Simons. *Condensed matter field theory*. Cambridge university press, 2010.

[254] David Poland, Slava Rychkov, and Alessandro Vichi. "The conformal bootstrap: Theory, numerical techniques, and applications". In: *Rev. Mod. Phys.* 91 (1 2019), p. 015002. DOI: 10.1103/RevModPhys.91.015002. URL: https://link.aps.org/doi/10.1103/RevModPhys.91.015002.

[255] Paul Ginsparg. *Applied Conformal Field Theory*. 1988. arXiv: hep-th/9108028 [hep-th].

[256] Philippe Francesco, Pierre Mathieu, and David Sénéchal. *Conformal field theory*. Springer Science & Business Media, 2012.

[257] Howard Georgi. *Lie algebras in particle physics: from isospin to unified theories*. Taylor & Francis, 2000.

[258] Hui Shao and Anders W. Sandvik. "Progress on stochastic analytic continuation of quantum Monte Carlo data". In: *Physics Reports* 1003 (2023). Progress on stochastic analytic continuation of quantum Monte Carlo data, pp. 1–88. ISSN: 0370-1573. DOI: https://doi.org/10.1016/j.physrep.2022.11.002. URL: https://www.sciencedirect.com/science/article/pii/S0370157322003921.